

DOCTORAL THESIS

Development of Applications for
High-Field Non-Hydrogenative
Parahydrogen Induced
Hyperpolarization for the
Analysis of Biological Fluids with
Nuclear Magnetic Resonance
Spectroscopy

Nele Reimets

TALLINN UNIVERSITY OF TECHNOLOGY
DOCTORAL THESIS
64/2024

Development of Applications for High-Field Non-Hydrogenative Parahydrogen Induced Hyperpolarization for the Analysis of Biological Fluids with Nuclear Magnetic Resonance Spectroscopy

NELE REIMETS



TALLINN UNIVERSITY OF TECHNOLOGY

School of Science

Department of Cybernetics

NATIONAL INSTITUTE OF CHEMICAL PHYSICS AND BIOPHYSICS

Laboratory of Chemical Physics

This dissertation was accepted for the defence of the degree Applied Physics and Mathematics
11/09/2024

Supervisor:

Dr Indrek Reile
Laboratory of Chemical Physics
National Institute of Chemical Physics and Biophysics
Tallinn, Estonia

Co-supervisor:

Dr Kerti Ausmees
Laboratory of Chemical Physics
National Institute of Chemical Physics and Biophysics
Tallinn, Estonia

Opponents:

Ms Anu M. Kantola
NMR Research Unit
Faculty of Science
University of Oulu
Oulu, Finland

Prof Tomasz Ratajczyk
Applied NMR group
Institute of Physical Chemistry
Polish Academy of Sciences
Warsaw, Poland

Defence of the thesis: 05/12/2024, Tallinn

Declaration:

Hereby I declare that this doctoral thesis, my original investigation and achievement, submitted for the doctoral degree at Tallinn University of Technology has not been submitted for doctoral or equivalent academic degree.

Nele Reimets



signature

Copyright: Nele Reimets, 2024

ISSN 2585-6898 (publication)

ISBN 978-9916-80-223-6 (publication)

ISSN 2585-6901 (PDF)

ISBN 978-9916-80-224-3 (PDF)

DOI <https://doi.org/10.23658/taltech.64/2024>

Printed by Koopia Niini & Rauam

Reimets, N. (2024). *Development of Applications for High-Field Non-Hydrogenative Parahydrogen Induced Hyperpolarization for the Analysis of Biological Fluids with Nuclear Magnetic Resonance Spectroscopy* [TalTech Press]. <https://doi.org/10.23658/taltech.64/2024>

TALLINNA TEHNIKAÜLIKOO
DOKTORITÖÖ
64/2024

**Paravesinikul põhineva mittehüdrogeeniva
hüperpolarisatsiooni-meetodi rakenduste
arendamine bioloogiliste vedelike analüüsiks
kõrges magnetväljas**

NELE REIMETS



Contents

List of Publications	7
Author's Contribution to the Publications	8
Introduction	9
Abbreviations	10
1 Theoretical Principles	11
1.1 Introduction to NMR Spectroscopy	11
1.1.1 Principles of NMR Spectroscopy	11
1.1.2 NMR Spectrum	14
1.2 Hyperpolarization	16
1.2.1 Parahydrogen	17
1.2.2 Parahydrogen-induced Polarization (PHIP)	19
1.2.3 Signal Amplification By Reversible Exchange (SABRE)	20
1.2.4 HF-nhPHIP Chemosensing	22
1.2.5 2D Zero-quantum Spectroscopy	24
1.3 Hyperpolarization in Biological Samples	31
1.3.1 The Future of HF-nhPHIP	32
2 Aims of the Study	33
3 Results and Discussion	34
3.1 Quantification and Identification of Analytes in Human Urine (Publication I)	34
3.1.1 Sample Preparation for the Targeted Approach	36
3.1.2 Determining Concentration Based on HF-nhPHIP Signals	41
3.1.3 Sample Preparation for the Untargeted Approach (Publication II)	43
3.2 Widening the Scope to Biopolymers (Publication III)	46
3.2.1 The Role of Co-substrate in HF-nhPHIP Chemoselectivity	46
3.2.2 Analysis of Oligopeptides Binding to the Iridium Catalyst	48
3.3 Optimization of Experimental Conditions	54
3.3.1 Creation of Hydrides Chemical Shift Database (Publication IV)	56
3.4 Comparative Analysis of Human and Dog Urine (Publication V)	58
4 Materials and Methods	67
4.1 Sample Preparation Methods for the Comparative Analysis of Human and Dog Urine	67
5 Summary	69
List of Figures	70
References	76
Acknowledgements	82
Abstract	83
Lühikokkuvõte	84
Appendix 1	85
Appendix 2	93
Appendix 3	99

Appendix 4	111
Appendix 5	123
Curriculum vitae.....	130
Elulookirjeldus.....	131

List of Publications

The list of author's publications, on the basis of which the thesis has been prepared:

- I Reimets, N.; Ausmees, K.; Vija, S.; Reile, I. Developing Analytical Applications for Parahydrogen Hyperpolarization: Urinary Elimination Pharmacokinetics of Nicotine. *Anal. Chem.* 2021, 93 (27), 9480–9485. <https://doi.org/10.1021/acs.analchem.1c01281>
- II Ausmees, K.; Reimets, N.; Reile, I. Parahydrogen Hyperpolarization of Minimally Altered Urine Samples for Sensitivity Enhanced NMR Metabolomics. *Chem. Commun.* 2022, 58 (3), 463–466. <https://doi.org/10.1039/D1CC05665D>
- III Reimets, N.; Ausmees, K.; Vija, S.; Trummal, A.; Uudsemaa, M.; Reile, I. Parahydrogen Hyperpolarized NMR Detection of Underivatized Short Oligopeptides. *Analyst* 2023, 148 (21), 5407–5415. <https://doi.org/10.1039/D3AN01345F>
- IV Ausmees, K.; Reimets, N.; Reile, I. Understanding Parahydrogen Hyperpolarized Urine Spectra: The Case of Adenosine Derivatives. *Molecules* 2022, 27 (3), 802. <https://doi.org/10.3390/MOLECULES27030802>
- V Reimets, N.; Ausmees, K.; Reile, I. Current State of the Art of Analyte Scope in Urine Metabolome Analysis by Non-Hydrogenative PHIP. *Journal of Magnetic Resonance Open*, 2024, 21, 100171. <https://doi.org/10.1016/j.jmro.2024.100171>

Author's Contribution to the Publications

Contribution to the papers in this thesis are:

- I Research design, data collection, data analysis, writing – original draft preparation, writing – review & editing, visualization
- II data collection, visualization
- III Research design, data collection, data analysis, writing – original draft preparation, writing – review & editing, visualization
- IV sample preparation, data collection
- V Research design, data collection, data analysis, writing – original draft preparation, writing – review & editing, visualization

Introduction

Nuclear magnetic resonance spectroscopy (NMR) is a widely used analytical tool in different research fields ranging from chemistry and biology to medicine and material sciences. NMR enables chemical structure analysis with the ability to quantify analytes within a sample. It has high reproducibility and it is non-destructive to the sample. However, the major problem with NMR lays in its low sensitivity, which makes signal detection of dilute samples time-consuming and unreasonable or in some cases completely impossible.

The sensitivity issue has been addressed by improving the hardware, software, and developing new measurement schemes. Regular NMR still has a limit of detection in micromolar concentration range, which is a problem as numerous compounds present in biological samples (e.g. urine) are more than an order of magnitude below that concentration. Advancements in engineering have introduced better equipment and magnets with stronger magnetic fields, nevertheless, these don't offer orders of magnitude improvements in signal intensity compared to the 21st century modern high field magnets.

On the other hand, the use of hyperpolarization techniques has had a significant impact on the advancement of NMR spectroscopy by improving its sensitivity. Among a variety of different hyperpolarization techniques, high-field non-hydrogenative PHIP (HF-nhPHIP) stands out for its robust setup. By using a singlet form of hydrogen gas, parahydrogen, NMR signal sensitivity is enhanced over 1000-fold and hence, allows the analysis of dilute samples. This thesis focuses on HF-nhPHIP, exploring its novel applications in analysing complex biological fluids.

The thesis covers how HF-nhPHIP can be utilized to study biological fluids and what information can be drawn from the obtained NMR spectra. Chapter 3.1 explains in detail how the analytical accuracy of HF-nhPHIP was achieved (Publication I) and what are the requirements to move towards metabolomics analysis (Chapter 3.1.3, Publication II).

Chapter 3.2.1 discusses how the chemoselectivity of HF-nhPHIP catalyst can be tuned to detect specific analytes. In Chapter 3.2.2, the application of HF-nhPHIP as a method to detect oligopeptides is discussed, acknowledging the difficulties involved in short peptide analysis (Publication III).

A set of guidelines on what to consider when using HF-nhPHIP approach is given in Chapter 3.3. Different sample preparation techniques are presented, which can be used to employ the HF-nhPHIP in targeted and untargeted analysis of complex biological samples. The development of methodologies for targeted and untargeted analysis represents a promising advancement of using NMR in the fields of metabolomics, pharmaceutical industry, and non-invasive diagnostics.

Chapter 3.3.1 presents a straightforward method for quick and easy signal assignment using a database (Publication IV).

Moving beyond the analysis of human urine, Chapter 3.4 of the thesis discusses the data extracted from HF-nhPHIP spectra of canine and human urine samples (Publication V).

Abbreviations

Ade	adenosine
ADP	adenosine diphosphate
AMP	adenosine monophosphate
ATP	adenosine triphosphate
DNP	dynamic nuclear polarization
dDNP	dissolution dynamic nuclear polarization
DFT	density-functional theory
DMP	2,6-dimethyl pyrazine
DQ	double-quantum coherence
FVAPFP	hexapeptide-11 consisting of amino acids Phe-Val-Ala-Pro-Phe-Pro
GGYR	papain inhibitor consisting of amino acids Gly-Gly-Tyr-Arg
HF-nhPHIP	high field non-hydrogenative PHIP
mtz	methyltriazole
nam	nicotinamide
NMR	nuclear magnetic resonance
NOE	nuclear Overhauser effect
pH	symbol for the acidity or alkalinity of a solution
pH ₂	parahydrogen
PHIP	parahydrogen induced hyperpolarization
ppm	parts per million
SABRE	signal amplification by reversible exchange
SPE	solid phase extraction
SQ	single-quantum coherence
ZQ	zero-quantum coherence
YGGFL	Leu-enkephalin consisting of amino acids Tyr-Gly-Gly-Phe-Leu
1-mAde	1-methyladenosine
2'-O-mAde	2'-O-methyladenosine
6N-mAde	6N-methyladenosine

1 Theoretical Principles

1.1 Introduction to NMR Spectroscopy

1.1.1 Principles of NMR Spectroscopy

Magnetic resonance is a physical phenomenon where atomic nuclei or electrons respond to magnetic fields by emitting or absorbing electromagnetic radiation. In nuclear magnetic resonance, we consider the electromagnetic interactions of a nucleus.

The nucleus of an atom has electromagnetic interactions with its surrounding – electrostatic because of charge, and magnetic because of magnetic dipole moment determined by nuclear spin quantum number. Depending on the number of protons and neutrons, the nucleus may have a zero or a non-zero nuclear spin quantum number (I). If the number of protons and neutrons is even, the nuclear spin quantum number is $I = 0$ (^{12}C , ^{16}O). However, if the number of protons and neutrons is odd, the nuclear spin quantum number can have an integer, e.g. $I = 1$ (^2H) or a half-integer value, e.g. $I = 1/2$ (^1H , ^{13}C , ^{15}N), $I = 5/2$ (^{17}O). A nucleus which has a non-zero nuclear spin possesses a magnetic dipole moment (Figure 1).¹

The nuclear magnetic moment (or nuclear magnetic dipole moment), μ is a vector quantity that represents the strength and orientation of a nucleus's magnetic field. It depends on the nuclear spin angular momentum \hat{I} , and nucleus specific gyromagnetic ratio γ (Equation 1).

$$\mu = \gamma \hat{I} \quad (1)$$

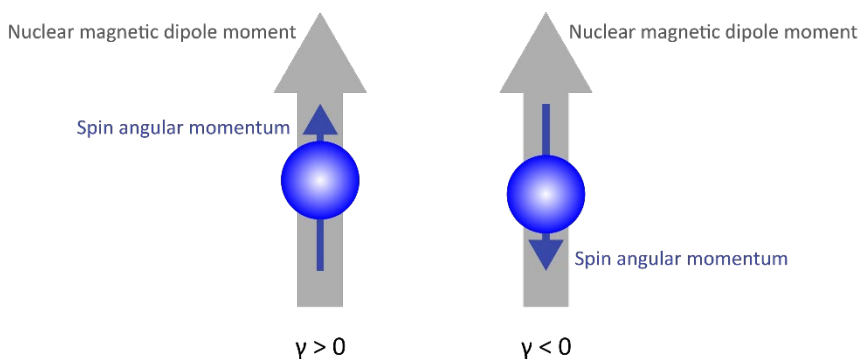


Figure 1. The nuclear magnetic dipole moment μ is determined by the nuclear spin angular momentum \hat{I} and nucleus specific gyromagnetic ratio γ .

The nuclear magnetic dipole moment determines how nuclei interact with external magnetic fields. When a nucleus with a non-zero magnetic moment is placed in an NMR magnet, it experiences a torque that tends to align its magnetic moment with the field. Because of the nuclear magnetic dipole moment and the nuclear spin states, the energy levels become quantized (distinct). The number of possible energy levels is determined by $2I + 1$ from Zeeman splitting (Figure 2). The quantization of energy levels is a fundamental aspect of quantum mechanics and is crucial for phenomena such as nuclear magnetic resonance (NMR) and electron spin resonance (ESR). In NMR, transitions between these quantized energy levels occur when the nucleus absorbs or emits

electromagnetic radiation of a frequency that matches the energy difference between the levels.

The mathematical description of the interaction between spin and magnetic fields is given by Hamiltonians. The nuclear spin Hamiltonian, denoted as $\hat{\mathcal{H}}$, represents the total energy operator for a system of nuclear spins and describes how the energy levels of the nuclear spins are affected by various interactions within the system (2).

$$\hat{\mathcal{H}} = \hat{\mathcal{H}}^{elec} + \hat{\mathcal{H}}^{mag} \quad (2)$$

It turns out that for nuclei with the nuclear spin quantum number $I = 1/2$, electric interactions vanish, $\hat{\mathcal{H}}^{elec} = 0$, as they do not depend on the orientation of the nucleus.¹ Therefore, for spin= $1/2$ nuclei, e.g. ^1H , ^{13}C , ^{15}N , ^{31}P , common atoms present in biological substances, only magnetic interactions, $\hat{\mathcal{H}}^{mag}$, need to be considered.

In the case of protons, which have $\gamma > 0$, the nuclear magnetic energy is lowest when the magnetic moment $\boldsymbol{\mu}$ aligns with the magnetic field \mathbf{B} , and highest when the magnetic moment is in the opposite direction.¹

$$\hat{\mathcal{H}}^{mag} = -\boldsymbol{\mu} \cdot \mathbf{B} \quad (3)$$

Conventionally, the external magnetic field \mathbf{B}_0 generated by the NMR magnet is along z-axis (Cartesian coordinates) and the minimal nuclear magnetic energy Hamiltonian is simply

$$\hat{\mathcal{H}}_{one\ spin} = -\gamma B_0 \hat{I}_z \quad (4)$$

where \hat{I}_z is a quantum mechanical operator that represents the component of nuclear spin angular momentum along the direction of the external magnetic field. The wavefunctions of this Hamiltonian are described by the eigenfunctions. There can be $2I + 1$ wavefunctions for the quantum mechanical operator \hat{I}_z . Eigenfunctions are dependent on the quantum number m , which can have values from $-I$ to $+I$ in integer steps.² This means that for spin= $1/2$ nuclei, m can be either $-\frac{1}{2}$ or $+\frac{1}{2}$ resulting in two eigenfunctions, $\psi_{+\frac{1}{2}}$ and $\psi_{-\frac{1}{2}}$. The eigenvalues of these eigenfunctions are the available energy levels. For convenience the energy levels are labelled as E_α and E_β :

$$E_\alpha = -\frac{1}{2} \hbar \gamma B_0 \quad (5)$$

$$E_\beta = +\frac{1}{2} \hbar \gamma B_0 \quad (6)$$

The energy difference between the allowed energy levels E_α and E_β is related to the Larmor frequency ω_0 (in rad s^{-1}) of a nucleus. Larmor frequency is proportional to the external magnetic field (Equation 7).

$$\omega_0 = -\gamma B_0 \quad (7)$$

Expressed in hertz (Hz), Larmor frequency ν_0 is defined as

$$\nu_0 = \frac{-\gamma B_0}{2\pi} \quad (8)$$

When spin= $\frac{1}{2}$ nuclei are placed in a magnetic field (like NMR magnet), Zeeman splitting introduces two energy levels: E_α and E_β (Equations 5 and 6), where spins tend to align either parallel (α -state) or antiparallel (β -state) with respect to the magnetic field (Figure 2). The population difference of nuclear spins aligned with or against an external magnetic field determines polarization (Equation 9). Higher polarization means there is a greater difference between the populations of the lower and higher energy nuclear spin states, leading to an enhanced NMR signal. Polarization is described by

$$p = \text{sgn}(\gamma) \frac{N_\alpha - N_\beta}{N_\alpha + N_\beta} \quad (9)$$

where N_α and N_β represent the number of spins in the respective state and $\text{sgn}(\gamma)$ is the sign of gyromagnetic ratio.

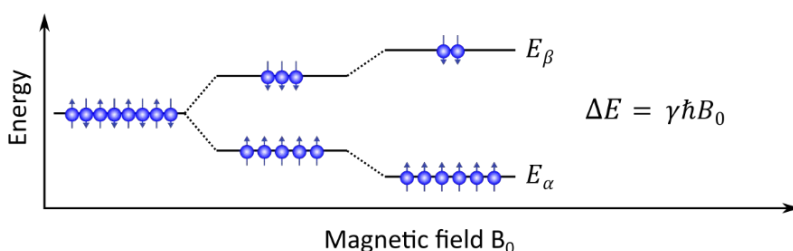


Figure 2. According to Zeeman splitting spin= $\frac{1}{2}$ nucleus has $2\frac{1}{2} + 1 = 2$ energy levels E_α and E_β , when placed in an NMR magnet with a magnetic field B_0 . At thermal equilibrium spins form an anisotropic distribution with a bias towards low magnetic energy state, which for $\gamma > 0$ like ^1H nucleus is E_α . This partial orientation along the magnetic field follows Boltzmann distribution and determines the level of polarization in the sample. The polarization increases as the strength of the external magnetic field increases.

The nuclear spins' tendency to align with the external magnetic field gives rise to net magnetic moment, also referred as longitudinal magnetization \mathbf{M} (Figure 3a). It is the vector sum of the individual magnetic moments of the nuclei with a non-zero spin. This net magnetization is central to NMR, as its manipulation through radiofrequency (RF) pulses and its subsequent relaxation produces the NMR signal. RF energy is used in NMR because it induces transitions between energy levels E_α and E_β without causing other types of molecular excitation.

To manipulate the aligned spins, a short-duration RF pulse is applied perpendicular to the static magnetic field B_0 and the longitudinal magnetization \mathbf{M} . The frequency of this RF pulse will be approximately equal to the Larmor frequency of the nuclear spins. On resonance RF pulse generates a magnetic field, which exceeds the B_0 field. This effectively tilts \mathbf{M} away from its initial alignment. The angle of rotation is determined by the duration and strength of the applied RF pulse.

The simplest NMR experiment uses a single 90° pulse. The spins are initially coherently aligned with z-axis (Figure 3a). After applying a 90° pulse ($\pi/2$ radians), they experience a rotation about x-axis, the net magnetization of spins will be along $-y$ -axis (Figure 3b). This creates a transverse magnetization. Initially, spins will precess around the z-axis at the Larmor frequency, but after a while, they will lose their coherence. This makes the transverse magnetization decay and longitudinal magnetization form along the z-axis due to spins realignment with the magnetic field (Figure 3c). During this process, oscillating magnetization vector \mathbf{M} generates detectable electric current in the receiver coil. This electric current can be drawn as a decaying sine wave as the nuclei realign. The wave is called free induction decay (FID) and is detected in time-domain by the NMR receiver coil, after which it is transformed to the frequency-domain using Fourier transformation to generate a conventional NMR spectrum.

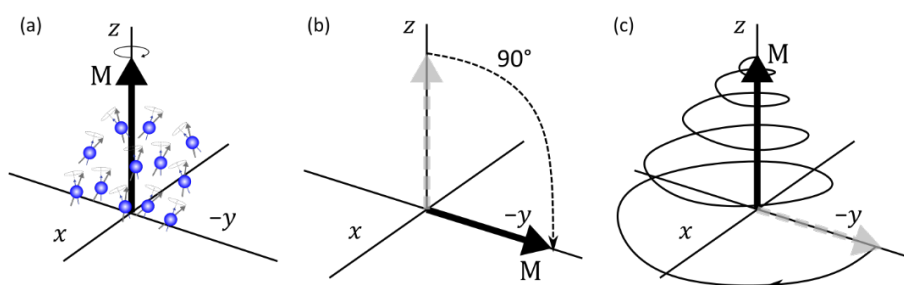


Figure 3. (a) Atomic nuclei partially align with the external magnetic field \mathbf{B}_0 and create a net magnetic moment, \mathbf{M} . (b) A short-duration radio frequency pulse rotates \mathbf{M} to the xy -plane, creating transverse magnetization. The field \mathbf{B}_0 generates torque on \mathbf{M} and makes nuclei precess at Larmor frequency. (c) After a while, spins lose their coherence, transverse net magnetization decays, and spins realign with \mathbf{B}_0 . During that process, oscillating magnetization vector creates electric current, which is detected in the receiver coil to get a spectrum.

1.1.2 NMR Spectrum

The electrons orbiting nuclei generate a secondary magnetic field that opposes \mathbf{B}_0 , effectively diminishing the magnetic field strength directly experienced by the nucleus. This slightly attenuated magnetic field is termed the effective magnetic field, \mathbf{B}_{eff} , and its strength varies among atoms with different chemical environments, influenced by the electron density surrounding the nucleus. The presence of neighbouring electronegative atoms (e.g., F, O, N, Cl, Br, etc.) that withdraw electrons modify the chemical environment surrounding the nucleus. In NMR, the phenomenon is known as shielding.

Because of the shielding effect, the structure of a molecule can be determined as different functional groups (e.g. CH_3 , CH_2 , OH) resonate at slightly different frequencies. To compare the frequencies of those functional groups without depending on the magnetic field strength chemical shift is used. The chemical shift δ is quantified in parts per million (ppm) as the difference between the resonance frequency of a nucleus (ν) and the reference frequency (ν_{ref}), often using tetramethylsilane (TMS) as the reference (Equation 10).

$$\delta = 10^6 \times \frac{\nu - \nu_{ref}}{\nu_{ref}} \quad (10)$$

Chemical shifts are useful for distinguishing between different chemical environments within molecules and determining molecular structures (Figure 4). The range of chemical shifts varies significantly among atoms, with typical ranges being 0–10 ppm for ^1H , 0–200 ppm for ^{13}C , and –250 to 250 ppm for ^{31}P . The stronger the magnetic field, the greater the separations between chemical shifts. For instance, if the chemical shift difference between two NMR peaks is 1 ppm, at 4.7 T magnet (from Equation 8) ^1H Larmor frequency is 200 MHz) this difference translates to a frequency separation of 200 Hz. At 18.8 T (800 MHz), the separation increases to 800 Hz, and at 28.2 T (1.2 GHz), it further increases to 1200 Hz. Thus, higher field magnets enhance resolution, facilitating more precise differentiation between closely related chemical environments within a molecule.

Besides chemical shift, spin-spin coupling, also known as J-coupling or scalar coupling, helps to unravel the NMR spectrum by providing detailed information about the molecular structure and the environment of nuclei within a molecule (Figure 4). Spin-spin coupling arises from the indirect interaction between the magnetic moments of nuclei through the bonding electrons that link them. The coupling constant J , which is measured in hertz (Hz) quantifies the strength of the spin-spin coupling. The value of J provides information about the spatial relationship and the bonding environment between the coupled nuclei, as it depends on the bond angle, bond length, and the type of atoms involved. Spin-spin coupling leads to the splitting of NMR signals into multiplets (doublets, triplets, quartets, etc.), depending on the number of neighbouring nuclei (n) with which a nucleus is coupled, and their spin quantum numbers (I). The number of peaks in a multiplet is given by $2nI + 1$ for equivalent nuclei. For spin= $\frac{1}{2}$ nuclei this would simply be $n + 1$ (Figure 4).

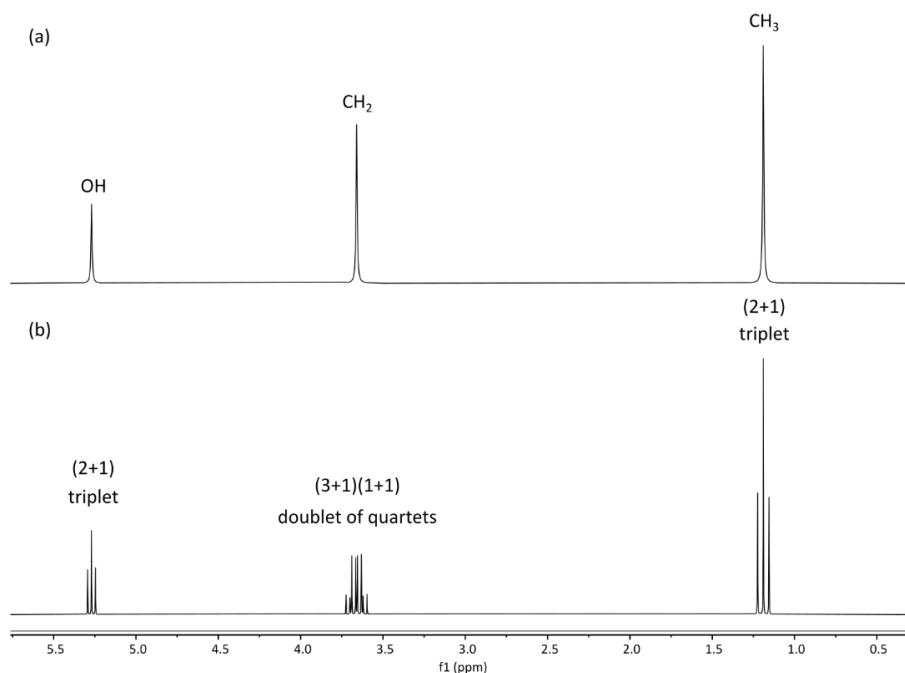


Figure 4. A simulated ^1H spectrum of ethanol ($\text{CH}_3\text{CH}_2\text{OH}$). The effect of electron shielding gives rise to three peaks, which represent three different chemical environments in a molecule. (a) If there would not be any spin-spin coupling between the spins. (b) In the case of spin-spin coupling, the signals are split into a triplet, doublet of quartets, and a triplet because of neighbouring nuclei ($n+1$) rule.

The intensity I of the NMR signal depends on various factors:

$$I \propto \frac{N_\alpha - N_\beta}{N_\alpha + N_\beta} = \tanh\left(\frac{\hbar\gamma B_0}{2kT}\right) \quad (11)$$

Here, N_α and N_β represent the number of spins in the respective state, \hbar is the reduced Planck's constant, γ is the gyromagnetic ratio of the nucleus, B_0 is the strength of the external magnetic field, k is the Boltzmann constant, T is the absolute temperature in Kelvin. The Equation (11) illustrates that signal intensity increases with a greater population difference between the spin states, achievable at lower temperatures, and/or at higher magnetic fields, and/or by observing nuclei with a high gyromagnetic ratio, like ^1H .

However, at room temperature, nuclear spins are almost evenly distributed between the two energy levels. The resulting thermal polarization of protons (^1H) is typically between 10^{-4} to 10^{-5} .³ This small polarization leads to an extremely low net magnetization, resulting in inherently weak NMR signals, challenging for samples at low concentrations. Gains in polarization, and thus signal intensity, can be achieved by changing variables according to Equation (11). Yet, orders of magnitude improvements in NMR sensitivity cannot be achieved. As a result, alternative approaches, known collectively as hyperpolarization techniques, have been developed to significantly enhance NMR signal intensity.

1.2 Hyperpolarization

There is a variety of hyperpolarization techniques,³ which all aim to create a non-equilibrium distribution of nuclear spins, exceeding thermal polarization. For spin= $\frac{1}{2}$ nuclei, this means that population difference between E_α and E_β energy levels is increased (Figure 5), which gives rise to enhanced NMR signals and improved signal-to-noise ratio. The two most widely used hyperpolarization techniques are Dynamic Nuclear Polarization (DNP) and parahydrogen-based methods.

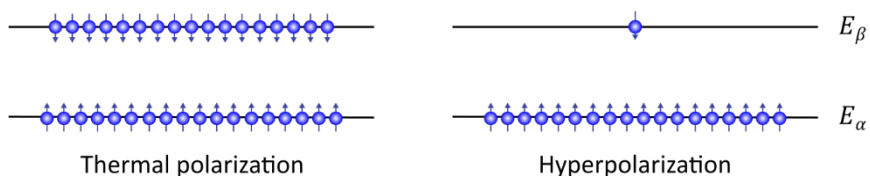


Figure 5. Hyperpolarization techniques manipulate spin states towards a significant population on one energy state. The higher population difference leads to a stronger NMR signal, which improves signal-to-noise ratio and increases sensitivity.

DNP is probably the more well-known out of the two. It was proposed and experimentally showed in 1953,⁴ soon after the discovery of NMR in 1946. DNP produces highly polarized spins using unpaired electrons (radicals) as its hyperpolarization source. Electrons have a much higher magnetic moment because of higher gyromagnetic ratio $\gamma_e = -28\,024.951 \cdot 2\pi \text{ MHz} \cdot \text{T}^{-1}$ compared to nuclear spins $\gamma_{^1\text{H}} = 42.577 \cdot 2\pi \text{ MHz} \cdot \text{T}^{-1}$. This significant difference means that electrons can achieve a higher level of polarization under the same conditions (11). It is worth noting, however, that paired electrons do not contribute a net magnetic moment due to their

opposing spins, which cancel each other out, and thus cannot be similarly polarized. In DNP, a microwave irradiation is used to excite the unpaired electrons and the excess polarization is transferred to nearby nuclear spins, significantly enhancing the nuclear spins' polarization. With the development of strong microwave sources in the 1990s, DNP became widely adopted in solid-state NMR and became commercially available.

In 2003, dissolution-DNP (dDNP) was introduced, expanding hyperpolarization through electrons to liquid samples.⁵ dDNP requires a rather sophisticated setup, including a polarizer (3.4-5 T) that can cool the sample down to 1-2 K, microwave source to irradiate the sample, a transfer line, an NMR magnet, and sometimes an automatic sample injection system (Figure 6).^{6,7} The dDNP workflow consists of minimum five steps. A liquid solution with a molecule of interest and a carrier of unpaired electrons (e.g. nitroxide radicals TEMPOL⁸ and TEMPO⁹) are mixed and cooled in a DNP polarizer to cryogenic temperatures (Figure 6). The solid sample* is then exposed to microwave irradiation to hyperpolarize the nuclear spins. Once polarization is maximized, the solid sample is quickly dissolved in a hot solvent, resulting in a highly polarized liquid solution. The obtained solution is promptly transferred to an NMR magnet through a transfer line for immediate measurement.^{5,10}

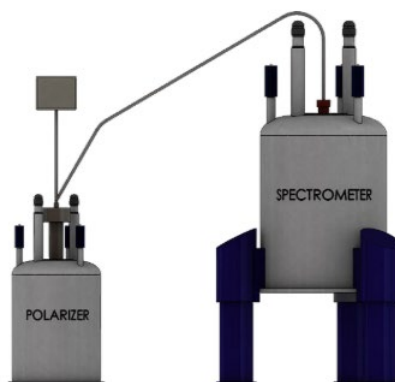


Figure 6. A schematic representation of a dDNP setup. After hyperpolarization in the DNP polarizer the sample is rapidly dissolved and transferred to the NMR magnet for acquisition. Reproduced and modified from ¹¹. Copyright (2021) Elsevier.

While dDNP is a powerful technique for achieving hyperpolarization, it's noteworthy that parahydrogen-based techniques have been around for a longer period.¹²⁻¹⁴ Parahydrogen provides a straightforward alternative for hyperpolarization in solution-state NMR, requiring a less complex and resource-intensive setup compared to dDNP.

1.2.1 Parahydrogen

Molecular hydrogen (H_2) comprises two coupled 1H nuclei. The coupled atoms with $I = 1/2$, form a system, which can be described by a linear combination of two eigenstates: spin up (α -state) and spin down (β -state). Such a system has four combinations[†] of the individual spin states $\alpha\alpha, \alpha\beta, \beta\alpha, \beta\beta$, through which two isomeric

* The sample should remain amorphous, rather than crystalline, during the solid phase to ensure efficient and uniform polarization.

[†] The combined spin states are obtained from tensor product operation in the Hilbert space.

forms, known as orthohydrogen and parahydrogen, can be distinguished. These isomers are characterized by differences in the orientation of their nuclear spins (Figure 7). Orthohydrogen with a total nuclear spin quantum number $I = 1$ and quantum number $m = -1, 0, 1$, gives rise to three triplet spin states (Equation 12)*, and has a symmetric rotational state.

$$I = 1 \begin{cases} |1, 1\rangle = |\alpha\alpha\rangle \\ |1, 0\rangle = \frac{1}{\sqrt{2}}(|\alpha\beta\rangle + |\beta\alpha\rangle) \\ |1, -1\rangle = |\beta\beta\rangle \end{cases} \quad (12)$$

Parahydrogen, denoted as pH₂, possesses a nuclear spin quantum number $I = 0$ and quantum number $m = 0$, resulting in a singlet spin state (Equation 13). Although parahydrogen's nuclear spin quantum number $I = 0$ renders it unobservable by NMR (Chapter 1.1), its highly correlated antisymmetric rotational state provides a unique opportunity for its application as a source of hyperpolarization.

$$I = 0 \begin{cases} |0, 0\rangle = \frac{1}{\sqrt{2}}(|\alpha\beta\rangle - |\beta\alpha\rangle) \end{cases} \quad (13)$$

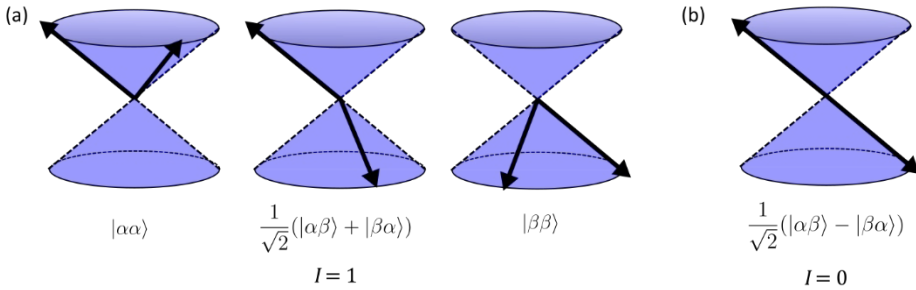


Figure 7. (a) Orthohydrogen and (b) parahydrogen spin isomers of molecular hydrogen. Orthohydrogen has a symmetric rotational state $I = 1$, while parahydrogen has an antisymmetric rotational state $I = 0$.

At room temperature H₂ gas ortho-para spin isomer ratio is 3:1, whereas at low temperatures (below 77 K), the low-energy pH₂ spin state is preferred (Figure 8). To produce 50%-enriched pH₂, hydrogen gas is brought into contact with a ferromagnetic catalyst (e.g. iron(III)oxide)¹⁵ in a liquid nitrogen bath. The catalyst enables fast ortho-para transition and because pH₂ is a long-lived nuclear spin state, it cannot convert back to orthohydrogen spontaneously. This allows to warm pH₂ back to room temperature without losing spin order. In reality, the conversion between ortho and para states happens slowly (over months) due to the presence of paramagnetic impurities such as O₂.

* Wavefunctions ψ_m are presented in Dirac notation.

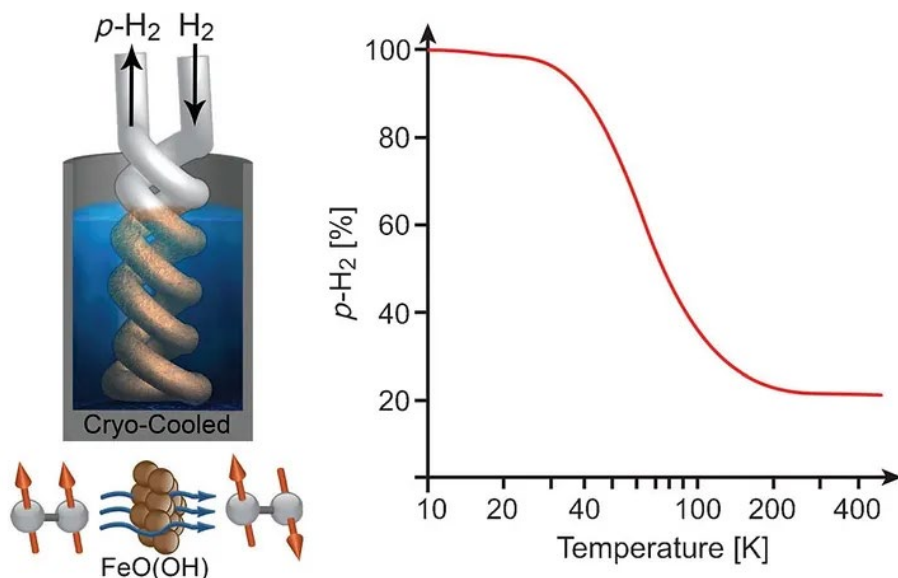


Figure 8. At room temperature (300 K) molecular H_2 gas comprises 75% ortho- and 25% para-isomers. Liquid N_2 temperature (77 K), at the presence of a ferromagnetic catalyst (e.g. iron(III)oxide or charcoal), allows for preparation of 50% pH_2 , whereas temperatures below 20 K enable production of >97% pH_2 fraction. By imbedding pH_2 generator inside a cryogenic storage dewar, pH_2 maintains its long-lived nuclear spin state outside of the dewar.¹⁵ Adapted with permission from ref. ¹⁶. Copyright (2015) Wiley-VCH GmbH, Weinheim.

1.2.2 Parahydrogen-induced Polarization (PHIP)

The first proposal of parahydrogen as a source of hyperpolarization was made by Bowers and Weitekamp in 1986.¹² In 1987, they were also the first to deliberately use pH_2 for NMR signal enhancement. They referred to their experiment as Parahydrogen And Synthesis Allows Dramatic Enhanced Nuclear Alignment (PASADENA).¹³ The PASADENA experiment utilizes pH_2 intrinsic non-equilibrium distribution of nuclear spin populations, described by $2\hat{I}_{1z}\hat{I}_{2z}$, where 1 and 2 refer to the two coupled hydrogen nuclei. For thermal equilibrium, the same notation would be $\hat{I}_{1z} + \hat{I}_{2z}$. Parahydrogen itself is not hyperpolarized, but its correlated spin state can be used to hyperpolarize molecules. When pH_2 is brought into contact with another molecule, the molecular symmetry of pH_2 can be broken.

Bowers and Weitekamp showed that a pair-wise addition of pH_2 to an asymmetrical unsaturated molecule with a double or a triple carbon-carbon bond (alkene or alkyne, respectively) induces hyperpolarization of the molecule.¹² When this is done at a high magnetic field (in an NMR magnet), pH_2 -derived protons become chemically non-equivalent. The transferred singlet state of pH_2 forms new equally populated spin states $\alpha\beta$ and $\beta\alpha$, with allowed transitions to unpopulated states $\alpha\alpha$ and $\beta\beta$ (Figure 9a and b).

Shortly after publishing PASADENA, Pravica and Weitekamp proposed another similar method called ALTADENA (Adiabatic Longitudinal Transport After Dissociation Engenders Nuclear Alignment).¹⁷ In ALTADENA, pH_2 addition and polarization is achieved outside the magnet, while acquisition is still conducted in a high-field NMR magnet for better

signal sensitivity and resolution. The singlet state of pH_2 remains in the molecule after hydrogenation reaction and governs only one eigenstate $\alpha\beta$ with allowed transitions to $\alpha\alpha$ and $\beta\beta$ (Figure 9c).

Since the introduction of ALTADENA and PASADENA, different experiments have been developed to maximize polarization and widen the application scope of pH_2 hyperpolarization. These experiments are commonly referred to as parahydrogen-induced polarization (PHIP).¹⁴

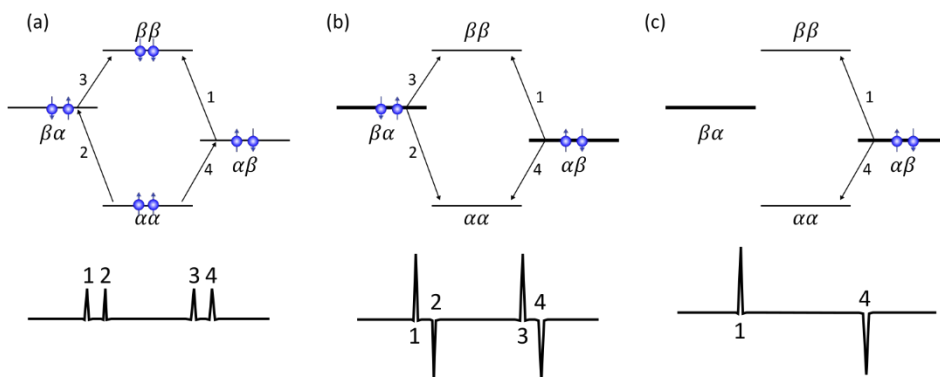


Figure 9. Energy level diagrams with possible transitions and the resulting spectra of (a) thermal polarization experiment with orthohydrogen (b) PASADENA experiment, (c) ALTADENA experiment.

1.2.3 Signal Amplification By Reversible Exchange (SABRE)

While parahydrogen-induced polarization (PHIP) has proven to be a relatively simple and cost-effective hyperpolarization method in NMR, its application is inherently restricted by relying on the hydrogenation of an unsymmetrical alkene or alkyne. In order to address these limitations, a notable advancement emerged in the form of Signal Amplification By Reversible Exchange (SABRE), which was introduced by Adams et al. in 2009.¹⁸ This pioneering approach marked a departure from the necessity of hydrogenation reactions to achieve hyperpolarized NMR signals, presenting a paradigm shift in pH_2 hyperpolarization techniques.

In SABRE, a transient organometallic complex is used to reversibly bind pH_2 and a molecule of interest, referred to as substrate (Figure 10). The antisymmetric spin order of pH_2 is spontaneously transferred through spin-spin interactions (scalar coupling network) to the nuclear spins of the substrate and converted to non-equilibrium magnetization at low magnetic field (outside of the NMR magnet).¹⁸ Hyperpolarized substrate is detected after its dissociation from the metal catalyst. Typical substrates hyperpolarized *via* SABRE are small molecules – pyridine and its derivatives, alkaloids, purines, nitriles, Schiff bases, diazoles, amines, amino acids.^{19,20}

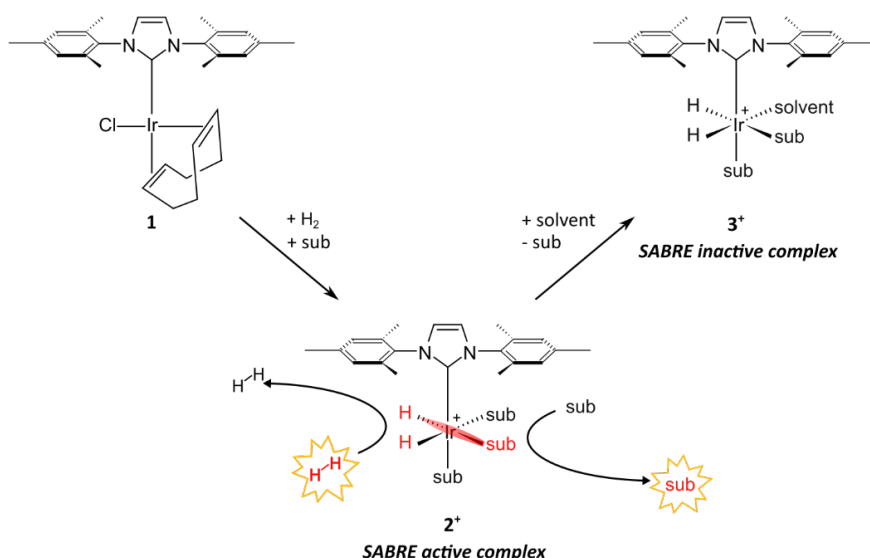


Figure 10. The schematic representation of SABRE. Iridium-based catalyst precursor **1**, $[\text{Ir}(\text{IMes})(\text{COD})\text{Cl}]$, where $\text{IMes} = 1,3\text{-bis}(2,4,6\text{-trimethylphenyl})\text{imidazol-2-ylidene}$, $\text{COD} = \text{cyclooctadiene}$,²¹ is mixed with substrate (sub) under parahydrogen pressure to form an active SABRE complex **2***. The correlated spin order of pH_2 spontaneously transfers to the substrate nuclear spins through J-coupling at low magnetic field. Continuous substrate exchange, association, and disassociation with the metal catalyst leads to the build-up of hyperpolarized substrate free in solution.

The concentration of a substrate has to be much higher than the concentration of the metal catalyst. This ensures that solvent molecules do not bind with the catalyst and consequently the formation of a SABRE inactive complex **3*** is avoided.¹⁹ Eshuis et al. implemented a co-substrate approach to enable hyperpolarization when substrate concentration is much lower than the catalyst precursor (Figure 11).²² They showed that adding a co-substrate, which has a stronger affinity for the iridium catalyst than the solvent, but a weaker affinity than substrates, the polarization transfer is preserved. This enabled to apply SABRE on dilute samples down to nanomolar concentrations.²² If the ratio of

$$[\text{sub}] \ll [\text{catalyst}] < [\text{co-sub}] \quad (14)$$

is violated, solvent molecules can bind with the catalyst and produce inactive complexes.²³

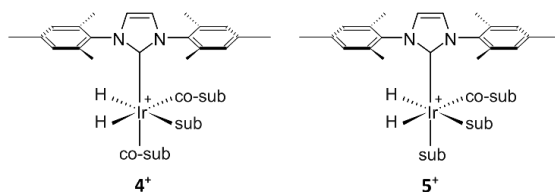


Figure 11. After the hydrogenation of the complex precursor **1**, metal complexes **4*** and **5*** can form at the presence of a co-substrate (co-sub). Provided that the ratio of $[\text{sub}] \ll [\text{catalyst}] < [\text{co-sub}]$ is kept, the formation of complex **5*** is unlikely.

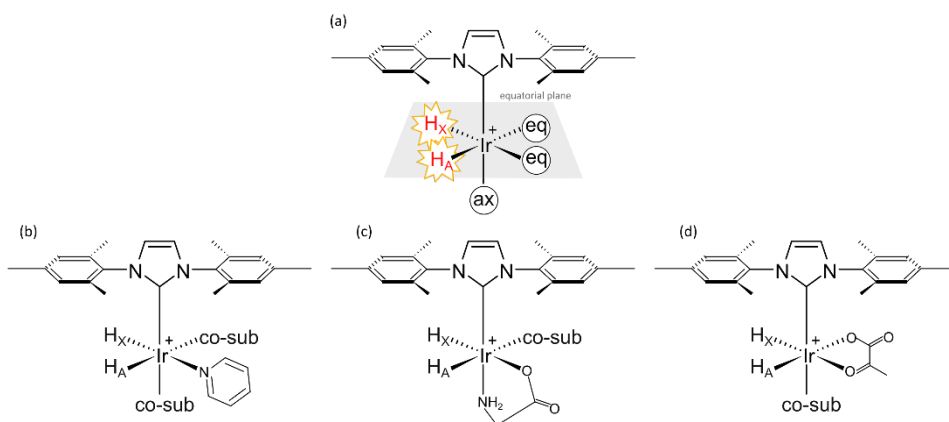


Figure 13. Schematic representation of the HF-nhPHIP complex. a) The iridium catalyst has three vacant binding sites: two in the equatorial plane (eq) and one in the axial position (ax). b) Pyridine associated through N-atom forming a monodentate binding. c) Glycine associated through N- and O-atoms forming a bidentate ax-eq complex. d) Pyruvate associated through O-atoms forming a bidentate eq-eq complex.

The chemical shifts of hydrides reflect the substrate bound to the active complex 4^+ (Figure 12).^{26,30} The resonance frequencies of hydrides fall into -15 to -29 ppm,²⁸ which greatly differs from typical ^1H signals in 0 to 10 ppm region. Based on the specific chemical shifts, it is possible to understand which nucleus is in *trans* position to the hydride in the equatorial plane.^{28,31,32} In a formed complex where nitrogen atom is *trans* to the hydride, chemical shifts fall into -20 to -24 ppm region. At the same time, a *trans* oxygen atom shifts hydride signals further away to -29 ppm,^{28,29} while sulphur atom gives rise to signals around -15 ppm.^{28,31}

Every substrate that binds to the iridium catalyst gives rise to a transient complex that features signals with a doublet structure due to the J-coupling between the two hydrides — H_A and H_X (Figure 13). Because H_A and H_X both represent the same transient complex, they are referred to as a pair of doublets. The number of doublet pairs (HF-nhPHIP signals) associated with one substrate depends on the structure of the binding substrate itself. An achiral molecule, e.g. nicotinamide, gives rise to only one doublet pair (Figure 14a).³³ On the other hand, when a chiral molecule, such as nicotine, associates with the iridium catalyst, two diastereomers are formed. This results in two pairs of doublets (Figure 14b).

When a molecule has more than one possible binding site, it gives additional signals — one pair of doublets per every binding site. For example, adenosine can associate with the iridium catalyst through two different N-atoms. Two pairs of doublets form because of this. On top of that, adenosine is a chiral analyte, which means that the number of observable signals is twice as many, resulting in four pairs of doublets (see Chapter 3.3.1 Figure 38).³³

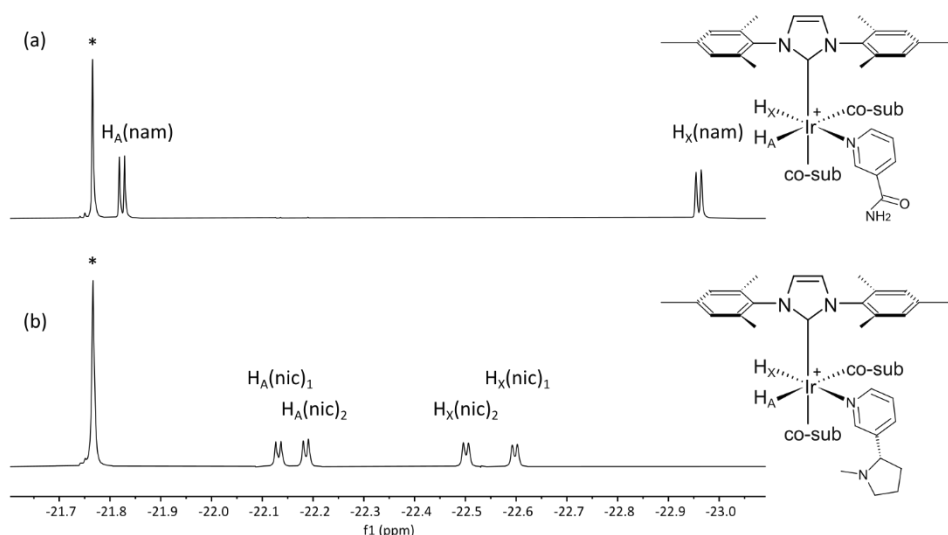


Figure 14. The HF-nhPHIP spectra of (a) nicotinamide and (b) nicotine. H_A and H_X form a pair of doublets because of the spin-spin coupling between the hydrides. The number of signal pairs that form per analyte depends on the structure of that analyte. While nicotinamide (nam) is an achiral compound and gives only one pair of doublets, nicotine (nic) is a chiral and forms two pairs of doublets, diastereomers with different physical properties.

Adding a co-substrate to the HF-nhPHIP NMR sample in excess ensures that complexes with more than one analyte are avoided. The probability of having multiple analytes associating with the iridium catalyst at the same time is therefore very low and such complexes (as shown in Figure 11 with complex **5**⁺) can be neglected, ensuring formation of complex **4**⁺. The choice of co-substrate and its concentration in the HF-nhPHIP catalyst system is important for tuning the selectivity and efficiency of the iridium chemosensor. A good co-substrate should coordinate to the iridium catalyst and enable the formation of complexes with low-concentrated analytes with a sufficient lifetime to be detected with HF-nhPHIP.³⁴ Different co-substrates allow for the detection of different types of analytes. For instance, methyltriazole (mtz) has proven to be an optimal choice for detecting N-heterocyclic analytes with HF-nhPHIP,^{25,26,35} while pyridine works well for amino acids.^{29,36}

1.2.5 2D Zero-quantum Spectroscopy

When only one substance is being detected with HF-nhPHIP, it is easy to understand, which H_A and H_X signals belong to the same complex (form a pair of doublets). However, it is rather complicated to assign hydrides signals to certain substrates in a complex mixture with hundreds of doublet pairs. To unravel the HF-nhPHIP spectra and determine which signals represent the same complex, two-dimensional (2D) zero-quantum (ZQ) spectroscopy can be used.^{25,37} Furthermore, Sellies et al. have shown that compounds possessing similar molecular structures give rise to hydrides that exhibit linear resonance patterns in a spectrum acquired through a 2D zero-quantum experiment.²⁵ The fact that hydrides chemical shifts and ZQ frequencies are not random, makes spectral analysis a lot easier.

Obtaining an NMR spectrum requires a transition from one spin state to the other. The change in spin orientation is determined by the quantum number m , which can increase or decrease by ± 1 . Therefore, a spin= $\frac{1}{2}$ nucleus can go from α -state to β -state or vice versa (Equations 15 and 16). This change in spin orientation is called a single-quantum transition and it can be detected directly.

$$\Delta m_{\alpha \rightarrow \beta} = m_{\beta} - m_{\alpha} = -\frac{1}{2} - \frac{1}{2} = -1 \quad (15)$$

$$\Delta m_{\beta \rightarrow \alpha} = m_{\alpha} - m_{\beta} = \frac{1}{2} - \left(-\frac{1}{2}\right) = 1 \quad (16)$$

It follows that in a system of two coupled spins, there are four single-quantum transitions (see also Figure 9a). Additionally, there are two multiple-quantum transitions: double-quantum and zero-quantum transition (Figure 15, Table 1), which can be detected indirectly using 2D experiments (Figure 16).

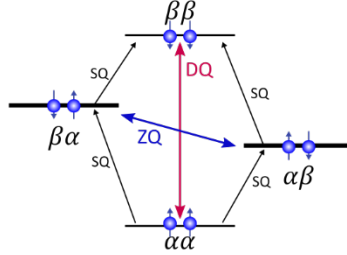


Figure 15. Possible transitions in a spin system of two spin= $\frac{1}{2}$ nuclei: SQ – single-quantum transition, DQ – double-quantum transition, ZQ – zero-quantum transition. DQ and ZQ are multiple-quantum transitions, which are directly unobservable. In parahydrogen hyperpolarization at high field like PASADENA experiment, $\alpha\beta$ and $\beta\alpha$ energy levels are overpopulated, sketched here as thicker lines.

Table 1. Spin state transitions in a two-spin system.

Transition	Spin state start	m_1	m_2	Spin state end	m_1	m_2	Δm
SQ	$\alpha\alpha$	$\frac{1}{2}$	$\frac{1}{2}$	$\alpha\beta$	$\frac{1}{2}$	$-\frac{1}{2}$	-1
SQ	$\alpha\alpha$	$\frac{1}{2}$	$\frac{1}{2}$	$\beta\alpha$	$-\frac{1}{2}$	$\frac{1}{2}$	-1
SQ	$\beta\alpha$	$-\frac{1}{2}$	$\frac{1}{2}$	$\beta\beta$	$-\frac{1}{2}$	$-\frac{1}{2}$	-1
SQ	$\alpha\beta$	$\frac{1}{2}$	$-\frac{1}{2}$	$\beta\beta$	$-\frac{1}{2}$	$-\frac{1}{2}$	-1
DQ	$\alpha\alpha$	$\frac{1}{2}$	$\frac{1}{2}$	$\beta\beta$	$-\frac{1}{2}$	$-\frac{1}{2}$	-2
ZQ	$\alpha\beta$	$\frac{1}{2}$	$-\frac{1}{2}$	$\beta\alpha$	$-\frac{1}{2}$	$\frac{1}{2}$	0

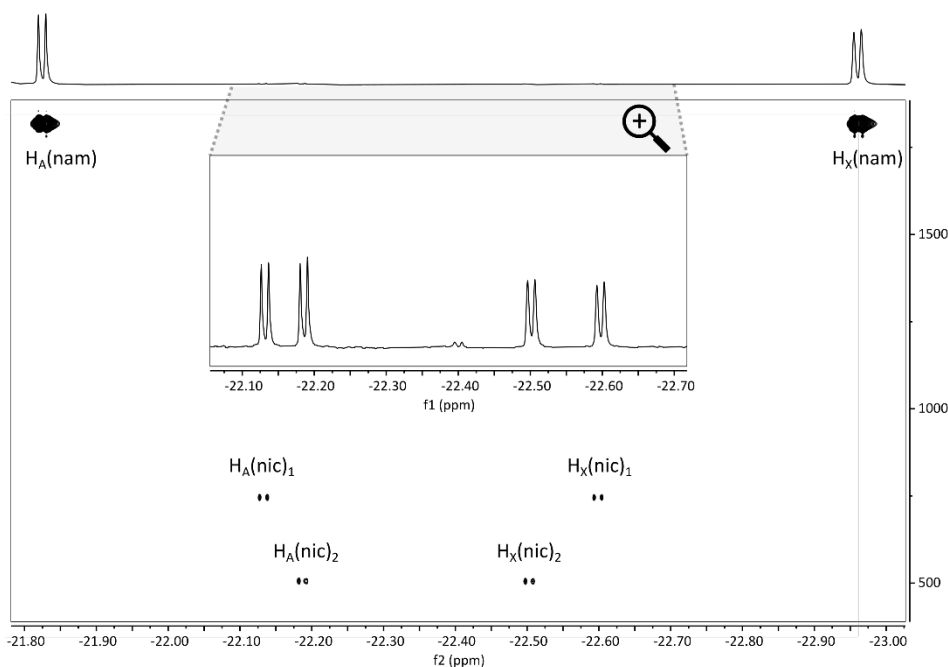


Figure 16. 2D zero-quantum experiment helps to determine which signals belong to the same complex as they have the same ZQ frequency in f_1 dimension (y-axis), meaning they are on the same horizontal line on a 2D spectrum. The abbreviations are the following: nic – nicotine, nam – nicotinamide. Although here both H_A and H_X have the same color-coding, they are in opposite phases. One hydride features an absorption, while the other dispersion lineshape as described by Equation (35). Upper trace shows a 1D spectrum of the same sample with a zoom into nicotine signals, which is present in the sample at much lower concentration compared to nicotinamide. All signals in 1D experiment are in absorption mode.

The hydrides in HF-nhPHIP are weakly coupled to each other, meaning that their spin-spin coupling constant J is much smaller than the difference of their Larmor frequencies. Such coupled spin system is referred as an AX spin system and can be represented with product operators \hat{I}_A and \hat{I}_X . Parahydrogen generates a non-equilibrium population $2\hat{I}_{Az}\hat{I}_{Xz}$, which can be turned into observable transverse magnetization after appropriate radio frequency and gradient impulses on the sample. A slightly modified pulse program, originally published by Sellies et al.²⁵, is sketched on Figure 17. For a better understanding of how the HF-nhPHIP experiment works, the pulse program analysis through spin operators is presented.

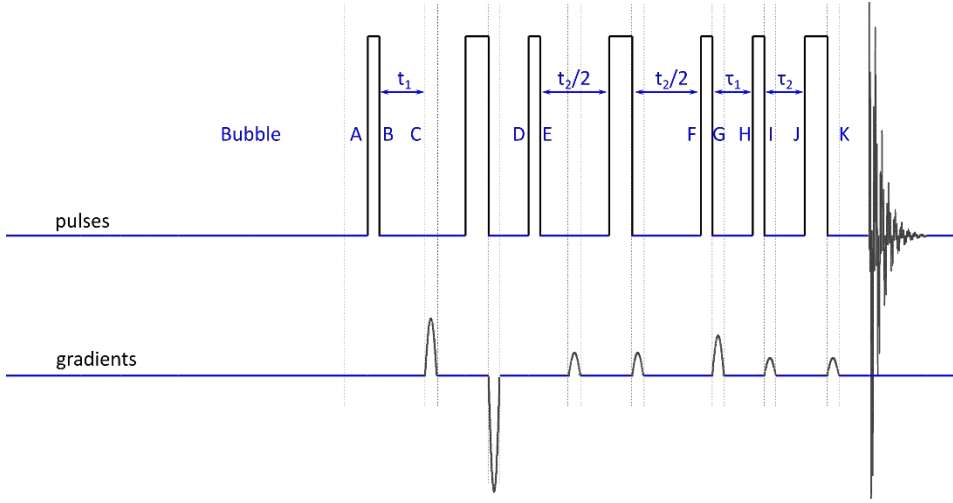


Figure 17. The pulse program scheme used for 2D zero-quantum (ZQ) experiments.

By applying a $\pi/2$ -pulse along the x -axis, the net magnetization is rotated to y -axis, resulting in multiple-quantum coherence operators.

From A to B:

$$2\hat{I}_{Az}\hat{I}_{Xz} \xrightarrow{\frac{\pi}{2}\hat{I}_{Ax} + \frac{\pi}{2}\hat{I}_{Xx}} 2\hat{I}_{Ay}\hat{I}_{Xy} \quad (17)$$

This multiple-quantum coherence $2\hat{I}_{Ay}\hat{I}_{Xy}$ is a mixture of double-quantum (DQ) and zero-quantum (ZQ) coherences.

$$2\hat{I}_{Ay}\hat{I}_{Xy} = -\frac{1}{2}\hat{D}Q_x + \frac{1}{2}\hat{Z}Q_x \quad (18)$$

$$\frac{1}{2}\hat{Z}Q_x = \frac{1}{2}(2\hat{I}_{Ax}\hat{I}_{Xx} + 2\hat{I}_{Ay}\hat{I}_{Xy}) \quad (19)$$

Both double-quantum and zero-quantum terms evolve under free evolution, as they are not affected by spin-spin coupling. Double-quantum coherence evolves as the sum of the Larmor frequencies of the two coupled spins. The zero-quantum coherence evolves as the difference of the Larmor frequencies. In the rotating frame, the Larmor frequencies correspond to the offsets*, Ω_A and Ω_X , of the two spins A and X .² The ZQ term is more beneficial in HF-nhPHIP, because the difference of offsets is not influenced by the chosen reference frequency (Equation 7). The ZQ term will evolve under the free precession during t_1 (Figure 17 B to C).

* Spin offset Ω is defined as the spectrometer reference frequency from the Larmor frequency of the signal: $\Omega = \omega_0 - \omega_{ref}$.

From B to C:

$$\xrightarrow{\Omega_A t_1 \hat{I}_{Az} + \Omega_X t_1 \hat{I}_{Xz}}$$

$$\frac{1}{2}[(2\hat{I}_{Ax}\hat{I}_{Xx} + 2\hat{I}_{Ay}\hat{I}_{Xy}) \cos((\Omega_A - \Omega_X)t_1) + (2\hat{I}_{Ay}\hat{I}_{Xx} - 2\hat{I}_{Ax}\hat{I}_{Xy}) \sin((\Omega_A - \Omega_X)t_1)] \quad (20)$$

It is possible to preserve ZQ coherence and suppress DQ coherence by applying gradient pulses. The coherence order of DQ is $p = \pm 2$, indicating that it can be dephased by gradients, while ZQ coherence order is $p = 0$, meaning it is not affected by gradients.² Two gradient pulses, differing in their power and in opposite phases, are applied to keep only the ZQ term. Additionally, a 180° pulse is applied to refocus the chemical shifts.

From C to D:

$$\xrightarrow{\pi \hat{I}_{Ax} + \pi \hat{I}_{Xx}}$$

$$\frac{1}{2}[(2\hat{I}_{Ax}\hat{I}_{Xx} + 2\hat{I}_{Ay}\hat{I}_{Xy}) \cos((\Omega_A - \Omega_X)t_1) + (2\hat{I}_{Ax}\hat{I}_{Xy} - 2\hat{I}_{Ay}\hat{I}_{Xx}) \sin((\Omega_A - \Omega_X)t_1)] \quad (21)$$

From D to E: anti-phase operators are created

$$\xrightarrow{\frac{\pi}{2} \hat{I}_{Ax} + \frac{\pi}{2} \hat{I}_{Xx}}$$

$$\frac{1}{2}[(2\hat{I}_{Ax}\hat{I}_{Xx} + 2\hat{I}_{Az}\hat{I}_{Xz}) \cos((\Omega_A - \Omega_X)t_1) + (2\hat{I}_{Ax}\hat{I}_{Xz} - 2\hat{I}_{Az}\hat{I}_{Xx}) \sin((\Omega_A - \Omega_X)t_1)] \quad (22)$$

The spin echoes during t_2 refocus the evolution under the chemical shift. The evolution under spin-spin coupling turns anti-phase operators back to in-phase operators.

From E to F:

$$\xrightarrow{2\pi J_{AX} t_2 \hat{I}_{Az} \hat{I}_{Xz}}$$

$$\frac{1}{2} \left\{ \left[(2\hat{I}_{Ax}\hat{I}_{Xx} + 2\hat{I}_{Az}\hat{I}_{Xz}) \cos((\Omega_A - \Omega_X)t_1) + (2\hat{I}_{Ax}\hat{I}_{Xz} - 2\hat{I}_{Az}\hat{I}_{Xx}) \sin((\Omega_A - \Omega_X)t_1) \right] \cos(\pi J_{AX} t_2) \right. \\ \left. + (\hat{I}_{Ay} - \hat{I}_{Xy}) \sin((\Omega_A - \Omega_X)t_1) \sin(\pi J_{AX} t_2) \right\} \quad (23)$$

When t_2 is calibrated so that $J_{AX} t_2 = 1/2$, the cosine term $\cos(\pi J_{AX} t_2)$ cancels out and the sine term $\sin(\pi J_{AX} t_2)$ equals 1, giving Equation (24).

$$\frac{1}{2}[(2\hat{I}_{Ax}\hat{I}_{Xx} + 2\hat{I}_{Az}\hat{I}_{Xz}) \cos((\Omega_A - \Omega_X)t_1) + (\hat{I}_{Ay} - \hat{I}_{Xy}) \sin((\Omega_A - \Omega_X)t_1)] \quad (24)$$

From F to G:

$$\xrightarrow{\frac{\pi}{2} \hat{I}_{Ax} + \frac{\pi}{2} \hat{I}_{Xx}}$$

$$\frac{1}{2}[(2\hat{I}_{Ax}\hat{I}_{Xx} + 2\hat{I}_{Ay}\hat{I}_{Xy}) \cos((\Omega_A - \Omega_X)t_1) + (\hat{I}_{Az} - \hat{I}_{Xz}) \sin((\Omega_A - \Omega_X)t_1)] \quad (25)$$

Once again one may recognize zero-quantum operator, which during period τ_1 goes from x -axis to y -axis.

From G to H:

$$\begin{aligned} & \xrightarrow{\Omega_A \tau_1 \hat{I}_{Az} + \Omega_X \tau_1 \hat{I}_{Xz}} \\ & \frac{1}{2} [(2\hat{I}_{Ax}\hat{I}_{Xx} + 2\hat{I}_{Ay}\hat{I}_{Xy}) \cos((\Omega_A - \Omega_X)t_1) \cos((\Omega_A - \Omega_X)\tau_1) \\ & + (2\hat{I}_{Ay}\hat{I}_{Xx} - 2\hat{I}_{Ax}\hat{I}_{Xy}) \cos((\Omega_A - \Omega_X)t_1) \sin((\Omega_A - \Omega_X)\tau_1) \\ & + (\hat{I}_{Az} - \hat{I}_{Xz}) \sin((\Omega_A - \Omega_X)t_1)] \end{aligned} \quad (26)$$

This is followed by $\pi/2$ -pulse along the x -axis for detection.

From H to I:

$$\begin{aligned} & \xrightarrow{\frac{\pi}{2} \hat{I}_{Ax} + \frac{\pi}{2} \hat{I}_{Xx}} \\ & \frac{1}{2} [(2\hat{I}_{Ax}\hat{I}_{Xx} + 2\hat{I}_{Az}\hat{I}_{Xz}) \cos((\Omega_A - \Omega_X)t_1) \cos((\Omega_A - \Omega_X)\tau_1) + \\ & + (2\hat{I}_{Az}\hat{I}_{Xx} - 2\hat{I}_{Ax}\hat{I}_{Xz}) \cos((\Omega_A - \Omega_X)t_1) \sin((\Omega_A - \Omega_X)\tau_1) + \\ & + (\hat{I}_{Xy} - \hat{I}_{Ay}) \sin((\Omega_A - \Omega_X)t_1)] \end{aligned} \quad (27)$$

Finally, a spin echo is applied to select only hydrides. In the current spin operator analysis τ_2 is chosen so that $J_{AX}\tau_2 = 1/2$, which simplifies the following equations. In real experiments, τ_2 was kept as short as possible.

From I to J:

$$\begin{aligned} & \xrightarrow{2\pi J_{AX}\tau_2 \hat{I}_{Az}\hat{I}_{Xz}} \\ & \frac{1}{2} [(2\hat{I}_{Ax}\hat{I}_{Xx} + 2\hat{I}_{Az}\hat{I}_{Xz}) \cos((\Omega_A - \Omega_X)t_1) \cos((\Omega_A - \Omega_X)\tau_1) + \\ & + (\hat{I}_{Xy} - \hat{I}_{Ay}) \cos((\Omega_A - \Omega_X)t_1) \sin((\Omega_A - \Omega_X)\tau_1) + \\ & + (2\hat{I}_{Ax}\hat{I}_{Xz} - 2\hat{I}_{Az}\hat{I}_{Xx}) \sin((\Omega_A - \Omega_X)t_1)] \end{aligned} \quad (28)$$

From J to K:

$$\begin{aligned} & \xrightarrow{\pi \hat{I}_{Ax} + \pi \hat{I}_{Xx}} \\ & \frac{1}{2} [(2\hat{I}_{Ax}\hat{I}_{Xx} + 2\hat{I}_{Az}\hat{I}_{Xz}) \cos((\Omega_A - \Omega_X)t_1) \cos((\Omega_A - \Omega_X)\tau_1) + \\ & + (-\hat{I}_{Xy} + \hat{I}_{Ay}) \cos((\Omega_A - \Omega_X)t_1) \sin((\Omega_A - \Omega_X)\tau_1) + \\ & + (-2\hat{I}_{Ax}\hat{I}_{Xz} + 2\hat{I}_{Az}\hat{I}_{Xx}) \sin((\Omega_A - \Omega_X)t_1)] \end{aligned} \quad (29)$$

The applied pulses cannot result perfect outcome because convection is consistently present in the sample. As a result, it is possible for unwanted anti-phase coherences to enter the detector and cause interference with the desired spectrum. To suppress unwanted anti-phase coherences, phase cycling is applied. This means that the second experiment is acquired with changed pulse phases. Equations (17) to (24) are valid for the second experiment (scan). Next, the coherence is changed by applying a $\pi/2$ -pulse along the $-x$ -axis. Following the same mathematical notation as before, but changing the phase of a pulse, the outcome is slightly different.

Second scan from F to G:

$$\xrightarrow{\frac{\pi}{2} \hat{I}_A(-x) + \frac{\pi}{2} \hat{I}_X(-x)}$$

$$\frac{1}{2}[(2\hat{I}_{Ax}\hat{I}_{Xx} + 2\hat{I}_{Ay}\hat{I}_{Xy}) \cos((\Omega_A - \Omega_X)t_1) + (-\hat{I}_{Az} + \hat{I}_{Xz}) \sin((\Omega_A - \Omega_X)t_1)] \quad (30)$$

One can recognize zero-quantum term, which, as shown before, goes from x -axis to y -axis during evolution period τ_1 .

Second scan from G to H:

$$\xrightarrow{\Omega_A \tau_1 \hat{I}_{Az} + \Omega_X \tau_1 \hat{I}_{Xz}}$$

$$\begin{aligned} & \frac{1}{2}[(2\hat{I}_{Ax}\hat{I}_{Xx} + 2\hat{I}_{Ay}\hat{I}_{Xy}) \cos((\Omega_A - \Omega_X)t_1) \cos((\Omega_A - \Omega_X)\tau_1) + \\ & + (2\hat{I}_{Ay}\hat{I}_{Xx} - 2\hat{I}_{Ax}\hat{I}_{Xy}) \cos((\Omega_A - \Omega_X)t_1) \sin((\Omega_A - \Omega_X)\tau_1) + \\ & + (-\hat{I}_{Az} + \hat{I}_{Xz}) \sin((\Omega_A - \Omega_X)t_1)] \end{aligned} \quad (31)$$

Followed by radio-frequency impulses and spin-spin evolution, the final product operator state is described by Equation (34).

Second scan from H to I:

$$\xrightarrow{\frac{\pi}{2} \hat{I}_{Ax} + \frac{\pi}{2} \hat{I}_{Xx}}$$

$$\begin{aligned} & \frac{1}{2}[(2\hat{I}_{Ax}\hat{I}_{Xx} + 2\hat{I}_{Az}\hat{I}_{Xz}) \cos((\Omega_A - \Omega_X)t_1) \cos((\Omega_A - \Omega_X)\tau_1) + \\ & + (2\hat{I}_{Az}\hat{I}_{Xx} - 2\hat{I}_{Ax}\hat{I}_{Xz}) \cos((\Omega_A - \Omega_X)t_1) \sin((\Omega_A - \Omega_X)\tau_1) + \\ & + (\hat{I}_{Ay} - \hat{I}_{Xy}) \sin((\Omega_A - \Omega_X)t_1)] \end{aligned} \quad (32)$$

Second scan from I to J:

$$\xrightarrow{2\pi J_{AX} \tau_2 \hat{I}_{Az} \hat{I}_{Xz}}$$

$$\begin{aligned} & \frac{1}{2}[(2\hat{I}_{Ax}\hat{I}_{Xx} + 2\hat{I}_{Az}\hat{I}_{Xz}) \cos((\Omega_A - \Omega_X)t_1) \cos((\Omega_A - \Omega_X)\tau_1) + \\ & + (\hat{I}_{Xy} - \hat{I}_{Ay}) \cos((\Omega_A - \Omega_X)t_1) \sin((\Omega_A - \Omega_X)\tau_1) + \\ & + (-2\hat{I}_{Ax}\hat{I}_{Xz} + 2\hat{I}_{Az}\hat{I}_{Xx}) \sin((\Omega_A - \Omega_X)t_1)] \end{aligned} \quad (33)$$

Second scan from J to K :

$$\begin{aligned} & \xrightarrow{\pi \hat{I}_{Ax} + \pi \hat{I}_{Xx}} \\ & \frac{1}{2} [(2\hat{I}_{Ax}\hat{I}_{Xx} + 2\hat{I}_{Az}\hat{I}_{Xz}) \cos((\Omega_A - \Omega_X)t_1) \cos((\Omega_A - \Omega_X)\tau_1) + \\ & + (-\hat{I}_{Xy} + \hat{I}_{Ay}) \cos((\Omega_A - \Omega_X)t_1) \sin((\Omega_A - \Omega_X)\tau_1) + \\ & + (2\hat{I}_{Ax}\hat{I}_{Xz} - 2\hat{I}_{Az}\hat{I}_{Xx}) \sin((\Omega_A - \Omega_X)t_1)] \end{aligned} \quad (34)$$

When the results of two experiments are added together, the anti-phase operators cancel out and one gets

$$\begin{aligned} & (2\hat{I}_{Ax}\hat{I}_{Xx} + 2\hat{I}_{Az}\hat{I}_{Xz}) \cos((\Omega_A - \Omega_X)t_1) \cos((\Omega_A - \Omega_X)\tau_1) \\ & + (\hat{I}_{Ay} - \hat{I}_{Xy}) \cos((\Omega_A - \Omega_X)t_1) \sin((\Omega_A - \Omega_X)\tau_1) \end{aligned} \quad (35)$$

From Equation (35) one may recognize a multiple-quantum coherence operator $2\hat{I}_{Ax}\hat{I}_{Xx}$, which is a mixture of double- and zero-quantum parts, and a non-equilibrium operator $2\hat{I}_{Az}\hat{I}_{Xz}$. Both of these are undetectable by NMR. The second term features in-phase y -magnetization operators \hat{I}_{Ay} and \hat{I}_{Xy} with opposite signs. These in-phase terms are detectable by NMR and are responsible for obtaining the spectrum. \hat{I}_{Ay} and \hat{I}_{Xy} represent the enhanced hydrides of the iridium complex, separated by the difference of their offsets. One may notice, that the two in-phase operators have opposite signs. This means they are detected in opposite phases, which results in absorption and dispersion lineshapes in a spectrum (Figure 16).

1.3 Hyperpolarization in Biological Samples

NMR is great in analytical applications like structural analysis, quality control, and quantitative analysis. Because of its non-invasive nature, NMR is also a good choice to study environmental influences on a specimen, observe real-time biological processes, study metabolic pathways, and perform trace analysis for quality control. However, regular NMR lacks the required sensitivity for the detection of low-concentration compounds and subtle molecular changes,³⁸ often present in biological samples.

Hyperpolarization techniques have opened new avenues for the detailed analysis of biological samples by detection of low concentrated analytes that were previously unattainable with NMR. Out of various hyperpolarization techniques, dDNP and non-hydrogenative PHIP have been successfully applied to biological fluids, natural extracts, and tissues.^{8,26,39,40}

Hermkens et al. demonstrated how continuous non-hydrogenative hyperpolarization at high magnetic field can be used to detect flavour components found in coffee²⁶ and whiskey²⁷ by targeting pyridine and pyrazine derivatives. Reile et al. developed a straightforward method to adapt the HF-nhPHIP technique for analysis of aqueous media through the use of solid phase extraction (SPE).³⁹ By applying the SPE procedure, they successfully prepared methanol extracts from urine, rendering these samples compatible with the iridium catalyst. This adaptation allowed for the detection of nitrogen-compounds in urine at sub- μ M concentrations.

While works by Hermkens et al. and Reile et al. utilized hydride-analyte correlations in homonuclear HSQC²⁶ and INEPT³⁹ experiments, Sellies et al. showed that information about the composition of the sample can be drawn from hydrides alone (2D zero-quantum spectroscopy).²⁵ Sellies et al. advanced the HF-nhPHIP for detecting and resolving a wider array of metabolites in urine at nanomolar concentrations. Expanding on the scope of HF-nhPHIP, subsequent research has ventured into amino acid detection. Sellies et al. illustrated that α -amino acids can be detected and quantified in urine samples,²⁹ while Dreisewerd et al. provided methods to discriminate and quantify D- and L- α -amino acids directly using 2D HF-nhPHIP zero quantum spectroscopy.³⁶

In parallel, dDNP has shown promising results in metabolomics through ¹³C detection.⁸ ¹³C is an attractive approach as it has a much wider chemical shift range compared to ¹H (Chapter 1.1.2) thereby improving resolution necessary for biological samples and mixtures. It has been applied to labelled cell and tissue extracts,^{41,42} plant extracts⁴³ and freeze-dried urine.⁴⁴ On the downside, dDNP faces challenges such as the need for free radicals, which may interfere with biological samples, and its limited sensitivity for relatively dilute biofluids.^{44,45} Nonetheless, dDNP ability to analyse extracts at natural ¹³C abundance highlights great potential.

In summary, both HF-nhPHIP and dDNP hyperpolarization techniques have greatly enhanced the applicability of NMR in the analysis of biological samples, each with its unique contributions and limitations. The future of this field lies in overcoming the existing technical challenges and exploring new applications, which will undoubtedly expand the understanding of complex biological systems and environmental samples.

1.3.1 The Future of HF-nhPHIP

Although, HF-nhPHIP is not ready for the commercial usage, it can be developed for various applications ranging from food and agriculture to medicine and pharmaceutical industries.

The publications by Hermkens et al.^{26,27} underscore the potential of HF-nhPHIP in analyte identification, important for stringent quality control, product development in the food and beverage industry, and authentication of premium goods. Moreover, the information obtained can serve the purpose of directing agricultural research towards optimizing crops, providing insights for the development of healthier food choices, and expanding into environmental monitoring, where a thorough analysis of composition holds significant importance.

The diagnostic potential of HF-nhPHIP in biofluid analysis has been shown by Reile et al. by detecting a doping substance in urine.³⁹ Besides doping assessment, the ability to detect compounds at low concentrations from biofluids can enable early detection of diseases, monitoring of disease progression, and evaluation of treatment efficacy. Furthermore, HF-nhPHIP technique could be used to identify metabolic abnormalities and biomarkers associated with diseases, likewise with other hyperpolarization techniques.^{41,42,46}

There is potential to discover novel biomarkers with HF-nhPHIP by lowering the detection threshold beyond what is currently available in regular NMR and expanding the metabolite detection. The HF-nhPHIP could pave the way for more in-depth analysis and diagnostics, ultimately leading to personalized medicine.

2 Aims of the Study

The goal of this thesis is to investigate and expand the HF-nhPHIP in analysing biological fluids. Prior to this work, HF-nhPHIP methodology had been demonstrated on a small number of analytes in technical research papers and working principles. Here, the HF-nhPHIP technique is demonstrated in practical applications for biofluid NMR with increased sensitivity.

Aims summarised:

- Assess the diagnostic and analytical potential of HF-nhPHIP by testing its accuracy and repeatability on following nicotine and cotinine excretion from the body after quitting smoking (Publication I).
- Develop an alternative sample preparation protocol to eliminate SPE treatment for the analysis of urine samples, while maintaining compatibility with urine and the iridium catalyst (Publication II).
- Widen the scope of HF-nhPHIP-detectable analytes to oligopeptides. Study the complexation of oligopeptides to the iridium catalyst (Publication III).
- Test if HF-nhPHIP signal assignment to specific analytes can be made easier and faster with establishing chemical shift database and whether it can be applied to urine analysis (Publication IV).
- Expand the application of HF-nhPHIP beyond the analysis of human urine (Publication V).

By focusing on these objectives, this research aims to highlight the adaptability and transformative capabilities of HF-nhPHIP in the field of analytical sciences, particularly when applied to the analysis of biological fluids.

3 Results and Discussion

3.1 Quantification and Identification of Analytes in Human Urine (Publication I)

Human urine presents a unique opportunity for non-invasive diagnostics and metabolic profiling as it contains over 3000 metabolites. These metabolites serve as biomarkers, reflecting physiological processes, dietary influences, and pathological changes within the body. However, most of the analytes are present in urine at low concentration, making their detection with regular NMR problematic.⁴⁷ While previous works had applied HF-nhPHIP on urine samples, following the dynamic changes in the human body had not been analysed with it. Therefore, a pharmacokinetic-like experiment was conducted to challenge HF-nhPHIP in a real-life scenario requiring high analytical accuracy.⁴⁸

In pharmacokinetics, the drug molecule's metabolism is carefully studied in a time-dependant manner to insure drug safety and assign dosage.^{49,50} To mimic that, HF-nhPHIP was used to target nicotine and cotinine in smokers urine. Nicotine is the primary active compound in tobacco and it is metabolized in the body to various metabolites, the primary one being cotinine. Cotinine is further metabolised into *trans*-3'-hydroxycotinine, which is the main tobacco-consumption related analyte found in urine. It is excreted in urine at a concentration approximately 3-4 times higher than nicotine or cotinine (Figure 18).⁵¹ The focus of the study was to apply HF-nhPHIP on low-concentration analytes, which can provide valuable information about the dosage and metabolism of nicotine in the body.⁵²

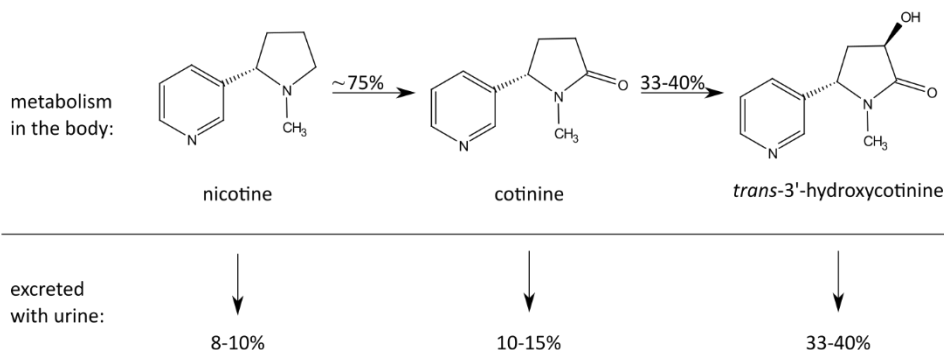


Figure 18. 75% of nicotine is metabolised to cotinine in the human body. Around 40% of cotinine is further metabolised into 3'-hydroxycotinine with stereoselectivity towards its *trans*-isomer. Unchanged nicotine and cotinine molecules are excreted with urine at around 10% each of total urinary nicotine, while the main metabolite found in smokers' urine *trans*-3'-hydroxycotinine is excreted at around 40%.⁵¹

The experiment involved the collection of samples, the preparation of samples prior to HF-nhPHIP measurement (described in Chapter 3.1.1), and the establishment of calibration curves (described in Chapter 3.1.2). Initially, to identify the spectral signatures of nicotine and cotinine within a complex urine matrix, known quantities of these substances were spiked into a urine sample obtained from a non-smoker (Figure 19). The subsequent recording of HF-nhPHIP spectra made it possible to distinguish the

signals of nicotine and cotinine, creating a reference point for further analysis. After establishing the chemical shifts of hydrides referring to nicotine and cotinine, the methodology was applied to analyse six urine samples collected from regular smokers. Nicotine and cotinine were successfully identified in all samples and their concentration in urine, determined with HF-nhPHIP, coincided with known literature values.

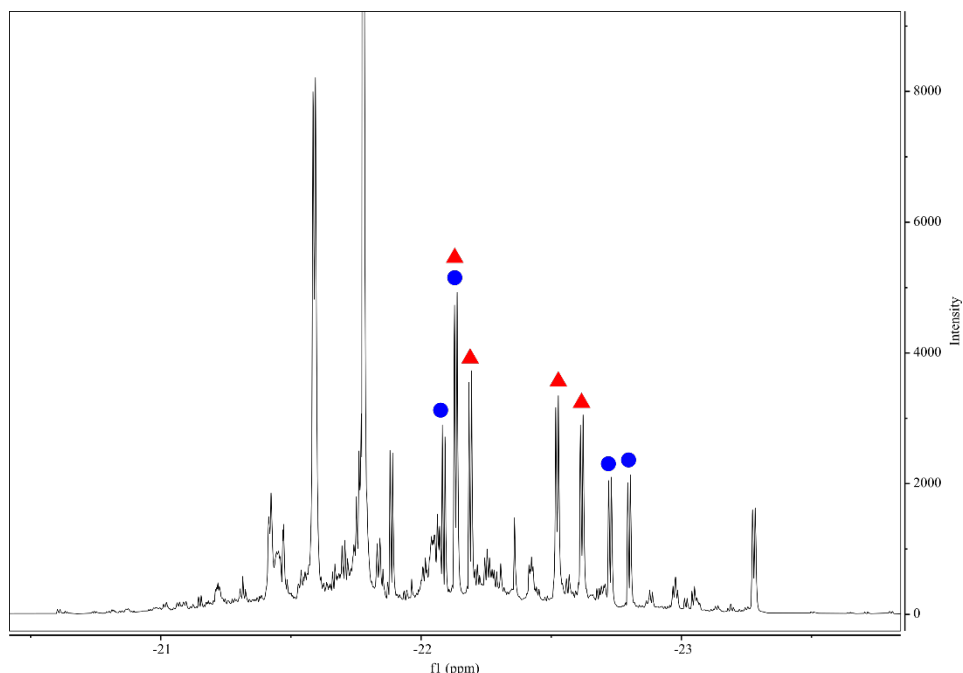


Figure 19. Nicotine (red triangles) and cotinine (blue circles) HF-nhPHIP signals in urine matrix assigned by standard addition method. While H_x signals (right) are well separated, H_A signals (left) are not. One of the diastereomers of cotinine and nicotine, resonate at the same 1H chemical shift. To improve resolution, 2D ZQ spectroscopy was implemented.

In an effort to monitor the pharmacokinetics of nicotine and cotinine clearance from the human body, smokers participating in the study were requested to cease smoking. Three volunteers complied, allowing for the collection of sequential urine samples post-cessation. By utilizing HF-nhPHIP, the analysis of these samples enabled the observation of nicotine and cotinine elimination kinetics, offering valuable insights into their metabolic degradation pathways and clearance rates. Furthermore, in order to replicate the impact of controlled nicotine dosage similar to therapeutic treatments rather than solely concentrating on elimination, a seventh participant used a nicotine patch as a nicotine source. The urine samples collected from this individual were analysed using the same technique.

During this phase of the study, a build-up of a new signal proximate to the established nicotine and cotinine HF-nhPHIP signals was observed (Figure 20). As Sellies et al. have shown,²⁵ hydrides that resonate close by typically belong to the same molecule class. The unknown signal became distinctly visible 24 hours post the administration of nicotine via a transdermal patch, as illustrated in Figure 20. This signal was also detected in the urine samples of habitual smokers, suggesting its association with nicotine metabolism

and structural similarity to cotinine. Leveraging this insight, the signal was hypothesized to emanate from *trans*-3'-hydroxycotinine, a deduction that was later validated through standard addition.

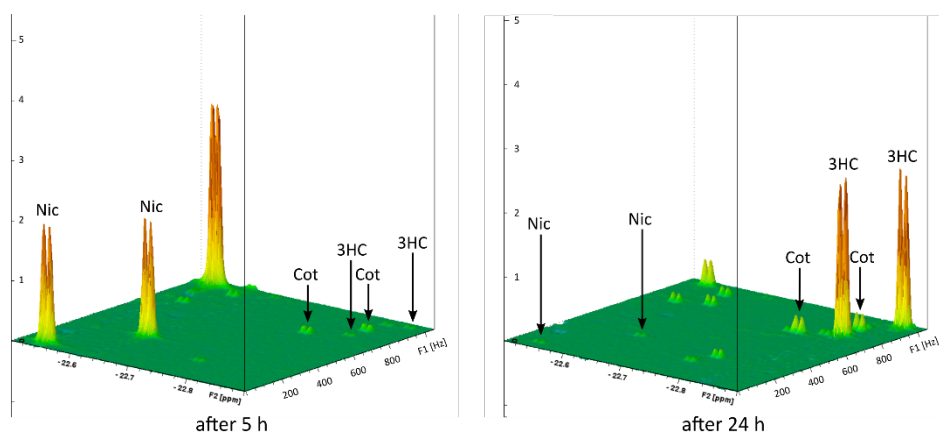


Figure 20. HF-nhPHIP spectra show the metabolic changes caused by nicotine consumption. A series of samples were collected from a volunteer who used a transdermal patch for nicotine administration. Nicotine (Nic) signals were clearly visible after 5 hours of applying the patch (left panel). 24 h (right panel) after applying the patch, Nic signals were almost gone, while cotinine (Cot) signals were still observable and *trans*-3'-hydroxycotinine (3HC) signals were the strongest.

3.1.1 Sample Preparation for the Targeted Approach

Solid-phase extraction (SPE) is a sample preparation technique used for separating specific compounds from a mixture.⁵³ This method involves passing the liquid mixture through a solid phase cartridge (adsorbent material) under controlled conditions, allowing the targeted compounds to adsorb onto the solid phase. Subsequent washing step removes undesired components, and a final elution step releases the adsorbed compounds for analysis.

SPE works well for making aqueous samples HF-nhPHIP compatible. It is easy to substitute water with organic solvents suitable for hyperpolarization, like methanol or chloroform.³⁹ Moreover, the selective nature of SPE is a significant asset. By utilizing an appropriate solid-phase sorbent, SPE can discriminate between polar and non-polar analytes, allowing to concentrate the sample for the target analytes.

For detecting nicotine and cotinine from smokers' urine, the SPE method was first optimized on laboratory-prepared water-samples with known concentrations of nicotine and cotinine. Three different reverse phase SPE cartridges were tested (Phenomenex Strata-X, Oasis HLB, and Biotage Isolute ENV+). To obtain the most of target analytes, analytes should be in a neutral state (without a charge), which can be achieved by changing the pH level. The most suitable pH level for nicotine and cotinine would be between pH 7...10.5. Water solutions at pH 8.6 and 10.6 were tested, out of which Phenomenex Strata-X (6 mL, 200 mg) and Oasis HLB (6 mL/200mg) outperformed Biotage Isolute ENV+ (Figure 21).

Although both Oasis HLB and Phenomenex Strata-X showed similar recovery rates for nicotine and cotinine, Strata-X cartridge performed slightly better at close to neutral conditions (pH 8.6) and was therefore chosen for further analysis. Next, water solutions

with known nicotine and cotinine concentrations at pH levels 7.4 and 8.6 were tested. It was seen that solution with pH 8.6 eluted analytes faster, but cumulatively pH 7.4 contained higher amount of nicotine and cotinine in the eluted extract. Therefore, pH 7.4 was chosen as the optimal pH level for Strata-X cartridge. Figure 22 displays a flowchart of the sample preparation procedure for the targeted approach for human urine samples.

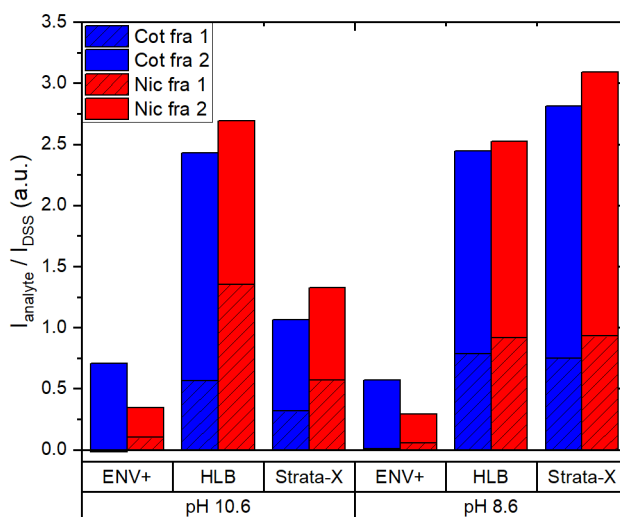


Figure 21. Comparison of SPE recoveries of nicotine and cotinine from Phenomenex Strata-X, Oasis HLB, and Biotage Isolute ENV+ cartridges. Urine samples were adjusted to either pH 10.6 or 8.6, SPE cartridges were washed with a buffer at the respective pH, analytes were extracted with methanol- d_4 . Analyte ^1H integrals obtained from quantitative NMR spectra were compared against the integral of an internal standard (DSS: Sodium trimethylsilylpropanesulfonate) added to the extract after the SPE procedure.

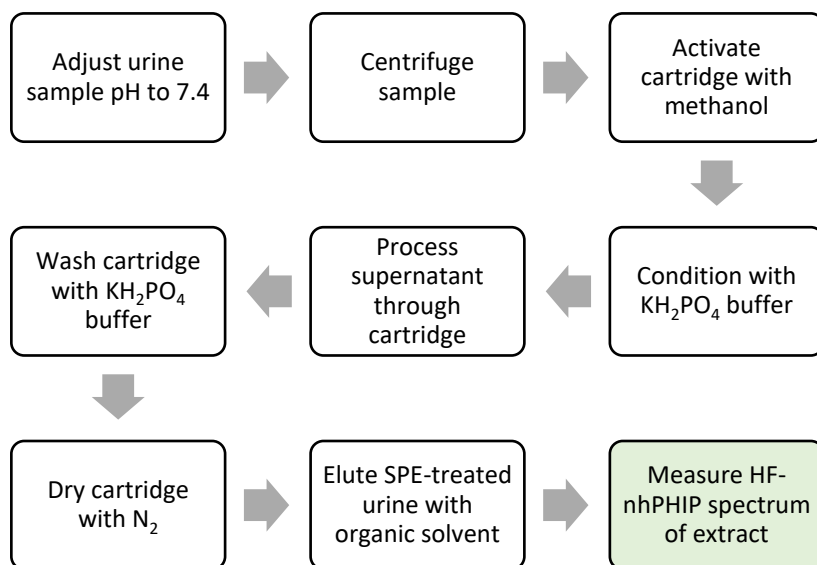


Figure 22. Flowchart of the SPE procedure.

Conditioning and washing the cartridge with buffer helps to maintain the pH level constant throughout the SPE procedure. However, the buffer solution itself may influence HF-nhPHIP spectra. To evaluate that, two urine SPE extracts obtained using either 50 mM KH_2PO_4 or 10 mM KH_2PO_4 buffer at pH 7.4 for conditioning and washing the cartridge were evaluated. 50 mM KH_2PO_4 buffer eluted amino acids, which in turn reduced the HF-nhPHIP signal intensities of nicotine and cotinine, which have weaker affinity towards the iridium catalyst compared to amino acids (Figure 23). In hope of improving the SPE method to target nicotine and cotinine, distilled water was used instead of the buffer. However, without controlling the pH level of the sample and using H_2O to wash the cartridge, a shift in nicotine signals was observed between different urine samples, while cotinine signals stayed in place (Figure 24). This means that nicotine is more susceptible to pH changes. When considering analytical applications, it is important that samples from various specimens maintain consistent properties, specifically with regards to HF-nhPHIP chemical shifts. Therefore, 10 mM KH_2PO_4 buffer at pH 7.4 was chosen for the SPE procedure.

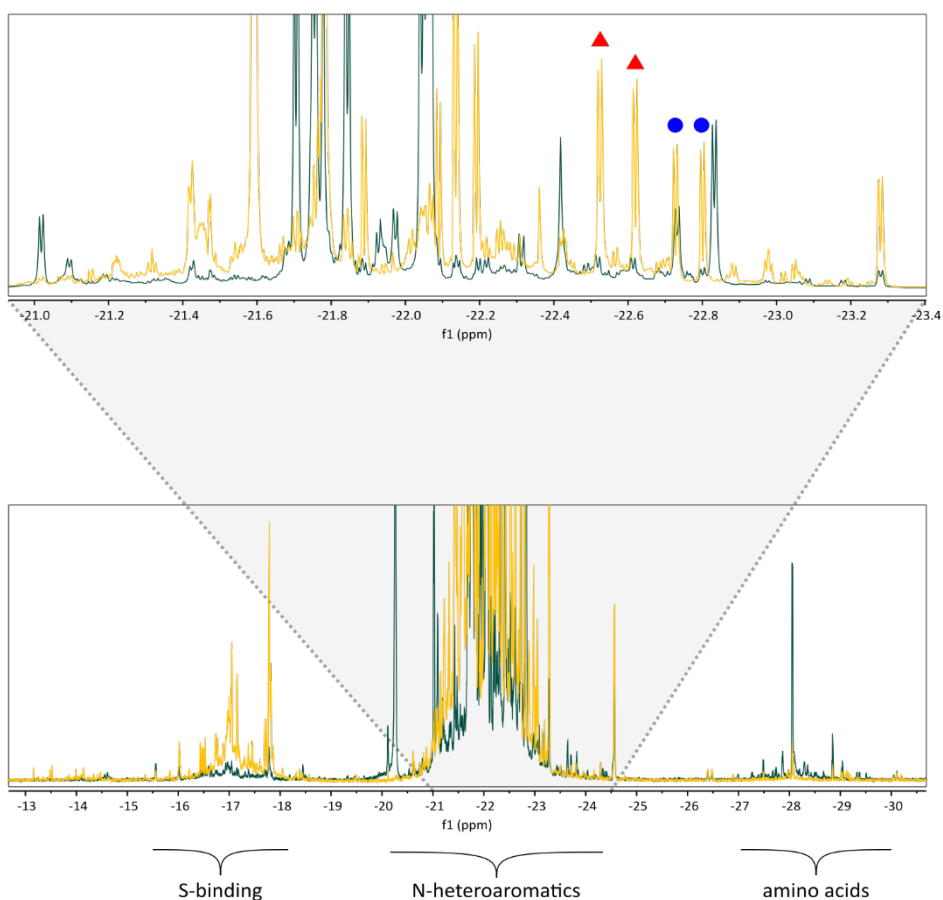


Figure 23. A comparison of two HF-nhPHIP spectra obtained from the same urine with either using a 10 mM KH_2PO_4 buffer (yellow) or 50 mM KH_2PO_4 buffer (green) in the SPE procedure. 50 mM KH_2PO_4 buffer elutes amino acids, while 10 mM buffer retains S-containing analytes. An expansion of the N-heteroaromatics region shows that nicotine (red triangles) and cotinine (blue circles) signals are more intensive when 10 mM KH_2PO_4 buffer is used.

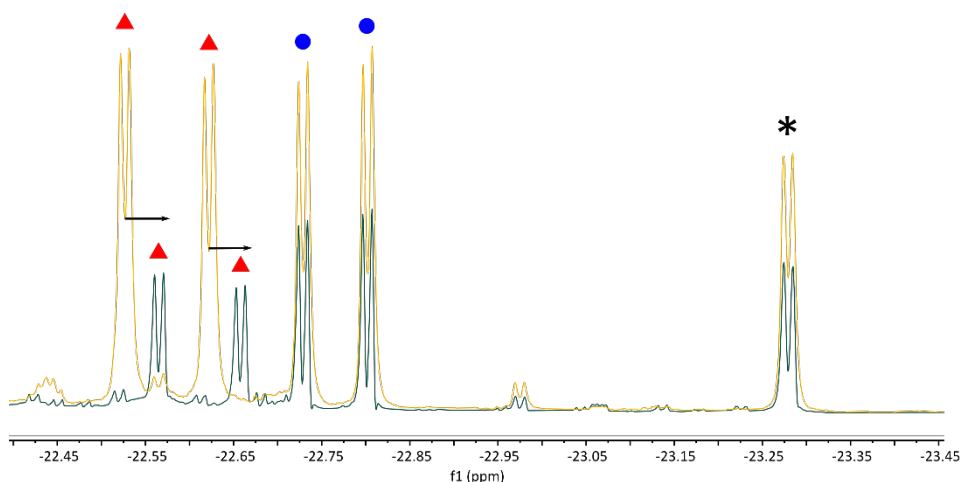


Figure 24. An expansion to H_x signals of nicotine (red triangles) and cotinine (blue circles) of two different urine extracts (green and yellow) obtained by using H_2O in wash step in SPE method. Nicotine HF-nhPHIP signals have shifted, while cotinine and 3-fluoropyridine (*), used as an internal standard, stayed in place.

Although methanol eluted nicotine and cotinine, the SPE protocol was not optimal for the targeted approach as methanol also extracted a lot of other analytes. With more analytes competing over binding to the iridium catalyst, the probability of nicotine and cotinine associating is low, which also reduces the NMR signal intensity. Moreover, as the number of analytes binding to the iridium catalyst increases, the spectrum becomes more populated with signals, thus adding complexity to the analysis. To improve the selectivity of the SPE, chloroform, which favours the release of less polar analytes compared to methanol, was used for elution. In addition, reducing the number of analytes in the obtained SPE extract, the recovery rates for nicotine and cotinine eluted with chloroform were above 90%, while the recovery with methanol was around 25% (Figure 25).

By combining the SPE method with HF-nhPHIP, it became possible to detect and measure nicotine and cotinine compounds at much lower concentrations compared to traditional NMR techniques. This approach achieved an impressive NMR detection limit of $0.1 \mu M$ and a quantitation limit of $0.7 \mu M$. In general, combining solid-phase extraction with parahydrogen hyperpolarization provides a method for analysing low-concentration analytes in urine, surpassing traditional methods in terms of sensitivity.

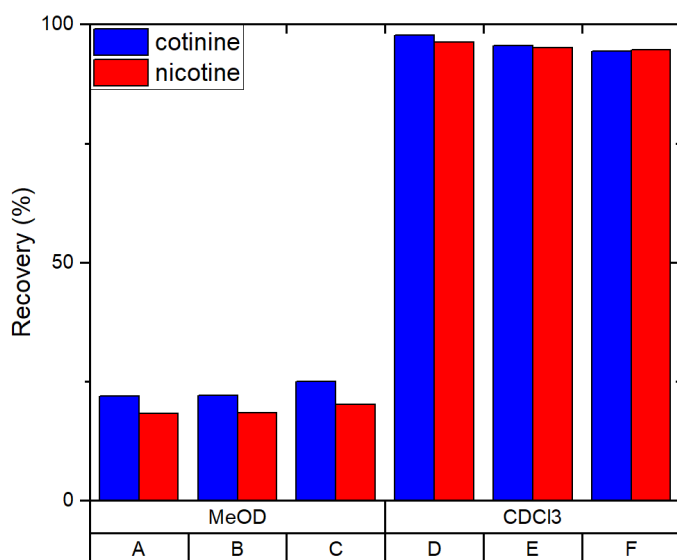


Figure 25. Comparison of SPE recoveries in different urines (provided by six volunteers A – F) of nicotine and cotinine extracted with methanol- d_4 or chloroform- d .

3.1.2 Determining Concentration Based on HF-nhPHIP Signals

Determining concentration in NMR vs. HF-nhPHIP differs. In regular NMR, signal intensity indicates concentration, however HF-nhPHIP signal integrals do not show concentration directly. They relate to hyperpolarization factors like catalyst binding kinetics, analyte's affinity towards the catalyst. Accurate quantification needs careful calibration for each analyte.

To accurately quantify nicotine and cotinine levels within urine samples, a series of standard solutions with known concentrations of nicotine and cotinine were measured in the urine matrix (collected from a non-smoker). Corresponding HF-nhPHIP signals were integrated to relate signal integrals with the concentration of an analyte in urine. The obtained calibration curves had a standard deviation below 11%, showing good repeatability (Figure 26). These calibration curves provided a basis for quantifying the concentrations of nicotine and cotinine in samples from smokers, enabling the quantitative study of nicotine metabolism kinetics.

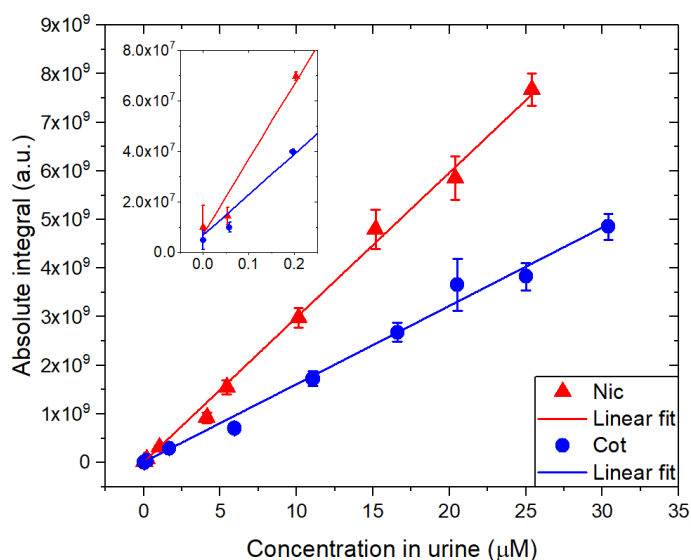


Figure 26. Calibration curves for nicotine (red) and cotinine (blue) based on the linear fitting of 10 data points. Three parallels were measured and averaged for every point. Error bars represent the standard deviation of the three parallels. Calibration curves are analyte-specific due to different iridium binding affinities. Reproduced from Publication I. Copyright 2021, American Chemical Society.

The calibration curves were also used to document two instances of passive smoking. In one case, an individual spent time in the presence of other smokers after quitting smoking for the sake of the experiment. As a result, a slight increase in the concentration of nicotine was observed in the sample taken the following day. In another case, a subject who served as a reference for non-smokers displayed nicotine and cotinine signals in one sample (Figure 27). Although, these signals were barely over noise level, they can be assigned with confidence because true signals exhibit a doublet structure, whereas noise does not. Upon further investigation, it was discovered that the subject had been exposed to tobacco smoke for a few hours on the previous night before providing the sample. This proves that HF-nhPHIP can be used to detect analytes present at very low concentrations in urine.

Furthermore, if an approximate value of an analyte is sufficient, a need for calibration curves can be replaced by a quicker approach. Sellies et al. showed that chemically similar compounds exhibit comparable affinities towards the iridium catalyst.²⁹ This means that individual calibration curves for each molecule can be avoided. Instead, a single calibration curve can be used to estimate concentrations in the sample quickly. HF-nhPHIP can be a valuable tool in analytical chemistry either by providing approximate concentration values by utilizing pre-made calibration curves or precise values through standard addition.

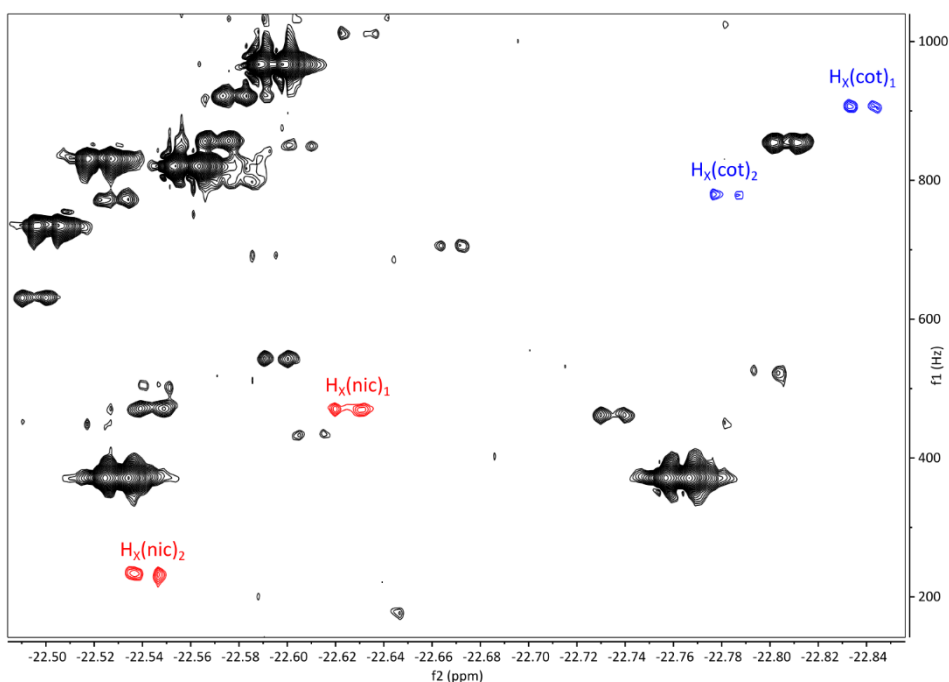


Figure 27. Residual nicotine (nic, red) and cotinine (cot, blue) H_x signals show passive smoking in the urine of a non-smoker. Signals can be distinguished from noise by their doublet structure. Because the signals are barely over noise level and are obscured by much stronger signals in a 1D experiment, they can easily go unnoticed.

3.1.3 Sample Preparation for the Untargeted Approach (Publication II)

SPE provides advantages in the selection of analytes, but its chemoselective nature can be a double-edged sword in metabolomics. It might exclude certain metabolites, limiting the scope of the analysis. To overcome limitations in additional chemoselectivity of SPE on top of HF-nhPHIP, and broaden the scope of HF-nhPHIP towards metabolomics, the sample should be treated as little as possible. However, when it comes to urine, it cannot be directly measured because of high concentration of urea in it. Although urea itself does not interfere with HF-nhPHIP experiment, its degradation product ammonia has high affinity towards the catalyst. The high affinity of ammonia leads to the catalyst complexing mainly with it, making binding for analytes with lower affinity challenging. This would be the complete opposite to what is needed in metabolomics. Therefore, eliminating ammonia is a crucial step.

The untargeted approach's sample preparation protocol removes ammonia in three simple steps (Figure 28). First, urine pH was adjusted to 11, under which urea chemically decomposes to ammonia and CO_2 at room temperature. Second, a simple lyophilization was used to remove ammonia and water from the urine sample. With the first two steps, ammonia stripped solids were obtained. Lastly, urine solids were reconstituted in methanol- d_4 and D_2O mixture and centrifuged to precipitate any insoluble molecules (e.g. salts, lipids). For the HF-nhPHIP experiment, the methanol supernatant solution was used.

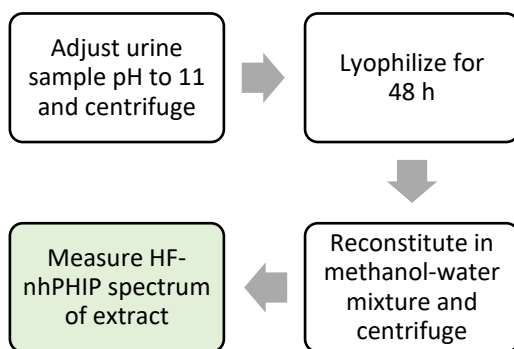


Figure 28. Flowchart for the urine sample preparation procedure for the untargeted approach.

As can be seen on Figure 29, spectra of targeted and untargeted HF-nhPHIP approaches differ in the number of signals and signal intensities. The SPE method releases adsorbed target compounds for the analysis in a smaller volume compared to the initial sample loading volume (Chapter 3.1.1). Adding this concentrated urine extract to the NMR tube increases also analytes' HF-nhPHIP signal intensities. In the experiment with nicotine and cotinine, both analytes were concentrated 3.7-fold in the NMR tube compared to the original urine (Publication I). On the contrary, in the untargeted approach urine has to be diluted 5-fold in the NMR tube as a large part of the low molecular weight urinary metabolome is retained during the ammonia stripping. Without dilution, the required iridium catalyst concentration to fulfil analyte/catalyst/co-substrate condition described by Equation (14), would have to be above catalyst's solubility in the methanol. As more analytes are present in the treated urine sample, a higher catalyst concentration (6 mM) compared to previous works (1.2 mM) is needed to avoid catalyst system oversaturation and maintain quantitative properties of the HF-nhPHIP method.

The untargeted approach is useful for obtaining an overview of the sample. It is more general than the SPE-based HF-nhPHIP as it allows to maintain metabolites with different polarities, such as pyridines, nucleobases, and nucleosides, in one sample and to detect them simultaneously. It is important to note, however, that some analytes will not survive pH 11 conditions and will be absent in the resulting spectrum. Because of the diversity of molecules present in urine, it is therefore advisable to utilize multiple sample preparation techniques during initial method development. Both the targeted approach involving SPE and the untargeted approach using pH 11 to remove ammonia are complimentary to each other. The two methods can be used independently based on the goal of the experiment or utilized together to acquire a more comprehensive overview of the specimen.

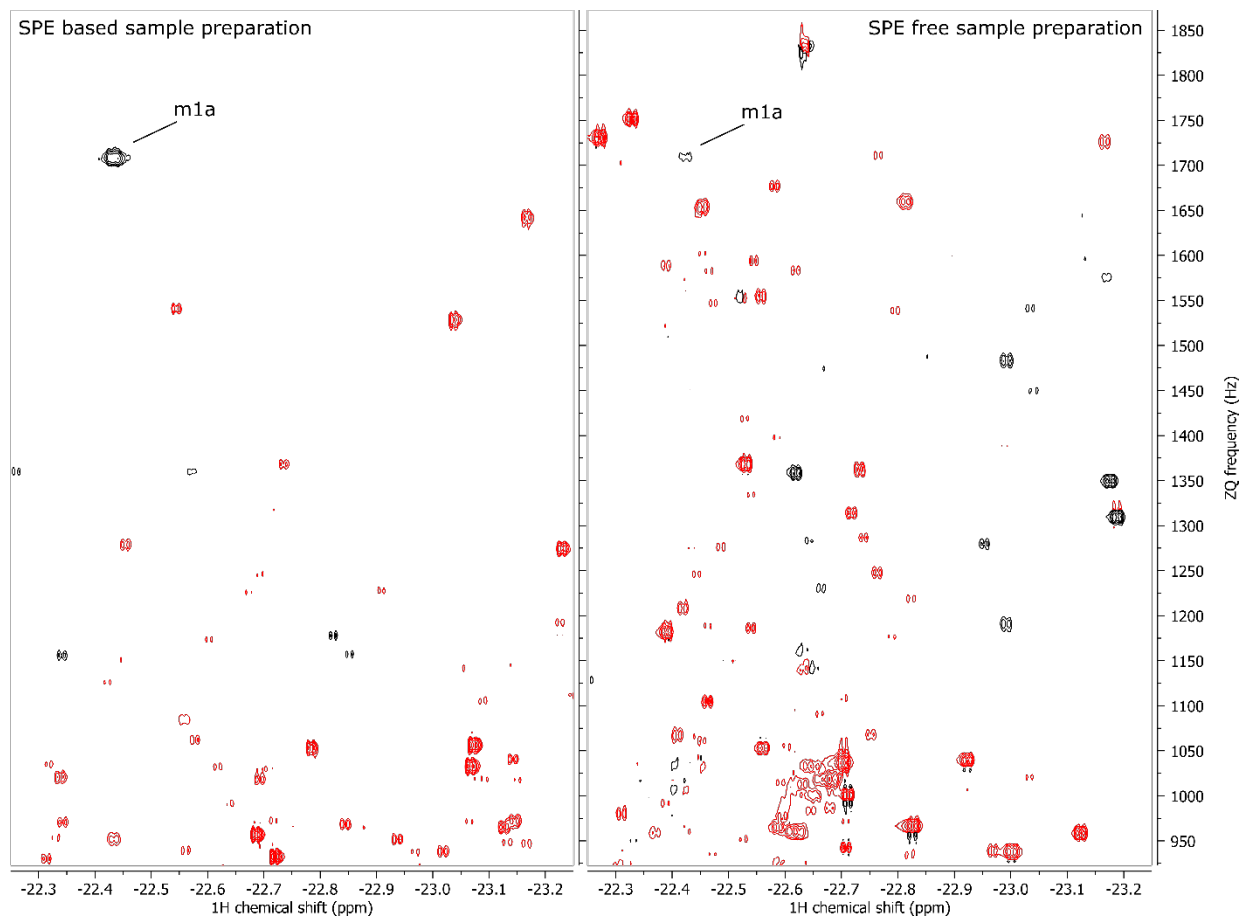


Figure 29. The spectra of a urine sample were obtained using two different approaches: targeted approach with SPE method, and untargeted approach with minimal sample preparation. The two methods retain different kind of analytes.

3.2 Widening the Scope to Biopolymers (Publication III)

3.2.1 The Role of Co-substrate in HF-nhPHIP Chemoselectivity

Sellies et al. demonstrated that by replacing a co-substrate 1-methyl-1,2,3-triazole with pyridine, amino acids can be detected directly from human urine.²⁹ However, their approach required heating the sample with amino acids to 50 °C for 7.5 min under strong basic conditions (pH 11) to obtain stable complexes. While basic conditions and high temperature are not a problem for amino acids, some biologically important analytes may be more affected. One of such analyte class is peptides. Basic conditions may potentially cause hydrolysis and oxidation of peptides.

To address this concern, a systematic screening of alternative co-substrates with different steric and electronic properties was conducted (Figure 30).⁵⁴ The impact of ten co-substrates (mtz, pyridine, and pyridine derivatives) on a mixture of amino acids (alanine, leucine, phenylalanine) was investigated in an alkaline environment as proposed by Sellies et al.²⁹. The iridium catalyst was activated with the co-substrates at room temperature (25 °C) for 2h after which the amino acids were added. The primary considerations in selecting the ideal co-substrate included the intensity of HF-nhPHIP signals, signal line width, number of signals generated per analyte, stability of signal intensity during prolonged measurements, and activation time of the iridium catalyst with the chosen co-substrate.

Out of the tested co-substrates, 4-fluoropyridine (spectrum 8 Figure 30) did not produce any observable HF-nhPHIP signals. The reason could be that 4-fluoropyridine may bind to the iridium catalyst so firmly that it prevents hydrogen exchange or it exchanges too fast to form a stable complex in the NMR time-scale. In either case, the conditions for hyperpolarization are violated.

The hydride signals corresponding to amino acids were weak when 1-methyl-1,2,3-triazole, 3-methylpyridine, 4-methylpyridine, 3,5-dimethylpyridine, and 3,5-difluoropyridine were used as a co-substrate. With 3,5-dimethylpyridine amino acids' HF-nhPHIP signals decreased by four-fold within 30 minutes, indicating instability of these complexes. A fluorine-replaced analogue 3,5-difluoropyridine exhibited wide signals, which can be associated with fast exchange kinetics. Additionally, the active complex 4^+ with this co-substrate formed after prolonged reaction period of 4 hours, which would be undesirable for practical applications. Amino acids' HF-nhPHIP signals obtained with other co-substrates suggest that the complexes do not form as effectively as anticipated for the experiment at room temperature.

Among the tested co-substrates, 3-fluoro-4-methylpyridine (3F4MePy) was identified as the optimal co-substrate (spectrum 10 Figure 30). It exhibited the strongest signals for amino acid HF-nhPHIP complexes under pH 11 and at a measurement temperature of 25 °C (Figure 30). Further studies showed 3F4MePy allows the formation of the HF-nhPHIP active complexes without the need for high temperature and provides excellent signals at 10 °C measuring temperature (Figure 31).

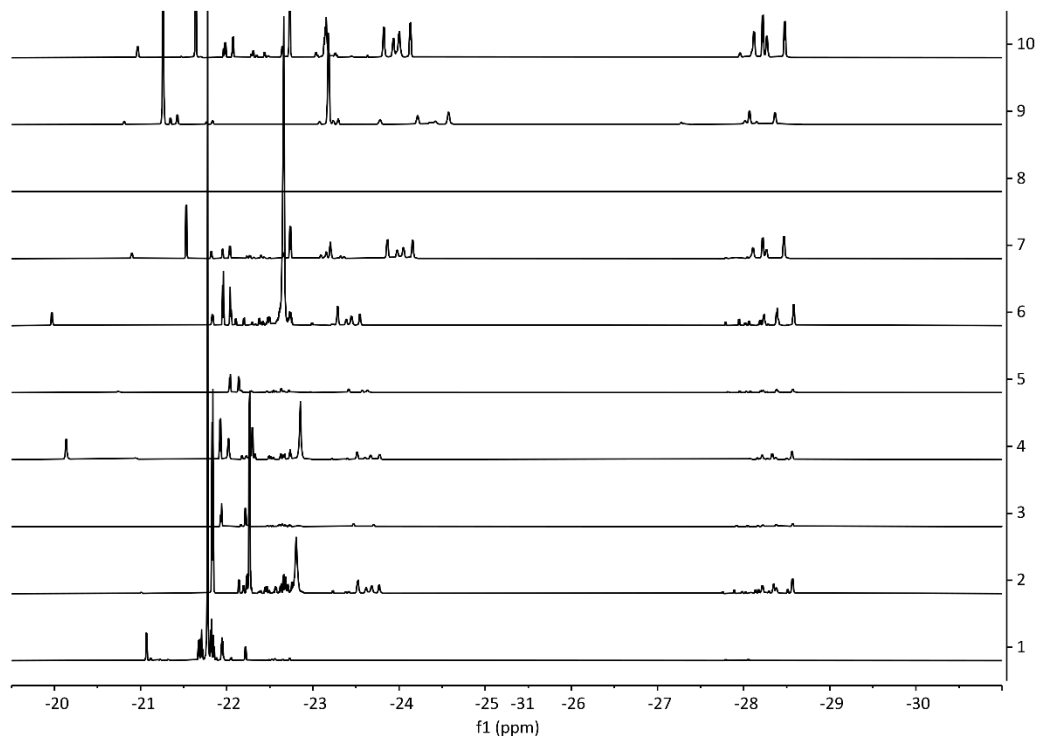


Figure 30. Screening of co-substrates on a mixture of alanine, leucine, phenylalanine under basic conditions recorded at 25°C. The suitability of a co-substrate was evaluated based on the HF-nhPHIP signal intensity, signal line width, and number of signals in -28 ppm region. The screened co-substrates were 1 – mtz, 2 – pyridine, 3 – 3-methylpyridine, 4 – 4-methylpyridine, 5 – 3,5-dimethylpyridine, 6 – 4-tertbutylpyridine, 7 – 3-fluoropyridine, 8 – 4-fluoropyridine (no observable signals), 9 – 3,5-difluoropyridine, 10 – 3-fluoro-4-methylpyridine.

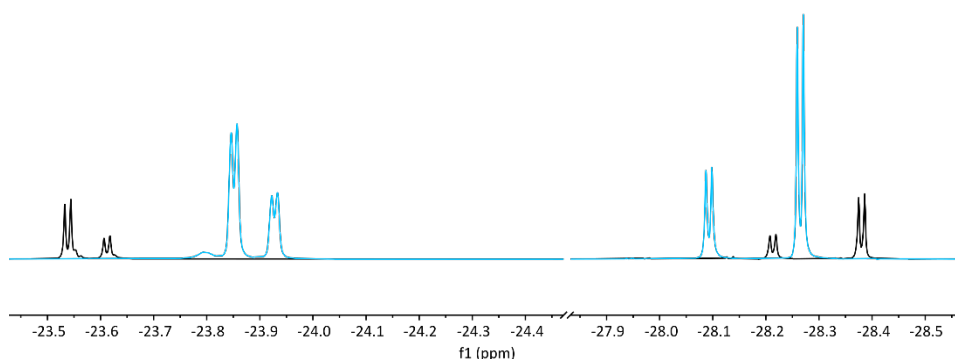


Figure 31. 3-fluoro-4-methylpyridine (aqua) proved to be a more suitable co-substrate over pyridine (black) to detect the amino acid alanine under basic conditions. The signals at δ -23.55 to -23.95 correspond to H_A , while those at δ -28.10 to -28.40 correspond to H_X of the same alanine-iridium complexes. The two signal pairs forming for both co-substrates represent the two diastereomers. There is a notable difference in resonance frequencies and signal intensities, but the relative intensity of the two diastereomers are approximately the same with either co-substrate. Spectra were measured at 10°C.

3.2.2 Analysis of Oligopeptides Binding to the Iridium Catalyst

Oligopeptides bridge a gap between small molecules and proteins, and are of great interest because of their diverse biological properties. Different applications of oligopeptides are actively being studied, including using them in cosmeceuticals,^{55,56} and in medicine and pharmaceuticals.^{57,58} Hyperpolarization of oligopeptides has been achieved before by chemical modifications (adding a hyperpolarizable tag), which adds an additional step to the workflow and may not always be feasible.

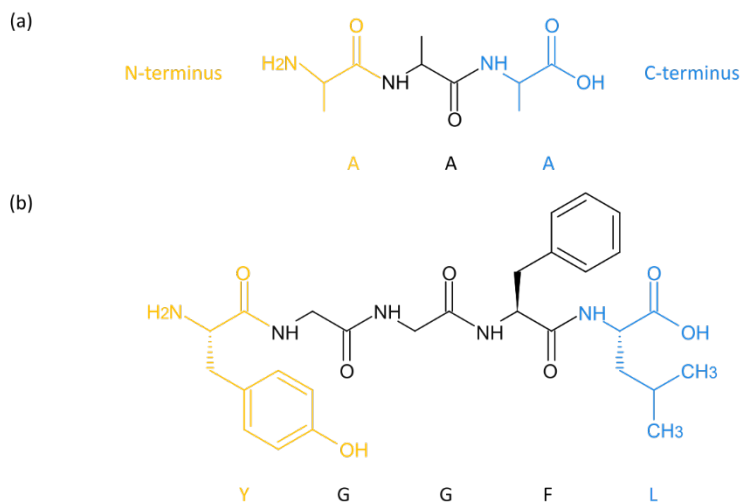


Figure 32. Oligopeptides comprise multiple amino acids, which are connected with peptide bonds, where N-terminus is the amino group ($-NH_2$, yellow) and C-terminus is the carboxyl group ($-COOH$, blue). (a) Alanine trimer comprising three alanine amino acids (AAA), (b) leucine-enkephalin, which comprises tyrosine, glycine, glycine, phenylalanine, and leucine (YGGFL).

Sellies et al.²⁹ found that α -amino acids can bind to the iridium catalyst in both monodentate and bidentate configurations. In the bidentate configuration, the analytes were coordinated through N- and O-atoms in axial-equatorial positions. However, they were unable to detect HF-nhPHIP signals of the equatorial bidentate configuration, suggesting that ligand dissociation in that system is too slow.

Contrary to amino acids, oligopeptides showed HF-nhPHIP signals of three configurations: monodentate (mono), bidentate through axial-equatorial positions (ax-eq), and bidentate in the equatorial plane (eq-eq) (Figure 13 and Figure 33). To understand the exact nature of oligopeptides' complexation to the iridium catalyst, multiple experiments were conducted, accompanied by quantum mechanical modelling method: density-functional theory (DFT).

Based on hydrides' chemical shifts, it is possible to understand the type of the atom through which the analyte is bound to the iridium, e.g. hydride *trans* to a N-atom resonates around δ -21...-23 ppm, while hydride *trans* to an O-atom at δ -27 and beyond.^{25,28} However, oligopeptides consist of multiple amino acids and have several N- and O-atoms that can contribute to binding to the catalyst (Figure 32). Therefore, chemical shifts do not refer explicitly which of the possible atoms is contributing to the formed configuration. To determine how oligopeptides bind to the iridium catalyst, alanine-consisting oligopeptides were used as model compounds.

First, alanine trimers (A_3) with modifications made to the amino ($-NH_2$) and carboxyl ($-COOH$) groups found at the beginning and end of a peptide chain, respectively, were synthesized and measured, to see which terminus is crucial for bidentate binding. Out of the tested A_3 oligopeptides only A_3 methyl ester gave HF-nhPHIP signals resonating in the proximity of pure A_3 . Observable signals confirmed that carboxyl group is not involved in oligopeptide binding as esterification of the C-terminus did not interfere. Oligopeptides need N-terminus for binding and cannot associate with the iridium catalyst when the amino group is modified with an acetyl group (N-acetyl A_3 and N-acetyl A_3 methyl ester). Neither of the A_3 peptides with blocked N-terminus produced observable HF-nhPHIP signals (see supporting information in Publication III).

Next, signals from different configurations were assigned by synthesizing and measuring ^{15}N -labelled alanine oligomers (Figure 33). Because ^{15}N is a spin-1/2 nucleus, it splits hydrides' doublet structure when it is in *trans* position to the hydride. A_3 methyl ester, where the first alanine was ^{15}N -labelled, showed signal splitting at δ -22.52 and -22.61 for mono configuration and δ -22.72 ppm for bidentate configuration (Figure 33b yellow triangles and red circles, Figure 13 binding modes (b) and (d)). A_4 methyl ester with ^{15}N -label in the second alanine did not show any HF-nhPHIP signal splitting. This proved that binding happens through the N-terminus, the first amino acid in the oligopeptide sequence.

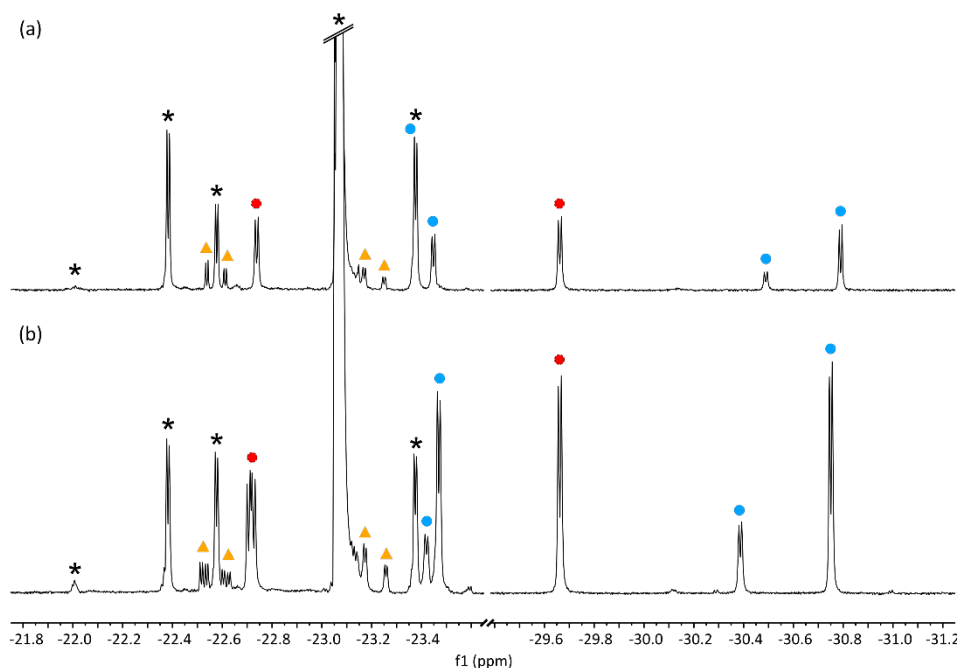


Figure 33. HF-nhPHIP spectra of ^{15}N -labelled oligopeptides (a) A-A- ^{15}N -A-A-OMe and (b) A- ^{15}N -A-A-OMe. Blue circles correspond to diastereomers of the ax-eq complex, red circles to the eq-eq complex, and yellow triangles to diastereomers of mono complex. Note that some signals overlap in 1D, but were resolved in 2D spectra. Signal splitting due to ^{15}N coupling can be seen only for (b) A- ^{15}N -A-A-OMe mono and eq-eq configurations' signals, confirming ^{15}N in axial and O in equatorial position. ax-eq shows no splitting, which indicates that ^{15}N must be in axial position. (a) A-A- ^{15}N -A-A-OMe does not feature ^{15}N splitting, meaning that only the N-terminus associates with the iridium catalyst to form all three configurations. Asterisk (*) denotes signals from the co-substrate 3-fluoro-4-methylpyridine (3F4MePy)-Ir-complex. Reproduced from Ref. ⁵⁴. Copyright 2023 The Authors. Published by Analyst.

The δ -30 ppm chemical shifts obtained from modified alanine trimers showed also that bidentate binding includes an O-atom, which has to be from one of the peptide bond carbonyl groups. Alanine trimer structure contains three carbonyl oxygen atoms (Figure 34, starting from N-terminus: O_i , O_{ii} , O_{iii}), where the first two are located in peptide bonds and the last is in the C-terminus. In principle, it would be possible to determine experimentally which of the O-atoms is binding to the iridium catalyst. This could be achieved by measuring A_3 peptides, where different oxygen atoms are O^{17} -labelled. However, the synthesis of such peptides with O^{17} is a costly procedure. Furthermore, due to O^{17} being a quadrupolar nucleus with spin-5/2, the NMR spectroscopy would be more complicated. Instead, density-functional theory (DFT) was used to determine the probabilities of different binding structures.

DFT is a computational modelling method, which calculates the electronic structures of atoms and molecules using electron density.⁵⁹ The structures of alanine oligomer complexes of varying lengths were estimated based on the energies calculated using DFT. DFT optimized oligopeptide structures when associating with the catalyst, are peptide length specific. While A_2 and A_3 peptides produced a 5-member cycle associating with O_i to the iridium, A_4 and longer peptides preferred the 8-member cycle through O_{ii} (Figure

34). Thus, longer peptides have more flexibility in their orientation around the catalyst core allowing for the formation of stabilizing intramolecular hydrogen bonds. This brings the molecule into energy efficient folded configuration.

To experimentally validate the results obtained by DFT modelling, NOE (the nuclear Overhauser effect) NMR experiments were done on thermally polarized samples. The NOE experiment reveals which nuclei are close in space to each other.⁶⁰ The effect is observable for nuclei, which are less than 5 Å apart. NOE experiments on alanine dimer and alanine trimer HF-nhPHIP complexes confirmed configurations suggested by DFT calculations. Alanine trimer showed NOE response between N_{iii}H and CH₃ of the first alanine residue (DFT suggested distance 3.5 Å), which can only appear in the case of a 5-member cycle (Figure 34a). Additionally, there was a NOE response between alanine trimer and catalyst IMes aromatic hydrogens that can only be present in that configuration.

Dimer showed a NOE response between N_{ii}H and CH₃ groups of both alanine residues, only present in the case of a 5-member cycle, and with IMes aromatic hydrogens (Figure 34d). While dimer and trimer formed 5-member cycles with the iridium catalyst, longer oligopeptides (e.g. alanine tetramer Figure 34b) prefer 8-member cycles.

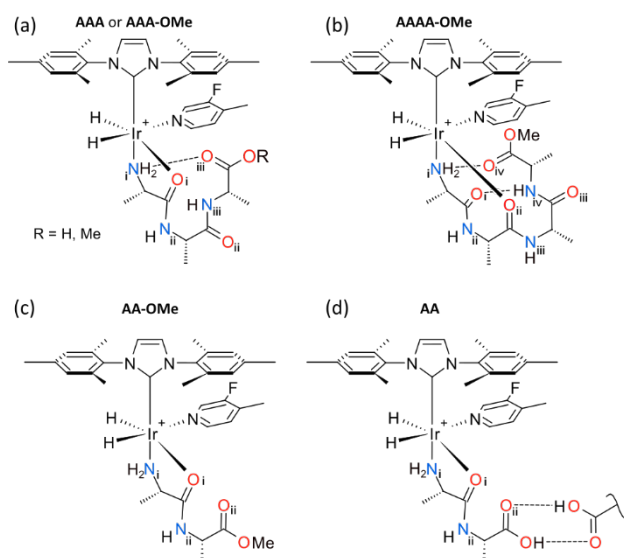


Figure 34. DFT calculations and NOE experiments confirmed bidentate configurations of alanine oligomers to the iridium catalyst (a) A₃ and A₃-OMe, (b) A₄-OMe, (c) A₂-OMe, and (d) A₂. A₂ and A₃ formed 5-member Ir-cycles, while A₄-OMe and A₅-OMe present more complex structures containing an 8-member cycle. Reproduced from Ref. ⁵⁴. Copyright 2023 The Authors. Published by Analyst.

For each oligopeptide three distinguishable complexes were observed* – mono, bidentate eq-eq, and bidentate ax-eq. Prolonged measurements at 10 °C showed that the signals of initially formed eq-eq and mono slowly decreased, while ax-eq signals increased, suggesting that eq-eq and mono have higher energies compared to ax-eq. This observation was supported by DFT calculations, stating that the energetically most stable

* Alanine dimer (AA) exhibited two eq-eq signal pairs, while other peptides showed only one signal pair for that configuration.

configuration for oligopeptides is the bidentate ax-eq configuration (as shown in Figure 34). Interestingly, kinetic complex eq-eq was HF-nhPHIP detectable for alanine oligomers, but not for amino acids.²⁹ This demonstrates that the stability of the formed complex is substrate-specific.

According to DFT, there is one additional configuration, where the atoms of ax-eq are bound to the iridium catalyst in reverse. Although reversed ax-eq configuration is theoretically possible, it was not observed experimentally. The reason may be that this configuration has too short of a lifetime in NMR experiment timescale.

Evidence suggests that the formation of a bidentate ax-eq configuration is not limited to alanine oligopeptides, but rather a favoured binding mode for other peptides as well. To cover a broad range of peptides with actual diagnostic, dermatological or biological value, papain inhibitor (GGYR), cosmeceutical peptide hexapeptide-11 (FVAPFP), and neuropeptide Leu-enkephalin (YGGFL) were selected for experiments. Preliminary results on oligopeptides comprising different amino acids showed signals in a similar region as alanine peptide-model compounds, H_A at -30.57 to -31.21 ppm and H_X at -23 ppm, with O-atom in the equatorial plane and N-atom in the axial position (Figure 35).

On the other hand, functional peptides showed that experimental conditions require optimization to get the best HF-nhPHIP signals for each individual oligopeptide complex. GGYR HF-nhPHIP signals were more intense when the peptide was first dissolved in water at neutral pH, lyophilised and reconstituted in methanol (Figure 35 solid lines). On the other hand, YGGFL signals had lower intensity when prepared under the same conditions. For YGGFL dissolving straight in methanol resulted in stronger signals (dashed lines). FVAPFP gave similar responses with either sample preparation protocol. Additionally, functional oligopeptides showed more intense signals at 25 °C, contrary to alanine oligopeptides. Naturally occurring oligopeptides were detected at even higher temperature, 35 °C from a urine sample prepared with the untargeted method (Figure 36).

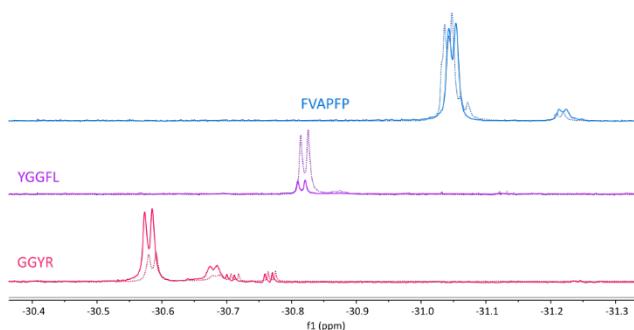


Figure 35. HF-nhPHIP H_A signals of functional oligopeptides: papain inhibitor (GGYR), neuropeptide Leu-enkephalin (YGGFL), and cosmeceutical peptide hexapeptide-11 (FVAPFP), measured at 25 °C. Two sample preparation protocols were followed: (a) solid lines: peptide was dissolved in water, pH corrected to 7.4–7.9, lyophilized and dissolved in methanol-d₄ prior nhPHIP measurement. Ratio of catalyst : 3F4MePy : oligopeptide was 1 : 18 : 0.08; (b) dashed lines: peptide was dissolved in methanol-d₄ as supplied. Ratio of catalyst : 3F4MePy : oligopeptide was 1 : 8 : 0.08. Comparison of spectra (a) and (b) demonstrates that nhPHIP performance is dependent on the particular oligopeptide, sample preparation and measurement conditions. Reproduced from Ref. ⁵⁴. Copyright 2023 The Authors. Published by Analyst.

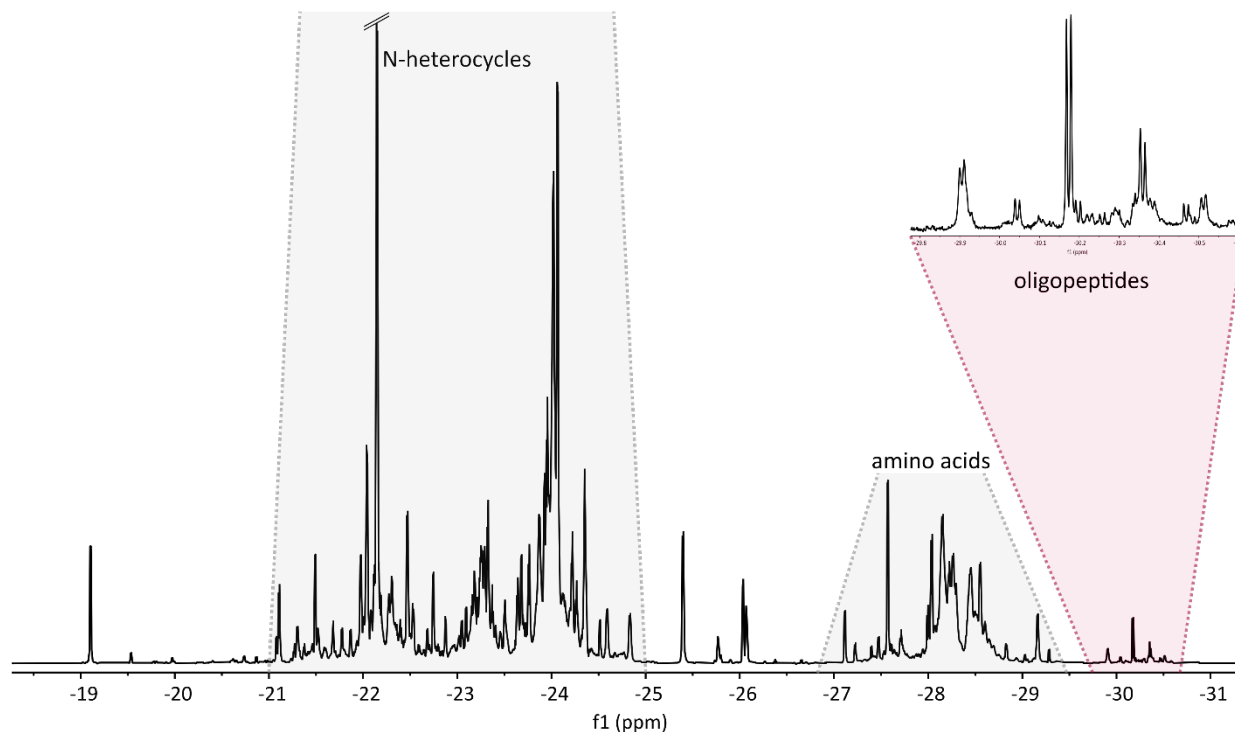


Figure 36. HF-nhPHIP spectrum of a urine sample. H_A signals characteristic to oligopeptides appear at around -30 ppm, whereas cosubstrate H_X signals are around -23 ppm. The untargeted approach was used to prepared the urine sample. Spectrum was recorded at 35°C . Reproduced from Ref. ⁵⁴. Copyright 2023 The Authors. Published by Analyst.

3.3 Optimization of Experimental Conditions

Accurate and reliable results in analytical techniques depend on optimizing sample preparation methods and measurement conditions. In the HF-nhPHIP system, several factors affect the system, such as the pH level, solvent, measurement temperature, pH_2 concentration in the sample, and the choice of a co-substrate (as discussed in Chapter 3.2.1). Changes in measurement conditions can cause shifts in the resonance frequencies of hydrides, making it difficult to accurately assign signals.

The importance of pH level. The importance of pH becomes clear when considering the different nature of analytes, each reacting differently to changes in acidity and basicity. For instance, under acidic conditions, analytes can become protonated, stopping them from interacting with the positively charged iridium catalyst (Figure 12).

Experiments with nicotine and cotinine showed that pH variations in the sample preparation prior to hyperpolarization has an impact on the HF-nhPHIP spectra (see Chapter 3.1.1). Uncontrolled pH environment in the SPE procedure results in poorly reproducible eluted sample extracts between different specimen and a shift of HF-nhPHIP hydrides' signals. Besides pH, buffer concentration is similarly important. Different concentrations enable to tune the selectivity of the SPE more towards the wanted analytes (Figure 23).

Sellies et al.²⁹ found that under basic conditions (pH 11.1), the hydride signals from amino acids association increased by 6-fold compared to the solutions with uncorrected pH. Compared to the thermal equilibrium, this resulted in a 300-fold enhancement. Whereas different amino acids had a similar response to pH, oligopeptides comprising various amino acids did not. This was evident with measuring functional oligopeptides: papain inhibitor, Leu-enkephalin, and hexapeptide-11 (see Chapter 3.2.2). Two different sample preparation methods were tested. The first one involved dissolving the peptide in water, correcting solution's pH to 7.4–7.9, lyophilizing and dissolving again in methanol. In the second method, peptide was dissolved in methanol as supplied. While there were no differences in HF-nhPHIP signals for hexapeptide-11, papain inhibitor and Leu-enkephalin showed opposite responses regarding the sample preparation method (Figure 35).

This underscores the importance of optimizing pH environment to suit the properties of the analyte being examined. Each analyte reacts differently, and the pH conditions that enhance hyperpolarization for one may not be effective for another.

The importance of solvent. Choosing the right solvent is important for optimal results with HF-nhPHIP. HF-nhPHIP works best in organic solvents, where both the iridium catalyst and pH_2 have good solubility. Methanol has been the primary solvent for HF-nhPHIP experiments, however it may not be the optimal choice for dissolving all analytes.

It might be necessary to use a solvent mixture. For example, when detecting HF-nhPHIP signals of nicotine and cotinine, methanol-chloroform mixture in the NMR tube was used. Although these analytes dissolve well in both methanol and chloroform, the SPE recovery of nicotine and cotinine was around 35-40% with methanol, while it was 95% with chloroform. Therefore, analytes were eluted with chloroform, while the HF-nhPHIP catalyst and co-substrate were dissolved in methanol. In the final NMR sample a solvent mixture (75% chloroform and 25% methanol vol/vol) was used to maintain high accuracy while accessing low concentrations (Chapters 3.1.1 and 3.1.2).

Sometimes analytes do not dissolve fully into an organic solvent. In such cases, water-methanol mixture can be used. However, water content in the NMR sample should be below 20% for optimal HF-nhPHIP performance.²⁹

The importance of temperature. Measurement temperature influences HF-nhPHIP experiment by mainly changing the analyte association/disassociation rate. In the case of alanine oligomers, the most intense HF-nhPHIP signals were observed at 10 °C. At lower temperatures, molecular motions and chemical processes slow down, prolonging the lifetime of the formed complex. For some molecules, higher temperatures may improve solubility or facilitate beneficial association/disassociation rates for hyperpolarization. This could explain the improved response of functional oligopeptides, which showed more intense signals at 25 °C and urine that had the best result at 35 °C (Chapter 3.2.2). Similarly to oligopeptides in urine, adenosine molecule shows better HF-nhPHIP response at 35 °C.⁶¹

For best practices, measurements should be done at various temperatures to determine the optimal value. If this cannot be done, using room temperature should yield a satisfactory outcome.

The importance of p_{H2} delivery. For analytical accuracy, p_{H2} concentration must be the same for every scan to ensure a uniform enhancement during the experiment. As p_{H2} is converted back to orthohydrogen after disassociating from iridium, its concentration in the sample reduces in time. To counteract that, fresh p_{H2} is bubbled into the NMR sample between every scan. Figure 37 displays the setup for the HF-nhPHIP experiment.

Bubbling p_{H2} into the sample is the most time-consuming step in the experiment time-scale. It is important to establish a balance between the bubbling duration, p_{H2} concentration in the sample, bubbling speed and pressure, and the length of the pulse program itself. While increasing the duration of bubbling time enhances the intensity of the spectrum, there comes a point where the benefits level off and no further improvement is observed. Instead of prolonging bubbling time, the emphasis should be on recording multiple experiments for improved results by signal averaging.

In the experiments discussed in this thesis, it was determined that a bubbling time of 2 seconds is the optimal duration for HF-nhPHIP experiments. This approach ensures efficient hyperpolarization without unnecessary liquid evaporation, balancing the need for increased signal strength with practical considerations.

In summary, a careful consideration of an appropriate sample preparation method and a nuanced optimization of the measurement conditions are essential for achieving high performance in analytical applications with HF-nhPHIP. Careful control of all the parameters ensures the reliability and applicability of the method.

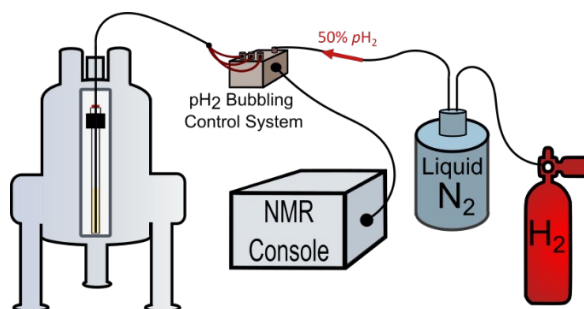


Figure 37. Schematic representation of a continuous hyperpolarization experiment setup. 50%-enriched pH_2 is produced in flow by catalytic conversion of cryo-cooled hydrogen gas. Hyperpolarization is sustained by bubbling pH_2 into the sample between every scan, while keeping the sample in steady-state during acquisition. Bubbling through the NMR sample is facilitated by a custom-built bubbling control system, described in the supporting information of Publication I. The bubbling control system is connected to the NMR console, which allows to implement and control pH_2 bubbling through the sample within the pulse program.

3.3.1 Creation of Hydrides Chemical Shift Database (Publication IV)

A significant challenge to the broader adoption of HF-nhPHIP in analytical practices is the assignment of hydrides signals to specific analytes. This is due to the reduced structural information conveyed by hydride signals compared to traditional NMR.²³ Although hydrides signals can be accurately assigned through internal standard addition,^{35,48} it is a rather time-consuming procedure, especially for biological fluids with hundreds of analytes. The development of a chemical shift database, tailored to catalogue hydrides' resonance frequencies, stands as a good alternative for signal assignment with standard addition. Such a database simplifies the signal assignment process by providing a reference framework against which unknown hydride signals can be matched. Thus, it makes it easier to identify analytes within a mixture.

This initiative has been demonstrated by creating a small yet expanding database that includes hyperpolarized spectral data of adenosines (Table 2), a group of metabolites with diagnostic importance. HF-nhPHIP spectra of seven different compounds were recorded with chemical shifts referenced to nicotinamide signal (H_x -22.935 ppm, Figure 38).

Since nicotinamide is an achiral molecule with a single binding site to associate with the iridium catalyst, it produces only one signal pair (Figure 38, *nam*). The other molecules give at least two signal pairs. The chemical shifts of both diastereomers of 1-methyladenosine (Table 2) are very similar, causing their signals to overlap and appear as one signal pair (Figure 38, 1-mAde). 6N-methyladenosine (Table 2) gives rise to two HF-nhPHIP signal pairs because its association to the iridium catalyst is restricted by the methyl group (Figure 38, 6N-mAde). Adenosine (Table 2, Ade) and 2'-O-methyladenosine (2'-O-mAde) both form two diastereomers because of their chirality. Additionally, they have two possible binding sites, which in total results in four signal pairs (Figure 38). Likewise, adenosine monophosphate (Table 2, AMP), adenosine diphosphate (ADP), and adenosine triphosphate (ATP) produce each four pairs. However, only three hydride signal pairs are clearly observable for AMP and ADP because two of their diastereomers' signals overlap (Figure 38).

The generated adenosines database was tested on human urine. The successful application of this database in identifying two analytes from urine, adenosine and 1-methyladenosine emphasizes the usefulness of the database in aiding the signal assignment of metabolites.^{33,35}

Table 2. Adenosines used in the study. Reproduced and corrected from Publication IV. Copyright 2022 by the authors. Licensee MDPI, Basel, Switzerland.

<div> </div>					
Analyte	Abbr.	R @ 1	R @ 6	R @ 2'	R @ 5'
Adenosine	Ade	-	H	H	H
1-methyladenosine	1-mAde	CH ₃	H	H	H
6N-methyladenosine	6N-mAde	-	CH ₃	H	H
2'-O-methyladenosine	2'-O-mAde	-	H	CH ₃	H
Adenosine monophosphate	AMP	-	H	H	PO ₃ H
Adenosine diphosphate	ADP	-	H	H	PO ₃ ⁻ PO ₃ H
Adenosine triphosphate	ATP	-	H	H	PO ₃ ⁻ PO ₃ ⁻ PO ₃ H

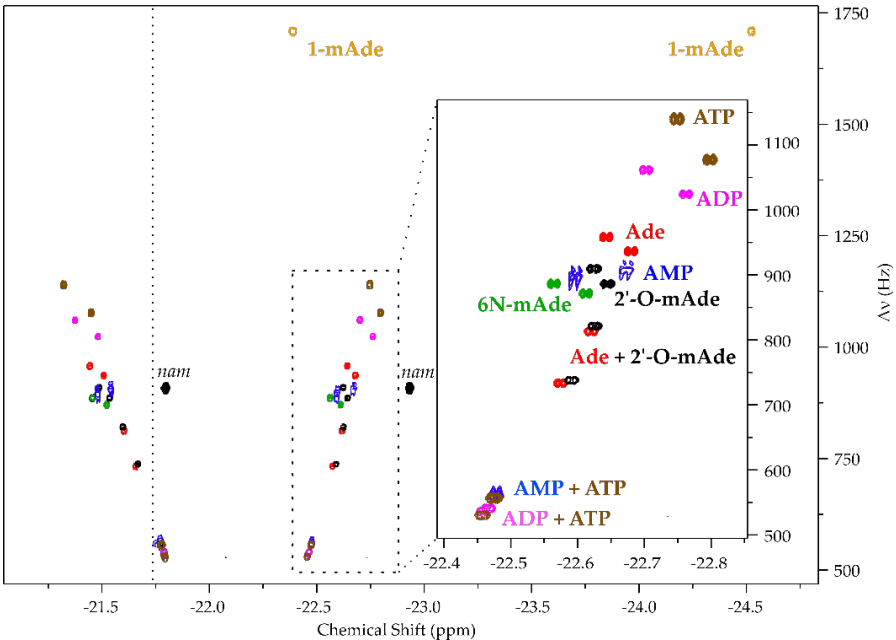


Figure 38. 2D HF-nhPHIP spectra of adenosine and its derivatives as annotated in Table 2. Reproduced and modified from Publication IV. Copyright (2022) by the authors. Licensee MDPI, Basel, Switzerland.

Based on the work with adenosines, a similar database approach has been used to assign signals of nicotine, cotinine, *trans*-3'-hydroxycotinine, and oligopeptides. It worked well in identifying and assigning signals in urine samples (Chapter 3.1) and in synthetic mixtures (Figure 39). In essence, the development of chemical shift databases for HF-nhPHIP enhances the technique's efficiency by enabling easier signal assignment and supporting higher throughput analysis. However, the creation of a database must involve careful recording of HF-nhPHIP spectra under controlled conditions. When the experimental conditions are different from the ones used to create the chemical shift database, a direct comparison of resonance frequencies becomes challenging (see Chapter 3.3).

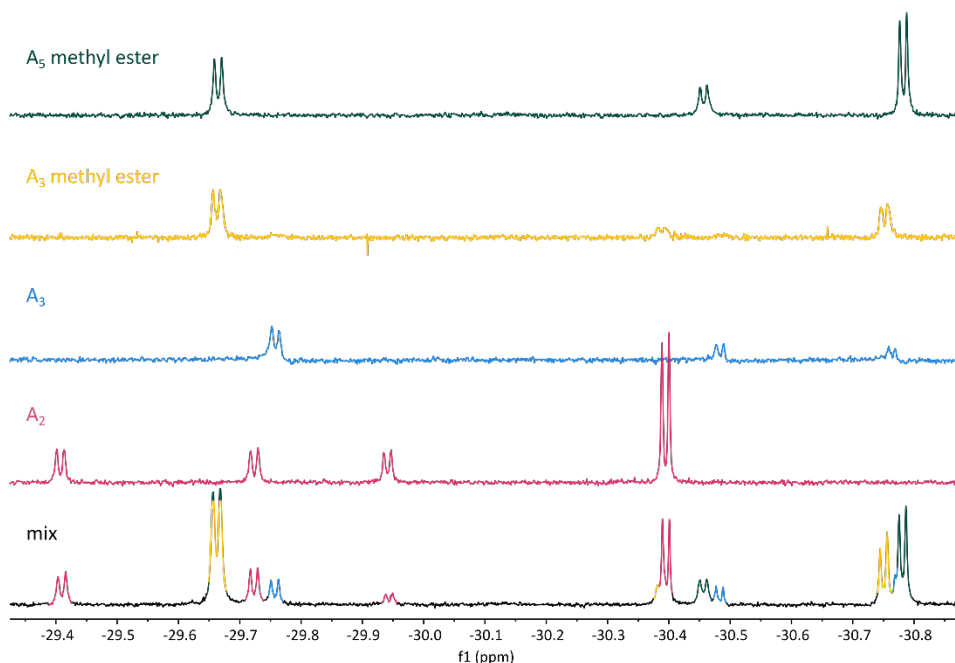


Figure 39. HF-nhPHIP spectrum of alanine oligopeptides mixture (bottom), where signals were assigned by superimposing spectra of known analytes (upper traces). The mixture composed of alanine pentamer (A₅) methyl ester, alanine trimer (A₃) and its methyl ester, and alanine dimer (A₂).

3.4 Comparative Analysis of Human and Dog Urine (Publication V)

The exploration of canine urine through NMR spectroscopy has been driven by the increasing recognition of dogs as valuable models for human diseases.⁶² Canines share our environment, exhibiting a similar range of genetic diversity and disease phenotypes, but with accelerated lifespans. This makes them ideal subjects for studying the onset and progression of various conditions, including metabolic and genetic disorders. For instance, metabolomics studies have been conducted to identify biomarkers for naturally occurring canine bladder cancer, which is similar to invasive human bladder cancer.⁶³ By exploring the metabolic fingerprints of canine urine and contrasting these with human samples, a better understanding of disease markers, improved diagnostic procedures, and potential therapeutic interventions may be developed.^{62,64,65}

Motivated by this, a comparison between canine and human urine was done with HF-nhPHIP. The aim was to determine whether hydride-driven analysis can differentiate between species and guide metabolic analysis. Four different hyperpolarization schemes were used: N-heteroaromatics targeted approach with SPE, amino acids targeted approach, oligopeptides targeted approach, and untargeted approach. Sample preparation methods are described in detail in Chapter 4.

The targeted approach with SPE (Method A, Chapter 4) focused on detecting pyrazines, specifically 2,6-dimethyl pyrazine (DMP), a molecule which is found in wolf urine.^{66,67} Hypothesising that a domestic dog shares a similar metabolic profile with a wolf, DMP could be present in canine urine as well. First, HF-nhPHIP signals were established by measuring a pure DMP sample. Second, canine urine and human urine for reference were measured and superimposed on the DMP spectrum (Figure 40). While DMP could not be identified in canine urine as initially expected, a diagonal line was detected in both canine and human urine spectra where the DMP signal resonated. The presence of pyrazines in both species is suggested by the overlapping of seven signals along that diagonal line. Likewise, nicotinamide (nam) and 1-methyladenosine (1-mAde) are present in both urines and their corresponding signals overlap nicely (Figure 41).

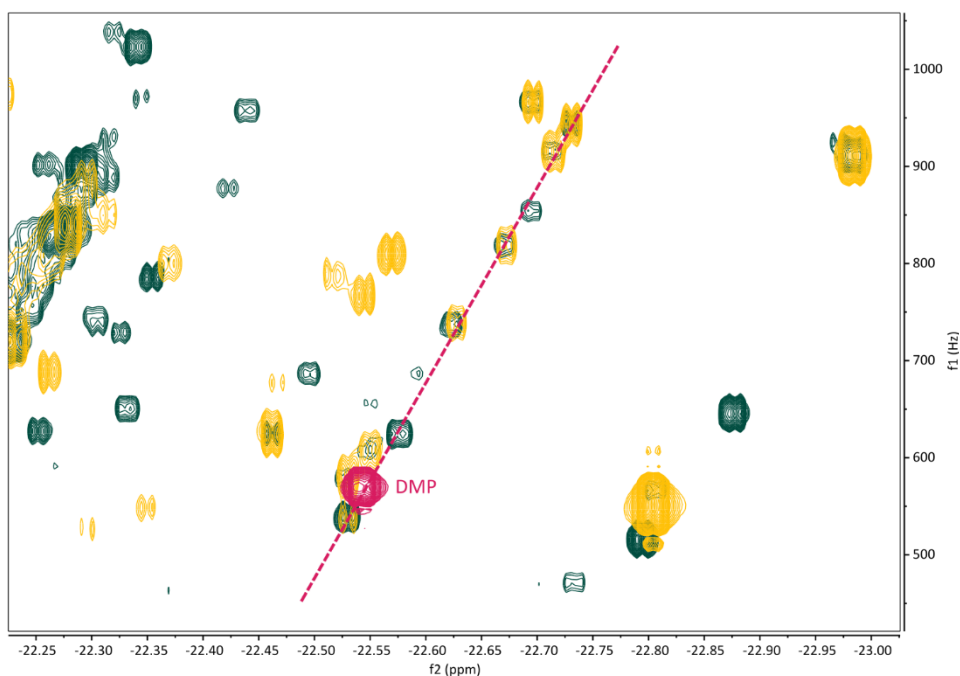


Figure 40. Superimposed HF-nhPHIP spectra of canine (yellow) and human urine (green), along with 2,6-dimethyl pyrazine (DMP, pink). Urine samples were prepared according to the targeted method with SPE described under Method A, Chapter 4. There are some signals which overlap in human and canine urines, while others do not. Although DMP signal could not be confirmed in either urine spectra, a clear diagonal (pink dashed line) suggests that both urine samples contain pyrazines.

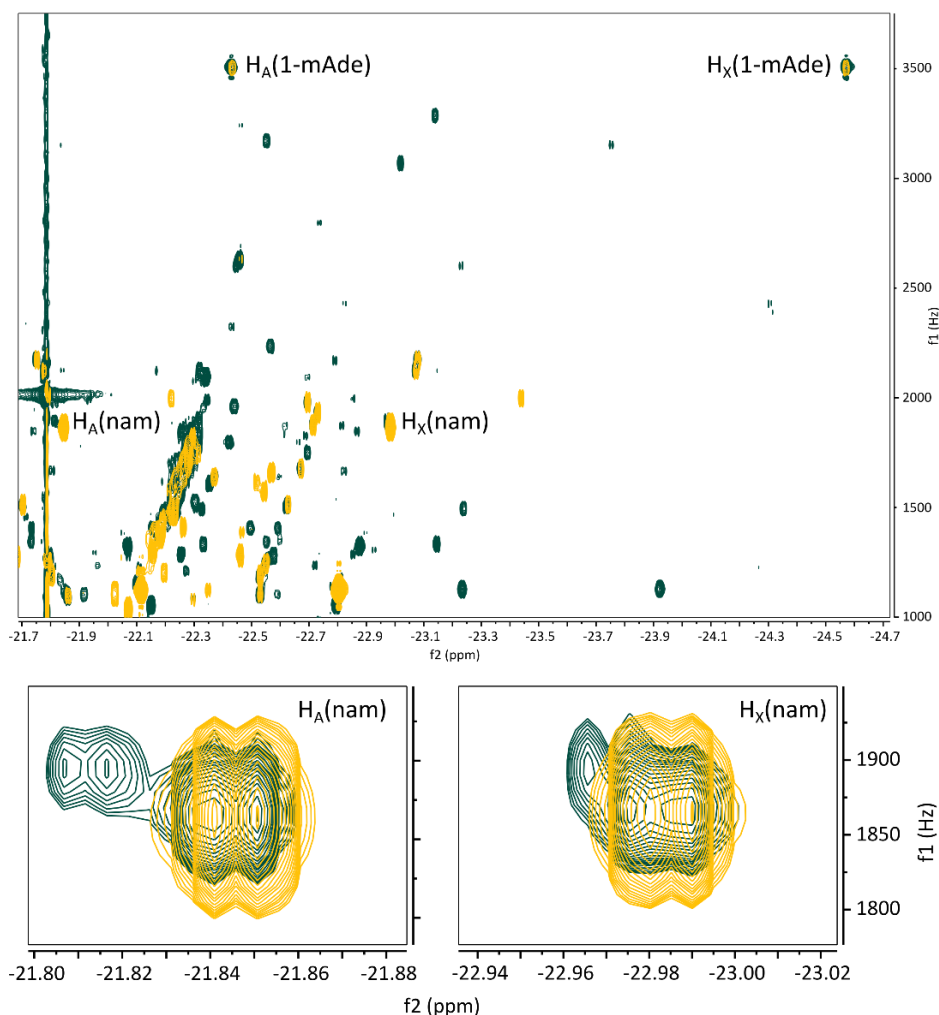


Figure 41. Superimposed HF-nhPHIP spectra of canine (yellow) and human urine (green) zoomed into the region of 1-methyladenosine (1-mAde) and nicotinamide (nam). The analytes were assigned using the chemical shift database (Chapter 3.3.1). The close-up of nam demonstrates the robustness of HF-nhPHIP as signals in both urine overlap nicely. Urine samples were prepared according to the targeted method described under Method A, Chapter 4.

Besides pyrazines, HF-nhPHIP H_X signals resonating at δ -16.4 to -17.9 ppm region are of great interest as these signals could arise from sulphur atom association with the iridium catalyst (Figure 42).^{28,31} Similarly to pyrazines, some signals overlap in both canine and human urine spectra, implying that these molecules are not species specific. On the other hand, there are signals which clearly represent only one specimen.

Furthermore, when urine samples were prepared with untargeted approach (Method B, Chapter 4) the difference between canine and human urine in the same spectral region was more prominent (Figure 43). While signals clustered together at δ -17 to -17.9 ppm in canine urine, human urine gave rise to signals at δ -18.8 ppm. By using different sample preparation methods (targeted or untargeted), new information can be obtained from the spectra. Figure 44 and Figure 45 show the full spectra of zoomed in regions in Figure 42 and Figure 43, respectively.

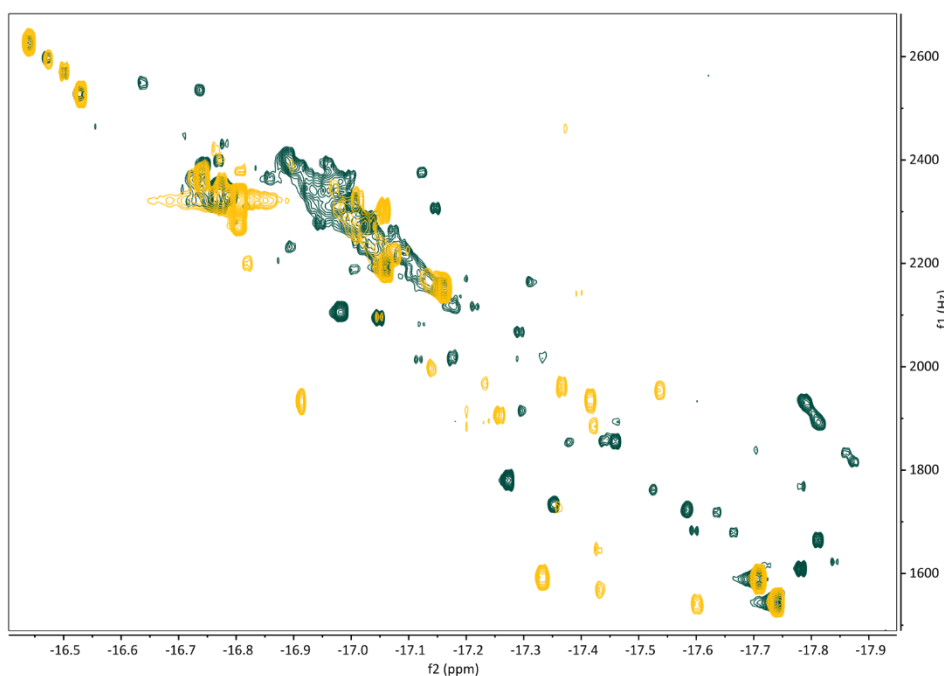


Figure 42. Superimposed HF-nhPHIP spectra of canine (yellow) and human urine (green). Urine samples were prepared according to the targeted method with SPE described under Method A, Chapter 4. There are clear differences between the two spectra with some signals better resolved than the others. Poor resolution of some signals may be due to deuteration of the complex.²⁹ Signals resonating at δ -16.4 to -17.9 ppm region could be from S-atom association, although these have not been experimentally confirmed.

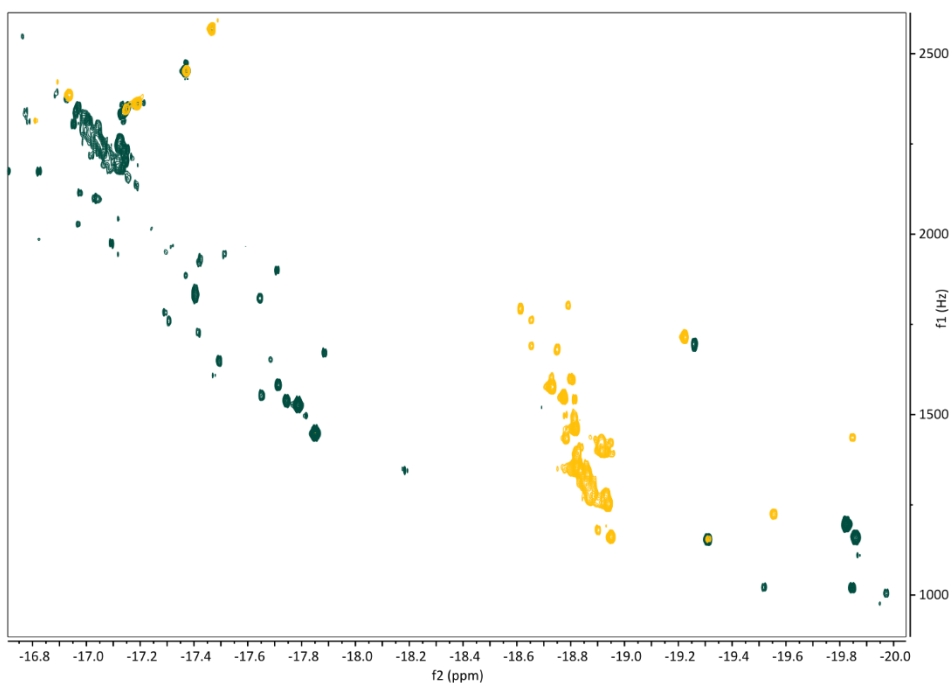


Figure 43. Superimposed HF-nhPHIP spectra of canine (yellow) and human urine (green). Urine samples were prepared according to the untargeted approach described under Method B, Chapter 4. Although a couple of signals coincide, the majority at δ -16.8 to -20.0 ppm region is very different, which for different species is expected.

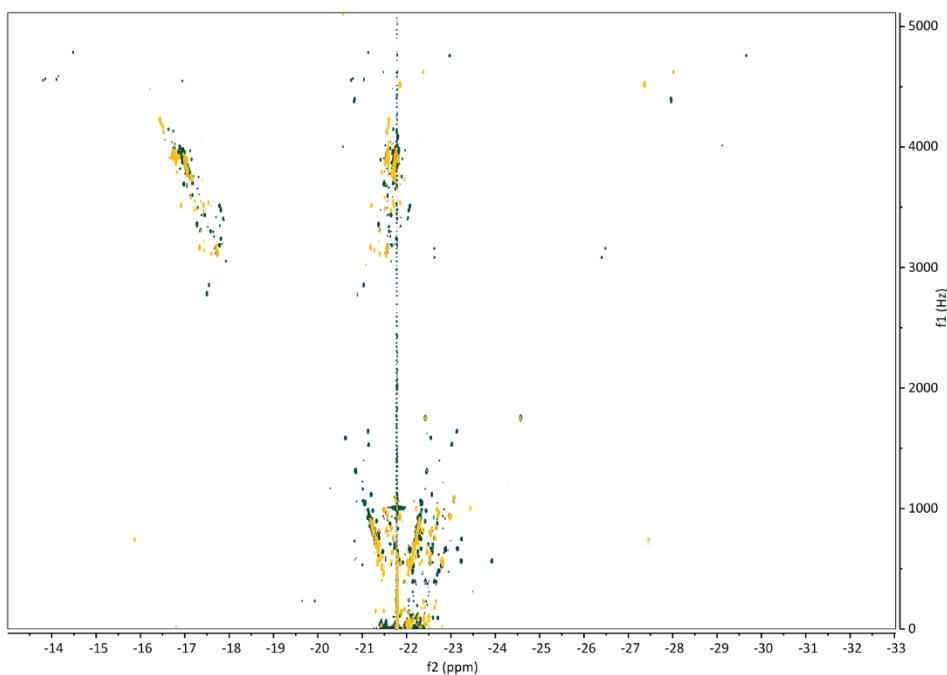


Figure 44. Superimposed HF-nhPHIP spectra of canine (yellow) and human urine (green). Urine samples were prepared according to the targeted method with SPE described under Method A, Chapter 4.

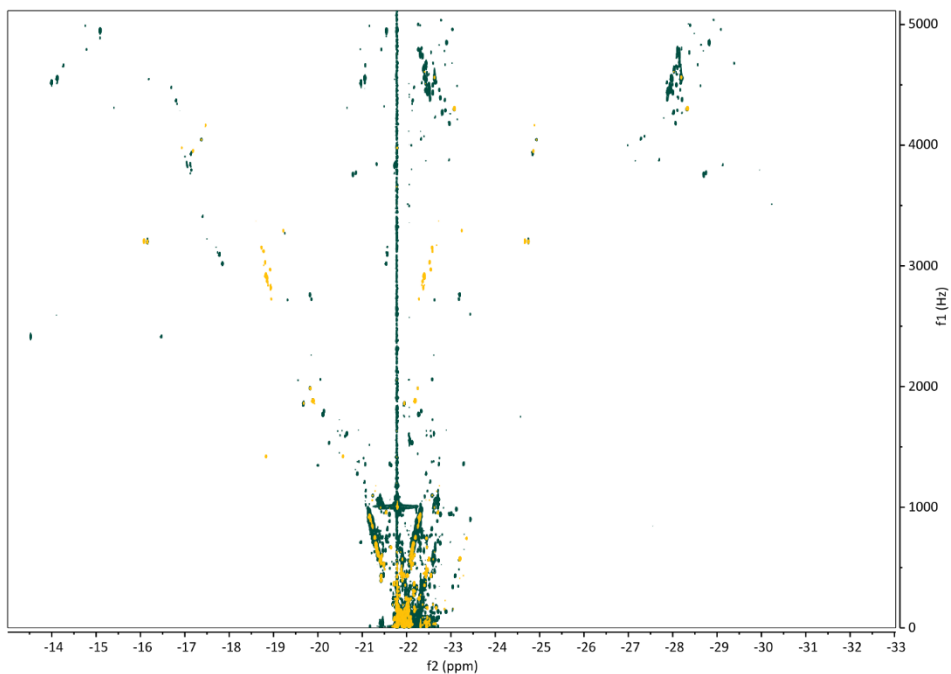


Figure 45. Superimposed HF-nhPHIP spectra of canine (yellow) and human urine (green). Urine samples were prepared according to the untargeted approach described under Method B, Chapter 4.

Targeted sample preparation Method C (Chapter 4) was used to detect amino acids. Both human and canine urine seem to contain the same proteinogenic α -amino acids (Figure 46). However, in human urine more than ten additional HF-nhPHIP signals were seen (Figure 46 green signals), which probably arise from amino acids beyond the 22 proteinogenic ones. On the other hand, dog urine exhibited two strong signal pairs around δ -17.0 and -24.4 ppm (Figure 47). These very intense signals compared to amino acids may be caused by the dog's consumption of a food supplement called Adaptil Express Tablets. The supplement is given to calm dogs during stressful situations, such as fireworks, and contains vitamin B1, which features a sulphur atom. Albeit chemical shifts suggest S-atom association, neither vitamin B1 nor amino acids cysteine and methionine could be detected in their pure form under similar measurement conditions. Further research is needed to determine the origin of these signals.

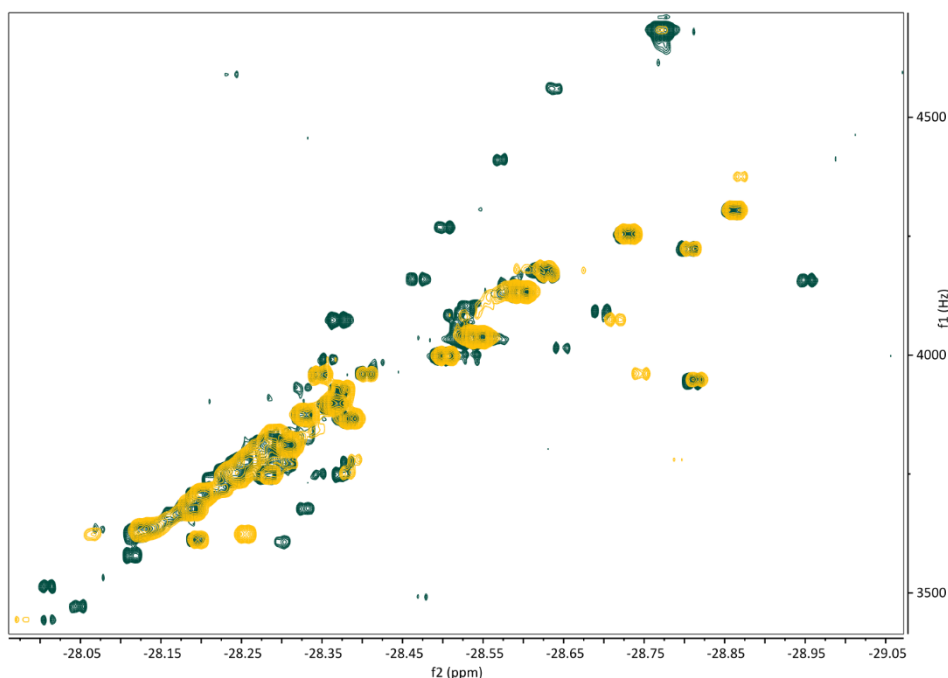


Figure 46. Superimposed HF-nhPHIP spectra of canine (yellow) and human urine (green) prepared according to Method C, Chapter 4, zoomed to amino acids region. Signals corresponding to amino acids have not been assigned explicitly, but both urines feature signals that coincide, meaning these amino acids are present in both samples. In human urine, there are some additional signals forming a diagonal with a steeper slope. These signals could arise from α -amino acids beyond the 22 proteinogenic ones.

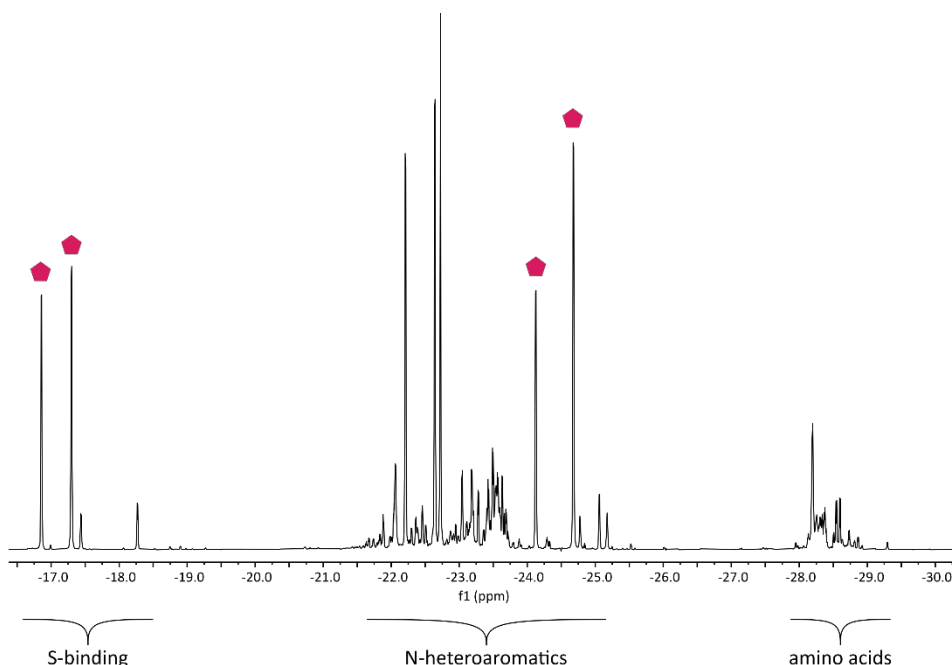


Figure 47. HF-nhPHIP spectrum of dog urine, prepared according to Method C, Chapter 4. Two very strong signal pairs can be seen, δ -17 and δ -24.5 ppm (pink pentagons), possibly due to S-atom association to the iridium catalyst.^{28,31} These signals were not present in human urine. Whether these signals are species specific, breed specific, or individual specific (inherent or dietary-caused) requires further research.

When focusing on oligopeptides, there were more signals observed in human urine than in canine urine (Figure 48). This result suggests that the oligopeptides being targeted are more abundant or have a higher concentration in human urine compared with canine urine. Further research is needed to investigate the specific oligopeptides involved and their potential significance.

HF-nhPHIP is a relatively new technique and the preliminary results show that we have limited knowledge of its capabilities. However, studying metabolic fingerprints with HF-nhPHIP has the potential to contribute to analytical applications. On the other hand, it is important to acknowledge that the use of HF-nhPHIP in studying metabolic fingerprints also presents certain limitations. For instance, interpreting metabolic fingerprints obtained through HF-nhPHIP is not straightforward. Therefore, its practical applications require careful consideration and further investigation.

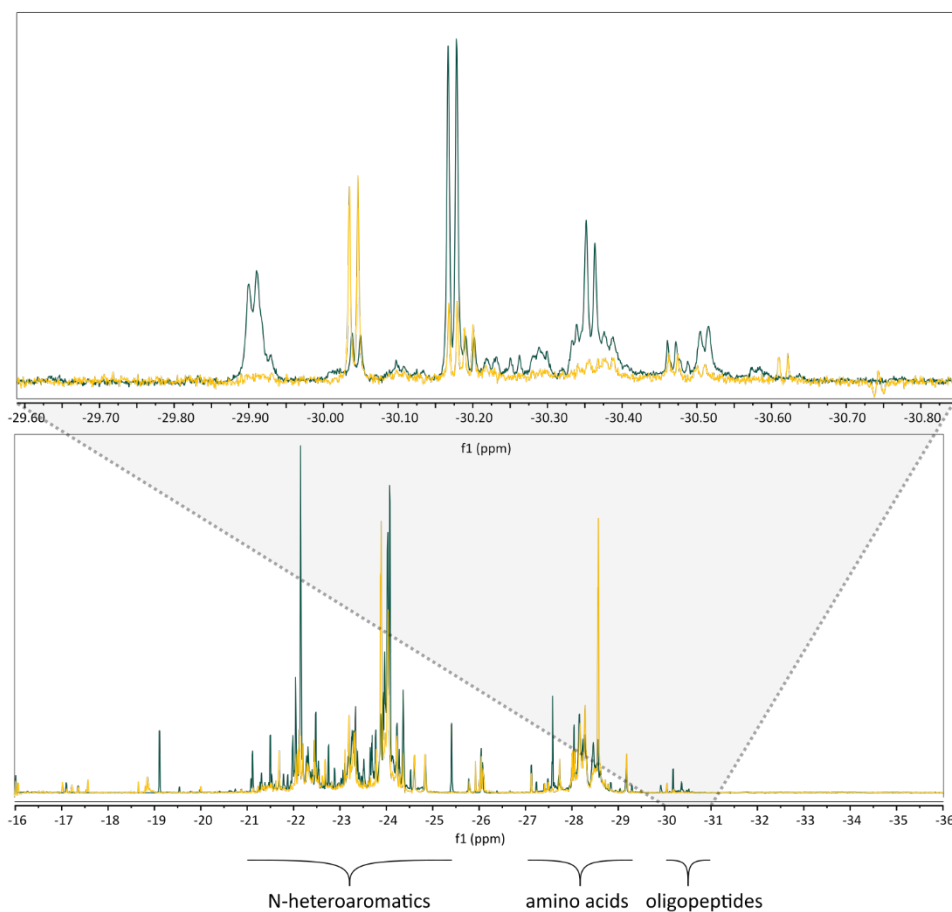


Figure 48. Superimposed HF-nhPHIP spectra of canine (yellow) and human urine (green) prepared according to Method D (Chapter 4) to detect oligopeptides. Although signals in oligopeptide region are much less intensive than signals of amino acids, a couple of H_x signals can be seen at δ -30 ppm region. At least four signals seem to arise from oligopeptides present in both urines.

4 Materials and Methods

4.1 Sample Preparation Methods for the Comparative Analysis of Human and Dog Urine

Method A. Experimental conditions for the N-heteroaromatics targeted approach with SPE. Oasis HLB 6cc/200mg cartridge was used for the SPE method. The cartridge was activated with 3 mL of methanol and conditioned with 3 mL of 10 mM KH_2PO_4 buffer solution. Urine was thawed in a water bath, corrected with NaOH to pH 7.4, and centrifuged for 12 min at 1825g (maximum allowed speed for 15 mL tubes). 5 mL of centrifuged urine without sediment was added to the cartridge. The cartridge was then washed with 3 mL of 10 mM KH_2PO_4 buffer solution and dried with constant N_2 flow at 1 bar for 30 min. Urine was extracted from the SPE cartridge with 1.6 mL of methanol- d_4 and stored at -80°C until NMR experiment.

The NMR sample comprised 1.2 mM $[\text{Ir}(\text{IMes})(\text{COD})\text{Cl}]$ (IMes = 1,3-bis(2,4,6-trimethylphenyl)imidazol-2-ylidene, COD = cyclooctadiene), 21.7 mM 1-methyl-1,2,3-triazole as co-substrate, and 475 μL of SPE-treated urine. Total sample volume was 600 μL with the ratio of iridium catalyst to co-substrate 1:18.

Method B. Experimental conditions for the untargeted approach. The urine pH was adjusted to 11 with NaOH and left to settle for approximately 1 hour. After that, the urine was centrifuged at the maximum allowed speed for 12 minutes at 1825g. The sediment-free urine was then divided into tubes, with each tube containing 2.4 mL of urine. These tubes were frozen using liquid nitrogen and subjected to lyophilization for 48 hours.

To dissolve the dried urine, 150 μL of D_2O and 450 μL of methanol- d_4 were added. The mixture of water and methanol with the urine was sonicated for 10 minutes and then centrifuged for 3 minutes at 1825g. The upper layer of this water-methanol urine mixture was used for the nhPHIP experiments.

The NMR sample comprised 5.7 mM $[\text{Ir}(\text{IMes})(\text{COD})\text{Cl}]$, 103 mM 1-methyl-1,2,3-triazole as co-substrate, and 30 μL of urine. Total sample volume was 600 μL with the ratio of iridium catalyst to co-substrate 1:18.

Method C. Experimental conditions for the amino acids targeted approach. Urine was used as supplied with no sample treatment. The NMR sample comprised 3.53 mM $[\text{Ir}(\text{IMes})(\text{COD})\text{Cl}]$ (170-176 μL of 12-12.4 mM stock solution), 63.5 mM pyridine as co-substrate (188-190 μL of 200-202 mM stock solution), 108 μL of 110 mM piperidine/piperidinium buffer, and 30 μL of urine. Total sample volume was 600 μL with the ratio of iridium catalyst to co-substrate 1:18.

Method D. Experimental conditions for the oligopeptides targeted approach. The urine pH was adjusted to 11 with NaOH and left to settle for approximately 1 hour. After that, the urine was centrifuged at the maximum allowed speed for 12 minutes at 1825g. The sediment-free urine was then divided into tubes, with each tube containing 2.4 mL of urine. These tubes were frozen using liquid nitrogen and subjected to lyophilization for 48 hours.

To dissolve the dried urine, 150 μL of D_2O and 450 μL of methanol- d_4 were added. The mixture of water and methanol with the urine was sonicated for 10 minutes and then centrifuged for 3 minutes at 1825g. The upper layer of this water-methanol urine mixture was used for the nhPHIP experiments.

The NMR sample comprised 3.2 mM $[\text{Ir}(\text{IMes})(\text{COD})\text{Cl}]$, 63.7 mM 3-fluoro-4-methylpyridine as co-substrate, and 30 μL of urine. Total sample volume was 600 μL with the ratio of iridium catalyst to co-substrate 1:18.

5 Summary

Through exploring the applications for high-field non-hydrogenative PHIP chemosensing in analysing biological fluids, this technique stands out in its ability to detect and quantifying dilute analytes in complex mixtures.

In this thesis, different sample preparation techniques for urine samples have been summarised. The diagnostic and analytical potential of HF-nhPHIP was shown with the targeted sample preparation approach with SPE, focusing on detecting nicotine and cotinine HF-nhPHIP signals from smokers' urine. By careful workflow optimization, it was possible to follow dynamic processes within the human body with high accuracy and repeatability, as demonstrated by recording nicotine withdrawal and administration. The findings of this experiment indicate that a similar strategy can be employed to extract precise data from urine for purposes like evaluating biomarkers or studying pharmacokinetics.

In addition, a sample preparation protocol was showcased to progress towards untargeted metabolomics analysis. Although the structural elucidation of analytes remains unavailable with HF-nhPHIP, the observed signals corresponding to the iridium-substrate complex can be assigned with different methods like standard addition, chemical shift databases, and linear patterns on 2D zero-quantum spectra. These signal assignment methods were implemented on urine samples and exhibited good performance when combined with meticulous sample preparation and NMR specific conditions.

Through precise adjustments to the chemical machinery of pH_2 hyperpolarization, the range of analytes detectable by HF-nhPHIP was effectively expanded to include oligopeptides. By integrating HF-nhPHIP, conventional NMR experiments, and DFT calculations, the investigation of how oligopeptides bind to the iridium catalyst has yielded valuable information about the underlying mechanisms of the hyperpolarization process. Experimental observations revealed three unique binding configurations, and the energetically favoured one. With this knowledge, it will be easier to optimise HF-nhPHIP conditions to target oligopeptides from biological fluids.

This thesis has utilized both targeted and untargeted experiments to showcase the effectiveness of HF-nhPHIP in accurately identifying and quantifying analytes within complex biological matrices. The capability of HF-nhPHIP to differentiate between species was demonstrated by detecting urine samples from both humans and canines.

List of Figures

- Figure 1. The nuclear magnetic dipole moment μ is determined by the nuclear spin angular momentum I and nucleus specific gyromagnetic ratio γ 11
- Figure 2. According to Zeeman splitting spin= $\frac{1}{2}$ nucleus has $2I + 1 = 2$ energy levels $E\alpha$ and $E\beta$, when placed in an NMR magnet with a magnetic field B_0 . At thermal equilibrium spins form an anisotropic distribution with a bias towards low magnetic energy state, which for $\gamma > 0$ like ^1H nucleus is $E\alpha$. This partial orientation along the magnetic field follows Boltzmann distribution and determines the level of polarization in the sample. The polarization increases as the strength of the external magnetic field increases. 13
- Figure 3. (a) Atomic nuclei partially align with the external magnetic field B_0 and create a net magnetic moment, M . (b) A short-duration radio frequency pulse rotates M to the xy -plane, creating transverse magnetization. The field B_0 generates torque on M and makes nuclei precess at Larmor frequency. (c) After a while, spins lose their coherence, transverse net magnetization decays, and spins realign with B_0 . During that process, oscillating magnetization vector creates electric current, which is detected in the receiver coil to get a spectrum. 14
- Figure 4. A simulated ^1H spectrum of ethanol ($\text{CH}_3\text{CH}_2\text{OH}$). The effect of electron shielding gives rise to three peaks, which represent three different chemical environments in a molecule. (a) If there would not be any spin-spin coupling between the spins. (b) In the case of spin-spin coupling, the signals are split into a triplet, doublet of quartets, and a triplet because of neighbouring nuclei ($n+1$) rule..... 15
- Figure 5. Hyperpolarization techniques manipulate spin states towards a significant population on one energy state. The higher population difference leads to a stronger NMR signal, which improves signal-to-noise ratio and increases sensitivity..... 16
- Figure 6. A schematic representation of a dDNP setup. After hyperpolarization in the DNP polarizer the sample is rapidly dissolved and transferred to the NMR magnet for acquisition. Reproduced and modified from ¹¹. Copyright (2021) Elsevier..... 17
- Figure 7. (a) Orthohydrogen and (b) parahydrogen spin isomers of molecular hydrogen. Orthohydrogen has a symmetric rotational state $I = 1$, while parahydrogen has an antisymmetric rotational state $I = 0$ 18
- Figure 8. At room temperature (300 K) molecular H_2 gas comprises 75% ortho- and 25% para-isomers. Liquid N_2 temperature (77 K), at the presence of a ferromagnetic catalyst (e.g. iron(III)oxide or charcoal), allows for preparation of 50% $p\text{H}_2$, whereas temperatures below 20 K enable production of >97% $p\text{H}_2$ fraction. By imbedding $p\text{H}_2$ generator inside a cryogenic storage dewar, $p\text{H}_2$ maintains its long-lived nuclear spin state outside of the dewar.¹⁵ Adapted with permission from ref. ¹⁶. Copyright (2015) Wiley-VCH GmbH, Weinheim..... 19
- Figure 9. Energy level diagrams with possible transitions and the resulting spectra of (a) thermal polarization experiment with orthohydrogen (b) PASADENA experiment, (c) ALTADENA experiment. 20

Figure 10. The schematic representation of SABRE. Iridium-based catalyst precursor **1**, $[\text{Ir}(\text{IMes})(\text{COD})\text{Cl}]$, where $\text{IMes} = 1,3\text{-bis}(2,4,6\text{-trimethylphenyl})\text{imidazol-2-ylidene}$, $\text{COD} = \text{cyclooctadiene}$,²¹ is mixed with substrate (*sub*) under parahydrogen pressure to form an active SABRE complex **2**⁺. The correlated spin order of pH_2 spontaneously transfers to the substrate nuclear spins through J-coupling at low magnetic field. Continuous substrate exchange, association, and disassociation with the metal catalyst leads to the build-up of hyperpolarized substrate free in solution. 21

Figure 11. After the hydrogenation of the complex precursor **1**, metal complexes **4**⁺ and **5**⁺ can form at the presence of a co-substrate (*co-sub*). Provided that the ratio of $[\text{sub}] \ll [\text{catalyst}] < [\text{co-sub}]$ is kept, the formation of complex **5**⁺ is unlikely. 21

Figure 12. Schematic representation of the active complex **4**⁺ in SABRE and HF-nhPHIP experiments. In SABRE, the correlated spin order of pH_2 spontaneously transfers to the substrate nuclear spins through spin-spin couplings at low field, hyperpolarizing the substrate. The hyperpolarized substrate disassociates from the catalyst and is detected free in the solution. In HF-nhPHIP, the singlet state of pH_2 is transferred to the magnetization of hydrides, resulting in enhanced NMR signals of hydrides. Substrate stays bound to the iridium complex, while the hydrides are detected. 22

Figure 13. Schematic representation of the HF-nhPHIP complex. a) The iridium catalyst has three vacant binding sites: two in the equatorial plane (*eq*) and one in the axial position (*ax*). b) Pyridine associated through N-atom forming a monodentate binding. c) Glycine associated through N- and O-atoms forming a bidentate *ax-eq* complex. d) Pyruvate associated through O-atoms forming a bidentate *eq-eq* complex. 23

Figure 14. The HF-nhPHIP spectra of (a) nicotinamide and (b) nicotine. H_A and H_X form a pair of doublets because of the spin-spin coupling between the hydrides. The number of signal pairs that form per analyte depends on the structure of that analyte. While nicotinamide (*nam*) is an achiral compound and gives only one pair of doublets, nicotine (*nic*) is a chiral and forms two pairs of doublets, diastereomers with different physical properties. 24

Figure 15. Possible transitions in a spin system of two $\text{spin}=\frac{1}{2}$ nuclei: SQ – single-quantum transition, DQ – double-quantum transition, ZQ – zero-quantum transition. DQ and ZQ are multiple-quantum transitions, which are directly unobservable. In parahydrogen hyperpolarization at high field like PASADENA experiment, $\alpha\beta$ and $\beta\alpha$ energy levels are overpopulated, sketched here as thicker lines. 25

Figure 16. 2D zero-quantum experiment helps to determine which signals belong to the same complex as they have the same ZQ frequency in f_1 dimension (*y*-axis), meaning they are on the same horizontal line on a 2D spectrum. The abbreviations are the following: *nic* - nicotine, *nam* – nicotinamide. Although here both H_A and H_X have the same color-coding, they are in opposite phases. One hydride features an absorption, while the other dispersion lineshape as described by Equation (35). Upper trace shows a 1D spectrum of the same sample with a zoom into nicotine signals, which is present in the sample at much lower concentration compared to nicotinamide. All signals in 1D experiment are in absorption mode. 26

Figure 17. The pulse program scheme used for 2D zero-quantum (ZQ) experiments.... 27

Figure 18. 75% of nicotine is metabolised to cotinine in the human body. Around 40% of cotinine is further metabolised into 3'-hydroxycotinine with stereoselectivity towards its trans-isomer. Unchanged nicotine and cotinine molecules are excreted with urine at around 10% each of total urinary nicotine, while the main metabolite found in smokers' urine trans-3'-hydroxycotinine is excreted at around 40%. ⁵¹	34
Figure 19. Nicotine (red triangles) and cotinine (blue circles) HF-nhPHIP signals in urine matrix assigned by standard addition method. While H _x signals (right) are well separated, H _A signals (left) are not. One of the diastereomers of cotinine and nicotine, resonate at the same ¹ H chemical shift. To improve resolution, 2D ZQ spectroscopy was implemented...	35
Figure 20. HF-nhPHIP spectra show the metabolic changes caused by nicotine consumption. A series of samples were collected from a volunteer who used a transdermal patch for nicotine administration. Nicotine (Nic) signals were clearly visible after 5 hours of applying the patch (left panel). 24 h (right panel) after applying the patch, Nic signals were almost gone, while cotinine (Cot) signals were still observable and trans-3'-hydroxycotinine (3HC) signals were the strongest.	36
Figure 21. Comparison of SPE recoveries of nicotine and cotinine from Phenomenex Strata-X, Oasis HLB, and Biotage Isolute ENV+ cartridges. Urine samples were adjusted to either pH 10.6 or 8.6, SPE cartridges were washed with a buffer at the respective pH, analytes were extracted with methanol-d ₄ . Analyte ¹ H integrals obtained from quantitative NMR spectra were compared against the integral of an internal standard (DSS: Sodium trimethylsilylpropanesulfonate) added to the extract after the SPE procedure.....	37
Figure 22. Flowchart of the SPE procedure.....	38
Figure 23. A comparison of two HF-nhPHIP spectra obtained from the same urine with either using a 10 mM KH ₂ PO ₄ buffer (yellow) or 50 mM KH ₂ PO ₄ buffer (green) in the SPE procedure. 50 mM KH ₂ PO ₄ buffer elutes amino acids, while 10 mM buffer retains S-containing analytes. An expansion of the N-heteroaromatics region shows that nicotine (red triangles) and cotinine (blue circles) signals are more intensive when 10 mM KH ₂ PO ₄ buffer is used.	39
Figure 24. An expansion to H _x signals of nicotine (red triangles) and cotinine (blue circles) of two different urine extracts (green and yellow) obtained by using H ₂ O in wash step in SPE method. Nicotine HF-nhPHIP signals have shifted, while cotinine and 3-fluoropyridine (*), used as an internal standard, stayed in place.....	40
Figure 25. Comparison of SPE recoveries in different urines (provided by six volunteers A – F) of nicotine and cotinine extracted with methanol-d ₄ or chloroform-d.	41
Figure 26. Calibration curves for nicotine (red) and cotinine (blue) based on the linear fitting of 10 data points. Three parallels were measured and averaged for every point. Error bars represent the standard deviation of the three parallels. Calibration curves are analyte-specific due to different iridium binding affinities. Reproduced from Publication I. Copyright 2021, American Chemical Society.....	42
Figure 27. Residual nicotine (nic, red) and cotinine (cot, blue) H _x signals show passive smoking in the urine of a non-smoker. Signals can be distinguished from noise by their doublet structure. Because the signals are barely over noise level and are obscured by much stronger signals in a 1D experiment, they can easily go unnoticed.....	43

Figure 28. Flowchart for the urine sample preparation procedure for the untargeted approach. 44

Figure 29. The spectra of a urine sample were obtained using two different approaches: targeted approach with SPE method, and untargeted approach with minimal sample preparation. The two methods retain different kind of analytes. 45

Figure 30. Screening of co-substrates on a mixture of alanine, leucine, phenylalanine under basic conditions recorded at 25 °C. The suitability of a co-substrate was evaluated based on the HF-nhPHIP signal intensity, signal line width, and number of signals in -28 ppm region. The screened co-substrates were 1 – mtz, 2 – pyridine, 3 – 3-methylpyridine, 4 – 4-methylpyridine, 5 – 3,5-dimethylpyridine, 6 – 4-tertbutylpyridine, 7 – 3-fluoropyridine, 8 – 4-fluoropyridine (no observable signals), 9 – 3,5-difluoropyridine, 10 – 3-fluoro-4-methylpyridine. 47

Figure 31. 3-fluoro-4-methylpyridine (aqua) proved to be a more suitable co-substrate over pyridine (black) to detect the amino acid alanine under basic conditions. The signals at δ -23.55 to -23.95 correspond to H_A , while those at δ -28.10 to -28.40 correspond to H_X of the same alanine-iridium complexes. The two signal pairs forming for both co-substrates represent the two diastereomers. There is a notable difference in resonance frequencies and signal intensities, but the relative intensity of the two diastereomers are approximately the same with either co-substrate. Spectra were measured at 10 °C. 48

Figure 32. Oligopeptides comprise multiple amino acids, which are connected with peptide bonds, where N-terminus is the amino group ($-NH_2$, yellow) and C-terminus is the carboxyl group ($-COOH$, blue). (a) Alanine trimer comprising three alanine amino acids (AAA), (b) leucine-enkephalin, which comprises tyrosine, glycine, glycine, phenylalanine, and leucine (YGGFL). 48

Figure 33. HF-nhPHIP spectra of ^{15}N -labelled oligopeptides (a) A-A[^{15}N]-A-A-OMe and (b) A[^{15}N]-A-A-OMe. Blue circles correspond to diastereomers of the ax-eq complex, red circles to the eq-eq complex, and yellow triangles to diastereomers of mono complex. Note that some signals overlap in 1D, but were resolved in 2D spectra. Signal splitting due to ^{15}N coupling can be seen only for (b) A[^{15}N]-A-A-OMe mono and eq-eq configurations' signals, confirming ^{15}N in axial and O in equatorial position. ax-eq shows no splitting, which indicates that ^{15}N must be in axial position. (a) A-A[^{15}N]-A-A-OMe does not feature ^{15}N splitting, meaning that only the N-terminus associates with the iridium catalyst to form all three configurations. Asterisk (*) denotes signals from the co-substrate 3-fluoro-4-methylpyridine (3F4MePy)-Ir-complex. Reproduced from Ref. ⁵⁴. Copyright 2023 The Authors. Published by Analyst. 50

Figure 34. DFT calculations and NOE experiments confirmed bidentate configurations of alanine oligomers to the iridium catalyst (a) A₃ and A₃-OMe, (b) A₄-OMe, (c) A₂-OMe, and (d) A₂. A₂ and A₃ formed 5-member Ir-cycls, while A₄-OMe and A₅-OMe present more complex structures containing an 8-member cycle. Reproduced from Ref. ⁵⁴. Copyright 2023 The Authors. Published by Analyst. 51

Figure 35. HF-nhPHIP H_A signals of functional oligopeptides: papain inhibitor (GGYR), neuropeptide Leu-enkephalin (YGGFL), and cosmeceutical peptide hexapeptide-11 (FVAPFP), measured at 25 °C. Two sample preparation protocols were followed: (a) solid lines: peptide was dissolved in water, pH corrected to 7.4–7.9, lyophilized and dissolved

in methanol-d₄ prior nhPHIP measurement. Ratio of catalyst : 3F4MePy : oligopeptide was 1 : 18 : 0.08; (b) dashed lines: peptide was dissolved in methanol-d₄ as supplied. Ratio of catalyst : 3F4MePy : oligopeptide was 1 : 8 : 0.08. Comparison of spectra (a) and (b) demonstrates that nhPHIP performance is dependent on the particular oligopeptide, sample preparation and measurement conditions. Reproduced from Ref. ⁵⁴. Copyright 2023 The Authors. Published by Analyst..... 52

Figure 36. HF-nhPHIP spectrum of a urine sample. H_A signals characteristic to oligopeptides appear at around -30 ppm, whereas cosubstrate H_X signals are around -23 ppm. The untargeted approach was used to prepared the urine sample. Spectrum was recorded at 35 °C. Reproduced from Ref. ⁵⁴. Copyright 2023 The Authors. Published by Analyst.53

Figure 37. Schematic representation of a continuous hyperpolarization experiment setup. 50%-enriched p_{H2} is produced in flow by catalytic conversion of cryo-cooled hydrogen gas. Hyperpolarization is sustained by bubbling p_{H2} into the sample between every scan, while keeping the sample in steady-state during acquisition. Bubbling through the NMR sample is facilitated by a custom-built bubbling control system, described in the supporting information of Publication I. The bubbling control system is connected to the NMR console, which allows to implement and control p_{H2} bubbling through the sample within the pulse program.....56

Figure 38. 2D HF-nhPHIP spectra of adenosine and its derivatives as annotated in Table 2. Reproduced and modified from Publication IV. Copyright (2022) by the authors. Licensee MDPI, Basel, Switzerland.57

Figure 39. HF-nhPHIP spectrum of alanine oligopeptides mixture (bottom), where signals were assigned by superimposing spectra of known analytes (upper traces). The mixture composed of alanine pentamer (A5) methyl ester, alanine trimer (A3) and its methyl ester, and alanine dimer (A2)..... 58

Figure 40. Superimposed HF-nhPHIP spectra of canine (yellow) and human urine (green), along with 2,6-dimethyl pyrazine (DMP, pink). Urine samples were prepared according to the targeted method with SPE described under Method A, Chapter 4. There are some signals which overlap in human and canine urines, while others do not. Although DMP signal could not be confirmed in either urine spectra, a clear diagonal (pink dashed line) suggests that both urine samples contain pyrazines. 59

Figure 41. Superimposed HF-nhPHIP spectra of canine (yellow) and human urine (green) zoomed into the region of 1-methyladenosine (1-mAde) and nicotinamide (nam). The analytes were assigned using the chemical shift database (Chapter 3.3.1). The close-up of nam demonstrates the robustness of HF-nhPHIP as signals in both urine overlap nicely. Urine samples were prepared according to the targeted method described under Method A, Chapter 4..... 60

Figure 42. Superimposed HF-nhPHIP spectra of canine (yellow) and human urine (green). Urine samples were prepared according to the targeted method with SPE described under Method A, Chapter 4. There are clear differences between the two spectra with some signals better resolved than the others. Poor resolution of some signals may be due to deuteration of the complex.²⁹ Signals resonating at δ -16.4 to -17.9 ppm region could be from S-atom association, although these have not been experimentally confirmed..... 61

Figure 43. Superimposed HF-nhPHIP spectra of canine (yellow) and human urine (green). Urine samples were prepared according to the untargeted approach described under Method B, Chapter 4. Although a couple of signals coincide, the majority at δ -16.8 to -20.0 ppm region is very different, which for different species is expected.....	62
Figure 44. Superimposed HF-nhPHIP spectra of canine (yellow) and human urine (green). Urine samples were prepared according to the targeted method with SPE described under Method A, Chapter 4.	63
Figure 45. Superimposed HF-nhPHIP spectra of canine (yellow) and human urine (green). Urine samples were prepared according to the untargeted approach described under Method B, Chapter 4.....	63
Figure 46. Superimposed HF-nhPHIP spectra of canine (yellow) and human urine (green) prepared according to Method C, Chapter 4, zoomed to amino acids region. Signals corresponding to amino acids have not been assigned explicitly, but both urines feature signals that coincide, meaning these amino acids are present in both samples. In human urine, there are some additional signals forming a diagonal with a steeper slope. These signals could arise from α -amino acids beyond the 22 proteinogenic ones.....	64
Figure 47. HF-nhPHIP spectrum of dog urine, prepared according to Method C, Chapter 4. Two very strong signal pairs can be seen, δ -17 and δ -24.5 ppm (pink pentagons), possibly due to S-atom association to the iridium catalyst. ^{28,31} These signals were not present in human urine. Whether these signals are species specific, breed specific, or individual specific (inherent or dietary-caused) requires further research.	65
Figure 48. Superimposed HF-nhPHIP spectra of canine (yellow) and human urine (green) prepared according to Method D (Chapter 4) to detect oligopeptides. Although signals in oligopeptide region are much less intensive than signals of amino acids, a couple of H _x signals can be seen at δ -30 ppm region. At least four signals seem to arise from oligopeptides present in both urines.....	66

References

- (1) Levitt, M. H. *Spin Dynamics. Basics of Nuclear Magnetic Resonance*; John Wiley & Sons Ltd, 2015.
- (2) Keeler, J. *Understanding NMR Spectroscopy*; John Wiley & Sons Ltd, 2010.
- (3) Eills, J.; Budker, D.; Cavagnero, S.; Chekmenev, E. Y.; Elliott, S. J.; Jannin, S.; Lesage, A.; Matysik, J.; Meersmann, T.; Prisner, T.; Reimer, J. A.; Yang, H.; Koptug, I. V. Spin Hyperpolarization in Modern Magnetic Resonance. *Chem. Rev.* **2023**, 123 (4), 1417–1551.
- (4) Slichter, C. P. The Discovery and Renaissance of Dynamic Nuclear Polarization. *Reports Prog. Phys.* **2014**, 77. <https://doi.org/10.1088/0034-4885/77/7/072501>.
- (5) Ardenkjær-Larsen, J. H.; Fridlund, B.; Gram, A.; Hansson, G.; Hansson, L.; Lerche, M. H.; Servin, R.; Thaning, M.; Golman, K. Increase in Signal-to-Noise Ratio of >10,000 Times in Liquid-State NMR. *Proc. Natl. Acad. Sci. U. S. A.* **2003**, 100 (18), 10158–10163. <https://doi.org/10.1073/pnas.1733835100>.
- (6) Jähnig, F.; Kwiatkowski, G.; Ernst, M. Conceptual and Instrumental Progress in Dissolution DNP. *J. Magn. Reson.* **2016**, 264, 22–29. <https://doi.org/10.1016/j.jmr.2015.12.024>.
- (7) Kress, T.; Che, K.; Epasto, L. M.; Kozak, F.; Negroni, M.; Olsen, G. L.; Selimovic, A.; Kurzbach, D. A Novel Sample Handling System for Dissolution Dynamic Nuclear Polarization Experiments. *Magn. Reson.* **2021**, 2 (1), 387–394. <https://doi.org/10.5194/MR-2-387-2021>.
- (8) Dey, A.; Charrier, B.; Ribay, V.; Dumez, J.-N.; Giraudeau, P. Hyperpolarized ¹H and ¹³C NMR Spectroscopy in a Single Experiment for Metabolomics. *Anal. Chem.* **2023**, 95, 16861–16867. <https://doi.org/10.1021/acs.analchem.3c02614>.
- (9) Jannin, S.; Dumez, J.-N. N.; Giraudeau, P.; Kurzbach, D. Application and Methodology of Dissolution Dynamic Nuclear Polarization in Physical, Chemical and Biological Contexts. *J. Magn. Reson.* **2019**, 305, 41–50. <https://doi.org/10.1016/j.jmr.2019.06.001>.
- (10) Ardenkjaer-Larsen, J. H. Introduction to Dissolution DNP: Overview, Instrumentation, and Human Applications. *eMagRes*. Blackwell Publishing Ltd 2018, pp 63–78. <https://doi.org/10.1002/9780470034590.emrstm1549>.
- (11) Elliott, S. J.; Stern, Q.; Ceillier, M.; Daraï, T. El; Cousin, S. F.; Cala, O.; Jannin, S. Practical Dissolution Dynamic Nuclear Polarization. <https://doi.org/10.1016/j.pnmrs.2021.04.002>.
- (12) Bowers, C. R.; Weitekamp, D. P. Transformation of Symmetrization Order to Nuclear-Spin Magnetization by Chemical Reaction and Nuclear Magnetic Resonance. *Phys. Rev. Lett.* **1986**, 57 (21), 2645–2648.
- (13) Bowers, C. R.; Weitekamp, D. P. Parahydrogen and Synthesis Allow Dramatically Enhanced Nuclear Alignment. *J. Am. Chem. Soc.* **1987**, 109 (18), 5541–5542.
- (14) Eisenschmid, T. C.; Kirss, R. U.; Deutsch, P. P.; Hommeltoft, S. I.; Eisenberg, R.; Bargon, J.; Lawler, R. G.; Balch, A. L. Para Hydrogen Induced Polarization in Hydrogenation Reactions. *J. Am. Chem. Soc.* **1987**, 109 (26), 8089–8091. <https://doi.org/10.1021/ja00260a026>.
- (15) Jeong, K.; Min, S.; Chae, H.; Namgoong, S. K. Detecting Low Concentrations of Unsaturated C-C Bonds by Parahydrogen-Induced Polarization Using an Efficient Home-Built Parahydrogen Generator. *Magn. Reson. Chem.* **2018**, 56 (11), 1089–1093. <https://doi.org/10.1002/mrc.4756>.

- (16) Nikolaou, P.; Goodson, B. M.; Chekmenev, E. Y. NMR Hyperpolarization Techniques for Biomedicine. *Chem. - A Eur. J.* **2015**, *21* (8), 3156–3166. <https://doi.org/10.1002/chem.201405253>.
- (17) Pravica, M. G.; Weitekamp, D. P. Net NMR Alignment by Adiabatic Transport of Parahydrogen Addition Products to High Magnetic Field. *Chem. Phys. Lett.* **1988**, *145* (4), 255–258. [https://doi.org/10.1016/0009-2614\(88\)80002-2](https://doi.org/10.1016/0009-2614(88)80002-2).
- (18) Adams, R. W.; Aguilar, J. A.; Atkinson, K. D.; Cowley, M. J.; Elliott, P. I. P.; Duckett, S. B.; Green, G. G. R.; Khazal, I. G.; López-Serrano, J.; Williamson, D. C. Reversible Interactions with Para-Hydrogen Enhance NMR Sensitivity by Polarization Transfer. *Science (80-.)* **2009**, *323* (5922), 1708–1711.
- (19) Barskiy, D. A.; Knecht, S.; Yurkovskaya, A. V.; Ivanov, K. L. SABRE: Chemical Kinetics and Spin Dynamics of the Formation of Hyperpolarization. *Prog. Nucl. Magn. Reson. Spectrosc.* **2019**, *114–115*, 33–70. <https://doi.org/10.1016/j.pnmrs.2019.05.005>.
- (20) Vaneeckhaute, E.; Tyburn, J.-M.; Kempf, J. G.; Martens, J. A.; Breynaert, E.; Vaneeckhaute, E.; Martens, J. A.; Breynaert, E. Reversible Parahydrogen Induced Hyperpolarization of ¹⁵N in Unmodified Amino Acids Unraveled at High Magnetic Field. **2023**. <https://doi.org/10.1002/adv.202207112>.
- (21) Cowley, M. J.; Adams, R. W.; Atkinson, K. D.; Cockett, M. C. R.; Duckett, S. B.; Green, G. G. R.; Lohman, J. A. B.; Kerssebaum, R.; Kilgour, D.; Mewis, R. E. Iridium N-Heterocyclic Carbene Complexes as Efficient Catalysts for Magnetization Transfer from Para-Hydrogen. *J. Am. Chem. Soc.* **2011**, *133* (16), 6134–6137. <https://doi.org/10.1021/ja200299u>.
- (22) Eshuis, N.; Hermkens, N.; van Weerdenburg, B. J. A.; Feiters, M. C.; Rutjes, F. P. J. T.; Wijmenga, S. S.; Tessari, M. Toward Nanomolar Detection by NMR through SABRE Hyperpolarization. *J. Am. Chem. Soc.* **2014**, *136* (7), 2695–2698.
- (23) Fraser, R.; Rutjes, F. P. J. T.; Feiters, M. C.; Tessari, M. Analysis of Complex Mixtures by Chemosensing NMR Using Para-Hydrogen-Induced Hyperpolarization. *Acc. Chem. Res.* **2022**, *55* (13), 1832–1844. <https://doi.org/10.1021/acs.accounts.1c00796>.
- (24) Eshuis, N.; Aspers, R. L. E. G.; van Weerdenburg, B. J. A.; Feiters, M. C.; Rutjes, F. P. J. T.; Wijmenga, S. S.; Tessari, M. 2D NMR Trace Analysis by Continuous Hyperpolarization at High Magnetic Field. *Angew. Chemie Int. Ed.* **2015**, *54* (48), 14527–14530.
- (25) Sellies, L.; Reile, I.; Aspers, R. L. E. G.; Feiters, M. C.; Rutjes, F. P. J. T.; Tessari, M. Parahydrogen Induced Hyperpolarization Provides a Tool for NMR Metabolomics at Nanomolar Concentrations. *Chem. Commun.* **2019**, *55* (50), 7235–7238. <https://doi.org/10.1039/C9CC02186H>.
- (26) Hermkens, N. K. J. J.; Eshuis, N.; van Weerdenburg, B. J. A. A.; Feiters, M. C.; Rutjes, F. P. J. T. J. T.; Wijmenga, S. S.; Tessari, M. NMR-Based Chemosensing via p-H₂ Hyperpolarization: Application to Natural Extracts. *Anal. Chem.* **2016**, *88* (6), 3406–3412. https://doi.org/10.1021/ACS.ANALCHEM.6B00184/SUPPL_FILE/AC6B00184_SI_001.PDF.
- (27) Hermkens, N. K. J.; Aspers, R. L. E. G.; Feiters, M. C.; Rutjes, F. P. J. T.; Tessari, M. Trace Analysis in Water-Alcohol Mixtures by Continuous p-H₂ Hyperpolarization at High Magnetic Field. *Magn. Reson. Chem.* **2018**, *56* (7), 633–640. <https://doi.org/10.1002/MRC.4692>.

- (28) Iali, W.; Roy, S. S.; Tickner, B. J.; Ahwal, F.; Kennerley, A. J.; Duckett, S. B. Hyperpolarising Pyruvate through Signal Amplification by Reversible Exchange (SABRE). *Angew. Chemie Int. Ed.* **2019**, *58* (30), 10271–10275. <https://doi.org/10.1002/ANIE.201905483>.
- (29) Sellies, L.; Aspers, R. L. E. G.; Feiters, M. C.; Rutjes, F. P. J. T.; Tessari, M. Para-Hydrogen Hyperpolarization Allows Direct NMR Detection of α -Amino Acids in Complex (Bio)Mixtures. *Angew. Chemie Int. Ed.* **2021**, *60* (52), 26954–26959. <https://doi.org/10.1002/ANIE.202109588>.
- (30) Sleigh, C. J.; Duckett, S. B.; Messerle, B. A. NMR Studies on Ligand Exchange at $[\text{IrH}_2\text{Cl}(\text{CO})(\text{PPh}_3)_2]$ and $[\text{IrH}_2\text{Cl}(\text{PPh}_3)_3]$ by Para-Hydrogen Induced Polarisation. *Chem. Commun.* **1996**, No. 21, 2395–2396. <https://doi.org/10.1039/CC9960002395>.
- (31) Tickner, B. J.; Lewis, J. S.; John, R. O.; Whitwood, A. C.; Duckett, S. B. Mechanistic Insight into Novel Sulfoxide Containing SABRE Polarisation Transfer Catalysts. *Dalt. Trans.* **2019**, *48* (40), 15198–15206. <https://doi.org/10.1039/C9DT02951F>.
- (32) Eshuis, N.; van Weerdenburg, B. J. A.; Feiters, M. C.; Rutjes, F. P. J. T.; Wijmenga, S. S.; Tessari, M. Quantitative Trace Analysis of Complex Mixtures Using SABRE Hyperpolarization. *Angew. Chemie Int. Ed.* **2015**, *54* (5), 1481–1484. <https://doi.org/10.1002/anie.201409795>.
- (33) Ausmees, K.; Reimets, N.; Reile, I. Understanding Parahydrogen Hyperpolarized Urine Spectra: The Case of Adenosine Derivatives. *Molecules* **2022**, *27* (3), 802. <https://doi.org/10.3390/MOLECULES27030802>.
- (34) Sellies, L.; E G Aspers, R. L.; Tessari, M. Determination of Hydrogen Exchange and Relaxation Parameters in PHIP Complexes at Micromolar Concentrations. *Magn. Reson.* **2021**, *2* (1), 331–340. <https://doi.org/10.5194/mr-2-331-2021>.
- (35) Ausmees, K.; Reimets, N.; Reile, I. Parahydrogen Hyperpolarization of Minimally Altered Urine Samples for Sensitivity Enhanced NMR Metabolomics. *Chem. Commun.* **2022**, *58* (3), 463–466. <https://doi.org/10.1039/D1CC05665D>.
- (36) Dreisewerd, L.; Aspers, R. L. E. G.; Feiters, M. C.; Rutjes, F. P. J. T.; Tessari, M. NMR Discrimination of D- and L- α -Amino Acids at Submicromolar Concentration via Parahydrogen-Induced Hyperpolarization. *J. Am. Chem. Soc.* **2023**. <https://doi.org/10.1021/JACS.2C11285>.
- (37) Zektzer, A. S.; Martin, G. E. Proton Zero Quantum Two-Dimensional NMR Spectroscopy: An Alternative to Proton Double Quantum Inadequate for Mapping Complex Proton Spin Systems of Natural Products. *J. Nat. Prod.* **1987**, *50* (3), 455–462. <https://doi.org/10.1021/NP50051A018>.
- (38) Stevanato, G.; Ding, Y.; Mamone, S.; Jagtap, A. P.; Korchak, S.; Glöggler, S. Real-Time Pyruvate Chemical Conversion Monitoring Enabled by PHIP. *J. Am. Chem. Soc.* **2023**, *145*, 5864–5871. <https://doi.org/10.1021/jacs.2c13198>.
- (39) Reile, I.; Eshuis, N.; Hermkens, N. K. J.; van Weerdenburg, B. J. A.; Feiters, M. C.; Rutjes, F. P. J. T.; Tessari, M.; Weerdenburg, B.; Feiters, M. C.; Rutjes, F. P. J. T.; Tessari, M. NMR Detection in Biofluid Extracts at Sub-UM Concentrations via Para-H₂ Induced Hyperpolarization. *Analyst* **2016**, *141* (13), 4001–4005. <https://doi.org/10.1039/C6AN00804F>.

- (40) Dumez, J.-N.; Milani, J.; Vuichoud, B.; Bornet, A.; Lalande-Martin, J.; Tea, I.; Yon, M.; Maucourt, M.; Deborde, C.; Moing, A.; Frydman, L.; Bodenhausen, G.; Jannin, S.; Giraudeau, P. Hyperpolarized NMR of Plant and Cancer Cell Extracts at Natural Abundance. *Analyst* **2015**, *140* (17), 5860–5863. <https://doi.org/10.1039/C5AN01203A>.
- (41) Frahm, A. B.; Hill, D.; Katsikis, S.; Andreassen, T.; Ardenkjær-Larsen, J. H.; Bathen, T. F.; Moestue, S. A.; Jensen, P. R.; Lerche, M. H. Classification and Biomarker Identification of Prostate Tissue from TRAMP Mice with Hyperpolarized ¹³C-SIRA. *Talanta* **2021**, *235*, 122812. <https://doi.org/10.1016/J.TALANTA.2021.122812>.
- (42) Frahm, A. B.; Jensen, P. R.; Ardenkjær-Larsen, J. H.; Yigit, D.; Lerche, M. H. Stable Isotope Resolved Metabolomics Classification of Prostate Cancer Cells Using Hyperpolarized NMR Data. *J. Magn. Reson.* **2020**, *316*, 106750. <https://doi.org/10.1016/J.JMR.2020.106750>.
- (43) Dey, A.; Charrier, B.; Martineau, E.; Deborde, C.; Gandriau, E.; Moing, A.; Jacob, D.; Eshchenko, D.; Schnell, M.; Melzi, R.; Kurzbach, D.; Ceillier, M.; Chappuis, Q.; Cousin, S. F.; Kempf, J. G.; Jannin, S.; Dumez, J.-N.; Giraudeau, P. Hyperpolarized NMR Metabolomics at Natural ¹³C Abundance. *Anal. Chem.* **2020**, *92* (22), 14867–14871. <https://doi.org/10.1021/acs.analchem.0c03510>.
- (44) Ribay, V.; Dey, A.; Charrier, B.; Praud, C.; Mandral, J.; Dumez, J. N.; Letertre, M. P. M.; Giraudeau, P. Hyperpolarized ¹³C NMR Spectroscopy of Urine Samples at Natural Abundance by Quantitative Dissolution Dynamic Nuclear Polarization. *Angew. Chemie - Int. Ed.* **2023**, *62* (27). <https://doi.org/10.1002/ANIE.202302110>.
- (45) Lê, T. P.; Buscemi, L.; Lepore, M.; Mishkovsky, M.; Hyacinthe, J.-N.; Hirt, L. Influence of DNP Polarizing Agents on Biochemical Processes: TEMPOL in Transient Ischemic Stroke. *ACS Chem. Neurosci* **2023**, *3013*, 3013–3018. <https://doi.org/10.1021/acschemneuro.3c00137>.
- (46) Hune, T.; Mamone, S.; Schroeder, H.; Jagtap, A. P.; Sternkopf, S.; Stevanato, G.; Korchak, S.; Fokken, C.; Müller, C. A.; Schmidt, A. B.; Becker, D.; Glöggler, S. Metabolic Tumor Imaging with Rapidly Signal-Enhanced 1-¹³C-Pyruvate-D3. *ChemPhysChem* **2023**, *24* (2), e202200615. <https://doi.org/10.1002/CPHC.202200615>.
- (47) Bouatra, S.; Aziat, F.; Mandal, R.; Guo, A. C.; Wilson, M. R.; Knox, C.; Bjorndahl, T. C.; Krishnamurthy, R.; Saleem, F.; Liu, P.; Dame, Z. T.; Poelzer, J.; Huynh, J.; Yallou, F. S.; Psychogios, N.; Dong, E.; Bogumil, R.; Roehring, C.; Wishart, D. S. The Human Urine Metabolome. *PLoS One* **2013**, *8* (9), 1–28. <https://doi.org/10.1371/journal.pone.0073076>.
- (48) Reimets, N.; Ausmees, K.; Vija, S.; Reile, I. Developing Analytical Applications for Parahydrogen Hyperpolarization: Urinary Elimination Pharmacokinetics of Nicotine. *Anal. Chem.* **2021**, *93* (27), 9480–9485. <https://doi.org/10.1021/acs.analchem.1c01281>.
- (49) Gallo, J. M. Pharmacokinetic/ Pharmacodynamic-Driven Drug Development. *Mt. Sinai J. Med. A J. Transl. Pers. Med.* **2010**, *77* (4), 381–388. <https://doi.org/10.1002/msj.20193>.
- (50) Ratain, M. J.; Plunkett, W. K. Principles of Pharmacokinetics. In *Holland-Frei Cancer Medicine. 6th edition.*; Kufe, D. W., Pollock, R. E., Weichselbaum, R. R., Bast, R. C., Gansler, T. S., Holland, J. F., Frei, E., Eds.; BC Decker, 2003.

- (51) Hukkanen, J.; Jacob, P.; Benowitz, N. L. Metabolism and Disposition Kinetics of Nicotine. *Pharmacol. Rev.* **2005**, *57* (1), 79–115. <https://doi.org/10.1124/pr.57.1.3>.
- (52) Moran, V. E. Cotinine: Beyond That Expected, More than a Biomarker of Tobacco Consumption. *Front. Pharmacol.* **2012**, *3* OCT, 1–9. <https://doi.org/10.3389/fphar.2012.00173>.
- (53) Walker, V.; Mills, G. A. Solid-Phase Extraction in Clinical Biochemistry. *Ann. Clin. Biochem.* **2002**, *39* (5), 464–477. <https://doi.org/10.1258/000456302320314476>.
- (54) Reimets, N.; Ausmees, K.; Vija, S.; Trummal, A.; Uudsemaa, M.; Reile, I. Parahydrogen Hyperpolarized NMR Detection of Underivatized Short Oligopeptides. *Analyst* **2023**, *148* (21), 5407–5415. <https://doi.org/10.1039/D3AN01345F>.
- (55) Kraeling, M. E. K.; Zhou, W.; Wang, P.; Ogunsola, O. A. In Vitro Skin Penetration of Acetyl Hexapeptide-8 from a Cosmetic Formulation. <http://dx.doi.org/10.3109/15569527.2014.894521> **2015**, *34* (1), 46–52. <https://doi.org/10.3109/15569527.2014.894521>.
- (56) Fields, K.; Falla, T. J.; Rodan, K.; Bush, L. Bioactive Peptides: Signaling the Future. *J. Cosmet. Dermatol.* **2009**, *8* (1), 8–13. <https://doi.org/10.1111/J.1473-2165.2009.00416.X>.
- (57) Iwanov, I.; Rossi, A.; Montesi, M.; Doytchinova, I.; Sargsyan, A.; Momekov, G.; Panseri, S.; Naydenova, E. Peptide-Based Targeted Cancer Therapeutics: Design, Synthesis and Biological Evaluation. *Eur. J. Pharm. Sci.* **2022**, *176*, 106249. <https://doi.org/10.1016/J.EJPS.2022.106249>.
- (58) Ji, Y.; Qiao, H.; He, J.; Li, W.; Chen, R.; Wang, J.; Wu, L.; Hu, R.; Duan, J.; Chen, Z. Functional Oligopeptide as a Novel Strategy for Drug Delivery. *J. Drug Target.* **2017**, *25* (7), 597–607. <https://doi.org/10.1080/1061186X.2017.1309044>.
- (59) Sholl, D. S.; Steckel, J. A. Density Functional Theory: A Practical Introduction. *Density Funct. Theory A Pract. Introd.* **2009**, 1–238. <https://doi.org/10.1002/9780470447710>.
- (60) Kumar, A.; Rani Grace, R. C. Nuclear Overhauser Effect. *Encycl. Spectrosc. Spectrom.* **2016**, 423–431. <https://doi.org/10.1016/B978-0-12-803224-4.00236-3>.
- (61) Pais, H. Enhancing the Sensitivity of Nuclear Magnetic Resonance Spectroscopy with Parahydrogen Hyperpolarisation and to Apply It in Cancer Diagnostics, Tallinn University of Technology School of Science, 2023.
- (62) Paoloni, M.; Khanna, C. Translation of New Cancer Treatments from Pet Dogs to Humans. *Nat. Rev. Cancer* **2008**, *82* **2008**, *8* (2), 147–156. <https://doi.org/10.1038/nrc2273>.
- (63) Zhang, J.; Wei, S.; Liu, L.; Nagana Gowda, G. A.; Bonney, P.; Stewart, J.; Knapp, D. W.; Raftery, D. NMR-Based Metabolomics Study of Canine Bladder Cancer. *Biochim. Biophys. Acta - Mol. Basis Dis.* **2012**, *1822* (11), 1807–1814. <https://doi.org/10.1016/J.BBADIS.2012.08.001>.
- (64) Lee, W.; Ko, B. J.; Sim, Y. E.; Suh, S.; Yoon, D.; Kim, S. Discrimination of Human Urine from Animal Urine Using ¹H-NMR. *J. Anal. Toxicol.* **2019**, *43* (1), 51–60. <https://doi.org/10.1093/JAT/BKY061>.
- (65) Viant, M. R.; Ludwig, C.; Rhodes, S.; Günther, U. L.; Allaway, D. Validation of a Urine Metabolome Fingerprint in Dog for Phenotypic Classification. *Metabolomics* **2007**, *3* (4), 453–463.

- (66) Osada, K.; Miyazono, S.; Kashiwayanagi, M. The Scent of Wolves: Pyrazine Analogs Induce Avoidance and Vigilance Behaviors in Prey. *Front. Neurosci.* **2015**, 9 (OCT), 1–11. <https://doi.org/10.3389/fnins.2015.00363>.
- (67) Osada, K.; Miyazono, S.; Kashiwayanagi, M. Pyrazine Analogs Are Active Components of Wolf Urine That Induce Avoidance and Fear-Related Behaviors in Deer. *Front. Behav. Neurosci.* **2014**, 8 (AUG), 1–7. <https://doi.org/10.3389/fnbeh.2014.00276>.

Acknowledgements

I extend my deepest gratitude to my supervisors, Dr Indrek Reile and Dr Kerti Ausmees, whose guidance, expertise, and unwavering support have been pivotal to my growth and the success of our projects. Their insightful feedback and constructive criticism have not only shaped this work but have also profoundly influenced my professional development and perspective.

I wish to express my sincere appreciation to my co-workers, Dr Kärt Reitel, Dr Merle Uudsemaa, Ms Sirje Vija, Dr Aleksander Trummal, and the entire NICPB, for their collaborative spirit and relentless dedication.

This work was funded by the Estonian Research Council grants PRG661 and PSG11, the Archimedes Foundation Center of Excellence project TK134, and by the Development Fund of the National Institute of Chemical Physics and Biophysics.

The written text's quality was improved through the aid of an AI tool ProWritingAid.

Abstract

Development of Applications for High-Field Non-Hydrogenative PHIP for the Analysis of Biological Fluids

The enhancement of Nuclear Magnetic Resonance (NMR) spectroscopy through hyperpolarization techniques, notably high-field non-hydrogenative Parahydrogen Induced Polarization (HF-nhPHIP), has opened up promising avenues for the detailed analysis of complex biological systems. This thesis explores the applications of HF-nhPHIP, with the goal of making advancements in the areas of metabolomics, pharmacokinetics, and non-invasive diagnostics. The work is driven by the necessity to surpass traditional NMR spectroscopy's limitations, such as low sensitivity and the challenge of detecting and quantifying low-abundance metabolites without altering the samples' chemical identity. HF-nhPHIP emerges as a solution to these challenges, enhancing both the sensitivity and selectivity of NMR analyses.

This research introduces novel contributions to NMR spectroscopy by improving NMR sensitivity for real applications. The thesis covers optimization of experimental conditions for HF-nhPHIP, elucidation of the binding mechanisms of oligopeptides to the iridium catalyst, and provides sample protocols for targeted and untargeted analyses of biological samples. It explores the impact of co-substrate on HF-nhPHIP chemoselectivity and optimizes experimental conditions for a wide range of applications, extending detection limits.

The findings reveal HF-nhPHIP potential in enhancing the detection and quantification of analytes within complex biological fluids, such as human and canine urine. By including DFT calculations a more in-depth understanding was achieved for oligopeptides detection with HF-nhPHIP. The development and application of HF-nhPHIP in the analysis of biological fluids marks a significant leap in NMR spectroscopy. This thesis establishes a groundwork for future exploration, highlighting parahydrogen hyperpolarization's vast potential in scientific and medical research.

Lühikokkuvõte

Kõrges magnetväljas paravesinikul põhineva mittehüdrogeenuva hüperpolarisatsiooni meetodi rakenduste arendamine bioloogiliste segude analüüsimiseks

Kõrges magnetväljas paravesinikul põhinev mittehüdrogeenuv hüperpolarisatsiooni meetod (HF-nhPHIP) on avanud paljulubavaid võimalusi keerukate bioloogiliste süsteemide detailseks analüüsimiseks tuumamagnetresonantsspektroskoopiaga (TMR). See doktoritöö uurib HF-nhPHIP uuenduslikke kasutusviise eesmärgiga teha edusamme metaboolmika, farmakokineetika ja mitteinvasiivsete diagnostikameetodite valdkondades. See töö on ajendatud vajadusest ületada traditsioonilise TMR spektroskoopia piiranguid nagu madal tundlikkus ja madalas kontsentratsioonis metaboliitide tuvastamise ning kvantifitseerimine. HF-nhPHIP ületab need piirangud, tõstes nii TMR analüüside tundlikkust kui ka selektiivsust, hõlbustades bioloogiliste protsesside mõistmist ja abistades farmatseutilistes uuringutes.

See uurimus tutvustab uudset lähenemist TMR spektroskoopias, optimeerides HF-nhPHIP eksperimentaalseid tingimusi, valgustades molekulide seostumismehhanisme iriidiumi katalüsaatoriga ning demonstreerides tehnika rakendatavust nii sihitatud kui ka sihitamata bioloogiliste proovide analüüsimiseks. Töö uudsus peitub selle võimes tõsta TMR spektroskoopia tundlikkust ja selektiivsust, laiendada tuvastatavate ainete hulka oligopeptiididele ning pakkuda uusi teadmisi HF-nhPHIP kontekstis toimuvate interaktsioonimehhanismide kohta.

HF-nhPHIP potentsiaal ainete tuvastamisel ja kvantifitseerimisel keerukates bioloogilistes segudes on näitlikustatud inimese uriini analüüsimisel. Laiendamaks meetodi kasutatavust, võrreldi inimese ja koera uriinispektreid. Lisaks sellele keskendus töö oligopeptiidide seondumismehhanismide uurimisele iriidiumi katalüsaatoriga, aidates kaasa hüperpolarisatsiooni protsessi sügavamale mõistmisele. Doktoritöö raames hinnatati kaas-substraadi mõju HF-nhPHIP kemoselektiivsusele ning optimeeriti eksperimentaalseid tingimusi laia rakenduste valiku jaoks.

Kokkuvõttes märgib HF-nhPHIP arendamine ja rakendamine bioloogiliste segude analüüsis olulist hüpet TMR spektroskoopias. See doktoritöö loob aluse tulevaseks uurimistööks, rõhutades selle suurt potentsiaali teadus- ja meditsiiniuuringutes.

Appendix 1

Publication I

Reimets, N.; Ausmees, K.; Vija, S.; Reile, I. Developing Analytical Applications for Parahydrogen Hyperpolarization: Urinary Elimination Pharmacokinetics of Nicotine. *Anal. Chem.* 2021, 93 (27), 9480–9485. <https://doi.org/10.1021/acs.analchem.1c01281>

Developing Analytical Applications for Parahydrogen Hyperpolarization: Urinary Elimination Pharmacokinetics of Nicotine

Nele Reimets, Kerti Ausmees, Sirje Vija, and Indrek Reile*

Cite This: *Anal. Chem.* 2021, 93, 9480–9485

Read Online

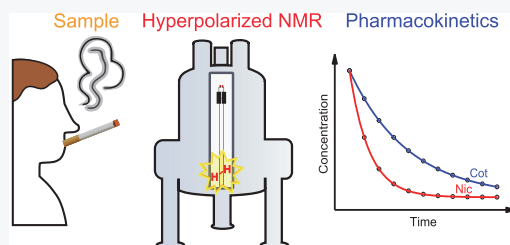
ACCESS |

Metrics & More

Article Recommendations

Supporting Information

ABSTRACT: Nuclear magnetic resonance spectroscopy (NMR) is a valuable analytical tool with applications in a vast array of research fields from chemistry and biology to medicine and beyond. NMR is renowned for its straightforward data interpretation and quantitative properties, making it attractive for pharmacokinetic applications, where drug metabolism pathways, concentrations, and kinetics need to be evaluated. However, pharmacologically active compounds and their metabolites in biofluids often appear in minute concentrations, well below the detection limit of NMR. Herein, we demonstrate how parahydrogen hyperpolarization overcomes this sensitivity barrier, allowing us to detect mid-nanomolar concentrations of a drug and a drug metabolite in a biofluid matrix. The performance of the method is demonstrated by monitoring nicotine and cotinine urinary elimination, reflected by their concentrations in urine during the onset and withdrawal from nicotine consumption. An NMR limit of detection of 0.1 μM and a limit of quantitation of 0.7 μM is achieved in a practical pharmacokinetics scenario where precise quantitative and qualitative analysis is desired.



Pharmacokinetics (PK) is an important step in the modern drug development process,¹ where the fate of a biologically active substance has to be understood to assure drug safety and develop optimal dosing regimens, carriers, drug forms, etc. PK involves the time-dependent study of a drug and its metabolites in biofluids to understand the (bio)chemical transformations that the drug undergoes.² Since such analytes usually occur in minute concentrations in complex biological matrices like blood or urine, exceptional resolution and sensitivity are desired from any technique to be used in PK.

Nuclear magnetic resonance spectroscopy (NMR) is recognized as one of the two most successful analytical techniques in biofluid analysis (the other being mass spectrometry).^{3,4} Yet, metabolites in biofluids often stay below the limit of detection (LOD) of NMR due to its moderate sensitivity. Hence, NMR is suitable for PK only when relatively high concentration analytes are expected.

Steady progress has been made toward improving NMR sensitivity by nuclear hyperpolarization (HP).^{5,6} Out of various HP methods,⁷ dissolution dynamic nuclear polarization (d-DNP)^{8,9} and parahydrogen (pH_2) hyperpolarization^{10,11} have been adapted for biomixture analysis. While pH_2 HP is somewhat limited by its scope of detectable analytes, it imposes lower demands on hardware, requiring relatively small investments on top of common NMR equipment.

The Tessari group has developed pH_2 HP techniques that allow continuous hyperpolarization with a scan repetition rate similar to regular NMR while constantly keeping the sample in a spectrometer.¹² Applications can utilize multiscan experi-

ments for the development of pulse sequences for signal averaging¹⁰ and/or multidimensional spectra.¹¹ Under such conditions, HP can be carried out similarly to traditional NMR.

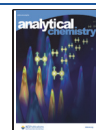
Herein, we demonstrate how on top of metabolic imaging applications,¹⁴ pH_2 HP can be used in PK research. As a proof of concept, pH_2 HP methodology was applied to the urine of humans exposed to nicotine (Nic). Two common intake methods were compared—smoking and absorption through the skin using a transdermal patch.

About 80% of Nic is metabolized into cotinine (Cot), which accumulates in the body¹⁵ and is therefore a more accurate descriptor of the smoking habit. Traces of Cot can be found in urine for more than 2 weeks after the last Nic intake¹⁶ and its concentration is used as a reference value to determine whether a person is a smoker.^{15,17,18} Nic and Cot are excreted unchanged at about only 10% from total Nic absorption,¹⁶ occurring in urine below the LOD of normal NMR. To prove the pH_2 HP methods' sensitivity and quantitative nature, we analyzed urinary elimination pharmacokinetics of Nic and Cot in the urine of seven volunteers.

Received: March 24, 2021

Accepted: June 17, 2021

Published: June 27, 2021



■ EXPERIMENTAL SECTION

Chemicals and Materials. All chemicals and consumables were acquired from common internationally recognized suppliers (details in the SI). All solutions, both stock solutions and NMR samples, were prepared gravimetrically. Iridium catalyst complex **1** precursor [Ir(Cl)(COD)(IMes)] was prepared according to published procedures.^{19,20} Cosubstrate 1-methyl-1,2,3-triazole (mtz) was synthesized as previously described,²¹ except the reaction temperature was lowered to $-21\text{ }^{\circ}\text{C}$ for higher regioselectivity, and final purification was done by vacuum distillation.

Sample Collection. Urine sample handling was approved by Research Ethics Committee of the National Institute for Health Development of Estonia (Decision No. 686). One non-smoker, six cigarette smokers (V1–V6, aged 21–60 years, smoking five or more cigarettes per day), and one transdermal patch user (V7, age 40 years) participated in the study. Smokers submitted initial samples while smoking casually. Three smokers quit smoking for 2 weeks and produced urine samples, starting with the morning after quitting. One volunteer refrained from any nicotine for a substantial time, before applying a nicotine patch (Nicorette Invisipatch TDP, 15 mg/16 h) and produced six samples: before applying the patch, 1.5, 5, 7, 10, and 24 h after application.

Urine Sample Handling. Urine samples were collected as morning first midstream urine, frozen within 2 h, and stored at $-80\text{ }^{\circ}\text{C}$. Samples were allowed to thaw over a room temperature water bath prior to sample preparation, centrifuged at 1825g for 12 min, pH adjusted to 7.4 with 1 M NaOH, and centrifuged again.

Solid-Phase Extraction (SPE). Three SPE cartridges were tested at pH 8.6 and 10.6 for both urine and buffer (Figure S5): isolate ENV+ (6 mL, 200 mg), Phenomenex Strata-X (6 mL, 200 mg), and Waters Oasis HLB (6 mL, 200 mg). It was known that approx. 800 μL of SPE extract contains the majority of analytes.¹⁰ Therefore, two fractions of methanol extracts were initially collected, each about 350–400 μL , and measured by qNMR. Recovery was evaluated by comparing the signal integrals of the analyte and the internal standard (DSS stock solution was gravimetrically spiked into the extract). Strata-X proved to be most effective in extracting Nic and Cot (Figure S5a). Further pH optimization was done with Strata-X, establishing pH 7.4 as optimal.

Initially, methanol- d_4 was used as the SPE eluent. It yielded a very complex extract with only 21% recoveries for Nic and Cot (Figures S5b and S6). More importantly, the analysis of such extracts displayed poor repeatability due to uncontrollable variations in matrix effects. Out of various tested solutions and mixtures, CDCl_3 was found to be a more suitable solvent, giving a simpler extract and 95% recoveries for Nic and Cot. CDCl_3 extracts also decreased sample-to-sample variations on matrix effects to a degree where they became negligible. In the optimal SPE protocol, Phenomenex Strata-X cartridges were activated with methanol, conditioned with a 10 mM KH_2PO_4 buffer solution at pH 7.4, loaded with 5 mL of pH 7.4 urine, eluted by gravity, washed with 3 mL of buffer, and dried with a constant N_2 flow (~ 1 bar overpressure) for 30 min. Analytes were eluted with 1.5 mL of CDCl_3 to produce approx. 1 mL of the extract, which was stored at $-20\text{ }^{\circ}\text{C}$ until analysis.

NMR Sample and Experiment. Active pH_2 HP catalyst **1** ($[\text{Ir}(\text{H}_2)(\text{IMes})(\text{mtz})_3]$, Figure 1b) was prepared in situ in an NMR tube. One hundred and fifty microliters of a mixture of

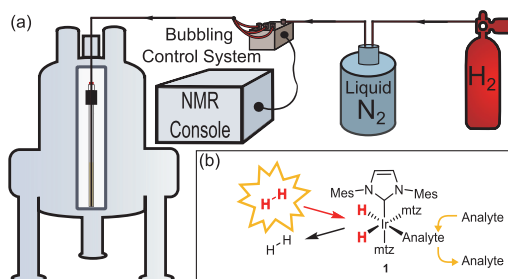


Figure 1. (a) Experimental setup—50% enriched pH_2 was produced in flow and bubbled through the sample under spectrometer control via a bubbling control system (Figure S4). The sample was loaded into an NMR tube (Figure S1), pressurized, and inserted into the spectrometer. (b) Active iridium catalyst complex **1** responsible for HP chemo-sensing.¹³

the $[\text{Ir}(\text{Cl})(\text{COD})(\text{IMes})]$ catalyst precursor and the 1-methyl-1,2,3-triazole (mtz) cosubstrate²² in methanol- d_4 was weighted into a 5 mm Norell IPV tube, pressurized under 5 bar of H_2 , shaken, and allowed to react for 2 h before adding 450 μL of the urine SPE extract in CDCl_3 . The final concentrations were 1.2 mM for **1** and 21.6 mM for mtz. The tube was connected to the HP setup, repressurized under 5 bar of H_2 , and inserted into an NMR spectrometer (Figure 1a). HP was facilitated by bubbling pH_2 through the sample under pulse program control.¹¹ Further detail on pH_2 preparation and bubbling control hardware is provided in the SI.

2D pH_2 HP spectra were recorded at $25\text{ }^{\circ}\text{C}$ on an 800 MHz Bruker Avance III spectrometer equipped with a He-cooled cryoprobe. Spectral widths were 16 000 and 2000 Hz in f_2 and f_1 dimensions, respectively. Data sets consisted of 16 384 (complex) \times 256 (real) points. pH_2 was bubbled through the sample for 2 s between scans. A 90° shifted square sine window function was applied in both dimensions and f_1 dimension was zero-filled to 2048 points before Fourier transformation. The dominant signal at -21.87 ppm in Figure 2 1D trace represents complex **1** with three mtz ligands. This signal was omitted from 2D spectra by time-domain convolution filtering²³ to avoid obscuring signals from low-concentration species (Figure S9).

Data Analysis. All calculations are based on integrals of signals in 2D ZQ spectra. Signal integration was done by predefined integration regions. A single calibration method was devised to cover the SPE recovery and HP efficiency. Calibration curves were chosen to contain 10 points and their standard deviation is based on three parallel SPE extract measurements of each point. Calibration measurements were tested for outliers with the Grubbs test and Dixon's Q -test (OriginPro 2017 software), none were identified. Linear fitting was used on the calibration points (OriginPro 2017), and the obtained R^2 (coefficient of determination) values were between 0.98 and 0.99. Nic and Cot concentrations in various urine samples were determined from the corresponding linear fits.

■ RESULTS AND DISCUSSION

The HP method¹¹ involves detecting pH_2 -derived hydrides of short-lived iridium complexes **1** (Figure 1b), which act as chemosensors¹³ of urinary metabolites.^{10,11} Spectral resolution is derived from the fact that each analyte, which reversibly

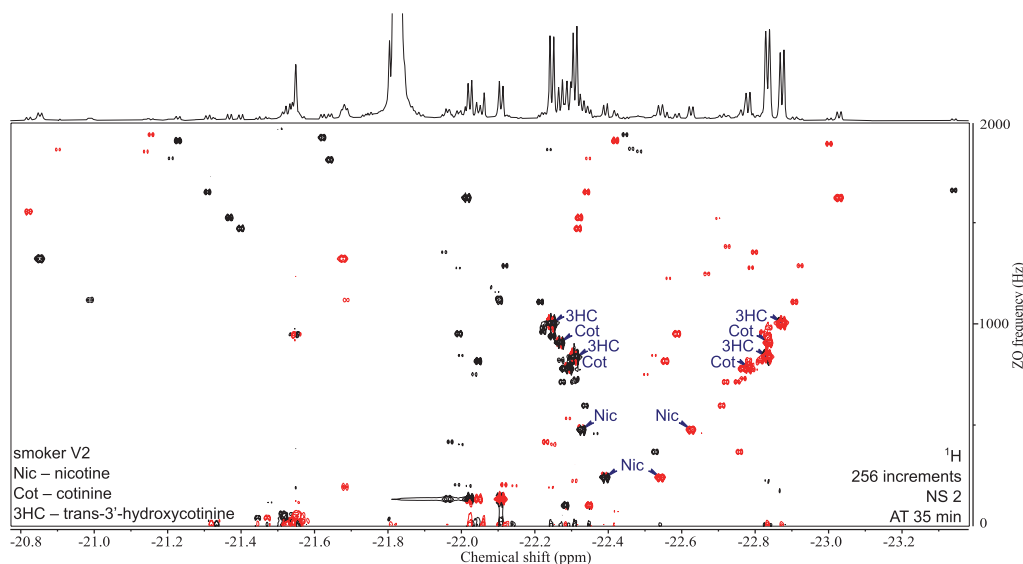


Figure 2. 2D ZQ pH_2 HP spectrum of a urine extract in $CDCl_3$. Each complex of an analyte and **1** gives rise to two opposite phase doublets at the same ZQ frequency.¹¹ Chiral analytes (i.e., Nic, Cot, and 3HC; Figure S10) can combine with **1** in two ways due to the stereogenic center on iridium in the complex, forming two diastereomers with different physical properties. Signals were assigned by internal standard addition during method development. Upper 1D trace recorded separately with the 1D SEPP sequence.³²

binds to **1**, forms a chemically distinct transient complex that resonates at specific frequencies.²⁴ Analyte-specific hydride signals are observed at around -22 ppm (Figure 2, horizontal trace), a normally signal-free region of the 1H spectrum. This removes non-iridium interacting analyte signals from the spectral window of interest, reducing the signal overlap that would occur over the 0–10 ppm region. Unlike most pH_2 HP approaches,^{10,12,13,22,25} polarization transfer from hydrides to analytes is not needed. Instead, the complex 1D spectrum of HP-enhanced hydride resonances is resolved by 2D zero quantum (ZQ) spectroscopy (Figure 2), which has been shown to provide 3 orders of magnitude signal enhancements.¹¹

HP performance depends on catalyst **1** affinity toward analytes and hydrogen solubility in the sample matrix. Water is not a favorable environment for **1**,¹⁰ and hydrogen gas has low solubility in aqueous media. Therefore, the method cannot be applied to urine directly, and solid-phase extraction (SPE) was used to obtain urine extracts in a more suitable solvent. Previous works^{10,11} have used methanol- d_4 as the SPE eluent, which produces a highly complex extract with hundreds of hyperpolarized signals.^{10,11} Resolution of this mixture by the ZQ technique¹¹ is possible (Figure S6), but it would take an impractical amount of time to acquire a sufficiently high-resolution 2D spectrum.

To reduce the number of analytes in the sample, SPE extracts were obtained in $CDCl_3$. Chloroform releases only less polar analytes, reducing the number of compounds capable of binding to **1** and allowing us to record a substantially simpler spectrum (Figure 2). Furthermore, SPE recovery of Nic and Cot was 95% with $CDCl_3$, three times higher than with methanol (Figure S5). If the analysis of the more polar fraction is also desired, a methanol extract could be collected and analyzed afterward (Figure S7).

The reduced spectral congestion in $CDCl_3$ allowed the reduction of the measurement time to 35 min per sample by spectral folding in f_1 dimension, without compromising the resolution or introducing signal overlap. We suggest that in potential routine applications, additional time savings are available by applying nonuniform sampling schemes to the experiment.²⁶

Unlike in normal NMR, signal integrals are related to concentration in an analyte-specific manner: they depend on the binding kinetics of **1** and the analyte²⁵ and the multipulse nature of the NMR experiment. Therefore, calibration is necessary for determining the actual analyte concentration.

Calibration curves were obtained via standard addition of Nic and Cot to a non-smoker's urine at realistic concentrations before SPE-based sample preparation (Figure 3).²⁷ A limit of quantitation (LOQ; SNR 20) was established at $0.2 \mu M$ concentration in urine with a standard deviation of less than 11%, demonstrating acceptable repeatability. Notably, we observed tobacco-related signals at about 30 nM concentration (SNR 3) in a non-smoker, indicating passive Nic exposure. Considering the 3.7-fold concentration of analytes during SPE, the NMR LOD in the sample tube is $0.1 \mu M$ and LOQ is $0.7 \mu M$.

Based on calibration curves, the concentrations of Nic and Cot in various urine samples were assigned and normalized with respect to the urine creatinine level to compensate for differences in fluid consumption.²⁸ Importantly, urinary concentrations of Nic and Cot depend on the smoking habit (nicotine concentration in a cigarette, number of cigarettes smoked during the day, etc.) and individual metabolism (age, rate of urine flow, urine pH level, etc.).^{16,29} Based on the average number of packs of cigarettes smoked per day multiplied by the number of years smoked, pack-year characteristics were estimated for each volunteer and found

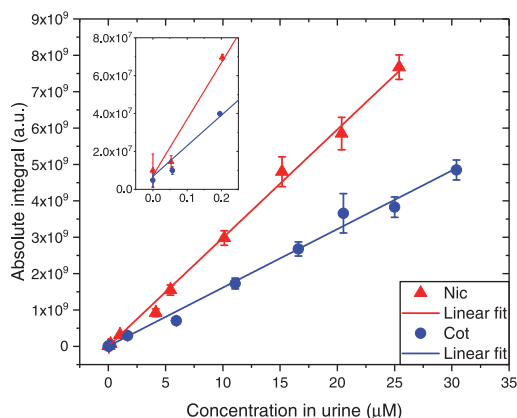


Figure 3. Calibration curves for Nic (red) and Cot (blue) based on the linear fitting of 10 data points (2D spectrum signal integrals). Three parallels were measured and averaged for every point. Error bars represent the standard deviation of the three parallels. Calibration curves are analyte-specific due to different iridium binding affinities.¹²

to correlate to analyte concentrations. The highest Nic and Cot levels ($C_{\text{Nic}U} = 6.4 \mu\text{M}$ and $C_{\text{Cot}U} = 20.3 \mu\text{M}$) were found in urine V4 (30 pack-years, Figure 4). The mean value for Nic and Cot among all smokers (mean $C_{\text{Nic}U} = 2.3 \mu\text{M}$ and mean $C_{\text{Cot}U} = 6.3 \mu\text{M}$) was comparable to what has been reported by other techniques—HPLC^{27,30} and LC/MS/MS.³¹

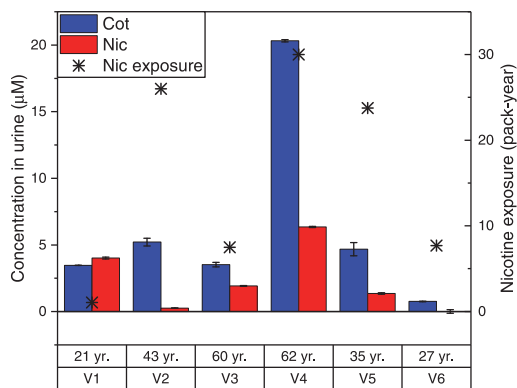


Figure 4. Maximum concentrations of Nic and Cot (normalized by creatinine concentration) in smokers' urine samples, measured before stopping the casual smoking habit. Error bars represent the standard deviation of three parallels.

To follow the elimination of Nic, volunteers were asked not to smoke for 2 weeks with no further restrictions on living habits (e.g., diet, physical activity, and social activity). Changes in Nic concentration after cessation of smoking can be seen in Figure 5a. Traces of Nic stayed in urine for a longer period in the older volunteer V3, as expected.^{16,32} Nic spike on day 9 was caused by smoking in the previous evening. Volunteer V2 was passively exposed to tobacco smoke on days 3 and 4, resulting in a slight increase of Nic on day 5. An experimental

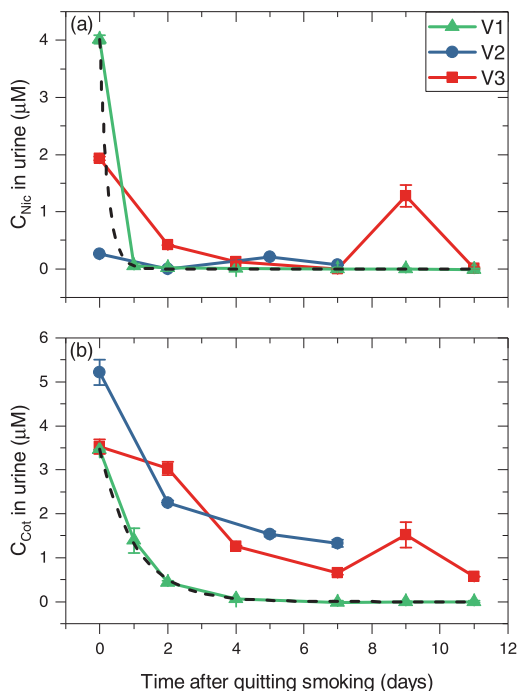


Figure 5. Nic (a) and Cot (b) concentrations (normalized by creatinine concentration) in urine with respect to time from the last cigarette. Error bars represent the standard deviation of three parallels. Exponential fitting in (a) and (b) (dashed line) was applied to V1 data; the R^2 value for both plots was 0.99.

urinary Nic elimination half-life $t_{1/2}$ was determined from exponential fitting³³ to V1 values. Nic reached half of its initial value ($C_{\text{max}U}/2 = 2.0 \mu\text{M}$) in 3.8 h.

The correlation between Cot and time from quitting smoking is plotted in Figure 5b. The concentration in urine reached zero relatively fast in a young person, V1. According to exponential fitting, Cot $t_{1/2} = 17$ h ($C_{\text{max}U}/2 = 1.7 \mu\text{M}$) matched well with other studies.^{32,34,35} In other volunteers, Cot decreased but stayed above $0.5 \mu\text{M}$. The higher Cot value in V2 (min $C_{\text{Cot}U} = 1.3 \mu\text{M}$), compared to an older person V3 (min $C_{\text{Cot}U} = 0.6 \mu\text{M}$), was probably due to passive Nic exposure during the experiment as well as individual metabolism and greater cumulative Nic exposure (26 vs 7.5 pack-years, Figure 4), during which Cot had accumulated in the body.

The effect of the transdermal patch was evaluated to assess a different route of administration (Figure 6). While smoking increases the Nic concentration rapidly, the transdermal patch is designed to release Nic gradually at a constant rate.¹⁶ Urinary Nic concentration started to increase after wearing a patch for 1.5 h and started to decrease after 10 h, as expected.^{16,32} Cot was detectable starting from 5 h. Nic dropped suddenly at 7.5 h, possibly due to heavy water consumption during the preceding 2.5 h, rendering normalization by creatinine unreliable.

In addition, the buildup of new signals was observed in the vicinity of Cot signals (Figures 6 and S8). These signals were

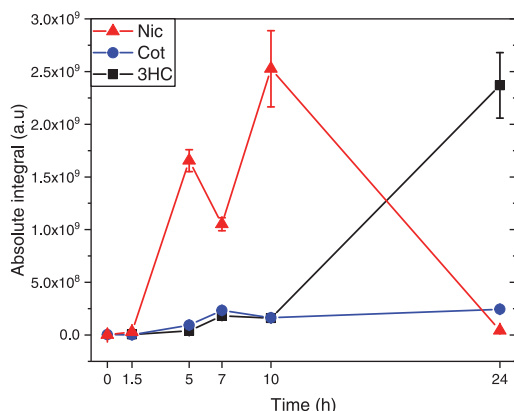


Figure 6. Integral values of Nic, Cot, and 3HC in urine plotted against time from applying a transdermal patch. Error bars represent the standard deviation of three parallels. Note that the figure displays signal integral values and not concentrations.

also present in smokers' urine samples (Figure 2), suggesting that they represent a Nic metabolite. It has been found that hydride signals of **1** corresponding to analytes with a similar molecular structure appear close to one another on the ZQ spectra.¹¹ Combining this with the underlying knowledge on Nic metabolism,¹⁶ new signals were identified by internal standard addition as *trans*-3'-hydroxycotinine (3HC), a major urinary Cot metabolite.^{15,16,32} The identification and observation of the 3HC buildup suggest that the method herein may be useful in cases where new and/or unexpected metabolites of intended analytes may appear.

CONCLUSIONS

Based on the examples of Nic and Cot, we showed that pH₂ HP can be used in PK applications to follow the decrease and increase of different analytes' concentrations in biofluids. We demonstrated that it is possible to quantify minute concentrations with good precision. In particular, molecules produced in the body at very low concentrations were quantified by NMR. pH₂ HP gave an NMR LOD of 0.1 μM and a LOQ of 0.7 μM. Combined with the 3.7-fold sample concentration by SPE, the whole method allows us to analyze urinary metabolites with a LOD of 30 nM and a LOQ of 0.2 μM with a standard deviation of 11%. We believe that concentrations as low as 10 nM in urine are detectable if higher pH₂ enrichment was used. Overall, this method opens new ways for monitoring dilute analytes, allowing NMR to be adopted in situations where it was not considered before. We suggest that sample preparation protocols can be developed for other biofluids and the method is not limited to urine.

ASSOCIATED CONTENT

Supporting Information

The Supporting Information is available free of charge at <https://pubs.acs.org/doi/10.1021/acs.analchem.1c01281>.

Details on chemicals; HP hardware setup; SPE method development and performance; sample preparation; spectroscopy, and additional spectral data (PDF)

AUTHOR INFORMATION

Corresponding Author

Indrek Reile – National Institute of Chemical Physics and Biophysics, 12618 Tallinn, Estonia; orcid.org/0000-0003-3278-7947; Email: indrek.reile@kbfi.ee

Authors

Nele Reimets – National Institute of Chemical Physics and Biophysics, 12618 Tallinn, Estonia

Kerti Ausmees – National Institute of Chemical Physics and Biophysics, 12618 Tallinn, Estonia

Sirje Vija – National Institute of Chemical Physics and Biophysics, 12618 Tallinn, Estonia

Complete contact information is available at: <https://pubs.acs.org/doi/10.1021/acs.analchem.1c01281>

Notes

The authors declare no competing financial interest.

ACKNOWLEDGMENTS

The authors thank Dr. Jaan Past for developing bubbling control system electronics. This work was financially supported by the Estonian Research Council grant PSG11 and the Center of Excellence TK134 of the Archimedes Foundation.

REFERENCES

- (1) Gallo, J. M. *Mt. Sinai J. Med.* **2010**, *77*, 381–388.
- (2) Ratain, M. J.; William, K. P. *Holland-Frei Cancer Medicine*, 6th ed.; BC Decker, 2003.
- (3) Malet-Martino, M. C.; Martino, R. *Clin. Pharmacokinet.* **1991**, *20*, 337–349.
- (4) Everett, J. R. *eMagRes*; John Wiley & Sons, Ltd: Chichester, U.K., 2015; Vol. 4, pp 137–150.
- (5) Witte, C.; Schröder, L. *NMR Biomed.* **2013**, *26*, 788–802.
- (6) Hovener, J.; Pravdivtsev, A. N.; Kidd, B.; Bowers, C. R.; Glöggler, S.; Kovtunov, K. V.; Plaumann, M.; Katz-Brull, R.; Buckenmaier, K.; Jerschow, A.; Reiner, F.; Theis, T.; Shchepin, R. V.; Wagner, S.; Zacharias, N. M. M.; Bhattacharya, P.; Chekmenev, E. Y. *Angew. Chem., Int. Ed.* **2018**, *2*, 2–25.
- (7) Nikolaou, P.; Goodson, B. M.; Chekmenev, E. Y. *Chem. - Eur. J.* **2015**, *21*, 3156–3166.
- (8) Dumez, J.-N.; Milani, J.; Vuichoud, B.; Bornet, A.; Lalande-Martin, J.; Tea, I.; Yon, M.; Maucourt, M.; Deborde, C.; Moing, A.; Frydman, L.; Bodenhausen, G.; Jannin, S.; Giraudeau, P. *Analyst* **2015**, *140*, S860–S863.
- (9) Dey, A.; Charrier, B.; Martineau, E.; Deborde, C.; Gandria, E.; Moing, A.; Jacob, D.; Eshchenko, D.; Schnell, M.; Melzi, R.; Kurzbach, D.; Ceillier, M.; Chappuis, Q.; Cousin, S. F.; Kempf, J. G.; Jannin, S.; Dumez, J. N.; Giraudeau, P. *Anal. Chem.* **2020**, 14867–14871.
- (10) Reile, I.; Eshuis, N.; Hermkens, N. K. J.; van Weerdenburg, B. J. A.; Feiters, M. C.; Rutjes, F. P. J. T.; Tessari, M. *Analyst* **2016**, *141*, 4001–4005.
- (11) Sellies, L.; Reile, I.; Aspers, R. L. E. G.; Feiters, M. C.; Rutjes, F. P. J. T.; Tessari, M. *Chem. Commun.* **2019**, *55*, 7235–7238.
- (12) Eshuis, N.; Aspers, R. L. E. G.; van Weerdenburg, B. J. A.; Feiters, M. C.; Rutjes, F. P. J. T.; Wijmenga, S. S.; Tessari, M. *Angew. Chem., Int. Ed.* **2015**, *54*, 14527–14530.
- (13) Hermkens, N. K. J.; Eshuis, N.; van Weerdenburg, B. J. A.; Feiters, M. C.; Rutjes, F. P. J. T.; Wijmenga, S. S.; Tessari, M. *Anal. Chem.* **2016**, *88*, 3406–3412.
- (14) Skinner, J. G.; Menichetti, L.; Flori, A.; Dost, A.; Schmidt, A. B.; Plaumann, M.; Gallagher, F. A.; Hövener, J.-B. *Mol. Imaging Biol.* **2018**, 1–17.
- (15) Moran, V. E. *Front. Pharmacol.* **2012**, *1*, 9.

- (16) Benowitz, N. L.; Hukkanen, J.; Jacob, P. *Handb. Exp. Pharmacol.* **2009**, 192, 29–60.
- (17) Jarvis, M. J.; Tunstall-Pedoe, H.; Feyerabend, C.; Vesey, C.; Saloojee, Y. *Am. J. Public Health* **1987**, 77, 1435–1438.
- (18) Florescu, A.; Ferrence, R.; Einarson, T.; Selby, P.; Soldin, O.; Koren, G. *Ther. Drug Monit.* **2009**, 31, 14–30.
- (19) Savka, R.; Plenio, H. *Dalton Trans.* **2015**, 44, 891–893.
- (20) Cowley, M. J.; Adams, R. W.; Atkinson, K. D.; Cockett, M. C. R.; Duckett, S. B.; Green, G. G. R.; Lohman, J. A. B.; Kerssebaum, R.; Kilgour, D.; Mewis, R. E. *J. Am. Chem. Soc.* **2011**, 133, 6134–6137.
- (21) Seefeld, M. A.; Rouse, M. B.; Heerding, D. A.; Peace, S.; Yamashita, D. S.; McNulty, K. C. Inhibitors of AKT activity. WO Patent WO2008/098104 A1, 2008.
- (22) Eshuis, N.; Hermkens, N.; van Weerdenburg, B. J. A.; Feiters, M. C.; Rutjes, F. P. J. T.; Wijmenga, S. S.; Tessari, M. *J. Am. Chem. Soc.* **2014**, 136, 2695–2698.
- (23) Marion, D.; Ikura, M.; Bax, A. *J. Magn. Reson.* **1989**, 84, 425–430.
- (24) Wood, N. J.; Brannigan, J. A.; Duckett, S. B.; Heath, S. L.; Wagstaff, J. *J. Am. Chem. Soc.* **2007**, 129, 11012–11013.
- (25) Eshuis, N.; van Weerdenburg, B. J. A.; Feiters, M. C.; Rutjes, F. P. J. T.; Wijmenga, S. S.; Tessari, M. *Angew. Chem., Int. Ed.* **2015**, 54, 1481–1484.
- (26) Schlippenbach, T.; von Oefner, P. J.; Gronwald, W. *Sci. Rep.* **2018**, 8, No. 4249.
- (27) Behera, D.; Uppal, R.; Majumdar, S. *Indian J. Med. Res.* **2003**, 118, 129–133.
- (28) Cassiède, M.; Nair, S.; Dueck, M.; Mino, J.; McKay, R.; Mercier, P.; Quémerais, B.; Lacy, P. *Clin. Chim. Acta* **2017**, 464, 37–43.
- (29) Matsukura, S.; Sakamoto, N.; Takahashi, K.; Matsuyama, H.; Muranaka, H. *Clin. Pharmacol. Ther.* **1979**, 25, 549–554.
- (30) Massadeh, A. M.; Gharaibeh, A. A.; Omari, K. W. *J. Chromatogr. Sci.* **2009**, 47, 170–177.
- (31) Xu, X.; Iba, M. M.; Weisel, C. P. *Clin. Chem.* **2004**, 50, 2323–2330.
- (32) Hukkanen, J.; Jacob, P.; Benowitz, N. L. *Pharmacol. Rev.* **2005**, 57, 79–115.
- (33) Urso, R.; Bardi, P.; Giorgi, G. *Eur. Rev. Med. Pharmacol. Sci.* **2002**, 6, 33–44.
- (34) Jarvis, M. J.; Russell, M. A. H.; Benowitz, N. L.; Feyerabend, C. *Am. J. Public Health* **1988**, 78, 696–698.
- (35) Haley, N. J.; Sepkovic, D. W.; Hoffmann, D. *Am. J. Public Health* **1989**, 79, 1046–1048.

Appendix 2

Publication II

Ausmees, K.; Reimets, N.; Reile, I. Parahydrogen Hyperpolarization of Minimally Altered Urine Samples for Sensitivity Enhanced NMR Metabolomics. *Chem. Commun.* 2022, 58 (3), 463–466. <https://doi.org/10.1039/D1CC05665D>



Cite this: *Chem. Commun.*, 2022, 58, 463

Received 7th October 2021,
Accepted 7th December 2021

DOI: 10.1039/d1cc05665d

rsc.li/chemcomm

Parahydrogen hyperpolarization of minimally altered urine samples for sensitivity enhanced NMR metabolomics†

Kerti Ausmees, Nele Reimets and Indrek Reile*

Parahydrogen hyperpolarization has been shown to enhance NMR sensitivity in urine analysis by several orders of magnitude if urine samples are prepared by solid phase extraction (SPE). We present a different approach, developed for minimal sample alteration before analysis. Removing SPE from the workflow allows to retain a wider range of metabolites and paves the way towards more universal hyperpolarized NMR metabolomics of low abundance metabolites.

Nuclear magnetic resonance (NMR) spectroscopy is one of the leading analytical techniques for the characterization and quantification of low-molecular-weight compounds in biological samples.¹ Its key advantages – relatively simple sample preparation, reproducibility, quantitative nature – make it attractive for metabolomics studies. Yet, in analyte rich body fluids, numerous endogenous molecules stay below the limit of detection (LOD) of NMR or fail to be resolved in the most sensitive ¹H NMR spectra.

Traditionally, NMR sensitivity has been increased by higher field magnets, cryogenically cooled probes and small volume microprobes^{2,3} – none of which are likely to deliver orders of magnitude sensitivity improvements in the near future. Alternatively, nuclear hyperpolarization (HP) techniques have been developed to improve sensitivity by generating non-equilibrium nuclear polarization by sample manipulation.^{4,5} Dissolution dynamic nuclear hyperpolarization (d-DNP)⁶ and non-hydrogenative parahydrogen hyperpolarization (pH₂-HP),⁷ in particular, have already matured to see applications in biomixture analysis.

pH₂-HP offers a solution for both the sensitivity and resolution challenges in urinary metabolomics,⁷ doping detection⁸ and pharmacokinetics.⁹ These examples have used a possible drawback of pH₂-HP in their benefit, as the process's inherent chemoselectivity reduces the number of detectable analytes, alleviating resolution issues. All mentioned works have relied

on solid phase extraction (SPE) to render urine compatible with pH₂-HP. SPE, however, is not always attractive for metabolomics since it adds another layer of chemoselectivity, further reducing the scope of detectable analytes. Herein we remove SPE from sample preparation by identifying ammonia as the most aggressive pH₂-HP interfering urine component and by eliminating it with minimal sample manipulation, retaining the majority of urinary metabolome. This allows detection of different polarity metabolites (a challenge for SPE), while still maintaining the quantitative properties¹¹ of pH₂-HP.

The pH₂-HP technique employed herein^{7,11} relies on adding an iridium-based hyperpolarization catalyst to the sample, which reversibly binds parahydrogen and analytes (Fig. 1). Metabolites that are capable of binding complex **1** are detected remotely *via* the hydride resonances of each analyte's transient

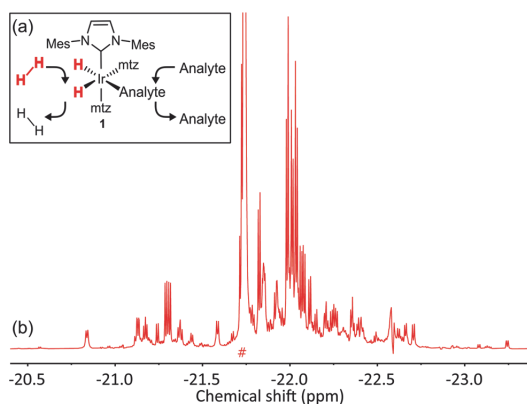


Fig. 1 The pH₂-HP process. (a) The process as carried out by an Ir-based catalyst **1** and an 18-fold excess of a co-substrate¹⁰ (1-methyl-1,2,3-triazol, **mtz**), collectively referred to as the catalyst system; (b) a hyperpolarized 1D spectrum of a urine sample, prepared by the method presented in this work. (#) denotes the symmetric complex with three **mtz** ligands (*i.e.*, analyte site occupied by **mtz**).

The National Institute of Chemical Physics and Biophysics (NICPB), Tallinn, Estonia. E-mail: indrek.reile@kbfi.ee

† Electronic supplementary information (ESI) available. See DOI: 10.1039/d1cc05665d

Communication

catalyst complexes at $-20. \dots -24$ ppm (Fig. 1) instead of their native resonances at $0. \dots 10$ ppm region, introducing two benefits. Firstly, the hydride signals are enhanced by up to 1000-fold,⁷ allowing detection of analytes below the LOD of regular NMR. Secondly, spectral overlap issues are alleviated as detection at -20 ppm region excludes overlap with non-catalyst-interacting metabolites. Moreover, in comparison to regular ^1H NMR where analytes can have numerous signals, hydride signals are reduced to a pair of doublets for each analyte,¹² further relieving spectral congestion. Due to the complex nature of urine and the chemical properties of the best performing $\text{pH}_2\text{-HP}$ catalysts (*e.g.*, poor water solubility), some form of sample manipulation prior to analysis is unavoidable. Compatibility with urine has been achieved by SPE, replacing water with a suitable solvent (alcohol⁷ or chloroform⁹) and removing $\text{pH}_2\text{-HP}$ interfering components. SPE fractionates analytes based on a particular chemical property (*e.g.*, analyte polarity), imposing an additional selective filter. This is beneficial for targeted analysis, allowing to concentrate desired analytes. However, when more universal analysis is desired (*e.g.*, metabolomics applications), SPE is a hindrance.

Sellies *et al.* showed that SPE can be skipped for urinary amino acids analysis and sample preparation is reduced to 20-fold dilution of urine in methanol, if the co-substrate is changed to pyridine.¹³ These conditions, however, are unsuitable for analysis of the rest of the metabolome since the high catalyst affinity of pyridine prevents the lower affinity metabolome from binding.¹⁰ Although **1** (with *mtz*) is known to tolerate low water concentrations in samples,¹⁴ when 30 μL of urine was diluted in 570 μL of methanolic solution of **1** (20-fold dilution), only two dominating doublets (-21.87 and -22.06 ppm) along with very few other hydride signals (Fig. 2a) were observed. Since urine is acidic, it can be rationalized that basic nitrogenous metabolites would be protonated, rendering them either unable to bind to **1** or insoluble in methanol. Increasing urine pH in an attempt to deprotonate analytes simply increased the two signals (Fig. 1b), which were attributed to complexes with urinary ammonia (NH_3), a known good ligand for **1**.¹⁵ Since the concentration of ammonia (*ca.* 30 mM)¹⁶ exceeds that of diagnostically valuable metabolites at low- μM levels by orders of magnitude, the higher affinity NH_3 excludes analysis of most of the otherwise catalyst interacting metabolome.

Consequently, urine sample preparation should focus on removal of ammonia, which is mostly formed by degradation of urea.¹⁷ Although the latter is a poor ligand for **1** and does not interfere with $\text{pH}_2\text{-HP}$,¹³ it is the major organic component of urine (up to 50% of organic solids). Since it would serve as an ammonia pool, urea should also be removed before analysis.

In principle, urea could be decomposed under mild conditions by the urease enzyme.¹⁸ However, urease treatment is known to introduce artifacts and misinterpretations into urine analysis¹⁸ and still requires removal of the resulting ammonia. The latter proved to be challenging, since under mild conditions ($\text{pH} < 8$) ammonia stays trapped in urine as nonvolatile salts and could not be removed by vacuum drying.

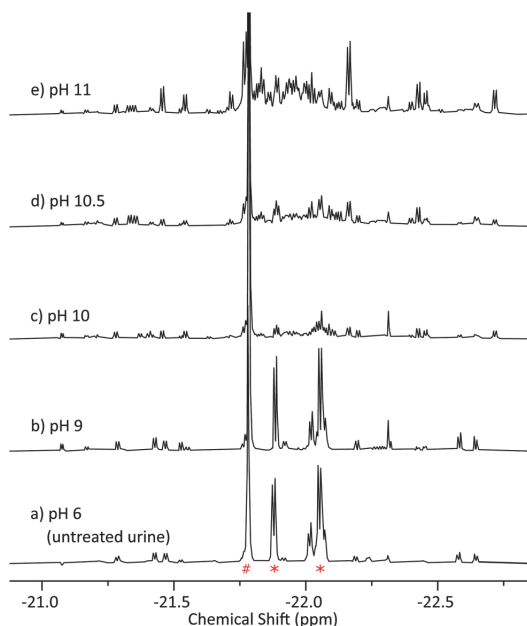


Fig. 2 1D $\text{pH}_2\text{-HP}$ spectra of urine samples prepared at different pH values. NH_3 removal was judged by the decrease of NH_3 related signals (*) and the increase of signals related to other metabolites. Residual NH_3 was also evaluated by regular ^1H NMR (ESI[†]).

Both tasks – hydrolysis of urea and ammonia stripping^{19,20} – were achieved at once if the pH of urine was raised to above the pK_a of ammonia ($\text{pH} > 9.3$). Screening of reaction conditions (Fig. 2c–e) proved that in the presence of a strong base (sodium hydroxide) urea is chemically decomposed at pH 11 at room temperature, allowing to skip urease treatment. As a precaution, to minimize the risk of undesired metabolome degradation, vacuum drying was substituted with lyophilization, leaving only trace amounts of residual NH_3 in the sample.

The process yields ammonia stripped solids that can be reconstituted, presenting an opportunity to produce a concentrated sample, similarly to SPE in earlier works.^{7–9} Concentration would be desired to compensate for sample dilution upon mixing with a methanolic (optimal solvent for $\text{pH}_2\text{-HP}$) solution of **1**. Accordingly, solids from 2.4 mL of ammonia stripped urine were reconstituted in 150 μL of D_2O (16-fold concentration). However, when the concentrate was mixed with methanol- d_4 solution of **1**, heavy precipitation occurred, as methanol does not solubilize all urinary salts, lipids, *etc.*

In order to remove the precipitate prior to introducing the solution of **1**, 450 μL of methanol- d_4 was added to the D_2O solution (1:3 vol/vol, reducing concentration factor to 4-fold) and centrifuged. 30 μL of the resulting supernatant was mixed with 570 μL of methanolic solution of **1**, producing a $\text{pH}_2\text{-HP}$ compatible 5-fold diluted urine sample with 1.25% vol/vol D_2O content. $\text{pH}_2\text{-HP}$ analysis of the mixture yielded a complex 1D spectrum of overlapping hydride signals (Fig. 1) that was

resolved with the 2D zero-quantum (ZQ) correlation experiment (Fig. 3),⁷ revealing the information rich response of the minimally altered urine sample.

Identification of analytes responsible for the signals is a challenge that at present is best addressed by internal standard addition¹¹ and by comparing hyperpolarized signal frequencies with external standards. We identified pyridine derivatives nicotine, cotinine, nicotinamide and 3-hydroxycotinine, that have previously been detected by SPE based approaches,^{8,9} but also adenine (nucleobase), adenosine, guanosine (nucleosides) and potential cancer biomarkers *N*₆-methyladenosine and *N*₁-methyladenosine (Fig. 3 and ESI†). Some of these (*e.g.*, adenine and nicotine) are of sufficiently different polarity and acid-base properties to make their concurrent isolation by SPE difficult. More elaborate assignment of signals, as well as developing new assignment strategies, remains a focus for ongoing research. It is already known that signals from structurally related compounds are diagonally aligned in the 2D ZQ spectra⁷ and spectral proximity can be combined with prior knowledge on metabolic pathways to methodologically guide standard addition – a strategy that we have used to identify an emerging drug metabolite in a pharmacokinetics study.⁹

The ability to use these signals for quantification of trace metabolites is a key feature of the pH₂-HP process.¹¹ A linear correlation of signal integrals to analyte concentrations is maintained as long as the cumulative concentration of catalyst-interacting analytes is substantially below the co-substrate (Fig. 1, **mtz**) concentration.²¹ This condition failed to be met with typical pH₂-HP catalyst and co-substrate concentrations (1.2 mM and 18 mM, respectively)^{8,9,11} with the sample preparation of this work. The quantitative regime was recovered when the catalyst system concentration was raised fivefold to 6 mM **1** and 108 mM **mtz** (see ESI†). We speculate that high catalyst loading is required since we are effectively introducing the whole methanol soluble fraction of urinary metabolome to the sample, resulting in a substantially higher cumulative concentration of catalyst interacting metabolites than in SPE extracts. Furthermore, certain high catalyst affinity metabolites (*e.g.* amino acids)¹³ can form irreversible complexes with Ir-catalysts, rendering them inaccessible to the rest of the metabolome.

Quantitative performance at raised catalyst loading was verified by internal standard addition series for 3-hydroxycotinine and 1-methyladenosine (Fig. 4). Both responded linearly within their

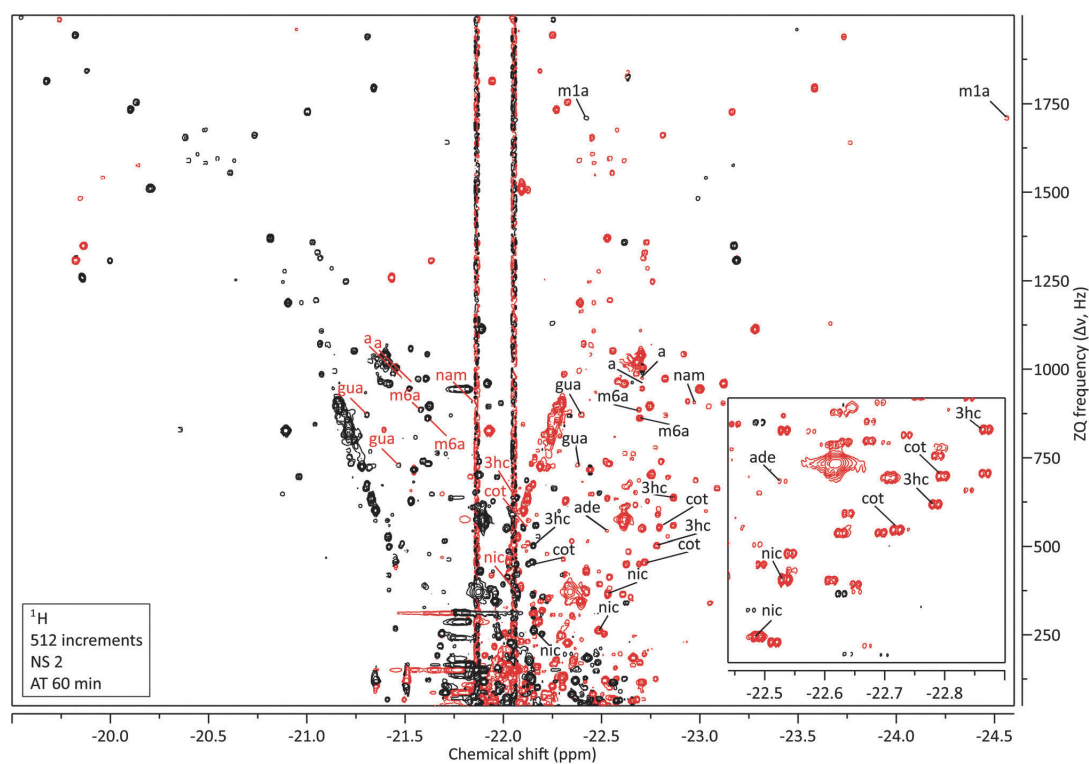


Fig. 3 2D ZQ spectrum of a smoker's urine sample: **m1a** – *N*₁-Methyladenosine, **m6a** – *N*₆-Methyladenosine, **3hc** – 3-hydroxycotinine, cot – cotinine, nic – nicotine, nam – nicotinamide, ade – adenine, a – adenosine, g – guanosine. Symmetric complex signal (Fig. 1, #) has been removed by convolution filtering. Remaining noise ridges at around –22 ppm are caused by residual ammonia. See Fig. S12 (ESI†) for a magnification of the spectrum and a graphical comparison to an SPE based sample.

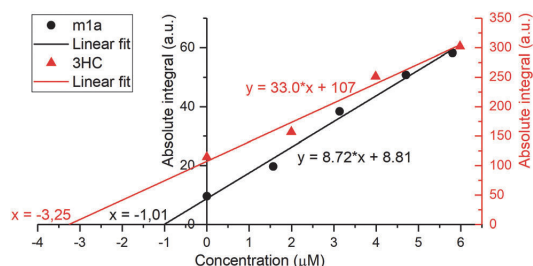


Fig. 4 Internal standard addition curves of hydride resonances^{7,11} allowed to establish analyte concentrations in urine as 16.3 μM for 3-hydroxycotinine and 5.0 μM for 1-methyladenosine (after considering the 5-fold urine dilution in sample preparation).

biologically relevant concentration ranges, confirming that applications can rely on a predictable relationship between signals and concentrations. However, due to the nature of the multipulse detection scheme,⁷ combined with analyte specific binding kinetics²² and relaxation,²³ individual calibration curves have to be established for each analyte.

In conclusion, we have verified that ammonia and methanol insoluble urine components are the main obstacles in analysing the iridium binding low-molecular weight urinary metabolome with the pH₂-HP process. We developed a sample preparation protocol that removes ammonia, urea (primary source of ammonia) as well as the methanol incompatible portion of the metabolome. This allows to avoid SPE and analyse minimally altered urine, yielding a highly complex hyperpolarized 2D ZQ NMR spectrum with a wealth of information. This technique can no doubt be adapted in targeted analysis experiments,^{8,9} but more importantly, it paves the way towards harnessing the added sensitivity in metabolomics studies in future research. Such applications would not necessarily require definite analyte identification nor quantification since samples would be classified based on metadata (*i.e.* disease state) and spectral features (*i.e.* the presence and intensity of signals). The chemoselectivity of the Ir-catalyst and analyte solubility in methanol would be the only filtering layers in the process, which will gain access to the unexplored metabolic information that lies below the LOD of regular NMR, compensating for the added complexity in sample preparation.

The authors acknowledge financial support from the research grant PSG11 of the Estonian Research Council, as well as from the Center of Excellence TK134 of the Archimedes Foundation. The authors wish to thank Dr Marco Tessari and Prof. Ivo Leito for helpful discussions.

Conflicts of interest

There are no conflicts to declare.

Notes and references

- J. L. Markley, R. Brüschweiler, A. S. Edison, H. R. Eghbalian, R. Powers, D. Raftery and D. S. Wishart, *Curr. Opin. Biotechnol.*, 2017, **43**, 34–40.
- D. S. Wishart, *TrAC, Trends Anal. Chem.*, 2008, **27**, 228–237.
- G. A. A. Nagana Gowda and D. Raftery, *J. Magn. Reson.*, 2015, **260**, 144–160.
- J. Hovener, A. N. Pravdivtsev, B. Kidd, C. R. Bowers, S. Glöggler, K. V. Kovtunov, M. Plaumann, R. Katz-Brull, K. Buckenmaier, A. Jerschow, F. Reineri, T. Theis, R. V. Shchepin, S. Wagner, N. M. M. Zacharias, P. Bhattacharya and E. Y. Chekmenev, *Angew. Chem., Int. Ed.*, 2018, **57**(35), 11140–11162.
- C. Witte and L. Schröder, *NMR Biomed.*, 2013, **26**, 788–802.
- A. Dey, B. Charrier, E. Martineau, C. Deborde, E. Gandria, A. Moing, D. Jacob, D. Eshchenko, M. Schnell, R. Melzi, D. Kurzbach, M. Ceillier, Q. Chappuis, S. F. Cousin, J. G. Kempf, S. Jannin, J.-N. Dumez and P. Giraudeau, *Anal. Chem.*, 2020, **92**, 14867–14871.
- L. Sellies, I. Reile, R. L. E. G. Aspers, M. C. Feiters, F. P. J. T. Rutjes and M. Tessari, *Chem. Commun.*, 2019, **55**, 7235–7238.
- I. Reile, N. Eshuis, N. K. J. Hermkens, B. J. A. van Weerdenburg, M. C. Feiters, F. P. J. T. Rutjes and M. Tessari, *Analyst*, 2016, **141**, 4001–4005.
- N. Reimets, K. Ausmees, S. Vija and I. Reile, *Anal. Chem.*, 2021, **93**, 9480–9485.
- N. Eshuis, N. Hermkens, B. J. A. van Weerdenburg, M. C. Feiters, F. P. J. T. Rutjes, S. S. Wijmenga and M. Tessari, *J. Am. Chem. Soc.*, 2014, **136**, 2695–2698.
- N. K. J. Hermkens, N. Eshuis, B. J. A. van Weerdenburg, M. C. Feiters, F. P. J. T. Rutjes, S. S. Wijmenga and M. Tessari, *Anal. Chem.*, 2016, **88**, 3406–3412.
- N. J. Wood, J. a. Brannigan, S. B. Duckett, S. L. Heath and J. Wagstaff, *J. Am. Chem. Soc.*, 2007, **129**, 11012–11013.
- L. Sellies, R. Aspers, M. C. Feiters, F. Rutjes and M. Tessari, *Angew. Chem., Int. Ed.*, DOI: 10.1002/anie.202109588.
- N. K. J. Hermkens, R. L. E. G. Aspers, M. C. Feiters, F. P. J. T. Rutjes and M. Tessari, *Magn. Reson. Chem.*, 2018, **56**, 633–640.
- W. Iali, P. J. Rayner and S. B. Duckett, *Sci. Adv.*, 2018, **4**, eaa06250.
- D. S. Wishart, Y. D. Feunang, A. Marcu, A. C. Guo, K. Liang, R. Vázquez-Fresno, T. Sajed, D. Johnson, C. Li, N. Karu, Z. Sayeeda, E. Lo, N. Assempour, M. Berjanskii, S. Singhal, D. Arndt, Y. Liang, H. Badran, J. Grant, A. Serra-Cayuela, Y. Liu, R. Mandal, V. Neveu, A. Pon, C. Knox, M. Wilson, C. Manach and A. Scalbert, *Nucleic Acids Res.*, 2018, **46**, D608–D617.
- L. Mazzei, F. Musiani and S. Ciurli, *J. Biol. Inorg. Chem.*, 2020, **25**, 829–845.
- M. Khodadadi and M. Pourfarzam, *Metabolomics*, 2020, **16**, 66.
- E. J. Kim, H. Kim and E. Lee, *Appl. Sci.*, 2021, **11**, 441.
- H. Ray, F. Perreault and T. H. Boyer, *Environ. Sci. Technol.*, 2020, **54**, 11556–11565.
- N. Eshuis, B. J. A. van Weerdenburg, M. C. Feiters, F. P. J. T. Rutjes, S. S. Wijmenga and M. Tessari, *Angew. Chem., Int. Ed.*, 2015, **54**, 1481–1484.
- N. K. J. Hermkens, M. C. Feiters, F. P. J. T. Rutjes, S. S. Wijmenga and M. Tessari, *J. Magn. Reson.*, 2017, **276**, 122–127.
- L. Sellies, R. L. E. G. Aspers and M. Tessari, *Magn. Reson.*, 2021, **2**, 331–340.

Appendix 3

Publication III

Reimets, N.; Ausmees, K.; Vija, S.; Trummal, A.; Uudsemaa, M.; Reile, I. Parahydrogen Hyperpolarized NMR Detection of Underivatized Short Oligopeptides. *Analyst* 2023, 148 (21), 5407–5415. <https://doi.org/10.1039/D3AN01345F>



Cite this: DOI: 10.1039/d3an01345f

Parahydrogen hyperpolarized NMR detection of underivatized short oligopeptides†

Nele Reimets, ^{a,b} Kerti Ausmees, ^a Sirje Vija,^a Aleksander Trummal, ^a
 Merle Uudsemaa ^a and Indrek Reile ^{*a}

Parahydrogen hyperpolarization has evolved into a versatile tool in NMR, allowing substantial sensitivity enhancements in analysis of biological samples. Herein we show how its application scope can be extended from small metabolites to underivatized oligopeptides in solution. Based on a homologous series of alanine oligomers, we report on an experimental and DFT study on the structure of the oligopeptide and hyperpolarization catalyst complexes formed in the process. We demonstrate that alanine oligomers coordinate to the iridium carbene-based catalyst in three different ways, each giving rise to distinctive hydride signals. Moreover, the exact structures of the transient oligopeptide-catalyst complexes are oligomer-specific. This work gives a first insight into how the organometallic iridium-N-heterocyclic carbene-based parahydrogen hyperpolarization catalyst interacts with biopolymers that have multiple catalyst binding sites. A preliminary application example is demonstrated for oligopeptide detection in urine, a complex biological mixture.

Received 4th August 2023,
 Accepted 25th September 2023
 DOI: 10.1039/d3an01345f

rsc.li/analyst

Introduction

Oligopeptides are a diverse family of small biopolymers consisting of 2–20 amino acids with a wide array of biological properties, *e.g.* target selectivity and affinity, biodegradability, and low toxicity.¹ They are absorbed through skin more efficiently than larger proteins and are therefore employed in cosmeceuticals.^{2,3} In medicine, oligopeptides are of interest as biomarkers or mediators of disease, and as drug candidates⁴ or drug transporters.⁵

Development and innovation in such broad application scope requires adequate analytical techniques. However, the complex nature of biological matrices and the often low abundance of oligopeptides makes analysis in their working environment challenging.^{6,7} Among the main complications in oligopeptide analysis are sample purification along with detection and quantitation in multicomponent samples.^{7–9} For instance, mass spectrometry analysis on biological samples is hampered by extensive ion suppression by more abundant compounds, complicating detection of low concentration short peptides.⁸

Nuclear magnetic resonance spectroscopy (NMR) is less hindered by sample matrix effects but lacks the required sensitivity and resolution. Low concentration biomolecules, including oligopeptides, frequently fail to be detected since they fall below the NMR limit of detection, cannot be spectrally resolved from signals of more abundant sample components, or frequently both – even on the ultra-high field instruments available today. However, this sensitivity barrier can be overcome by various nuclear hyperpolarization techniques which drastically increase NMR signals.¹⁰ So far, dissolution DNP^{11,12} and parahydrogen-based hyperpolarization techniques (SABRE, PHIP, nhPHIP)¹³ have been demonstrated to be applicable for the analysis of biological mixtures and metabolites.^{14,15}

Detection of oligopeptides by parahydrogen (pH₂) hyperpolarization has been achieved before only by chemical modification of analytes. Examples include inserting unsaturated labels into peptide side chains¹⁶ or into disulfide bridged oligopeptides¹⁷ to enable hydrogenative PHIP. Alternatively, an iridium-interacting pyridine tag has been synthetically incorporated into oligopeptides for SABRE hyperpolarization.^{18,19}

In this work we show how pH₂ hyperpolarization can be used to detect short oligopeptides without prior chemical modification by high-field non-hydrogenative parahydrogen induced polarization (HF-nhPHIP *aka* nhPHIP, Fig. 1).²⁰ An elaborate study on the structure of the organometallic complexes that facilitate hyperpolarized detection of oligopeptides is shown for alanine oligomers as model compounds. Experimental NMR and DFT results give insight into nhPHIP catalyst coordination of multidentate biopolymers. In addition,

^aNational Institute of Chemical Physics and Biophysics, Akadeemia tee 23, Tallinn 12618, Estonia. E-mail: indrek.reile@kbfi.ee

^bSchool of Science, Tallinn University of Technology, Ehitajate tee 5, Tallinn 19086, Estonia

†Electronic supplementary information (ESI) available: Three documents containing further information on sample preparation, oligopeptide synthesis procedures and characterization, nhPHIP spectra and associated content (SI_nhPHIP); technical details and detailed results from DFT calculations (SI_DFT); and structural analysis data for nhPHIP complexes (SI_NMR). See DOI: <https://doi.org/10.1039/d3an01345f>

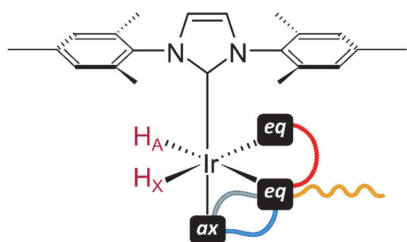


Fig. 1 Schematic representation of the nhPHIP complex $[\text{Ir}(\text{IMes})(\text{H}_2(\text{sub})_{\text{eq}}(\text{sub})_{\text{eq}}(\text{sub})_{\text{ax}})\text{Cl}]$. pH_2 derived hyperpolarized hydrides H_A and H_X are detected, while pH_2 and substrates (sub, an analyte or a cosubstrate) reversibly associate with the catalyst. H_A and H_X chemical shifts reflect the type of substrate *trans* to their position. Oligopeptides can form mono- and bidentate complexes via eq (yellow), eq-eq (red), ax-eq (blue) and reversed ax-eq (gray) sites. Any ax or eq site not occupied by an analyte is taken up by a cosubstrate which is present in excess.

we demonstrate that the approach can be applied to oligopeptide sequences consisting of various amino acids and is compatible with the complex biofluid matrix of urine.

Results and discussion

nhPHIP system optimization

The working principles of nhPHIP have been reviewed in detail recently.²⁰ In short, it does not require chemical modifi-

cation of analytes, only their binding to the iridium catalyst (Fig. 1). After an analyte associates to the catalyst, a new complex is formed, which will give rise to specific hyperpolarization-enhanced signals H_A and H_X between -15 and -30 ppm in ^1H spectra. Based on these signals, trace quantities of analytes can be detected and quantified.^{15,21–25} Selectivity towards various analyte classes can be optimized by changing the cosubstrate in the catalyst system, where methyl-triazole (mtz) has emerged as the optimal choice for N-heterocyclic analytes^{15,23,26} and pyridine for amino acids.^{27,28}

Tuning the nhPHIP system towards amino acids with pyridine as cosubstrate²⁸ involved heating the sample to 50°C under strong basic conditions ($\text{pH } 11$) – a potentially undesirable combination due to possible hydrolysis and oxidation of peptides.²⁹ A screening of ten alternative cosubstrates with different steric and electronic properties³⁰ (SI_nhPHIP Fig. S1†) on a mixture of amino acids (Ala, Leu, Phe) under basic conditions revealed 3-fluoro-4-methylpyridine (3F4MePy) as optimal, since it forms the desired amino acid catalyst complex spontaneously at room temperature.

Combining the modified system of Ir-IMes catalyst and 3F4MePy cosubstrate with alanine trimer (A_3) or pentamer (A_5) under basic conditions without heating formed distinguishable hydride signals around $\delta -23.2$ and $\delta -30.6$ ppm (Fig. 2a and SI_nhPHIP Fig. S3†). Since the signal pattern for both oligopeptides was similar to what has been reported for amino acids, formation of an analogous axial-equatorial bidentate

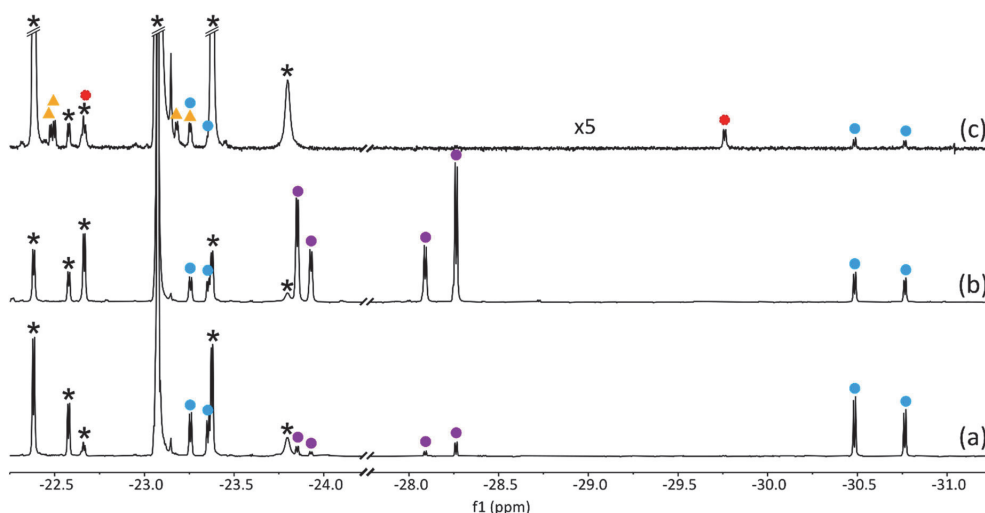


Fig. 2 nhPHIP spectra of (a) A_3 under basic conditions, (b) A_3 under basic conditions after heating at 50°C for 7.5 min, (c) A_3 with no additional base or heating. Blue circles correspond to the diastereomers of A_3 ax-eq complex, red circles to eq-eq complex, and yellow triangles to the diastereomers of mono complex. Violet circles represent ax-eq signals of the two diastereomers of monomeric alanine-iridium complex.²⁸ Signals which overlap in 1D were assigned from a 2D spectrum (see SI_nhPHIP Fig. S4†). Asterisk (*) denotes signals from iridium-complex of 3F4MePy, solvent, and impurities. Samples contained a 1 : 18 : 0.08 ratio of catalyst : 3F4MePy : A_3 . All spectra measured at 10°C sample temperature. Note that heating the sample under basic conditions increased monomer signals (violet circles) (a) vs. (b). Monomer complexation was suppressed when no additional base and heating were applied (c).

complex (ax-eq) can be assumed (Fig. 2, blue circles δ -23.26 and -30.48, δ -23.36 and -30.76 ppm; SI_nhPHIP Fig. S3† for A₃).^{20,28}

The spectrum also showed traces of Ala monomer as impurity (Fig. 2, purple circles H_X -23.85 and -23.93 ppm, H_A -28.26 and -28.09 ppm, and SI_nhPHIP Fig. S3†), undetectable by regular NMR. Heating the sample over a 50 °C water bath for 7.5 min, followed by nhPHIP measurement at 10 °C, increased monomer signals, while relative intensity of oligopeptide signals decreased (Fig. 2b and Fig. S3†). This suggests complexation of Ala monomer is favored over oligomers under basic conditions and heating accelerates the formation of the thermodynamically preferred monomer complex.²⁸

Monomer complexation was suppressed when no additional base and heating were applied (Fig. 2c), giving a possibility to tune the method toward oligopeptide detection and avoid amino acid binding to the catalyst. This modification revealed additional hydrides' signal pairs, which correspond to the bidentate eq-eq (Fig. 2c, red circles δ -22.66 and -29.76 ppm) and monodentate mono (Fig. 2c, yellow triangles δ -22.48 and -23.25 ppm, and δ -22.50 and -23.18 ppm) analyte binding modes (Fig. 1). While the general hydride signal pattern of ax-eq complex is similar to Ala monomer, the noticeable 2–3 ppm chemical shift difference points towards notable variations in oligopeptide binding to iridium (Fig. 2).

Elucidation of oligopeptide binding modes using A₃ as a model compound

Hydride signals H_A and H_X are present only when an analyte associates to the iridium catalyst. Chemical shifts of these signals indicate the type of the functional group *trans* to a hydride signal. Oligopeptide complexes' H_A signals at -30 ppm region coincide, in addition to amino acids, with literature examples for hydrides *trans* to eq-eq bidentate O-binding of pyruvate^{31,32} or oxalate.³³ However, oligopeptide binding by multiple O-sites is ruled out by H_X chemical shifts of A₃ at -23.35 and -23.26 ppm (Fig. 2 blue circles), suggesting the involvement of an N-ligand. While this con-

dition could also be met by monodentate O-binding from A₃ C-terminus and a 3F4MePy unit in the other eq site, it is unlikely, since hydride signals for a C-terminus model compound valeric acid were not observable. Monodentate N-terminus binding (mono), on the other hand, is possible, since the *sec*-butylamine signals resonate at -19.9 and -22.3 ppm, specific to nitrogen binding in the equatorial plane (SI_nhPHIP Fig. S5†). The above supports the hypothesis of a bidentate complex with O-binding *trans* to H_A around δ -30 ppm and N-binding *trans* to H_X around δ -23 ppm (see 2D correlation spectra in SI_nhPHIP Fig. S4†).

In order to elaborate which N and O sites of A₃ participate in binding, N-acetyl A₃ (Ac-A-A-A), N-acetyl A₃ methyl ester (Ac-A-A-A-OMe) and A₃ methyl ester (A₃-OMe) were synthesized (see synthesis details in SI_nhPHIP, nhPHIP spectra in SI_nhPHIP Fig. S6†). Only A₃-OMe gave rise to observable hydride signals with H_A chemical shifts remarkably similar to A₃ (SI_nhPHIP Fig. S7†). This confirms that the C-terminus is not involved in catalyst binding, also supported by the observation that hydride chemical shifts for A₃ do not change noticeably under basic or neutral conditions (Fig. 2 spectrum a vs. c). Therefore, while the N-terminus is crucial for bidentate catalyst binding, the C-terminus is not involved, and O-binding is likely provided by one of the peptide bond carbonyl groups.

Further experimental evidence on A₃-catalyst complexes' configurations was obtained from analysis of nhPHIP hydride spectra from labeled A[¹⁵N]-A-A-OMe (Fig. 3 and SI_nhPHIP Fig. S8 and S9†). ¹⁵N induced coupling of 17.44 Hz and 17.52 Hz on H_A signals at -22.53 and -22.62 ppm, respectively, confirmed the presence of two diastereomeric mono configurations (Fig. 3, yellow triangles). Their associated H_X signals at δ -23.17 and δ -23.26 ppm are in agreement with the *trans* nitrogenous heteroaromatic cosubstrate (3F4MePy). Likewise, the eq-eq complex was confirmed by a 16.16 Hz ²J_{NH} coupling for H_X signal at δ -22.72 ppm. Its coupling partner H_A is a doublet at δ -29.66 ppm, indicating a *trans* O-ligand (Fig. 3, red circles). Note that the analogous eq-eq complex was not

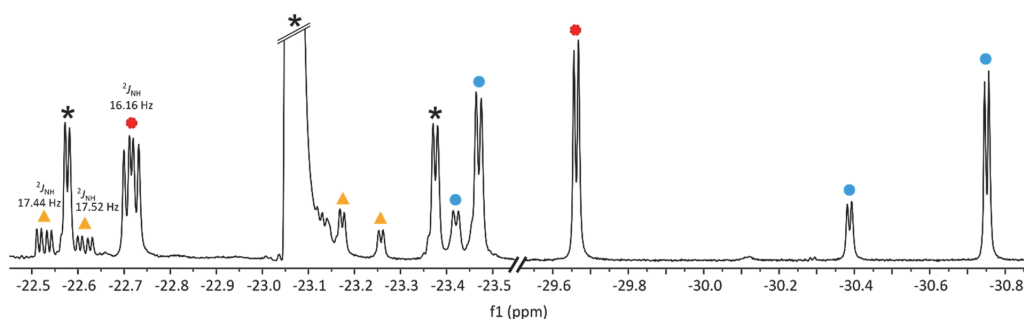


Fig. 3 nhPHIP spectrum of ¹⁵N-labelled A₃ methyl ester A[¹⁵N]-A-A-OMe gives rise to hydrides' signals of ax-eq (blue circles), eq-eq (red circles), and mono (yellow triangles) configurations. Signal splitting due to ¹⁵N coupling can be seen in mono and eq-eq configurations' signals. ax-eq shows no splitting, confirming N_i in axial and O_i in equatorial position. Asterisk (*) denotes signals from the 3F4MePy-Ir-complex. The sample contained a 1 : 8 : 0.6 ratio of catalyst : 3F4MePy : A[¹⁵N]-A-A-OMe. Recorded at 10 °C sample temperature.

nhPHIP observable for amino acids,²⁸ suggesting that hydrogen exchange kinetics is more favorable for oligopeptides.

Hydride signal pairs at δ -23.42 and -23.47 ppm (H_X), associated with δ -30.39 and -30.75 ppm (H_A), were identical to A_3 -OMe and did not exhibit any multiplicity that would indicate equatorial ^{15}N binding (Fig. 3, blue circles). This supports the diastereomeric ax-eq complex structure. While the experimental evidence from above excludes the C-terminus oxygen binding, it does not allow to establish which of the remaining A_3 O-sites are involved.

DFT calculations: from L-alanine to A_3

Further insight into the structures of involved complexes was sought from DFT calculations. The preferred contact topology in the coordination sphere around the iridium atom was established for equilibrium N- and O-binding modes for the $[\text{Ir}(\text{IMes})(\text{H})_2(3\text{F4MePy})(\text{L-Ala})]^+$ model complex containing monomeric deprotonated L-alanine. Such choice of a model system allowed to cross-validate calculation results with published experimental work on amino acid catalyst complexes,²⁸ thereby verifying the reliability of the chosen DFT methods.

Calculations showed that the binding pattern with N-terminus in ax and C-terminus oxygen in eq plane is the energetically favored bidentate L-Ala-catalyst-complex, in agreement with experimental results from Tessari group²⁸ as well as with the recent gas-phase DFT study,³⁴ further confirming strong prevalence of the bidentate ax-eq binding mode for alanine (see SI_DFT†). Additionally, according to DFT, there are two bidentate binding topologies of higher energy: reversed ax-eq and eq-eq (Fig. 1).

Applying all three bidentate contact geometries, along with the mono configuration, and optimizing for the A_3 -OMe complex, showed that the most stable binding pattern features bidentate ax-eq coordination with N-terminus in ax position (Fig. 4a). Calculations towards establishing the particular O-site involved in eq binding were carried out in parallel for A_3 -OMe and A_3 . These structures contain three carbonyl oxygen atoms (starting from N-terminus O_i , O_{ii} , O_{iii}) where the first two are located in peptide bonds and the last is in the C-terminus. Any of these can potentially bind to iridium in the eq site to form the ax-eq configuration. DFT calculations (see SI_DFT†) revealed that the preferred bidentate binding to the iridium catalyst involves oxygen O_i yielding a 5-membered cycle (Fig. 4a). Both A_3 -OMe and A_3 maintain a similar binding site topology as a single deprotonated alanine, but without the involvement of strong electrostatic interactions of the latter.

Iridium catalyst complexes of A_3 -OMe and A_3 are additionally stabilized by an intramolecular hydrogen bond between the $N_i\text{H}$ and O_{iii} sites (3.2 Å distance between heavy atoms, Fig. 4a). Such a configuration places the third peptide bond N_{iii} hydrogen on average 3.5 Å distance from the methyl of the first alanine residue – confirmed experimentally by an observable NOE contact between the two sites (NOE data in SI_NMR†).

Analogously to L-alanine, the trimer has two further higher energy bidentate binding topologies: reversed ax-eq and eq-eq. In contrast to a single amino acid, the reversed ax-eq,

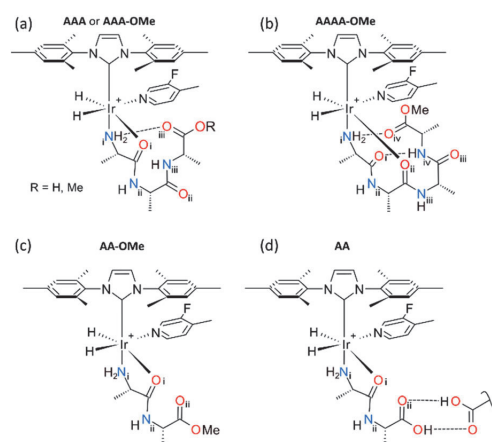


Fig. 4 Bidentate binding to the iridium catalyst of (a) A_3 and A_3 -OMe, (b) A_4 -OMe, (c) A_2 -OMe, and (d) A_2 . DFT calculations (see SI_DFT†) reveal that A_2 and A_3 preferred bidentate binding configurations involve $N_i\text{H}$ and O_i , forming a 5-membered Ir-cycle. A single intramolecular hydrogen bond between a $N_i\text{H}$ moiety and the O_{iii} contributes to stabilization of the A_3 complex. A_2 and A_2 -OMe complexes lack intramolecular hydrogen bonding. A_4 -OMe and A_5 -OMe (SI_DFT†) present more complex structures, containing an 8-membered cycle and multiple intramolecular hydrogen bonds.

where the N-terminus is in an eq position and O in an ax, is the highest energy configuration for A_3 -OMe. Therefore, DFT calculations confirm that complexes with both H_A and H_X experimental chemical shifts in the -22...-23 ppm region do not involve O-binding and belong to the N-only mono configuration. The third possible bidentate complex, the eq-eq, is energetically between the reversed ax-eq and the mono complex. The negligible Boltzmann probabilities of these configurations (around 1% for mono and close to zero for both eq-eq and reversed ax-eq) suggest that at equilibrium conditions they may appear only in trace amounts. However, mono and eq-eq were experimentally observed (Fig. 2c & 3), indicating that the thermodynamic equilibrium had not been reached at current experimental conditions and these complexes are likely subject to kinetic decay.

Structures of other alanine oligomer-catalyst complexes

nhPHIP of longer alanine oligomers A_4 -OMe, A_5 -OMe and A_6 -OMe (Fig. 5) display similar experimental hydrides' chemical shifts to A_3 -OMe and A_3 . The alanine octamer and decamer did not give any nhPHIP signals, probably due to poor longer oligomer solubility in methanol.

To evaluate whether the similar chemical shifts correspond to the same binding configurations and intramolecular hydrogen bonding patterns as for A_3 -OMe, the lowest energy ax-eq coordination topologies were selected for DFT studies of tetra- and pentamer esters. Simulations indicated preferential binding of A_4 -OMe and A_5 -OMe to the catalyst *via* O_{ii} equatorial coordination, leading to an 8-membered Ir-cycle (Fig. 4b

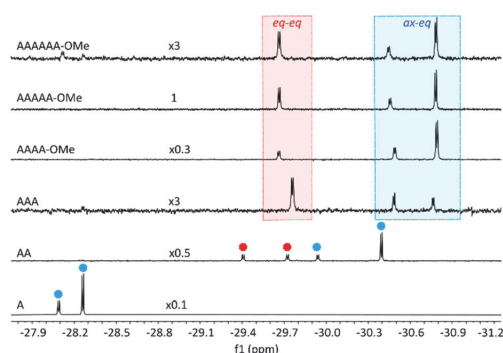


Fig. 5 The nhPHIP H_A ax-eq (blue) and eq-eq (red) signals of monomer to hexamer as indicated on the figure. Tetra-, penta-, and hexamer were analyzed in methyl ester form due to their poor solubility in carboxylic acid form and difficulties in deprotecting the C-terminus. Spectra recorded at 10 °C.

and SI_DFT†). Two intramolecular hydrogen bonds support formation of such structures. One hydrogen bond forms between N_iH and O_{iv} and the other between O_i and $N_{iv}H$ sites, with 2.8–2.9 Å and 3.0 Å distances between heavy atoms, respectively.

Catalyst binding of the alanine dimer and its methyl ester present a more complex case. A_2 -OMe complexation is driven by an eq contact of O_i with Ir, forming a 5-membered cycle (Fig. 4c), similarly to A_3 -OMe and A_3 . These calculation results are supported by the proximity of the H_A chemical shifts to those of A_3 (SI_nhPHIP Fig. S10†). Due to the lower flexibility of the truncated oligopeptide chain, the formation of an intramolecular hydrogen bond between N_iH and the sole remaining carbonyl oxygen (O_{ii}) is prevented.

While longer oligomers bind similarly, regardless of esterification of their C-termini, the dimer does not. H_A chemical shifts for A_2 appear in between those of the alanine monomer and other alanine oligomers (Fig. 5). This could be indicative of either structural or electronic changes localized at the C-terminus of A_2 , leading to an increase of negative charge at the $-COOH$ moiety, resembling a deprotonated Ala monomer. This would lead to an Ala-like catalyst binding pattern that is governed by electrostatics and results in an 8-membered cycle. However, experimental observation of A_2 NOE contacts (see SI_NMR†) that are characteristic of the 5-membered cycle indicate that full deprotonation of $-COOH$ is unlikely. Instead, theoretical simulations suggest the possibility of A_2 tail-to-tail dimerization with a second A_2 molecule on top of bidentate binding with the Ir-catalyst (Fig. 4d). In this configuration, the C-terminus acquires partial carboxylate character according to equilibrium bond length estimates at the double $-COOH$ interface. In addition, the second A_2 unit of the dimer probably benefits from additional stabilizing interactions with the remote parts of the iridium complex (see SI_DFT†). While the possibility of such dimerization was also computationally

observed for A_3 , the relative proximity of the A_2 C-terminus to the Ir-atom as compared with other alanine oligomer complexes may explain the distinct chemical shifts of its corresponding hydrides' signals (Fig. 5).

Formation of equilibrium ax-eq complex

Experimental results for A_3 support the initial formation of higher energy kinetic products, as suggested by DFT. Monitoring the sample for an extended time showed that hydride signals of eq-eq and mono slowly decrease while those of ax-eq increase at typical 10 °C measurement conditions. Keeping the sample at a relatively mild temperature of a 37.5 °C water bath for 5 min, followed directly by nhPHIP measurement at 10 °C, resulted in a 2.7-fold increase of ax-eq hydride signals, while the eq-eq and mono configurations' signals decreased (Fig. 6). The same procedure at a 50 °C water bath resulted in a 7-to-9-fold ax-eq signal increase compared to a non-heated sample, with those of higher energy complexes barely detectable.

Repeated heating of the sample at the same temperature did not increase ax-eq signals further, suggesting a thermodynamic equilibrium had been reached (SI_nhPHIP Fig. S12†). The structure of the ax-eq complex, which exists as two diastereomers, was characterized by 1H , COSY, NOESY, HSQC and HMBC spectra (see SI_NMR†).

According to 1H NMR, oligopeptides complex only partially to the Ir-catalyst, whereas amino acids are almost entirely in a bound form under equimolar concentrations.²⁸ Bound-to-unbound ratio of A_3 was approximately 50:50 at thermodynamic equilibrium. This means that unlike for single amino acids, the nhPHIP signals which correspond to oligopeptides do not represent the whole analyte available in solution. Thus, alanine oligomers' binding efficiency is similar to N-heterocycles, which typically bind to the catalyst partially.³⁵

Interestingly, the kinetically favored eq-eq configuration was nhPHIP detectable for alanine oligomers (Fig. 5), unlike for amino acids.²⁸ The nhPHIP efficiency of this complex is very high, since in thermally polarized measurements the corresponding eq-eq signals were barely detectable. However, these signals are less informative than the ax-eq signals,

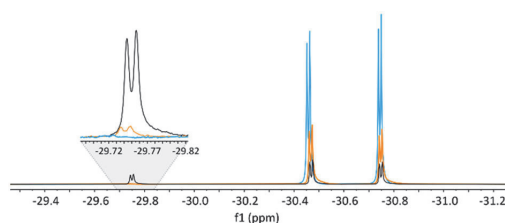


Fig. 6 nhPHIP H_A signals of A_3 before heating (black), after heating at 37.5 °C for 5 min (orange), and after heating at 50 °C for additional 5 min (blue). ax-eq signals increase with heating, while the signals of kinetic complex eq-eq decrease. Spectra recorded at 10 °C.

which vary more in their chemical shifts among the tested oligomers (SI_nhPHIP Fig. S11†).

The thermodynamically favored A_3 ax-eq hydrides' signals were enhanced up to 38-fold (see SI_nhPHIP Fig. S13†) with nhPHIP, corresponding to approx. 1400-fold reduction in NMR measurement time. The relatively modest enhancement factor, compared to what has been reported for small molecules,²³ could be a property of the particular model compound. We hypothesize that different nhPHIP efficiencies may emerge for oligopeptides consisting of more diverse amino acid sequences and there could be room for further nhPHIP system optimization for particular applications.

Detecting short oligopeptides in human urine

Preliminary nhPHIP experiments on different functional oligopeptides, chosen to cover a range of potential applications, showed that H_A and H_X signals resonate in the same spectral region as for alanine oligomers (H_A at -30.57 to -31.21 ppm and H_X at -23 ppm, Fig. 7). Therefore, the method herein is not limited to the chosen model compounds. Oligopeptides consisting of various amino acids are detectable and it is likely that similar oligopeptide-catalyst binding modes are involved.

It is known from nhPHIP of N-heterocycles that experimental parameters need to be re-evaluated when analyzing standard solutions²² or same analytes in the complex matrix of a biofluid.¹⁵ Applying the urine sample preparation procedure developed for urinary nucleosides by Ausmees *et al.* allowed simultaneous observation of H_A signals (Fig. 8) for several oligopeptides (-30 ppm region) as well as for amino acids (-28 ppm region). The procedure involved raising the pH of urine with sodium hydroxide, probably needed to counteract the naturally acidic nature of urine, under which nitrogenous analytes can be protonated.

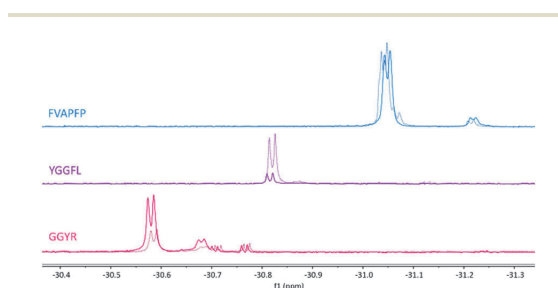


Fig. 7 nhPHIP H_A signals of functional oligopeptides: papain inhibitor (GGYR), neuropeptide Leu-enkephalin (YGGFL), and cosmeceutical peptide hexapeptide-11 (FVAPFP), measured at 25°C . Two sample preparation protocols were followed: (a) solid lines: peptide was dissolved in water, pH corrected to 7.4–7.9, lyophilized and dissolved in methanol- d_4 prior nhPHIP measurement. Ratio of catalyst : 3F4MePy : oligopeptide was 1 : 18 : 0.08; (b) dashed lines: peptide was dissolved in methanol- d_4 as supplied. Ratio of catalyst : 3F4MePy : oligopeptide was 1 : 8 : 0.08. Comparison of spectra (a) and (b) demonstrates that nhPHIP performance is dependent on the particular oligopeptide, sample preparation and measurement conditions.

These results indicate that nhPHIP can be used for the study of the peptidome of body fluids (peptidomics). This emerging field of research currently relies on mass spectroscopy coupled with HPLC or CE, where extensive sample preparation is needed to enrich short peptides over matrix compounds.²⁹ nhPHIP could be a relatively easy to implement alternative that allows to conduct peptidomics by NMR.

Experimental

Chemicals and materials

Iridium catalyst complex precursor $[\text{Ir}(\text{Cl})(\text{COD})(\text{IMes})]$ and oligopeptide esters were synthesized according to literature procedures, see SI_nhPHIP† for details. Synthesized compounds were characterized and validated by HR-MS and NMR.

NMR sample and experiment

The active nhPHIP catalyst $[\text{Ir}(\text{IMes})(\text{H})_2(3\text{-fluoro-4-methylpyridine})_3]^+$ was prepared *in situ* in a 5 mm intermediate pressure valved NMR tube. The concentration of $[\text{Ir}(\text{Cl})(\text{COD})(\text{IMes})]$ catalyst precursor was 1.2 mM and the concentration of a cosubstrate 3-fluoro-4-methylpyridine was either 21.6 mM or 9.6 mM, (details in SI_nhPHIP†) in the tube. The mixture was pressurized under 5 bar of H_2 , shaken and left to react for 2 h before adding the methanolic oligopeptide solution. The target concentration of an oligopeptide was either 0.1 mM or 1.0 mM in the tube. Total sample volume was 600 μL . Solutions were prepared in methanol- d_4 or methanol- d_3 . The pressure tube was connected to the nhPHIP setup and inserted into an NMR spectrometer for measurements.²¹ nhPHIP experiments were carried out on an 800 MHz Bruker Avance III spectrometer equipped with a room temperature inverse probe or a cryogenically cooled probe. Hyperpolarized spectra were recorded at 25°C and 10°C using the SEPP pulse sequence for 1D and zero-quantum COSY for 2D measurements. Spectra were acquired similarly as described in ref. 21. A 500 MHz Agilent DD2 spectrometer was used for quality control of chemicals and synthesis products. Detailed descriptions of experimental procedures can be found in SI_nhPHIP.†

Computational methods

Geometry optimizations of the nhPHIP complexes with L-alanine and related oligopeptides were carried out using the PBE^{36,37} density functional with D2³⁸ empirical dispersion correction in implicit methanol solvent within IEFPCM³⁹ approximation. LANL2DZ^{40–42} basis set augmented with an f-exponent of 0.9380, along with respective ECP, was used for the Ir atom, while 6-311G(d,p)^{43,44} split-valence triple-zeta basis with the standard set of polarization functions was selected for atoms other than Ir. The similar computational protocol yielded mean absolute deviation of approximately 1.0 kcal mol^{-1} for the Gibbs free energies of Ir-catalyzed reactions.⁴⁵ Subsequently, the harmonic normal mode analysis, using the same level of theory, confirmed the true minima nature of all optimized structures on respective potential

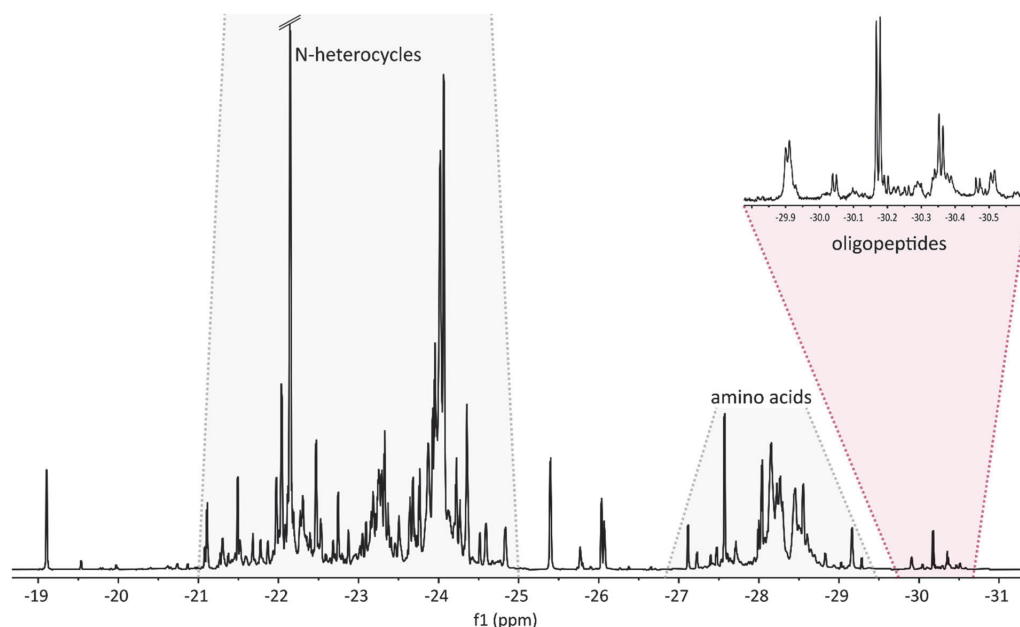


Fig. 8 nhPHP spectrum of a urine sample. Signal regions for amino acids and oligopeptides are annotated. H_A signals characteristic to oligopeptides appear in a distinct spectral region (around -30 ppm), whereas cosubstrate H_X signals are around -23 ppm, as expected for a hydride *trans* to an N-heterocycle. Spectrum was acquired from a whole urine sample, prepared as described by Ausmees *et al.*,¹⁵ heated at 50 °C for 7.5 min and recorded at 35 °C. nhPHP sample consisted of 3.1 mM IrImes catalyst, 63 mM 3F4MePy, and 30 μ L of concentrated urine sample in a total sample volume of 600 μ L.

energy surfaces. Energy corrections due to thermal degrees of freedom were evaluated at 298.15 K. For L-alanine, alternative single-point electronic energies were also calculated for respective optimized structures using second-order Douglas–Kroll–Hess scalar-relativistic Hamiltonian (DKH-2)^{46–49} and the corresponding all-electron TZP-DKH⁵⁰ basis set on the Ir atom while keeping all other parameters intact. Gaussian 16⁵¹ software package was used for all quantum chemical calculations. Further computational details are provided in SI_DFT.†

Conclusions

This work shows how underivatized alanine oligomer model compounds (di- to hexamer) bind to the Ir-Imes catalyst and give rise to sensitivity-enhanced nhPHP signals. These signals appear in a spectral region of -30 ppm and are clearly resolved from the densely populated regular 1H signals between 0 – 10 ppm. Moreover, the unique chemical shifts allow to distinguish oligopeptides from other known classes of nhPHP analytes like amino acids and N-heterocyclic compounds in complex biological mixtures.

Alanine oligopeptide nhPHP-catalyst complexes were studied by DFT calculations, revealing monodentate binding

by oligopeptide N-terminus and three bidentate binding configurations by simultaneous N- and O-binding in *ax* and *eq* positions. The structures of catalyst complexes are oligomer-specific and include either 5- or 8-membered cyclic structures, which are stabilized by intramolecular hydrogen bonding. The thermodynamically preferred 5-membered *ax*–*eq* complex of an alanine di- and trimer was characterized by NMR.

These results give insight into how the versatile Ir-Imes catalyst system, which has previously been used for detection of low molecular weight metabolites, can be extended to complex biological molecules with multiple binding sites. While the full scope of the approach has not been explored yet and extracting structural information about analytes from nhPHP signals remains challenging,²⁰ the work herein lays the basic concepts for expanding nhPHP to biopolymers, *e.g.*, for applications in non-residue specific short oligopeptides' detection in complex biological mixtures, *e.g.*, in urine.

Author contributions

NR carried out nhPHP and NMR measurements and data analysis. KA supervised synthesis of oligopeptides and [Ir(Cl)(COD)(Imes)]; characterized the iridium complexes. SV carried out synthesis of oligopeptides. AT and MU performed DFT cal-

culations and analyzed computational data. IR conceptualized the idea and supervised the project. The manuscript was written through contributions of all authors.

Conflicts of interest

There are no conflicts to declare.

Acknowledgements

We thank Dr Kati Helmja for HR-MS analysis. Quantum chemical calculations were in part carried out at the High-Performance Computing Center of the University of Tartu. We are grateful to Prof. Peeter Burk for assistance with Gaussian calculations.

The authors greatly appreciate funding from the Ministry of Education and Research, Republic of Estonia (Estonian Research Council grants PRG661 and PSG11), from the European Regional Development Fund (project TK134 "EQUiTANT") and from the Development Fund of the National Institute of Chemical Physics and Biophysics. We thank the Estonian Center of Analytical Chemistry (<https://www.akki.ee>, TT4) for their support.

References

- V. Apostolopoulos, J. Bojarska, T.-T. Chai, S. Elnagdy, K. Kaczmarek, J. Matsoukas, R. New, K. Parang, O. P. Lopez, H. Parhiz, C. O. Perera, M. Pickholz, M. Remko, M. Saviano, M. Skwarczynski, Y. Tang, W. M. Wolf, T. Yoshiya, J. Zabrocki, P. Zielenkiewicz, M. AlKhazindar, V. Barriga, K. Kelaidonis, E. M. Sarasia and I. Toth, *Molecules*, 2021, **26**, 430.
- M. E. K. Kraeling, W. Zhou, P. Wang and O. A. Ogunsola, *Cutaneous Ocul. Toxicol.*, 2015, **34**, 46–52.
- K. Fields, T. J. Falla, K. Rodan and L. Bush, *J. Cosmet. Dermatol.*, 2009, **8**, 8–13.
- I. Iwanov, A. Rossi, M. Montesi, I. Doytchinova, A. Sargsyan, G. Momekov, S. Panseri and E. Naydenova, *Eur. J. Pharm. Sci.*, 2022, **176**, 106249.
- Y. Ji, H. Qiao, J. He, W. Li, R. Chen, J. Wang, L. Wu, R. Hu, J. Duan and Z. Chen, *J. Drug Targeting*, 2017, **25**, 597–607.
- B. A. Palanski, N. Weng, L. Zhang, A. J. Hilmer, L. A. Fall, K. Swaminathan, B. Jabri, C. Sousa, N. Q. Fernandez-Becker, C. Khosla and J. E. Elias, *Nat. Commun.*, 2022, **13**, 888.
- A. Cerrato, S. E. Aita, A. L. Capriotti, C. Cavaliere, C. M. Montone, A. Laganà and S. Piovesana, *Talanta*, 2020, **219**, 121262.
- S. Piovesana, A. L. Capriotti, A. Cerrato, C. Crescenzi, G. La Barbera, A. Laganà, C. M. Montone and C. Cavaliere, *Anal. Chem.*, 2019, **91**, 11474–11481.
- C. M. Montone, A. L. Capriotti, A. Cerrato, M. Antonelli, G. La Barbera, S. Piovesana, A. Laganà and C. Cavaliere, *Anal. Bioanal. Chem.*, 2019, **411**, 3395–3404.
- K. V. Kovtunov, E. V. Pokochueva, O. G. Salnikov, S. F. Cousin, D. Kurzbach, B. Vuichoud, S. Jannin, E. Y. Chekmenev, B. M. Goodson, D. A. Barskiy and I. V. Koptug, *Chem. – Asian J.*, 2018, **13**, 1857–1871.
- S. Jannin, J.-N. Dumez, P. Giraudeau and D. Kurzbach, *J. Magn. Reson.*, 2019, **305**, 41–50.
- L. M. Epasto, K. Che, F. Kozak, A. Selimovic, P. Kaderavek and D. Kurzbach, *Sci. Adv.*, 2022, **8**, 5179.
- J. Hövener, A. N. Pravdivtsev, B. Kidd, C. R. Bowers, S. Glöggler, K. V. Kovtunov, M. Plaumann, R. Katz-Brull, K. Buckenmaier, A. Jerschow, F. Reineri, T. Theis, R. V. Shchepin, S. Wagner, P. Bhattacharya, N. M. Zacharias and E. Y. Chekmenev, *Angew. Chem., Int. Ed.*, 2018, **57**, 11140–11162.
- A. Dey, B. Charrier, E. Martineau, C. Deborde, E. Gandriaux, A. Moing, D. Jacob, D. Eshchenko, M. Schnell, R. Melzi, D. Kurzbach, M. Ceillier, Q. Chappuis, S. F. Cousin, J. G. Kempf, S. Jannin, J.-N. Dumez and P. Giraudeau, *Anal. Chem.*, 2020, **92**, 14867–14871.
- K. Ausmees, N. Reimets and I. Reile, *Chem. Commun.*, 2022, **58**, 463–466.
- M. Körner, G. Sauer, A. Heil, D. Nasu, M. Empting, D. Tietze, S. Voigt, H. Weidler, T. Gutmann, O. Avrutina, H. Kolmar, T. Ratajczyk and G. Buntkowsky, *Chem. Commun.*, 2013, **49**, 7839–7841.
- M. Fleckenstein, K. Herr, F. Theiß, S. Knecht, L. Wienands, M. Brodrecht, M. Reggelin and G. Buntkowsky, *Sci. Rep.*, 2022, **12**, 2337.
- T. Ratajczyk, T. Gutmann, P. Bernatowicz, G. Buntkowsky, J. Frydel and B. Fedorczyk, *Chem. – Eur. J.*, 2015, **21**, 12616–12619.
- T. Ratajczyk, G. Buntkowsky, T. Gutmann, B. Fedorczyk, A. Mames, M. Pietrzak, Z. Puzio and P. G. Szkudlarek, *ChemBioChem*, 2021, **22**, 855–860.
- R. Fraser, F. P. J. T. Rutjes, M. C. Feiters and M. Tessari, *Acc. Chem. Res.*, 2022, **55**, 1832–1844.
- N. Reimets, K. Ausmees, S. Vija and I. Reile, *Anal. Chem.*, 2021, **93**, 9480–9485.
- K. Ausmees, N. Reimets and I. Reile, *Molecules*, 2022, **27**, 802.
- L. Sellies, I. Reile, R. L. E. G. Aspers, M. C. Feiters, F. P. J. T. Rutjes and M. Tessari, *Chem. Commun.*, 2019, **55**, 7235–7238.
- I. Reile, N. Eshuis, N. K. J. Hermkens, B. J. A. van Weerdenburg, M. C. Feiters, F. P. J. T. Rutjes and M. Tessari, *Analyst*, 2016, **141**, 4001–4005.
- N. J. Wood, J. A. Brannigan, S. B. Duckett, S. L. Heath and J. Wagstaff, *J. Am. Chem. Soc.*, 2007, **129**, 11012–11013.
- N. K. J. Hermkens, N. Eshuis, B. J. A. van Weerdenburg, M. C. Feiters, F. P. J. T. Rutjes, S. S. Wijmenga and M. Tessari, *Anal. Chem.*, 2016, **88**, 3406–3412.
- L. Dreisewerd, R. L. E. G. Aspers, M. C. Feiters, F. P. J. T. Rutjes and M. Tessari, *J. Am. Chem. Soc.*, 2023, **145**, 1518–1523.

- 28 L. Sellies, R. L. E. G. Aspers, M. C. Feiters, F. P. J. T. Rutjes and M. Tessari, *Angew. Chem., Int. Ed.*, 2021, **60**, 26954–26959.
- 29 R. Hellinger, A. Sigurdsson, W. Wu, E. V. Romanova, L. Li, J. V. Sweedler, R. D. Süßmuth and C. W. Gruber, *Nat. Rev. Methods Primers*, 2023, **3**, 25.
- 30 P. J. Rayner, M. J. Burns, E. J. Fear and S. B. Duckett, *Magn. Reson. Chem.*, 2021, **59**, 1187–1198.
- 31 B. J. Tickner, J. S. Lewis, R. O. John, A. C. Whitwood and S. B. Duckett, *Dalton Trans.*, 2019, **48**, 15198–15206.
- 32 W. Iali, S. S. Roy, B. J. Tickner, F. Ahwal, A. J. Kennerley and S. B. Duckett, *Angew. Chem., Int. Ed.*, 2019, **58**, 10271–10275.
- 33 S. S. Roy, W. Iali, G. A. I. Moustafa and M. H. Levitt, *Chem. Commun.*, 2022, **58**, 2291–2294.
- 34 M. J. Bouma, R. L. E. G. Aspers, M. Tessari, F. P. J. T. Rutjes, R. Fraser and M. C. Feiters, *Eur. J. Inorg. Chem.*, 2023, **26**, e202300260.
- 35 N. Eshuis, R. L. E. G. Aspers, B. J. A. van Weerdenburg, M. C. Feiters, F. P. J. T. Rutjes, S. S. Wijmenga and M. Tessari, *Angew. Chem., Int. Ed.*, 2015, **54**, 14527–14530.
- 36 J. P. Perdew, K. Burke and M. Ernzerhof, *Phys. Rev. Lett.*, 1996, **77**, 3865–3868.
- 37 J. P. Perdew, K. Burke and M. Ernzerhof, *Phys. Rev. Lett.*, 1997, **78**, 1396–1396.
- 38 S. Grimme, *J. Comput. Chem.*, 2006, **27**, 1787–1799.
- 39 J. Tomasi, B. Mennucci and R. Cammi, *Chem. Rev.*, 2005, **105**, 2999–3094.
- 40 P. J. Dunning Jr. and T. H. Hay, *Modern Theoretical Chemistry*, Plenum, New York, 1977.
- 41 P. J. Hay and W. R. Wadt, *J. Chem. Phys.*, 1985, **82**, 299–310.
- 42 P. J. Hay and W. R. Wadt, *J. Chem. Phys.*, 1985, **82**, 270–283.
- 43 A. D. McLean and G. S. Chandler, *J. Chem. Phys.*, 1980, **72**, 5639–5648.
- 44 R. Krishnan, J. S. Binkley, R. Seeger and J. A. Pople, *J. Chem. Phys.*, 1980, **72**, 650–654.
- 45 K. H. Hopmann, *Organometallics*, 2016, **35**, 3795–3807.
- 46 M. Douglas and N. M. Kroll, *Ann. Phys.*, 1974, **82**, 89–155.
- 47 G. Jansen and B. A. Hess, *Phys. Rev. A*, 1989, **39**, 6017.
- 48 B. A. Hess, *Phys. Rev. A*, 1985, **32**, 756–763.
- 49 B. A. Hess, *Phys. Rev. A*, 1986, **33**, 3742–3748.
- 50 L. S. C. Martins, F. E. Jorge and S. F. Machado, *Mol. Phys.*, 2015, **113**, 3578–3586.
- 51 M. J. Frisch, G. W. Trucks, H. B. Schlegel, G. E. Scuseria, M. A. Robb, J. R. Cheeseman, G. Scalmani, V. Barone, G. A. Petersson, H. Nakatsuji, X. Li, M. Caricato, A. V. Marenich, J. Bloino, B. G. Janesko, R. Gomperts, B. Mennucci, H. P. Hratchian, J. V. Ortiz, A. F. Izmaylov, J. L. Sonnenberg, D. Williams-Young, F. L. F. Ding, F. Egidi, J. Goings, B. Peng, A. Petrone, T. Henderson, D. Ranasinghe, V. G. Zakrzewski, J. Gao, N. Rega, G. Zheng, W. Liang, M. H. M. Ehara, K. Toyota, R. Fukuda, J. Hasegawa, M. Ishida, T. Nakajima, Y. Honda, O. Kitao, H. Nakai, T. Vreven, K. Throssell, J. A. J. Montgomery, J. E. Peralta, F. Ogliaro, M. J. Bearpark, J. J. Heyd, E. N. Brothers, K. N. Kudin, V. N. Staroverov, T. A. Keith, R. Kobayashi, J. Normand, K. Raghavachari, A. P. Rendell, J. C. Burant, S. S. Iyengar, J. Tomasi, M. Cossi, J. M. Millam, M. Klene, C. Adamo, R. Cammi, J. W. Ochterski, R. L. Martin, K. Morokuma, O. Farkas, J. B. Foresman, D. J. Fox and I. Gaussian, *R. C. 01. Gaussian 16*, Wallingford CT, 2016.

Appendix 4

Publication IV

Ausmees, K.; Reimets, N.; Reile, I. Understanding Parahydrogen Hyperpolarized Urine Spectra: The Case of Adenosine Derivatives. *Molecules* 2022, 27 (3), 802. <https://doi.org/10.3390/MOLECULES27030802>

Communication

Understanding Parahydrogen Hyperpolarized Urine Spectra: The Case of Adenosine Derivatives

Kerti Ausmees [†] , Nele Reimets [†]  and Indrek Reile ^{*} 

National Institute of Chemical Physics and Biophysics, Akadeemia tee 23, 12618 Tallinn, Estonia; kerti.ausmees@kbfi.ee (K.A.); nele.reimets@kbfi.ee (N.R.)

^{*} Correspondence: indrek.reile@kbfi.ee; Tel.: +372-639-8325

[†] These authors contributed equally to this work.

Abstract: Parahydrogen hyperpolarization has emerged as a promising tool for sensitivity-enhanced NMR metabolomics. It allows resolution and quantification of NMR signals of certain classes of low-abundance metabolites that would otherwise be undetectable. Applications have been implemented in pharmacokinetics and doping drug detection, demonstrating the versatility of the technique. Yet, in order for the method to be adopted by the analytical community, certain limitations have to be understood and overcome. One such question is NMR signal assignment. At present, the only reliable way to establish the identity of an analyte that gives rise to certain parahydrogen hyperpolarized NMR signals is internal standard addition, which can be laborious. Herein we show that analogously to regular NMR metabolomics, generating libraries of hyperpolarized analyte signals is a viable way to address this limitation. We present hyperpolarized spectral data of adenosines and give an early example of identifying them from a urine sample with the small library. Doing so, we verify the detectability of a class of diagnostically valuable metabolites: adenosine and its derivatives, some of which are cancer biomarkers, and some are central to cellular energy management (e.g., ATP).

Keywords: parahydrogen; NMR; hyperpolarization; metabolomics; signal assignment; adenosines



Citation: Ausmees, K.; Reimets, N.; Reile, I. Understanding Parahydrogen Hyperpolarized Urine Spectra: The Case of Adenosine Derivatives. *Molecules* **2022**, *27*, 802. <https://doi.org/10.3390/molecules27030802>

Academic Editor: Danila Barskiy

Received: 31 December 2021

Accepted: 21 January 2022

Published: 26 January 2022

Publisher's Note: MDPI stays neutral with regard to jurisdictional claims in published maps and institutional affiliations.



Copyright: © 2022 by the authors. Licensee MDPI, Basel, Switzerland. This article is an open access article distributed under the terms and conditions of the Creative Commons Attribution (CC BY) license (<https://creativecommons.org/licenses/by/4.0/>).

1. Introduction

Nuclear Magnetic Resonance spectroscopy (NMR) is among the most successful analytical techniques for metabolomics research. NMR has found widespread application in the field due to its high reproducibility, quantitative nature, and the ability to provide relatively simple analyte identification by structural information embedded into NMR signals or comparison with spectral databases [1]. These strengths have allowed NMR metabolomics studies to be conducted in a vast array of research fields, ranging from food science to medical research and biomarker discovery. Yet, all applications are limited by the sensitivity of NMR, excluding the detection of a large and interesting part of the metabolome that appears below the NMR limit of detection (LOD) [2].

Nuclear hyperpolarization techniques have been developed to increase NMR sensitivity by generating non-Boltzmann nuclear polarization, thereby boosting sensitivity [3]. Out of several hyperpolarization techniques available, parahydrogen hyperpolarization has lately garnered attention in the analysis of biological fluids. In particular, the parahydrogen (pH_2) hyperpolarized chemosensing technique [4] has been used for the study of various biological mixtures such as flavor compounds in coffee extracts [4] and whiskey [5]. A modification of the technique has been demonstrated to work in SPE extracts of human urine [6] and in (almost) whole urine [7], allowing for the detection of endogenous urinary metabolites below the LOD of regular NMR.

1.1. Parahydrogen Hyperpolarized Chemosensing

Instead of directly measuring NMR signals of analytes **1** (Figure 1), hyperpolarized chemosensing relies on the ability of **1** to reversibly bind to an iridium-based catalyst **2**.

Upon binding, complex **3** is formed that presents two pH_2 sourced hydride signals' doublets (Figure 1) at the $-20 \dots -30$ ppm region. Chemical shifts of complex **3** hydride resonances are characteristic to each analyte **1** and function as their chemosensors [4]. Intensities of the hydride signals are up to 1000-fold enhanced [6] and the atypical detection region allows for the separation of hyperpolarized dilute analyte signals from the more abundant not-catalyst-interacting analytes. However, it also gives rise to three limitations: analyte scope, quantification, and signal assignment.

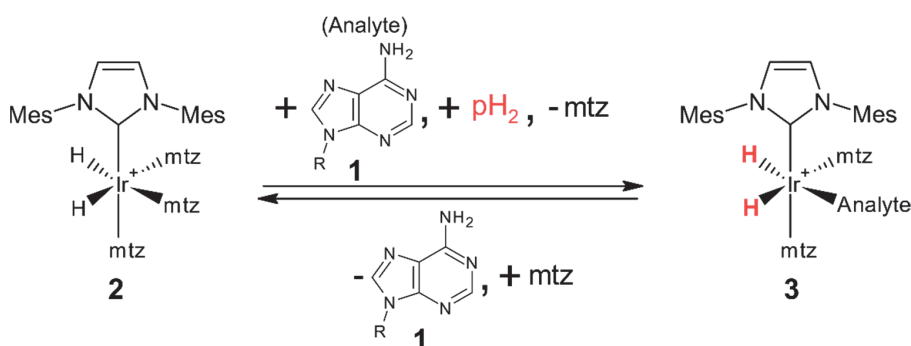


Figure 1. The principle of chemosensing by pH_2 -induced hyperpolarization [4]. Complexes **3** are transient in nature, which is necessary for the incorporation of a new analyte and fresh pH_2 . Mes denotes 1,3,5-trimethylphenyl group, known as mesityl group; *mtz* denotes 1-methyl-1,2,3-triazol.

Analyte scope of the method is limited by its chemoselectivity, making it less universal than traditional NMR as it detects only analytes capable of binding to **2**. Yet, chemoselectivity can also be viewed as a strength—the method enhances signals which would otherwise be undetectable and enables the resolution of their hydride resonances in the atypical $-20 \dots -30$ ppm region instead of the crowded $0 \dots 10$ ppm region [4]. Furthermore, the complexity of published hyperpolarized urine spectra [6–9] demonstrates that even the catalyst's limited chemical scope allows for the detection of large numbers of metabolites. The list of known **2** binding analytes is growing and includes, on top of nitrogenous heteroaromatics, pyruvate [10], tagged oligopeptides [11,12], amino acids [13,14], nitriles [15], and sulfur heteroaromatics [16], suggesting the chemoselectivity envelope is wide.

The method is not quantitative in the same way as traditional 1H NMR, since multi-pulse NMR detection schemes and analyte-specific complex **3** dissociation kinetics [17], hydrogen exchange rate and relaxation [18] properties are involved. However, similarly to regular 2D NMR [19], quantification can be achieved by analyte-specific calibration curves [4–9,13]. When exact values are not necessary, concentrations can be estimated by comparison of signals representing chemically similar analytes [13].

Signal assignment is arguably the most notable limitation hindering wider adoption of the technique. Since hydride signals do not carry as much structural information as traditional NMR, the only reliable way of assigning signals has proven to be internal standard addition [4,7,9]. The most practical pulse sequence for hyperpolarized chemosensing [6], which can also be carried out as very fast experiments [20], resolves hydride signals (red in Figure 1) according to their mutual zero quantum (ZQ) frequency in the indirect dimension of 2D spectra. Signals of structurally similar analytes have been found to form linear patterns in the 2D ZQ plots ([6] and Figure 2). These patterns aid identification [6,9] but the physical explanation for their formation has not been described yet.

Notably, chemical shifts of hydride signals of different complexes **3** have proven to be largely identical in methanolic urine samples and in simple methanol solutions [7]. Consequently, it should be feasible to compile libraries of analyte signals, which could be applied for signal assignment in complex samples. Herein we present our work on compiling

the first such library by establishing a group of valuable metabolites, rationalizing their interactions with a catalyst **2** and applying the small initial library to a biofluid derived sample. We suggest this work presents a practical workflow for understanding complex hyperpolarized spectra and for developing new applications.

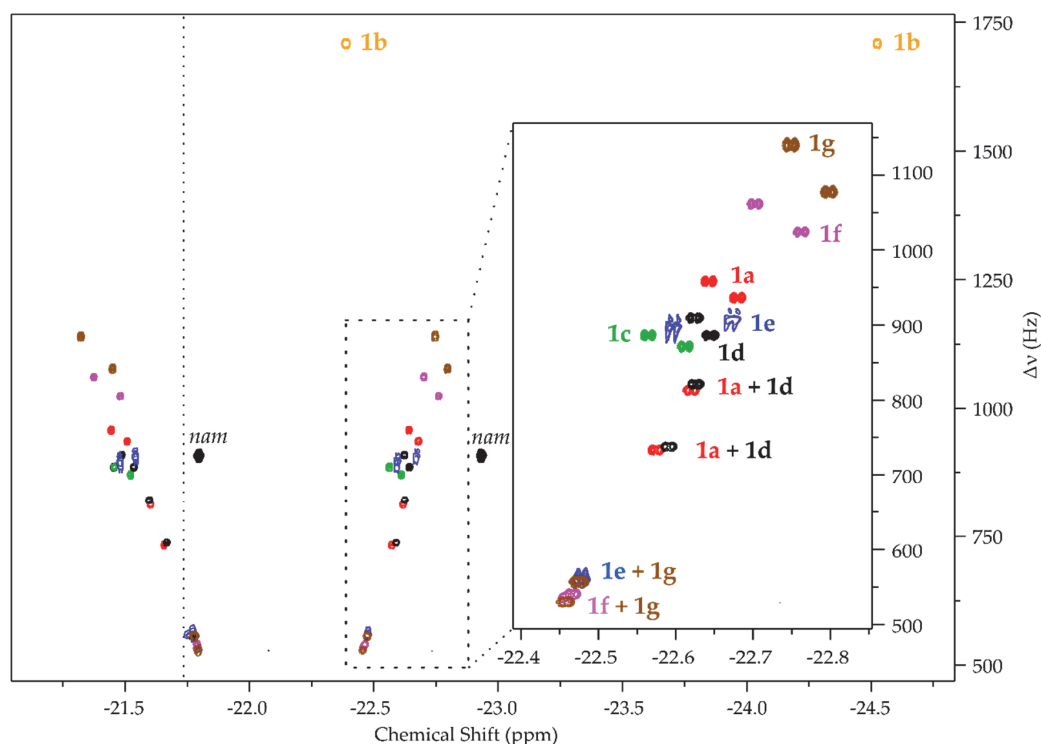


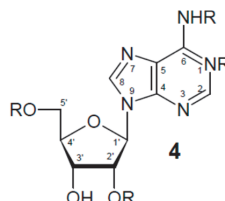
Figure 2. Hyperpolarized 2D ZQ spectra [6] of the adenosines' library. Spectra of all compounds have been recorded separately, referenced to *nam* signal (using -22.935 ppm for right hand hydride signal [6]) and superimposed. For clarity, all hydride signals for a certain compound are presented in the same color, although the doublet pairs are detected in opposite phase. All analytes (**1a–1g**) present at least two clearly resolved signal pairs. The dominating signal of complex **2** (dotted line at -21.74 ppm, see Figure S1 Supplementary Materials) was omitted from the spectra by convolution filtering. See Figure S2 for hyperpolarized hydrides' 1D spectra of all analytes and Table S1 for chemical shifts of hydride signals.

1.2. Analytical Value of Adenosine Derivatives

Adenine, the nitrogenous base of adenosine, was among the first biological analytes detected by its iridium-bound derivative's hydride signals [21], suggesting that the study of its different modifications should be feasible. Adenosine has been hyperpolarized by **2** in a SABRE experiment [22], and adenosine detection by hyperpolarized chemosensing has been demonstrated in urine SPE extracts [6] and minimally altered urine [7]. In terms of (bio)analytical utility, the concentrations of adenosine and its methylated derivatives in urine correlate to increased protein turnover in several pathological processes [23], including tumors [24]. The urine of cancer patients is expected to contain elevated concentrations of methylated adenosines [25], such as 1-methyladenosine **1b** (Table 1). N6-methyladenosine **1c** and 2'-O-methyladenosine **1d** have been suggested as cancer biomarkers [26,27] that increase in correlation to tumor size [28]. Urinary concen-

tration of these analytes is in the sub- to low- μM region [29], excluding their detection by regular NMR and rendering them attractive targets for methodology development.

Table 1. Adenosines used in the study.



Analyte	No	R @ 1	R @ 6	R @ 2'	R @ 5'
Adenosine	1a	H	H	H	H
1-Methyladenosine *	1b	CH ₃	H	H	H
6N-Methyladenosine	1c	H	CH ₃	H	H
2'-O-Methyladenosine	1d	H	H	CH ₃	H
AMP	1e	H	H	H	PO ₃ H
ADP	1f	H	H	H	PO ₃ -PO ₃ H
ATP	1g	H	H	H	PO ₃ -PO ₃ -PO ₃ H

* **1b** likely adopts the neutral imino conformer structure in methanol (see Figure S4).

Phosphorylated adenosines (AMP, ADP, and ATP), on the other hand, form the central pinnacle of cellular energy metabolism. While AMP and ADP are also present in urine in low concentrations [29], the more attractive analytical utility of all three may lie in bioenergetics research, uncovering the mechanisms of chemical energy production, and utilization in healthy and malignant cells [30]. ³¹P NMR has traditionally been used for the selective detection of such phosphometabolites in complex cellular extracts, but the lower sensitivity of ³¹P NMR, in combination with the low concentrations of such analytes, has required extensive acquisition times [31]. The detection and resolution of such analytes by hyperpolarized chemosensing would present a further practical application.

2. Results

Building the Library

Our strategy consisted of recording the hyperpolarized hydride spectra of a series of adenosine derivatives to confirm if the chemical modification of an analyte relatively far away from its catalyst binding site would incur detectable differences on hydride chemical shifts. Data acquired for this purpose would also comprise the initial small library that can be used to assign signals in biological samples. According to Wood et al., adenine binds iridium from its 1-, 3- and 9-positions [21] of the purine structure (see structure in Table 1). It can be assumed that adenosine also binds **2** via its nitrogenous base. However, the 9-position is occupied by the ribose moiety in adenosine, leaving only two sites accessible.

The test system used for evaluating a series of adenosine derivatives **1a–1g** (Table 1) consisted of typical concentrations of the catalyst and cosubstrate (1.2 mM of **2**, 18-fold excess of *mtz* over iridium) [9], 100 μM of an analyte, and 20 μM of nicotinamide (*nam*). A relatively high analyte concentration was chosen for the convenient detection of the analyte in good SNR conditions and *nam* was used as the internal reference for hydride chemical shifts. Adenosine **1a** has been observed previously to give rise to four pairs of hydride signals [6], which was also seen herein (Figures 2 and S2). Since the catalytic center of **2** is prochiral, it forms two diastereomers upon coordination to a chiral analyte (see discussion in SI of ref. [13]). As **1a** has two possible binding sites, the expected number of hydride signals is doubled, yielding four pairs of signals.

The four pairs of hydride resonances of **1a** complex were two- to three-fold less intense than the signals corresponding to five-fold less concentrated *nam* (Figure S1), since **1a** is distributed among four diastereomeric complexes, whereas all of catalyst bound *nam* (achiral, single binding site) contributes to a single pair of hydride signals. Moreover, the detection conditions (e.g., **2** and *mtz* concentration, sample temperature) may be less optimal for **1a** as hyperpolarization efficiencies are likely to be different due to differences in analyte and hydrogen exchange and relaxation parameters associated with either analyte. Importantly, hydride signal integrals for analytes **1a–1d** and **1e–1g** were found to deviate two-fold within the two groups of similar analytes (e.g., among **1a–1d** and **1e–1g**). Between the groups, the largest signal **1a** and weakest **1f** deviated by five-fold. This suggests that approximate quantification of similar adenosines can be carried out by comparing their signals.

In comparison to **1a**, the 2'-O-methylated **1d** gave the most similar signal response, yielding a pattern of four pairs of hydride signals that are slightly shifted (Figure 2). This proves that modification of an analyte relatively far away from the binding site manifests detectable influences on hydride signals. Although half of the hydride signals corresponding to **1a** and **1d** partially overlap, others are well-resolved. N6-methylated **1c**, on the other hand, gives only two signal responses [6], presumably because N6-methylation inhibits N1 binding due to added nearby steric bulk. Confirming the actual binding regimes, however, remains the subject for future work.

N1-methylated **1b** gives the most unexpected spectral pattern, which has also been observed before [6,7]: it seems to give rise to just a single pair of hydride signals that are noticeably shifted in the spectrum. These two signals, upon closer observation, have some internal structure (Figure S3), suggesting that they may be due to two closely overlapping diastereomers. That would explain the number of signals, since one of the catalyst binding sites (N1) is blocked for **1b**, but not their chemical shifts. It is known that N1-methylation of adenine base [32,33] forces it to adopt a different tautomeric (imine) form (Figure S4) and strongly affects its basicity [34]. We suggest this is the reason for the noticeable difference of their catalyst complex hydride chemical shifts, although the exact active catalyst binding site remains unknown.

In the bioenergetics application scenario, detection and resolution of adenosine, AMP, ADP, and ATP is required. It was found that modification of adenosine with different numbers of phosphate groups at its most distant 5'-O-position rendered all four resolvable by their catalyst complex hydride signals. Unlike for **1a**, two of the four diastereomeric complex hydride signal pairs overlap totally for **1e** (AMP; Figures 2 and S5) and partially for **1f** (ADP) and **1g** (ATP; Figures 2 and S5). The same signals also overlap among all three, but the other hydride signal pairs are well-resolved. Unlike for any other analyte, **1e** signals were found to be of irregular shape on the 2D ZQ spectrum. This was caused by a change in hydride signal chemical shifts during 2D acquisition (see comparison of 1D hydride spectra at sample preparation and 1.5 h later in Figure S6). Since *nam* signals remain at the same frequency, we suggest that this change is not caused by processes interfering with the catalyst or *mtz*, but may be the result of gradual deuteration of the analyte during acquisition. A similar process was observed for pyridine by Sellies et al. [13] with similar magnitude changes to the chemical shifts occurring (here 11.5 Hz for the rightmost doublet).

3. Discussion

The acquired information can be used for signal assignment when hydride spectral database is superimposed onto complex spectra of biofluids (Figure 3). That way, signals of compounds in the database could be easily recognized. Herein, this was tested on a urine SPE extract, which was prepared with an SPE protocol modified from previous work [8].

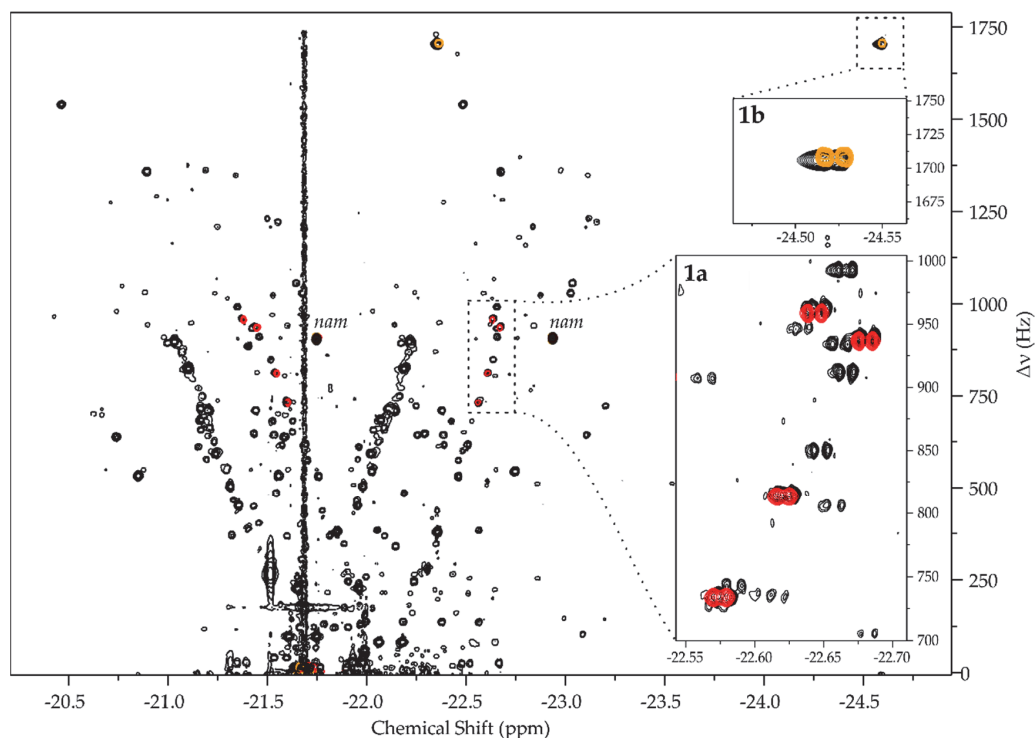


Figure 3. Hyperpolarized 2D ZQ spectrum of urine SPE extract overlaid with spectra of (**1a**) (red) and (**1b**) (beige), referenced to *nam* signal (using -22.935 ppm for right hand hydride signal [6]). All hydride signals of the same analyte are presented in the same color, although the doublet pairs are detected in opposite phase [6].

Since the protocol was directed toward the extraction of apolar to mildly polar analytes, the detection of phosphonucleotides **1e**, **1f**, and **1g** was not expected. The retention of other tested analytes was possible, considering **1a–1c** were identified by spiking in a similarly prepared SPE extract [6]. Overlaying the database and the experimental spectrum demonstrated an overlap of signals from **1a** and **1b**, whereas at the expected locations of **1c** and **1d**, SNR was too weak to confirm the analytes.

The inability to detect **1c** and **1d** may have been caused by two factors. Firstly, the particular urine sample was obtained from a healthy non-smoking volunteer without any known underlying disease. The lack of medical conditions that are expected to increase urinary methylated adenosine concentrations is likely to contribute to their low abundance in the tested sample. There are alternative SPE procedures that would provide more effective retention of adenosines by covalent bonding to the ribose *cis*-diol moiety [35], if detection of the less abundant derivatives is desired.

Secondly, since the work was aimed toward verifying the resolution of the analytes and confirming the applicability of the concept of libraries, maximum sensitivity was not a priority. Consequently, all spectra were acquired with 50% pH_2 and without a cryoprobe, which has been commonly applied in prior instances of hyperpolarized chemosensing in urine samples [6–9,13]. A cryoprobe would further increase sensitivity by three- to four-fold [36], while increasing pH_2 enrichment to 100% would result in an additional threefold increase [37]. Hence, an order of magnitude sensitivity increase would be available by upgrading both the pH_2 source and the NMR probe.

All things considered, the ability to assign low- μ M **1a** and **1b** on a room temperature probe by library overlap is a positive result that demonstrates the feasibility of the

strategy. Moreover, measured chemical shifts of **1a**, **1b**, and **1c** hydride signals coincide with an earlier report [6], suggesting that such libraries would have universality over different instrumentation and different SPE sample preparation procedures. Hereby we have demonstrated the following concepts:

- $p\text{H}_2$ hyperpolarized chemosensing is remarkably sensitive to relatively small changes in analyte structure, allowing for the resolution of series of structurally highly similar metabolites, including closely related isomers (i.e., **1b**, **1c**, **1d**).
- Libraries (Table S1) can be built for the assignment of specific families of metabolites. With a few exceptions (e.g., **1b**), the observation of Sellies et al. [6] that signals of similar analytes form linear patterns in the ZQ spectra holds.
- Libraries can be applied by a straightforward superposition of experimental and database spectra.
- The databases would have universality across different instruments, laboratories, and variations in sample preparation procedures.

This work adds to the $p\text{H}_2$ hyperpolarization toolbox, presenting a strategy for understanding the complex hydride spectra from the parahydrogen hyperpolarized chemosensing experiment. Building practical applications by using the spectral data provided herein, and adding to this data, will be the focus of our future work.

4. Materials and Methods

NMR experiments were conducted at sample temperature of 25 °C on an 800 MHz Bruker Avance III spectrometer equipped with a 5 mm TXI probe. Hyperpolarization was carried out in 5 mm Norell S-5-500-IPV-7 pressure tubes with a previously described hyperpolarization setup [9]. $p\text{H}_2$ was prepared in flow, as described previously [9]. Hyperpolarized 1D SEPP spectra (Figures S1–S3, S5 and S6) and hyperpolarized 2D ZQ spectra (Figures 2 and 3) were acquired with previously published pulse sequences [6], utilizing high power hard pulses and shaped *reburp* pulses that covered all signals of interest. One-dimensional spectra were acquired in 64 scans. Two-dimensional data were acquired in 320 increments over 2500 Hz in f_1 , except for **1b** and urine SPE extract, for which 512 increments were acquired over 3500 Hz spectral width. Two scans per increment were acquired in all cases. Processing was done following earlier described principles [6,9] with Mestrenova 14.2 software.

Waters Oasis HLB® 6 mL / 200 mg cartridges were used for solid phase extraction (SPE). Methanol used to activate the cartridges was obtained from Honeywell Riedel-de Haën™. Analytes were eluted with, and experiments were conducted in, methanol- d_4 obtained from Deutero GmbH. 1-methyladenosine was acquired from Cayman Chemicals. Nicotinamide and adenosine were acquired from TCI Chemicals. N6-methyladenosine and 2'-O-methyladenosine were acquired from Carbosynth. AMP, ADP, and ATP were obtained from Sigma Aldrich. All chemicals were used as supplied. Catalyst **2** precursor [Ir(Cl)(COD)(Imes)] and cosubstrate 1-methyl-1,2,3-triazol (*mtz*) were synthesized in-house by the same methods [6,7,9] as previously described.

1 . . . 2 mM stock solutions of all analytes in methanol- d_4 were prepared gravimetrically. NMR samples were prepared by adding 150 μL of 4.8 mM solution of [Ir(Cl)(COD)(Imes)], 13 μL of 1 M stock solution of *mtz*, and 37 μL of methanol- d_4 to a pressure tube, pressurizing the sample under 5 bar of H_2 , shaking the tube and allowing the catalyst to convert to its active form **2** in 2 h. Then, appropriate amounts of analyte stock solutions and methanol- d_4 were added to reach 1.2 mM concentration of **2**, 20 μM of *nam* and 100 μM of the particular analyte in 600 μL of total sample volume. The tube was connected to the hyperpolarization setup [9] for NMR experiments.

A urine sample was collected from a healthy non-smoking volunteer as morning first midstream urine and frozen at -80°C . Prior to analysis, the sample was thawed over a room temperature water bath, pH-adjusted to 8.0 with 1 M NaOH and centrifuged for 12 min at $1825\times g$. SPE of the resulting urine sample was carried out by activating the SPE cartridge with 5 mL of methanol, conditioning it with 3 mL of 10 mM pH 8.0

phosphate buffer., loading 5 mL of urine and eluting it by light nitrogen overpressure above the cartridge (approx. 2–3 mL/min). The cartridge was washed with 3 mL of 10 mM pH 8.0 phosphate buffer and dried for 30 min with a nitrogen flow generated by 1 bar N₂ overpressure above the cartridge. Finally, analytes were eluted by adding 1.2 mL of methanol-d₄, which yielded approximately 800 µL of extract. For hyperpolarization experiments, 450 µL of the extract was mixed with the preactivated solution of **2** and *mtz* (1.2 mM final concentration of **2**, 18-fold excess of *mtz*).

Supplementary Materials: The following supporting information is available online, Figure S1: Hyperpolarized 1D hydride spectrum of adenosine **1a** sample; Figure S2: Hyperpolarized 1D spectra of the hydride spectral regions of the same samples as main text Figure 2; Figure S3: The structure of **1b** hydride signals; Figure S4: 1-Methyladenosine **1b** neutral iminium tautomer; Figure S5: Comparison of 1D hydride spectra of AMP (**1e**), ADP (**1f**) and ATP (**1g**); Figure S6: 1D hyperpolarized hydride spectra of the same **1e** containing sample within minutes from preparing the sample (red) and 1 h later (black); Table S1: Library of hydride chemical shifts of complexes **3** for adenosine derivatives **1**.

Author Contributions: Conceptualization, I.R.; methodology, K.A., N.R. and I.R.; investigation, K.A., N.R. and I.R.; writing—original draft preparation, I.R.; writing—review and editing, K.A. and N.R.; funding acquisition, K.A. and I.R. All authors have read and agreed to the published version of the manuscript.

Funding: This research was funded by the Estonian Research Council, grant number PSG11, and the Archimedes Foundation, Center of Excellence project TK134.

Institutional Review Board Statement: Urine sample handling was approved by the Estonian Research Ethics Committee of the National Institute for Health Development of Estonia (Decision No. 686). Urine sample used in this study was donated by a healthy adult (37 years of age). Excess urine sample material was discarded in accordance with local regulations on handling human-derived samples.

Informed Consent Statement: Informed consent was obtained from all subjects involved in the study.

Data Availability Statement: The data presented in this study are openly available in Mendeley Data at 10.17632/3cwx4d472.1.

Conflicts of Interest: The authors declare no conflict of interest.

Sample Availability: Compounds **1a–1g** and *nam* were acquired commercially. Samples of catalyst **2** precursor [Ir(Cl)(COD)(Imes)] and cosubstrate 1-methyl-1,2,3-triazol (*mtz*) are available from the authors.

References

- Emwas, A.-H.M.; Salek, R.M.; Griffin, J.L.; Merzaban, J. NMR-based metabolomics in human disease diagnosis: Applications, limitations, and recommendations. *Metabolomics* **2013**, *9*, 1048–1072. [\[CrossRef\]](#)
- Markley, J.L.; Brüschweiler, R.; Edison, A.S.; Eghbalnia, H.R.; Powers, R.; Raftery, D.; Wishart, D.S. The future of NMR-based metabolomics. *Curr. Opin. Biotechnol.* **2017**, *43*, 34–40. [\[CrossRef\]](#) [\[PubMed\]](#)
- Kovtunov, K.V.; Pokochueva, E.V.; Salnikov, O.G.; Cousin, S.F.; Kurzbach, D.; Vuichoud, B.; Jannin, S.; Chekmenev, E.Y.; Goodson, B.M.; Barskiy, D.A.; et al. Hyperpolarized NMR Spectroscopy: D-DNP, PHIP, and SABRE Techniques. *Chem.-Asian J.* **2018**, *13*, 1857–1871. [\[CrossRef\]](#) [\[PubMed\]](#)
- Hermkens, N.K.J.; Eshuis, N.; van Weerdenburg, B.J.A.; Feiters, M.C.; Rutjes, F.P.J.T.; Wijmenga, S.S.; Tessari, M. NMR-Based Chemosensing via *p*-H₂ Hyperpolarization: Application to Natural Extracts. *Anal. Chem.* **2016**, *88*, 3406–3412. [\[CrossRef\]](#)
- Hermkens, N.K.J.; Aspers, R.L.E.G.; Feiters, M.C.; Rutjes, F.P.J.T.; Tessari, M. Trace analysis in water-alcohol mixtures by continuous *p*-H₂ hyperpolarization at high magnetic field. *Magn. Reson. Chem.* **2018**, *56*, 633–640. [\[CrossRef\]](#)
- Sellies, L.; Reile, I.; Aspers, R.L.E.G.; Feiters, M.C.; Rutjes, F.P.J.T.; Tessari, M. Parahydrogen induced hyperpolarization provides a tool for NMR metabolomics at nanomolar concentrations. *Chem. Commun.* **2019**, *55*, 7235–7238. [\[CrossRef\]](#)
- Ausmees, K.; Reimets, N.; Reile, I. Parahydrogen hyperpolarization of minimally altered urine samples for sensitivity enhanced NMR metabolomics. *Chem. Commun.* **2022**, *58*, 463–466. [\[CrossRef\]](#)
- Reile, I.; Eshuis, N.; Hermkens, N.K.J.; van Weerdenburg, B.J.A.; Feiters, M.C.; Rutjes, F.P.J.T.; Tessari, M. NMR detection in biofluid extracts at sub-µM concentrations via *para*-H₂ induced hyperpolarization. *Analyst* **2016**, *141*, 4001–4005. [\[CrossRef\]](#)
- Reimets, N.; Ausmees, K.; Vija, S.; Reile, I. Developing Analytical Applications for Parahydrogen Hyperpolarization: Urinary Elimination Pharmacokinetics of Nicotine. *Anal. Chem.* **2021**, *93*, 9480–9485. [\[CrossRef\]](#)

10. Adelabu, I.; TomHon, P.; Kabir, M.S.H.; Nantogma, S.; Abdulmojeed, M.; Mandzhieva, I.; Ettedgui, J.; Swenson, R.E.; Krishna, M.C.; Goodson, B.M.; et al. Order-Unity ^{13}C Nuclear Polarization of $[1\text{-}^{13}\text{C}]$ Pyruvate in Seconds and the Interplay of Water and SABRE Enhancement. *ChemPhysChem* **2022**, *23*, e202100839. [[CrossRef](#)]
11. Ratajczyk, T.; Gutmann, T.; Bernatowicz, P.; Buntkowsky, G.; Frydel, J.; Fedorczyk, B. NMR Signal Enhancement by Effective SABRE Labeling of Oligopeptides. *Chem.-Eur. J.* **2015**, *21*, 12616–12619. [[CrossRef](#)] [[PubMed](#)]
12. Ratajczyk, T.; Buntkowsky, G.; Gutmann, T.; Fedorczyk, B.; Mames, A.; Pietrzak, M.; Puzio, Z.; Szkudlarek, P.G. Magnetic Resonance Signal Amplification by Reversible Exchange of Selective PyFALGEA Oligopeptide Ligands Towards Epidermal Growth Factor Receptors. *ChemBioChem* **2021**, *22*, 855–860. [[CrossRef](#)] [[PubMed](#)]
13. Sellies, L.; Aspers, R.L.E.G.; Feiters, M.C.; Rutjes, F.P.J.T.; Tessari, M. Parahydrogen Hyperpolarization Allows Direct NMR Detection of α -Amino Acids in Complex (Bio)mixtures. *Angew. Chem. Int. Ed.* **2021**, *60*, 26954–26959. [[CrossRef](#)] [[PubMed](#)]
14. Pravdivtsev, A.N.; Buntkowsky, G.; Duckett, S.B.; Koptuyg, I.V.; Hövener, J.-B. Parahydrogen-Induced Polarization of Amino Acids. *Angew. Chem. Int. Ed.* **2021**, *60*, 23496–23507. [[CrossRef](#)]
15. Kim, S.; Min, S.; Chae, H.; Jeong, H.J.; Namgoong, S.K.; Oh, S.; Jeong, K. Hyperpolarization of Nitrile Compounds Using Signal Amplification by Reversible Exchange. *Molecules* **2020**, *25*, 3347. [[CrossRef](#)]
16. Shchepin, R.V.; Barskiy, D.A.; Coffey, A.M.; Goodson, B.M.; Chekmenev, E.Y. NMR Signal Amplification by Reversible Exchange of Sulfur-Heterocyclic Compounds Found In Petroleum. *ChemistrySelect* **2016**, *1*, 2552–2555. [[CrossRef](#)]
17. Hermkens, N.K.J.; Feiters, M.C.; Rutjes, F.P.J.T.; Wijmenga, S.S.; Tessari, M. High field hyperpolarization-EXSY experiment for fast determination of dissociation rates in SABRE complexes. *J. Magn. Reson.* **2017**, *276*, 122–127. [[CrossRef](#)]
18. Sellies, L.; Aspers, R.L.E.G.; Tessari, M. Determination of hydrogen exchange and relaxation parameters in PHIP complexes at micromolar concentrations. *Magn. Reson.* **2021**, *2*, 331–340. [[CrossRef](#)]
19. Giraudeau, P. Quantitative 2D liquid-state NMR. *Magn. Reson. Chem.* **2014**, *52*, 259–272. [[CrossRef](#)]
20. Aspers, R.L.E.G.; Tessari, M. An approach to fast 2D nuclear magnetic resonance at low concentration based on $p\text{-H}_2$ -induced polarization and nonuniform sampling. *Magn. Reson. Chem.* **2021**, *59*, 1236–1243. [[CrossRef](#)]
21. Wood, N.J.; Brannigan, J.A.; Duckett, S.B.; Heath, S.L.; Wagstaff, J. Detection of Picomole Amounts of Biological Substrates by para -Hydrogen-Enhanced NMR Methods in Conjunction with a Suitable Receptor Complex. *J. Am. Chem. Soc.* **2007**, *129*, 11012–11013. [[CrossRef](#)] [[PubMed](#)]
22. Hövener, J.-B.; Schwaderlapp, N.; Lickert, T.; Duckett, S.B.; Mewis, R.E.; Highton, L.A.R.; Kenny, S.M.; Green, G.G.R.; Leibfritz, D.; Korvink, J.G.; et al. A hyperpolarized equilibrium for magnetic resonance. *Nat. Commun.* **2013**, *4*, 2946. [[CrossRef](#)] [[PubMed](#)]
23. Seidel, A.; Brunner, S.; Seidel, P.; Fritz, G.I.; Herbarth, O. Modified nucleosides: An accurate tumour marker for clinical diagnosis of cancer, early detection and therapy control. *Br. J. Cancer* **2006**, *94*, 1726–1733. [[CrossRef](#)] [[PubMed](#)]
24. Patejko, M.; Struck-Lewicka, W.; Siluk, D.; Waszczuk-Jankowska, M.; Markuszewski, M.J. Urinary Nucleosides and Deoxynucleosides. In *Advances in Clinical Chemistry*; Elsevier: Amsterdam, The Netherlands, 2018; Volume 83, pp. 1–51. ISBN 9780128152072.
25. Struck, W.; Siluk, D.; Yumba-Mpanga, A.; Markuszewski, M.; Kaliszan, R.; Markuszewski, M.J. Liquid chromatography tandem mass spectrometry study of urinary nucleosides as potential cancer markers. *J. Chromatogr. A* **2013**, *1283*, 122–131. [[CrossRef](#)] [[PubMed](#)]
26. Hsu, W.-Y.; Chen, C.-J.; Huang, Y.-C.; Tsai, F.-J.; Jeng, L.-B.; Lai, C.-C. Urinary Nucleosides as Biomarkers of Breast, Colon, Lung, and Gastric Cancer in Taiwanese. *PLoS ONE* **2013**, *8*, e81701. [[CrossRef](#)]
27. Seidel, A.; Seidel, P.; Manuwald, O.; Herbarth, O. Modified nucleosides as biomarkers for early cancer diagnose in exposed populations. *Environ. Toxicol.* **2015**, *30*, 956–967. [[CrossRef](#)]
28. Altobelli, E.; Angeletti, P.M.; Latella, G. Role of Urinary Biomarkers in the Diagnosis of Adenoma and Colorectal Cancer: A Systematic Review and Meta-Analysis. *J. Cancer* **2016**, *7*, 1984–2004. [[CrossRef](#)]
29. Bouatra, S.; Aziat, F.; Mandal, R.; Guo, A.C.; Wilson, M.R.; Knox, C.; Bjorn Dahl, T.C.; Krishnamurthy, R.; Saleem, F.; Liu, P.; et al. The human urine metabolome. *PLoS ONE* **2013**, *8*, e73076. [[CrossRef](#)]
30. Pavlova, N.N.; Thompson, C.B. The Emerging Hallmarks of Cancer Metabolism. *Cell Metab.* **2016**, *23*, 27–47. [[CrossRef](#)]
31. Pucar, D.; Dzeja, P.P.; Bast, P.; Gumina, R.J.; Drahl, C.; Lim, L.; Juranic, N.; Macura, S.; Terzic, A. Mapping hypoxia-induced bioenergetic rearrangements and metabolic signaling by ^{18}O -assisted ^{31}P NMR and ^1H NMR spectroscopy. *Mol. Cell. Biochem.* **2004**, *256*, 281–289. [[CrossRef](#)]
32. Dreyfus, M.; Dodin, G.; Bensauade, O.; Dubois, J.E. Tautomerism of purines. 2. Amino-imino tautomerism in 1-alkyladenines. *J. Am. Chem. Soc.* **1977**, *99*, 7027–7037. [[CrossRef](#)]
33. Lippert, B.; Schöllhorn, H.; Thewalt, U. Metal-stabilized rare tautomers of nucleobases. 4. on the question of adenine tautomerization by a coordinated platinum(II). *Inorg. Chim. Acta* **1992**, *198–200*, 723–732. [[CrossRef](#)]
34. Kapinos, L.E.; Opershall, B.P.; Larsen, E.; Sigel, H. Understanding the Acid-Base Properties of Adenosine: The Intrinsic Basicities of N1, N3 and N7. *Chem.-Eur. J.* **2011**, *17*, 8156–8164. [[CrossRef](#)]
35. Lu, Z.; Wang, Q.; Wang, M.; Fu, S.; Zhang, Q.; Zhang, Z.; Zhao, H.; Liu, Y.; Huang, Z.; Xie, Z.; et al. Using UHPLC Q-Trap/MS as a complementary technique to in-depth mine UPLC Q-TOF/MS data for identifying modified nucleosides in urine. *J. Chromatogr. B* **2017**, *1051*, 108–117. [[CrossRef](#)]
36. Kovacs, H.; Moskau, D.; Spraul, M. Cryogenically cooled probes—A leap in NMR technology. *Prog. Nucl. Magn. Reson. Spectrosc.* **2005**, *46*, 131–155. [[CrossRef](#)]
37. Natterer, J.; Bargon, J. Parahydrogen induced polarization. *Prog. Nucl. Magn. Reson. Spectrosc.* **1997**, *31*, 293–315. [[CrossRef](#)]

Appendix 5

Publication V

Reimets, N.; Ausmees, K.; Reile, I. Current State of the Art of Analyte Scope in Urine Metabolome Analysis by Non-Hydrogenative PHIP. *Journal of Magnetic Resonance Open*, 2024, 21, 100171. <https://doi.org/10.1016/j.jmro.2024.100171>



Contents lists available at ScienceDirect

Journal of Magnetic Resonance Open

journal homepage: www.sciencedirect.com/journal/journal-of-magnetic-resonance-open

Current state of the art of analyte scope in urine metabolome analysis by non-hydrogenative PHIP

Nele Reimets, Kerti Ausmees, Indrek Reile *

National Institute of Chemical Physics and Biophysics, Akadeemia tee 23, Tallinn 12618, Estonia

ARTICLE INFO

Keywords:

Biofluids
Urine
Metabolomics
NMR
Parahydrogen
Hyperpolarization

ABSTRACT

Non-hydrogenative PHIP (nh-PHIP) is an NMR signal enhancement technique that offers several orders of magnitude gains in detection sensitivity. It is one of the few hyperpolarization methods that have been demonstrated to be applicable to chemical analysis of biological samples and potentially metabolomics. It is, however, a chemoselective method and needs to be tuned to particular analyte and metabolite classes at a time.

Herein, we present a systematic study where we apply four nh-PHIP modifications to urine samples from two different species – human and dog. Firstly, this allows to explore the whole analyte class scope and present what information is nh-PHIP capable of providing by varying the composition of the nh-PHIP catalyst system and the sample preparation protocol. Secondly, comparing hyperpolarized spectra from urines from different species demonstrates that this hyperpolarization technique is robust and tolerant of possibly considerable matrix differences: signals of the same metabolites appear at same chemical shifts from urines that differ from one-another much more than is likely in a realistic metabolomics study. Thereby we propose the idea that nh-PHIP is ready for application in metabolomics experiments.

Introduction

The study of biofluids by metabolomics experiments is one of the central ways to understand how the biochemistry of organisms operates and responds to different conditions and inputs like disease, treatment, environmental change, diet, etc. [1] Harnessing and understanding this information is a challenge due to the size of the metabolome and its diversity [2], both in terms of chemical nature and dynamic range of concentrations. Therefore, metabolomics research is a very active area, with new applications and methods being intensively developed [3].

NMR is one of the leading tools for metabolomics research [3], where it excels in its analyte scope, but suffers from limited sensitivity. This has been the motivation behind introduction of hyperpolarization (HP) to biofluid NMR and metabolomics to broaden the accessible concentration range [4]. Up to date, at least three different hyperpolarization techniques have been successfully adapted to handle the complexity of a human biofluid: dissolution-DNP (d-DNP) [5], photo-CIDNP [6] and non-hydrogenative PHIP (nh-PHIP) [7]. Differences in the operating principles of various HP methods [8] cause all to have distinctive performance profiles and particular benefits for different application scenarios. In urine analysis for instance, d-DNP is most successful in

enhancing ^{13}C signals for quaternary carbon sites [9] and photo-CIDNP has selectivity towards aromatic amino acids [6]. The recently reviewed nh-PHIP technique [10] was initially developed for the detection N-heterocyclic analytes [11][7], but has been expanded to amino acids [12,13] and oligopeptides [14]. It is capable of accessing 30 nM analyte concentrations if combined with sample preparation by solid phase extraction (SPE) [15].

However, no HP method can be treated as a universal tool and an understanding of their scope and robustness is required to be able to select the optimal approach for a particular application. Herein we apply several sample preparation and nh-PHIP catalyst system modifications to the same specimens of human and canine urine, resulting in a qualitative demonstration of the type of information that is available from nh-PHIP. These results constitute the first example of different nh-PHIP modifications applied to the same samples, allowing to present the scope of the method in urinary metabolome analysis and proving that nh-PHIP tolerates considerable variations in sample matrix. This information can be used to direct the choice of nh-PHIP methods when applying HP to targeted or semi-untargeted NMR metabolomics.

* Corresponding author.

E-mail address: indrek.reile@kbfi.ee (I. Reile).<https://doi.org/10.1016/j.jmro.2024.100171>

Available online 28 October 2024

2666-4410/© 2024 The Authors. Published by Elsevier Inc. This is an open access article under the CC BY-NC-ND license (<http://creativecommons.org/licenses/by-nc-nd/4.0/>).

Samples and methods

Admittedly, human and canine urines are clearly different and being able to tell them apart may carry only limited value. Obvious metabolome differences are to be expected, but urines from both still consist of mostly the same metabolites [16]. We have previously shown that nh-PHIP signals' chemical shifts and intensities for nicotine and its metabolites are reproduced to a very good degree in urines from different human subjects [15]. However, considering the differences of the two species under study, human and canine urine likely present matrix differences and matrix effects that are substantially beyond what was encountered in a study involving just one species. A demonstration that nh-PHIP tolerates such differences and gives hyperpolarized signals for each analyte at reproducible chemical shifts would prove its utility and robustness in larger and more realistic metabolomics studies. nh-PHIP is a chemoselective process based on coordination of analytes to the hyperpolarization catalyst (Fig. 1). It cannot provide completely untargeted analysis as the ability to coordinate to the catalyst will always provide a layer of analyte filtering. Still, its chemoselectivity can be tuned towards different analyte classes (Table 1) by changing the cosubstrate of the catalyst in a semi-untargeted experiment (methods 2–4), or it can be tailored to detect very specific analytes by targeted SPE based sample preparation (method 1).

Method 1: targeted nh-PHIP of urinary N-heterocyclic compounds. Since the Ir-N-heterocyclic carbene based nh-PHIP catalyst performs poorly in high water content samples [22], all biofluid sample preparation approaches aim to reduce the water content in the NMR sample. One of the best ways of achieving this in a targeted experiment is solid phase extraction (SPE). It allows to enrich the sample in desired analytes while changing the solvent from water to a more nh-PHIP favorable medium, e.g., methanol [7] or chloroform [15]. We have used SPE to concentrate specific low-abundance N-heterocyclic analytes like nicotine and its metabolites [15] from urine, while removing components that interfere with nh-PHIP heteroaromatics (e.g., amino acids and ammonia).

Method 2: semi-untargeted nh-PHIP of urinary N-heterocyclic compounds. Attempts to broaden the analyte scope [21] showed that omitting SPE is possible if water is replaced and the main nh-PHIP interfering components in urine (ammonia and its source, urea) are removed by other means. This yields more information rich HP NMR spectra, retaining all non-volatile urine components that dissolve in the methanolic nh-PHIP sample environment. However, since volatiles and methanol-insoluble metabolites are lost and the spectrum still represents mostly N-heterocycles, the “SPE-free” approach can be considered a

Table 1

Modifications of the nh-PHIP experiment. All associated 1D spectra were acquired with the SEPP sequence that refocuses PHIP derived antiphase signals into in-phase doublets [18]. All 2D spectra were acquired with the nh-PHIP hyperpolarized zero-quantum (ZQ) technique that resolves the hydride signals according to their mutual ZQ frequency in the indirect domain [7]. Further technical details for sample preparation and NMR methods are available in the SI.

Method	Selectivity mechanism	Target compounds	Co-substrate	References
1	SPE and catalyst coordination	Specific N-heteroaromatics	mtz	[7,15,19,20]
2	Analyte solubility and catalyst coordination	General N-heteroaromatics	mtz	[21]
3	Analyte solubility and catalyst coordination	Amino acids	pyridine	[12]
4	Analyte solubility and catalyst coordination	Oligopeptides	3-fluoro-4-methylpyridine	[14]

semi-untargeted modification of method 1. Importantly, whereas methods 1, 2 and 4 yield samples that are stable for hours and can be re-measured by nh-PHIP multiple times, method 2 can yield samples with a significantly shorter lifetime.

Method 3: semi-untargeted nh-PHIP of amino acids. Analysis of amino acids was achieved by the Tessari group in 2021, wherein a modification of the nh-PHIP catalyst system cosubstrate component (Fig. 1, b) tuned it towards detection of proteogenic amino acids [12]. If applied to the same urines as methods 1 and 2, it allows to complement N-heterocyclic metabolites with the amino acid profiles of the same biological material. Most importantly, this approach requires no urine sample preparation. Simply mixing a small amount of urine with a mixture containing the nh-PHIP catalyst system results in a sample where the urinary ammonia and urea do not pose a problem anymore.

Method 4: semi-untargeted nh-PHIP of oligopeptides. Finally, a further modification of the procedure directs the detection profile towards oligopeptides. Replacing the pyridine cosubstrate in method 3 with 3-fluoro-4-methylpyridine allows to detect both synthetic and natural oligopeptides, but at its present state of the art it cannot be used to characterize unknown oligopeptides.

Results and discussion

The first comparison of urines from both species was done in the N-heterocycles detection regime (Fig. 2). Overlaying the spectra from human and canine urines revealed that there are substantial amounts of N-heterocyclic metabolites that overlap. This suggests that the matrix effect differences in SPE extracts are fully tolerated by the nh-PHIP catalyst system. The conclusion is that SPE-based sample treatment for nh-PHIP can be used for comparing different urines without expecting signal stability issues from matrix effects.

The nh-PHIP signal region that corresponds to pyrazine and adenosine derivatives appears remarkably similar for the two species (Fig. 2, line b). However, these spectra represent only two samples and no urine concentration normalization was done. Therefore, similarities in signal intensities may be accidental, but the emergence of the same signal patterns in the adenosines' region is logical as the same nucleosides are expected to appear in both species. Overall, there seem to be more signal responses from the human sample (Fig. 2, black), but identification of such signals is beyond the scope of this work and would not necessarily be important to metabolomics projects that aim for classification of samples.

Even more N-heterocycle signal responses were obtained when SPE

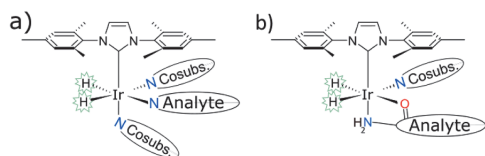


Fig. 1. Catalyst systems for different nh-PHIP modifications are synthesized in situ in the NMR tube. Each analyte is detected by evaluating the chemical shifts of the hyperpolarized hydride nuclei (highlighted in green). These signals are very sensitive to the identity of the coordinating analyte and are usually 2...3-orders of magnitude enhanced over regular NMR. Using the hydrides for hyperpolarized detection for biologically relevant analytes was first suggested almost 20 years ago [17] and later developed into a 2D hyperpolarized NMR chemosensing technique [7,11]. a) For detecting N-heterocyclic analytes (Table 1, methods 1–2), the catalyst system consists of the iridium-based catalyst (e.g., 1 mM) and an 18-fold excess (e.g., 18 mM) of a specific cosubstrate 1-methyl-1,2,3-triazol. The catalyst forms transient complexes with analytes; b) for detecting amino acids and oligopeptides (Table 1, methods 3–4), the cosubstrate is changed to pyridine (for amino acids) or 3-fluoro-4-methyl pyridine (for oligopeptides). They form more stable bidentate complexes with the catalyst by heating the sample prior to analysis.

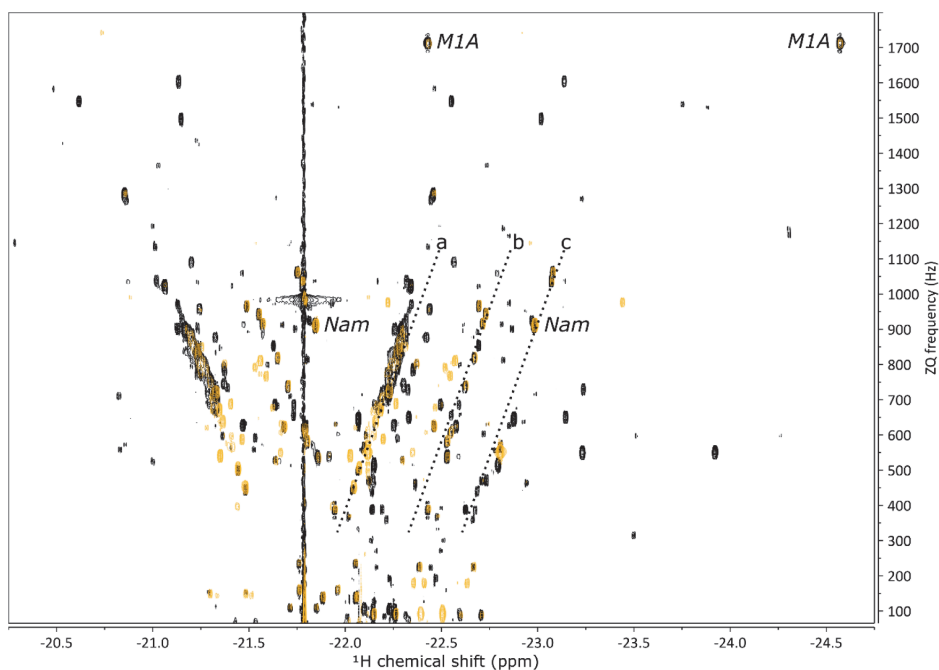


Fig. 2. 2D nh-PHIP spectra of dog (yellow) and human (black) urine SPE extracts. Both samples prepared and analyzed under identical conditions. Hydride resonances of certain metabolite classes can be recognized from earlier publications: 'a' marks the usual locations for signals representing guanosine and imidazole derivatives [7]; 'b' marks typical signal regions for pyrazines, adenosine and its derivatives [7,20]; 'c' marks pyridine derivatives, e.g., nicotinamide [7,20]. Chemical shifts and the ZQ frequency of annotated hydride signals for nicotinamide (Nam) and 1-methyl adenosine (M1A) coincide with previously published database values [20].

was omitted from sample preparation with Method 2 (Figure S1), but the overall conclusions remained. While some metabolites still overlap, the SPE-free approach also yields more analytes that seem to either be specific to dog or at a significantly higher concentration in canine urine. As a side-effect, this procedure also retains urinary amino acids, which form significantly more stable bidentate complexes with the catalyst (Fig. 1, b) [12], making it inaccessible to N-heterocycles. While this will, in principle, allow simultaneous detection of amino acids and N-heterocyclic metabolites (Figure S2), the formation of amino acid complexes with 1-methyl-1,2,3-triazol is slow and causes the sample to change during measurement. We have circumvented this issue by increasing the Ir-catalyst loading severalfold to retain sufficient N-heterocycle specific complex (Fig. 1, a), even in the presence of amino acids. However, in practice this does not always yield stable samples, and the practical sample lifetime is usually around 1–2 h

A similar trend repeats itself when the same samples are subjected to the amino acids' detection protocol (method 3) with pyridine as cosubstrate (Fig. 1, b). Both urines present mostly overlapping amino acid signals, albeit at different relative concentrations (Fig. 3). This is the expected result since the main proteinogenic amino acids are universal across species. But also, a series of distinctive (suspected) amino acid signals (dotted line in Fig. 3) were observed only in human urine. These results suggest that nh-PHIP is also suitable for reliable evaluation of amino acid profiles in different urines, yielding signals at the same chemical shifts if same amino acids are present in both samples.

Finally, a modification of the amino acid detection protocol, wherein the pyridine cosubstrate is replaced with 3-fluoro-4-methyl pyridine [14], was tested on the oligopeptide profiles of the same urines (method 4, Fig. 4). The resulting oligopeptide signal spectrum is comparatively weak both in terms of signal intensities and numbers of signals at the

typical hydride chemical shifts region for oligopeptides at around -30 ppm. We suggest that although nh-PHIP performance of these particular urinary oligopeptides may not be optimal, there are very little oligopeptides in healthy subjects' urines in the first place as they are hydrolyzed to amino acids and reabsorbed renally [23,24]. If more detailed oligopeptides' nh-PHIP spectra are required, some form of analyte pre-concentration is advised.

Detected oligopeptide signals were few enough to be mostly distinguishable by 1D nh-PHIP experiments, although 2D detection schemes would be feasible as well. Importantly, most oligopeptide signals that were detected in canine urine overlapped with same signals in human sample, demonstrating that also oligopeptide detection is reliable across very different urines. As a further note, the oligopeptide detection protocol also retains amino acid detection capability (Figure S3). The overall amino acid signal intensities were very high, but due to the change in cosubstrate (Fig. 1, b), the chemical shifts of the amino acid containing complexes hydride signals are not compatible with the database from Sellies et al. [12].

Conclusions

This contribution demonstrates that nh-PHIP can be used to compare urines from considerably different origins. We acknowledge that the sensitivity enhancement comes at a price in the available spectroscopic information, since the hyperpolarized hydride signals (Fig. 1) carry very limited direct structural information. Yet, the chemical shifts of these signals in all explored spectral areas and analyte types are robust enough for detecting the same analytes at the same chemical shifts and spotting analytes that are unique to a particular sample. It has been demonstrated that such signals can be assigned by internal standard spiking [7] or by

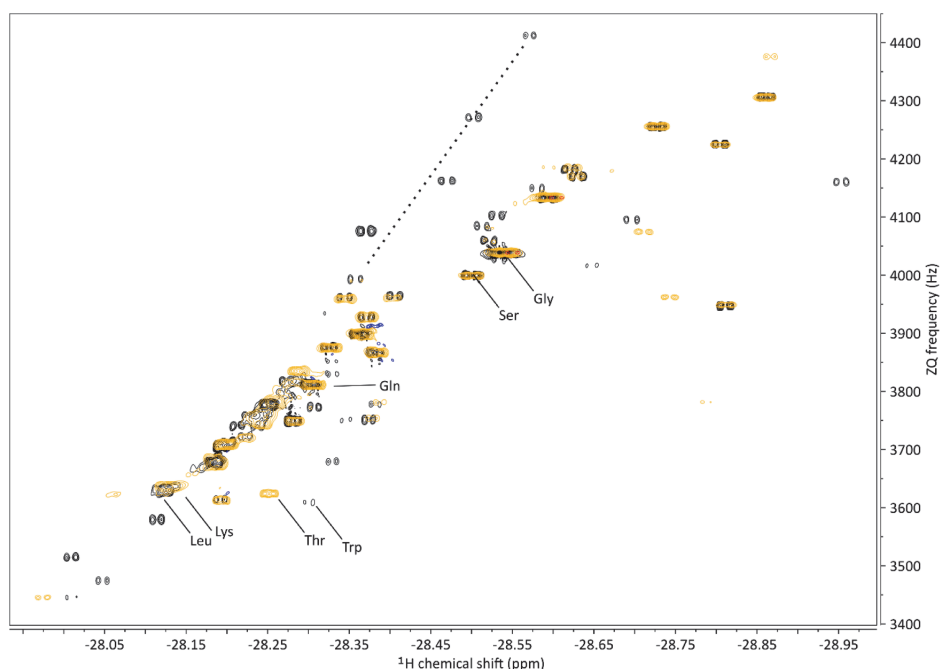


Fig. 3. Comparison nh-PHIP detectable amino acid profiles. For illustrative purposes, some arbitrarily chosen amino acids were annotated by comparison with data from Ref. [12], which includes hydrides' chemical shifts for 18 amino acids. Human sample specific signals (dotted line) represent heretofore unknown amino acids or amino acid-like metabolites.

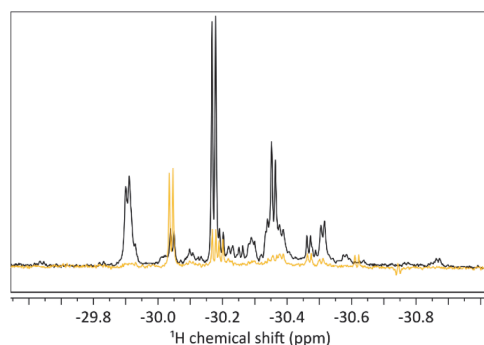


Fig. 4. Comparison of oligopeptide profiles from human (black) and canine (yellow) urines. Some signals clearly overlap, while the human sample seems to be richer in oligopeptides.

building a reference database [20]. Therefore, nh-PHIP is becoming a mature enough method to be considered for practical metabolomics research. It also presents the opportunity to quantify analytes [12,15,19,21] by internal standard calibration. While this involves more steps than regular NMR, it may still present a benefit over quantification in mass spectrometry (MS) of biofluids, where isotopically labelled reference standards are often required [25].

The spectra above demonstrate, how specific metabolite classes can be resolved in urine samples by applying different nh-PHIP modifications that have not been directly compared before. Although such comparison results in different datasets for different analyte classes, it is not necessarily a problem as the metabolomics community has already

adopted multi-omics approaches where different analytical modalities are integrated in a single study [26]. In the same lines, we suggest that all or some modifications of nh-PHIP can be used in future metabolomics studies and integrated into a single dataset that may also include regular NMR metabolomics and MS data. That way hyperpolarized NMR could be used to expand the dynamic range of NMR detectable metabolites, expanding its application scope.

CRediT authorship contribution statement

Nele Reimets: Writing – review & editing, Investigation, Data curation, Conceptualization. **Kerti Ausmees:** Writing – review & editing, Supervision, Data curation, Conceptualization. **Indrek Reile:** Writing – original draft, Supervision, Project administration, Funding acquisition, Formal analysis, Data curation, Conceptualization.

Declaration of competing interest

The authors declare that they have no known competing financial interests or personal relationships that could have appeared to influence the work reported in this paper.

Acknowledgements

We acknowledge financial support from the Development Fund of the National Institute of Chemical physics and Biophysics. The project was supported by the Estonian Centre of Analytical Chemistry (AKKI, TT4).

Supplementary materials

Supplementary material associated with this article can be found, in

the online version, at doi:10.1016/j.jmro.2024.100171.

Data availability

Data will be made available on request.

References

- [1] M.A. Siddiqui, S. Pandey, A. Azim, N. Sinha, M.H. Siddiqui, Metabolomics: an emerging potential approach to decipher critical illnesses, *Biophys. Chem.* 267 (2020) 106462, <https://doi.org/10.1016/j.bpc.2020.106462>.
- [2] D.S. Wishart, A. Guo, E. Oler, F. Wang, A. Anjum, H. Peters, R. Dizon, Z. Sayeeda, S. Tian, B.L. Lee, M. Berjanskii, R. Mah, M. Yamamoto, J. Jovel, C. Torres-Calzada, M. Hiebert-Giesbrecht, V.W. Lui, D. Varshavi, D. Varshavi, D. Allen, D. Arndt, N. Khetarpal, A. Sivakumaran, K. Harford, S. Sanford, K. Yee, X. Cao, Z. Budinski, J. Liigand, L. Zhang, J. Zheng, R. Mandal, N. Karu, M. Dambrova, H.B. Schiöth, R. Greiner, V. Gautam, HMDB 5.0: the human metabolome database for 2022, *Nucleic Acids Res.* 50 (2022) D622–D631, <https://doi.org/10.1093/nar/gkab1062>.
- [3] D.S. Wishart, L.L. Cheng, V. Copié, A.S. Edison, H.R. Eghbalnia, J.C. Hoch, G. J. Gouveia, W. Pathmasiri, R. Powers, T.B. Schock, L.W. Sumner, M. Uchimiya, NMR and metabolomics—a roadmap for the future, *Metabolites* 12 (2022) 678, <https://doi.org/10.3390/metabo12080678>.
- [4] V. Ribay, C. Praud, M.P.M. Letertre, J.-N. Dumez, P. Giraudeau, Hyperpolarized NMR metabolomics, *Curr. Opin. Chem. Biol.* 74 (2023) 102307, <https://doi.org/10.1016/j.cbpa.2023.102307>.
- [5] A. Dey, B. Charrier, K. Lemaitre, V. Ribay, D. Eshchenko, M. Schnell, R. Melzi, Q. Stern, S.F. Cousin, J.G. Kempf, S. Jannin, J.-N. Dumez, P. Giraudeau, Fine optimization of a dissolution dynamic nuclear polarization experimental setting for 13 C NMR of metabolic samples, *Magn. Reson.* 3 (2022) 183–202, <https://doi.org/10.5194/MR-3-183-2022>.
- [6] L.T. Kuhn, S. Weber, J. Bargon, T. Parella, M. P. M. Pérez-Trujillo, Hyperpolarization-enhanced NMR spectroscopy of unaltered biofluids using photo-CIDNP, *Anal. Chem.* 96 (2024) 102–109, <https://doi.org/10.1021/acs.analchem.3c03215>.
- [7] L. Sellies, I. Reile, R.L.E.G. Aspers, M.C. Feiters, F.P.J.T. Rutjes, M. Tessari, Parahydrogen induced hyperpolarization provides a tool for NMR metabolomics at nanomolar concentrations, *Chem. Commun.* 55 (2019) 7235–7238, <https://doi.org/10.1039/C9CC02186H>.
- [8] J. Eills, D. Budker, S. Cavagnero, E.Y. Chekmenev, S.J. Elliott, S. Jannin, A. Lesage, J. Matysik, T. Meersmann, T. Prisner, J.A. Reimer, H. Yang, I.V. Koptiug, Spin hyperpolarization in modern magnetic resonance, *Chem. Rev.* 123 (2023) 1417–1551, <https://doi.org/10.1021/acs.chemrev.2c00534>.
- [9] V. Ribay, A. Dey, B. Charrier, C. Praud, J. Mandral, J. Dumez, M.P.M. Letertre, P. Giraudeau, Hyperpolarized 13 C NMR spectroscopy of urine samples at natural abundance by quantitative dissolution dynamic nuclear polarization, *Angew. Chemie Int. Ed.* 62 (2023), <https://doi.org/10.1002/anie.202302110>.
- [10] R. Fraser, F.P.J.T. Rutjes, M.C. Feiters, M. Tessari, Analysis of complex mixtures by chemosensing NMR using para -hydrogen-induced hyperpolarization, *Acc. Chem. Res.* 55 (2022) 1832–1844, <https://doi.org/10.1021/acs.accounts.1c00796>.
- [11] N.K.J. Hermkens, N. Eshuis, B.J.A. van Weerdenburg, M.C. Feiters, F.P.J.T. Rutjes, S.S. Wijmenga, M. Tessari, NMR-based chemosensing via p -H 2 hyperpolarization: application to natural extracts, *Anal. Chem.* 88 (2016) 3406–3412, <https://doi.org/10.1021/acs.analchem.6b00184>.
- [12] L. Sellies, R.L.E.G. Aspers, M.C. Feiters, F.P.J.T. Rutjes, M. Tessari, Parahydrogen hyperpolarization allows direct NMR detection of α -amino acids in complex (Bio) mixtures, *Angew. Chemie Int. Ed.* 60 (2021) 26954–26959, <https://doi.org/10.1002/anie.202109588>.
- [13] L. Dreisewerd, R.L.E.G. Aspers, M.C. Feiters, F.P.J.T. Rutjes, M. Tessari, NMR discrimination of D- and L- α -Amino Acids at submicromolar concentration via parahydrogen-induced hyperpolarization, *J. Am. Chem. Soc.* 145 (2023) 1518–1523, <https://doi.org/10.1021/jacs.2c11285>.
- [14] N. Reimets, K. Ausmees, S. Vija, A. Trummal, M. Uudsemaa, I. Reile, Parahydrogen hyperpolarized NMR detection of underivatized short oligopeptides, *Analyst* 148 (2023) 5407–5415, <https://doi.org/10.1039/D3AN01345F>.
- [15] N. Reimets, K. Ausmees, S. Vija, I. Reile, Developing analytical applications for parahydrogen hyperpolarization: urinary elimination pharmacokinetics of nicotine, *Anal. Chem.* 93 (2021) 9480–9485, <https://doi.org/10.1021/acs.analchem.1c01281>.
- [16] P.M. Whalley, M. Bartels, K.S. Bentley, M. Corvaro, D. Funk, M.W. Himmelstein, B. Neumann, C. Strupp, F. Zhang, J. Mehta, An in vitro approach for comparative interspecies metabolism of agrochemicals, *Regul. Toxicol. Pharmacol.* 88 (2017) 322–327, <https://doi.org/10.1016/j.yrtph.2017.03.020>.
- [17] N.J. Wood, J.A. Brannigan, S.B. Duckett, S.L. Heath, J. Wagstaff, Detection of picomole amounts of biological substrates by para -hydrogen-enhanced NMR methods in conjunction with a suitable receptor complex, *J. Am. Chem. Soc.* 129 (2007) 11012–11013, <https://doi.org/10.1021/ja074286k>.
- [18] N. Eshuis, R.L.E.G. Aspers, B.J.A. van Weerdenburg, M.C. Feiters, F.P.J.T. Rutjes, S. S. Wijmenga, M. Tessari, 2D NMR trace analysis by continuous hyperpolarization at high magnetic field, *Angew. Chemie Int. Ed.* 54 (2015) 14527–14530, <https://doi.org/10.1002/anie.201507831>.
- [19] I. Reile, N. Eshuis, N.K.J. Hermkens, B.J.A. van Weerdenburg, M.C. Feiters, F.P.J.T. Rutjes, M. Tessari, NMR detection in biofluid extracts at sub- μ M concentrations via para-H 2 induced hyperpolarization, *Analyst* 141 (2016) 4001–4005, <https://doi.org/10.1039/C6AN00804F>.
- [20] K. Ausmees, N. Reimets, I. Reile, Understanding parahydrogen hyperpolarized urine spectra: the case of adenosine derivatives, *Molecules* 27 (2022) 802, <https://doi.org/10.3390/molecules27030802>.
- [21] K. Ausmees, N. Reimets, I. Reile, Parahydrogen hyperpolarization of minimally altered urine samples for sensitivity enhanced NMR metabolomics, *Chem. Commun.* 58 (2022) 463–466, <https://doi.org/10.1039/D1CC05665D>.
- [22] N.K.J. Hermkens, R.L.E.G. Aspers, M.C. Feiters, F.P.J.T. Rutjes, M. Tessari, Trace analysis in water-alcohol mixtures by continuous p -H 2 hyperpolarization at high magnetic field, *Magn. Reson. Chem.* 56 (2018) 633–640, <https://doi.org/10.1002/mrc.4692>.
- [23] S. Silbernagl, The renal handling of amino acids and oligopeptides, *Physiol. Rev.* 68 (1988) 911–1007, <https://doi.org/10.1152/physrev.1988.68.3.911>.
- [24] M. Gekle, Renal tubule albumin transport, *Annu. Rev. Physiol.* 67 (2005) 573–594, <https://doi.org/10.1146/annurev.physiol.67.031103.154845>.
- [25] S. Alseekh, A. Aharoni, Y. Brotman, K. Contrepolis, J. D'Auria, J. Ewald, J.C. Ewald, P.D. Fraser, P. Giavalisco, R.D. Hall, M. Heinemann, H. Link, J. Luo, S. Neumann, J. Nielsen, L. Perez de Souza, K. Saito, U. Sauer, F.C. Schroeder, S. Schuster, G. Siuzdak, A. Skirycz, L.W. Sumner, M.P. Snyder, H. Tang, T. Tohge, Y. Wang, W. Wen, S. Wu, G. Xu, N. Zamboni, A.R. Fernie, Mass spectrometry-based metabolomics: a guide for annotation, quantification and best reporting practices, *Nat. Methods* 18 (2021) 747–756, <https://doi.org/10.1038/s41592-021-01197-1>.
- [26] M.P.M. Letertre, G. Dervilly, P. Giraudeau, Combined nuclear magnetic resonance spectroscopy and mass spectrometry approaches for metabolomics, *Anal. Chem.* 93 (2021) 500–518, <https://doi.org/10.1021/acs.analchem.0c04371>.

Curriculum vitae

Personal data

Name:	Nele Reimets
Date of birth:	03.04.1996
Place of birth:	Tallinn, Estonia
Citizenship:	Estonian

Contact data

E-mail:	nele.reimets@kbfi.ee
---------	----------------------

Education

2020–2024	Tallinn University of Technology, PhD
2018–2020	Tallinn University of Technology, MSc
2015–2018	Tallinn University of Technology, BSc
2012–2015	Gustav Adolf Grammar School

Language competence

Estonian	native
English	proficient
Swedish	independent
Russian	beginner

Professional employment

01.09.2020–31.08.2024	National Institute of Chemical Physics and Biophysics, Junior Researcher (1.00)
01.07.2018–24.08.2018	European Organization for Nuclear Research CERN, Summer Student (1.00)
01.04.2017–30.06.2017	North Estonia Medical Centre Foundation, trainee (0.50)

Honours & awards

2023	Kristjan Jaak Short Study Visit Scholarship
2023	SMASH 2023 Scholarship
2022	SMASH 2022 Scholarship
2022	Kristjan Jaak Short Study Visit Scholarship
2022	Dora Pluss Scholarship
2021	Student stipend at the International Hyperpolarization Conference HYP21
2021	Dora Pluss Scholarship
2019	Dora Pluss Scholarship
2017	Cambrex Tallinn Bachelor Scholarship

R&D related managerial and administrative work

2023–...	Tallinn University of Technology member of the Senat's Scientific Committee
2023–2023	Tallinn University of Technology member of the Senat

Teaching and supervision

01.-06.2022	Supervising two undergraduates
01.-04.2021	Supervising an undergraduate

Elulookirjeldus

Isikuandmed

Nimi:	Nele Reimets
Sünniaeg:	03.04.1996
Sünnikoht:	Tallinn, Eesti
Kodakondsus:	Eesti

Kontaktandmed

E-post:	nele.reimets@kbfi.ee
---------	----------------------

Hariduskäik

2020–2024	Tallinna Tehnikaülikool, PhD
2018–2020	Tallinna Tehnikaülikool, MSc
2015–2018	Tallinna Tehnikaülikool, BSc
2012–2015	Gustav Adolfi Gümnaasium

Keelteoskus

eesti keel	emakeel
inglise keel	kõrgtase
rootsi keel	kesktase
vene keel	algtase

Teenistuskäik

01.09.2020–31.08.2024	Keemilise ja Bioloogilise Füüsika Instituut, nooremteadur (1,00)
01.07.2018–24.08.2018	Euroopa Tuumauuringute Keskus CERN, suvetudeng/praktikant (1,00)
01.04.2017–30.06.2017	SA Põhja-Eesti Regionaalhaigla, praktikant (0,50)

Teaduspreemiad ja tunnustused

2023	Kristjan Jaagu välislähetuste stipendium
2023	SMASH 2023 stipendium
2022	SMASH 2022 stipendium
2022	Kristjan Jaagu välislähetuste stipendium
2022	Dora Pluss „Lühiajaline õpiränne” stipendium
2021	Rahvusvahelise hüperpolarisatsiooni konverentsi HYP21 stipendium
2021	Dora Pluss „Lühiajaline õpiränne” stipendium
2019	Dora Pluss „Lühiajaline õpiränne” stipendium
2017	Cambrex Tallinn stipendium

Teadusorganisatsiooniline ja -administratiivne tegevus

2023–...	Tallinna Tehnikaülikooli senati teaduskomisjoni liige
2023–2023	Tallinna Tehnikaülikooli Senati liige

Juhendamised

01.-06.2022	Bakalaureuseõppe tudengite praktikatöö juhendaja
01.-04.2021	Bakalaureuseõppe tudengi praktikatöö juhendaja

ISSN 2585-6901 (PDF)
ISBN 978-9916-80-224-3 (PDF)